112

CENTRAL RESEARCH LIBRARY
DOCUMENT COLLECTION

ORNL-2693
Controlled Thermonuclear Processes
TID-4500 (14th ed.)

MARTIN MARIETTA ENERGY SYSTEMS LIBRARIES
3 4456 0361308 9

THERMONUCLEAR PROJECT SEMIANNUAL REPORT

FOR PERIOD ENDING JANUARY 31, 1959

OAK RIDGE NATIONAL LABORATORY
CENTRAL RESEARCH LIBRARY
CIRCULATION SECTION
4500N ROOM 175
LIBRARY LOAN COPY
DO NOT TRANSFER TO ANOTHER PERSON
If you wish someone else to see this report, send in name with report and the library will arrange a loan.
UCN-7969 (3 9-77)

OAK RIDGE NATIONAL LABORATORY
operated by
UNION CARBIDE CORPORATION
for the
U.S. ATOMIC ENERGY COMMISSION

Printed in USA. Price $2.75. Available from the

Office of Technical Services
Department of Commerce
Washington 25, D.C.

LEGAL NOTICE

This report was prepared as an account of Government sponsored work. Neither the United States, nor the Commission, nor any person acting on behalf of the Commission:

A. Makes any warranty or representation, expressed or implied, with respect to the accuracy, completeness, or usefulness of the information contained in this report, or that the use of any information, apparatus, method, or process disclosed in this report may not infringe privately owned rights; or

B. Assumes any liabilities with respect to the use of, or for damages resulting from the use of any information, apparatus, method, or process disclosed in this report.

As used in the above, "person acting on behalf of the Commission" includes any employee or contractor of the Commission, or employee of such contractor, to the extent that such employee or contractor of the Commission, or employee of such contractor prepares, disseminates, or provides access to, any information pursuant to his employment or contract with the Commission, or his employment with such contractor.

ORNL-2693
Controlled Thermonuclear Processes
TID-4500 (14th ed.)

Contract No. W-7405-eng-26

THERMONUCLEAR PROJECT SEMIANNUAL REPORT

For Period Ending January 31, 1959

DATE ISSUED

MAY - 5 1959

OAK RIDGE NATIONAL LABORATORY
Oak Ridge, Tennessee
operated by
UNION CARBIDE CORPORATION
for the
U. S. ATOMIC ENERGY COMMISSION

MARTIN MARIETTA ENERGY SYSTEMS LIBRARIES

3 4456 0361308 9

THERMONUCLEAR PROJECT SEMIANNUAL REPORT

INTRODUCTION

This document describes the progress of the ORNL Thermonuclear Program, the "Sherwood Project," since the publication of the preliminary report (*The ORNL Thermonuclear Program*, ORNL-2457, Jan. 15, 1958). Work is still largely devoted to the Direct Current Experiment (DCX), the first of the planned stages of the program, although some conceptual work has been done on the second stage, the DCX-2 (formerly called ORION). The principal events sought in the DCX are a trapped beam, "burnout," and a definite thermonuclear reaction; it is hoped that a more nearly self-sustaining reaction will be achieved in the DCX-2. A definite thermonuclear reaction has not been achieved, but a proton plasma with a density of $\sim 10^9$–10^{10} particles/cm^3 has been trapped for 12 to 14 msec at $\sim 5 \times 10^{-7}$ mm Hg. Burnout, whereby impurity atoms in the plasma region will be removed by ionization faster than new ones enter the region, is being approached from two directions: improvements in the vacuum system and increase of the ion beam input current. In the past six months the ion beam current has been increased from 200 μa to 4–5 ma, and the reliability of the DCX machine has been very much improved. The improved reliability has permitted extended studies of hydrogen and carbon arc plasmas, and much new information is being gathered. Some of the characteristics of the machine are as follows:

Mirror field strength	9500 gauss in midplane, 2100 gauss at center of coils (now run at 6700 gauss for H_2^+ experiments)
Power required for mirror fields	2700 kw (dc)
Maximum plasma density	10^9 to 10^{10} protons/cm^3 at 5×10^{-7} mm Hg
Maximum plasma containment time	12 to 14 msec at maximum density
Ion beam current, I	4 to 5 ma at 600 kev (10 ma maximum)
Best vacuum attained	$\sim 3.5 \times 10^{-7}$ mm Hg (with arc running) 2.5×10^{-8} mm Hg (without arc, and after 24-hr baking)
Pressure requirements for burnout	$2I \times 10^{-8}$ mm Hg (for deuterons in deuterium) $2.5I \times 10^{-7}$ mm Hg (for protons in hydrogen)
Carbon arc plasma frequency	140,000 Mc
Carbon arc electron density	2×10^{14} electrons/cm^3
Carbon arc cathode consumption	8 in. in 2 hr of operation

THE DCX GENEVA EXHIBIT

E. D. Shipley M. Rankin

Fusion research was a major theme of the Second United Nations International Conference on the Peaceful Uses of Atomic Energy held at Geneva, Switzerland, during September 1958, and Project Sherwood at ORNL designed and built two operating, low-energy machines (DCX-EP) for the United States Fusion Exhibit. Figure I shows one of these machines at the exhibit area.

The basic principles of DCX machines were demonstrated and developments in component parts such as ion sources and electrode assemblies were displayed. The trapped ring of energetic atomic ions – formed by molecular dissociation by a carbon arc in a magnetic field and made incandescent by interaction with a cloud of added particles – was visible. A photograph of the ring, as seen through a side window of the DCX, is shown in Fig. II. Five papers covering the fundamental theoretical and experimental studies on Project Sherwood at ORNL were presented by members of the Laboratory.

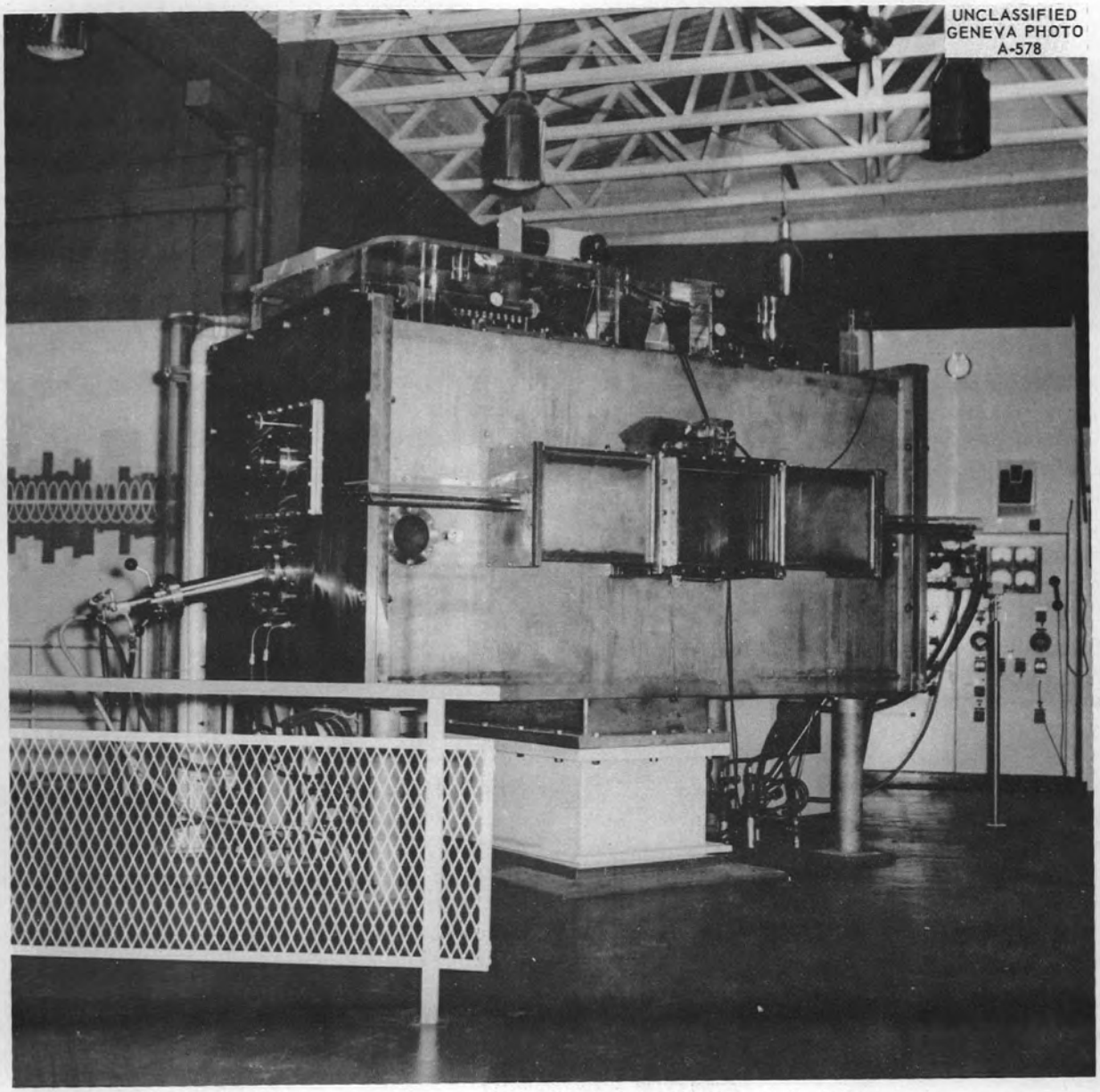

Fig. I. DCX-EP at Geneva.

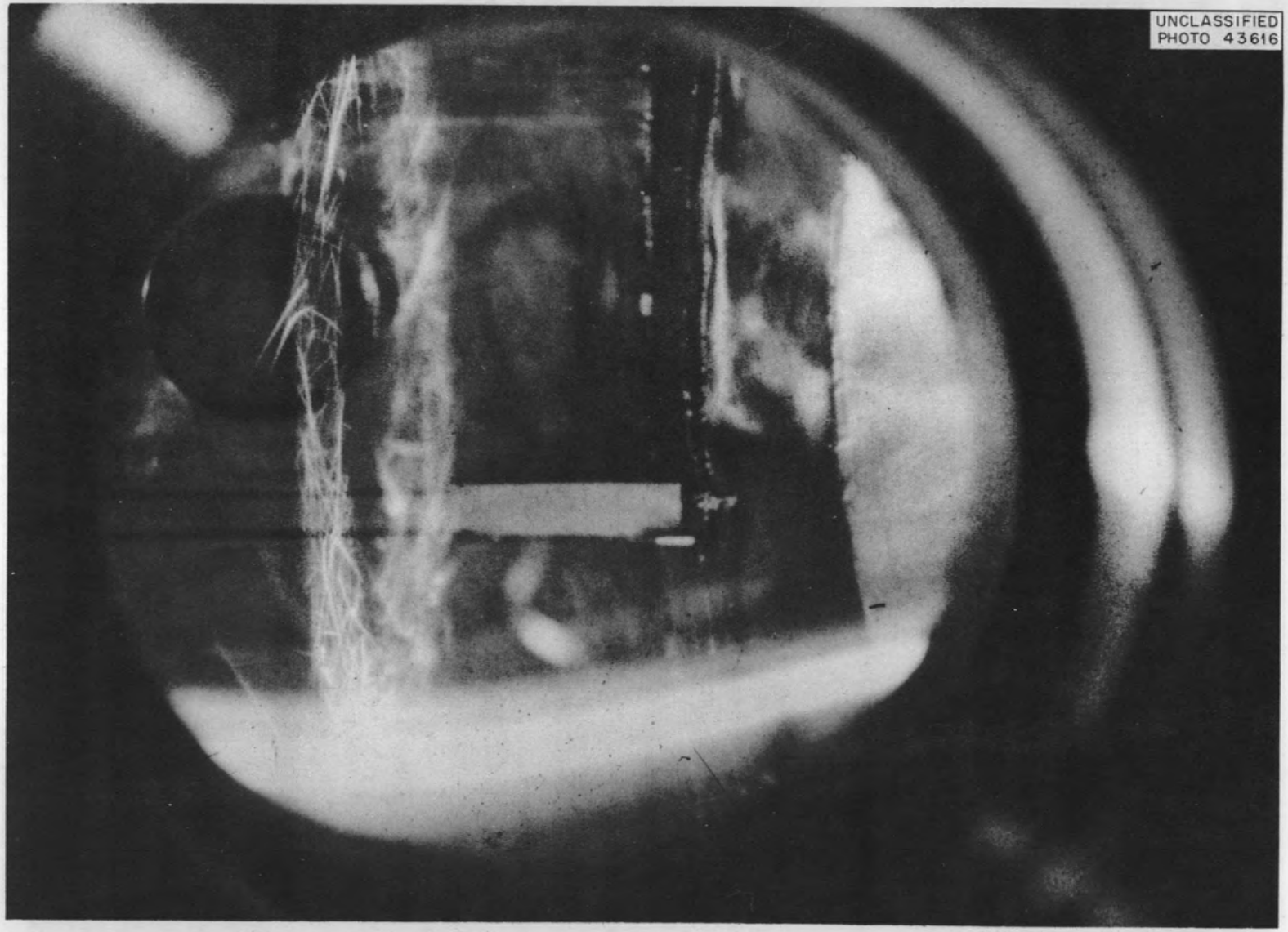

Fig. 11. Trapped Ion Ring in DCX-EP.

Some of the specifications for the DCX Geneva machines are:

Magnetic field strength	
At mirrors	4000 gauss
At machine center	2000 gauss
Operating pressure	10^{-5} mm Hg
Power requirements	
Alternating current	288 kw
Direct current (magnet coils)	600 kw
Ion source	300-ma, 30-kev grid type molecular
Ion beam energy	20,000 ev
Cooling-water requirements	175 gpm
Total cost of equipment	$350,000

Preparation of the Geneva Exhibit was, of necessity, achieved in a short time by a concentrated effort. The rapid sequence of development is indicated by the following (highly condensed) time table.

March 28, 1958	Decision made to build two DCX machines
April 8–May 2, 1958	Design and development
May 2–June 10, 1958	Fabrication and assembling of machines
June 10–July 28, 1958	Debugging period at ORNL; a boat shipment of heavy parts was made on June 17, and air shipments of vacuum tanks, ion sources, and roughing pumps were made on July 16 and 25
August 4–September 1, 1958	Debugging at Geneva site
September 1–September 13, 1958	Operation of machines during exhibit

One of the two experimental DCX devices which were used during the scientific exposition in Geneva is being adapted for experiments with a new 130-kev H_2^+ and D_2^+ ion source. Studies about ion beam focusing are being made for this device.

GENEVA EXHIBIT ION SOURCE

J. S. Luce

A requirement for the ion source of the Geneva Exhibit machine, dictated by practical considerations of voltage limitations and possible vacuum systems, was that it give a high current at approximately 30 kv. After extensive modifications, made necessary by the inhomogeneity of the Geneva DCX magnetic field, the grid-type source previously developed at ORNL was used satisfactorily.

To study the problems presented by the inhomogeneous field, the Geneva field was simulated by the addition of auxiliary coils to a portion of the electromagnetic track. In this facility the source drain system, the arc geometry, and focusing problems were studied.

Addition of a very small dump near the beam exit slit was found to be the only change needed in the drain system. The arc geometry was changed experimentally until conditions comparable to operation in a uniform magnetic field were achieved.

The most difficult problem was proper focusing of the beam to intersect the carbon arc. Axial forces were such as to produce convergence of the beam at the midplane. This axial focusing caused radial defocusing, so that the beam had an undesirable radial spread as it passed through the arc. The radial defocusing problem was solved by shaping the accelerating grid in such a way that electrostatic forces overcame the magnetic axial focusing forces. Determination of radial focusing in the nonuniform field was done mathematically.

Six sources were designed and built from the specifications which resulted from the program just outlined. It was found that their operation was quite stable and dependable. Beams of D_2^+ in excess of 500 ma from a source having 1 in.^{2} of arc area and an acceleration potential of 30 kv were common. It was found desirable to limit the sources at Geneva to 100 to 200 ma because of the undesirable neutron flux. Also, higher current was not needed. The good visible rings of trapped D^+ achieved with injected currents below 200 ma were due to the surprisingly good pressure which reduced charge exchange and increased the lifetime of the trapped particles.

THE BEHAVIOR OF SMALL PARTICLES DROPPED IN THE CARBON ARC

J. S. Luce

Successful operation of the carbon arc and grid ion source was achieved more or less on schedule, but the appearance of the trapped ring of atomic ions proved to be a disappointment. It had been expected that a sparse, uniform cloud of carbon particles, covering the entire region through which the ion beam circulated, would be heated to incandescence by the trapped ions and thus reveal them as a glowing ring – and "shakers" of two types had been built to provide such a cloud. However, experience soon showed that the carbon did not penetrate the entire region and that only a part of the ring was made visible. Since both shaker units were shipped to Geneva before this problem was solved, it was necessary to mock up the arc and beam arrangement in a Beta tank so that experiments aimed at making the entire beam visible could be continued.

During the course of these experiments it was found that rotational forces set up in a plasma region near the arc caused small carbon pieces (1 to 30 μ) to be thrown out violently at right angles so that the region through which the trapped atomic beam passed was only partially filled with carbon.

After a great deal of experimentation it was found that molybdenum metal of 3- to 30-μ size would penetrate the rotating plasma and almost touch the arc before being thrown out. In this manner the ring was eventually made completely visible. It was found that metals heavier than molybdenum (such as tungsten) would actually penetrate into the main arc column, causing the arc to become unstable and sometimes to go out.

SUMMARY

PART I. DCX EXPERIMENTAL PROGRAM

1. DCX PLASMA STUDIES

Neutral particle collection, microwave equipment, and mathematical approximations were used in studies of the DCX plasma. Of particular interest were the density and containment time of the plasma; the portion of the injected ion current which could be accounted for by measurement of the neutral particles created by charge exchange (and the variation, if any, of this total accountable current with decrease of pressure); the relationship of plasma density and small-amplitude oscillations; ion orbits and containment; and the distributions of deuterons and electrons in plasma.

1.1. Studies of DCX Plasma by Neutral Particle Collection

Measurements of decay times and the spatial extent of plasmas trapped in DCX have been attempted. At the lowest pressures achieved (5×10^{-7} mm Hg), a proton plasma density $\sim 10^9$ to 10^{10} cm^{-3} was trapped for a mean time of 12 to 14 msec. At these pressures, the trapped beam, which is confined to a thin torus at higher background pressures (10^{-5} mm Hg), appears to have spread along the magnetic axis to a width of perhaps 8 in.

1.2. Microwave Diagnostics of DCX Plasma

One microwave measurement of a deuterium plasma gave brief indications of a plasma density of 1×10^{11} electrons/cm^3; but succeeding runs with hydrogen, whose density may have been below the limit of detection of the instrument used (1×10^{10} electrons/cm^3), gave no such indications. An interferometer was constructed which should, after minor modifications, permit measurements down to 3×10^9 electrons/cm^3. In an attempt to increase phase-shift detection sensitivity and the signal-to-noise ratio and to eliminate the effects of slow thermal and mechanical drifts, equipment is being developed for synchronous detection of the interferometer output with the DCX input beam switched on and off at a constant rate.

1.3. Plasma Containment

Ion Orbits in DCX Plasma. – Single ion orbits in the azimuthally symmetric DCX magnetic field in the absence of collisions were studied with the aid of the Oracle. The emphasis of the work was on orbits encircling the axis of symmetry of the field. Among these orbits there is a class absolutely contained.

Unstable Plasma Oscillations in a Magnetic Field. – Linearized Vlasov equations were used in a study of small-amplitude oscillations of a quasi-neutral plasma in a uniform, time-independent, externally produced magnetic field. Perturbations of the magnetic field were neglected. Instability of a deuterium plasma is predicted when its density exceeds about 10^7 particles/cm^3 in a magnetic field of about 10^4 gauss (the field used in the DCX). The theory presented gives no information about the factors which must ultimately limit the amplitude of the oscillations.

1.4. Deuteron and Electron Distributions in DCX

Transport equations are being solved numerically to determine the transient and steady-state energy distribution of ions and electrons in the DCX plasma.

2. CARBON ARC STUDIES

The objectives of the measurements and calculations described here are:

1. a better understanding of molecular dissociation in the DCX,
2. knowledge of possible arc-induced loss mechanisms for energetic ions,
3. utilization of the comparatively stable plasma characteristics of the carbon arc in the evolution of a reasonable mathematical model which should yield a better understanding of plasma physics,
4. an increased knowledge of ion and electron drift velocities, current densities, and ordered motion.

2.1. Some Spectroscopic Studies of the Energetic Carbon Arc

Spectroscopic studies of the 5-ft-long, 300-amp carbon arc showed Doppler broadening corresponding to ion motions with kinetic energy of 50 ev

(400,000°K). Slant effects were observed which were believed to indicate localized variations in the electric, and possibly the magnetic, fields within the arc core. Oxygen resonance lines and very strong resonance lines of C^+, C^{++}, and C^{3+} were observed in the Long Solenoid Machine (LSM) and the DCX. The electron energies required to excite various states of carbon and oxygen are tabulated. Preliminary studies of the intensity variation of selected lines and integrated visible light indicate an increase of average electron flux with current. The upper limits of electron temperature are thought to be ~20 ev at 300 amp and 31 ev at 160 amp – and if the trend toward higher electron energies at lower currents continues, loss of DCX plasma heat in the arc region should decrease.

Earlier studies of unusual Doppler slant and broadening effects have been extended to include the high-pressure PIG discharge (mode I plasma), the low-pressure PIG discharge (mode II plasma), and the high-current vacuum carbon arc. The reduced heat losses from these arc plasmas (losses are almost entirely by radiation, with conduction and convection negligible) apparently result in the entrapment of larger amounts of energy than would occur in conventional atmospheric-pressure arcs.

2.2. A Mass Spectrometric Analysis of the Constituents of the Carbon Arc

First results of a mass spectrometric analysis of a short carbon arc verify spectrographic evidence of existence of triply ionized carbon in the arc, though in smaller amounts (~1.25%) than spectrography indicated for a longer arc.

2.3. Microwave Diagnostics of the Carbon Arc

Knowledge of the electron density in the carbon arc is essential to an understanding of its function in the molecular breakup of the D_2^+ beam. Microwave measurements, for an arc current of 300 amp and a magnetic field of 2600 gauss, have tentatively established that the plasma frequency of the arc is ~140,000 Mc, corresponding to an electron density of $\sim 2 \times 10^{14}$ electrons/cm^3.

2.4. Cross-Section Calculations for Dissociation of D_2^+ by Carbon Arc

In order to test the hypothesis that the dissociation of the D_2^+ molecules is caused by the observed triply ionized carbon of the carbon arc, the dissociation cross section is being calculated by two different approximations.

2.5. Carbon Arc Floating Potential Measurements

In an attempt to determine the floating potential distribution in the carbon arc an axially movable potential probe was inserted in the LSM and flipped through the arc at ~100 in./sec. The axial potential distribution so determined was plotted. There were indications that the potentials observed were somewhat affected by probe temperature and that there was partial shorting of the probe electrode; accordingly, it is planned to increase the probe flipping speed, improve the probe insulation from the arc, and improve the trajectory and mirror ratio of the arc. A special assembly, to be used principally in studying probing methods, has been constructed.

2.6. Carbon Arc Total Radiation Studies

Electromagnetic radiation from a 3- to 6-ft-long, magnetically constrained, vacuum carbon arc was studied as it varied with position along the arc and as it depended upon the interposition of various filters, the arc current, and the magnetic field intensity. Specially designed circular-foil radiometers were used. The data indicated that the anode radiation peak occurred at ¼ in. from the anode and that total radiation was 30% lower near the cathode than near the anode, that a significant proportion of the radiation is from triply ionized carbon, that at ~200 amp a current-dependent change of conduction mode occurs in the arc, and that radiation increases almost linearly with magnetic field intensity.

3. ION SOURCE AND ACCELERATOR STUDIES

3.1. Ion Source Development

In an attempt to solve the problems involved in the injection of higher ion currents into the DCX, initial studies were devoted to two modes of operation (low and high impedance) of PIG-type sources. The high-impedance type, with a 10-kv ion acceleration, a source pressure of 7×10^{-4} mm Hg of hydrogen, and 50-ma anode current, produced a maximum output of 14 ma, extracted through a ⅜-in. hole.

Changes in the configurations of the intermediate electrode and the anode plate of a modified Von Ardenne source had little effect on the maximum

output of 15 ma at 50 kv, detected 14 in. from the lens. However, the alignment of the holes in these parts and in the accelerator electrode was extremely critical.

Changes in the accelerator electrode arrangement of another modified Von Ardenne-type source permitted output currents of 50 ma, at 60-kv acceleration.

A new high-gradient accelerator tube for the DCX was designed and installed, and new ion-source test equipment was constructed to handle higher currents.

High-Voltage Regulator for DCX. – Irregular operation, the result of mechanical wear, of the old high-voltage regulator of the DCX accelerator necessitated its replacement.

A newly designed regulator was installed on December 1, 1958, and has functioned, after calibration, without further adjustment. The new regulator can bring the voltage from zero to 560,000 v in ~3 sec and, at the operating point, hold voltage excursions to within 500 v.

4. VACUUM SYSTEM STUDIES

4.1. The DCX Vacuum System Problem

The creation of a thermonuclear plasma in the DCX requires that the density of the neutral gas within the plasma be reduced to about 10^7 atoms/cm^3. It is hoped that, if the pressure in the system can be dropped below a certain level, "burnout" will occur (i.e., gas atoms in the region occupied by the deuterium plasma will be ionized at a greater rate than new ones enter the region; the deuteron density, limited up to this point by charge exchange, will increase until it reaches a limit – set by mirror losses – at which the plasma interior is effectively shielded from atoms incident on the surface). For a given input current I (in ma) the achievement of burnout is estimated to require a pressure below $2I \times 10^{-8}$ mm Hg for deuterons in deuterium and $2.5I \times 10^{-7}$ for protons in hydrogen.

The attainment of the required vacuum is complicated by the carbon arc, which as yet maintains the pressure above 10^{-7} mm Hg, and by the influx of gas represented by the ion beam. The first complication will be attacked by an investigation of the pressures associated with arc operation, and the second by high-speed ionic pumping utilizing the ionizing power of the trapped particles.

4.2. Design and Construction of the PPF

A device intended for the study of both problems (the PIG-Pump Facility, or PPF) has been constructed. It is hoped that the background gas that is ionized by the trapped deuterons or protons will be removed by a more or less elaborate configuration of negatively charged electrodes placed just behind the magnetic mirrors. The name PIG plates has been given to the electrodes because the principle involved in their action is reminiscent of that of a Philips Ion Gage.

4.3. Tests of Oil Diffusion Pumps for the DCX

Three models of oil diffusion pumps have been tested, and no significant difference in their performance was noted. Attempts at a general solution of the pressure-fluctuation problem indicated that a radical change in the method of heating the pump fluid is probably needed. A Vac-Ion pump was found to be useful only for carefully selected applications.

PART II. SUPPORTING BASIC AND APPLIED RESEARCH

5. EXPLORATORY PHYSICS

5.1. Arc Development

A 50-ft-long carbon arc assembly is being constructed for studies of the higher ion energies believed to be associated with increasing arc length. The equipment will be evacuable and employ a solenoidal magnetic field. It will also be used in studies of PIG-type discharges, high-density plasmas, D_2^+ breakup, and deuterium arcs.

5.2. Multistage-Grid Ion Sources

In an attempt to overcome the inherently low voltage limitation on the ORNL-developed grid ion sources, a multistage grid source is being designed which, if successful, should produce a 600-kev beam. A source of this type is also being considered for operation within the containing field of the DCX rather than in the present injection system.

6. SPUTTERING

6.1. Sputtering Effects of Some Energetic Ions on Various Metals

Among the impurities that cool a hot plasma are the atoms "sputtered" from the container walls by energetic ions. Since the DCX injection system provides a steady supply of such ions, and since the proposed higher-amperage beams (see Secs 5.2 and 3.1) will probably increase this supply, a study of the sputtering effect of certain ions upon various metals has been undertaken and will be extended. Data have been tabulated for sputtering of copper by argon, helium, and deuterium ions; and for aluminum by helium and argon. The sputtering ratios (numbers of atoms sputtered per incident ion) were highest for copper bombarded by argon ($\sim$8.8 at 30 kev) and lowest for copper bombarded by helium and deuterium ($<$0.2 at 30 kev). Other ratios were about 2 and 3.

7. AUXILIARY EQUIPMENT AND SERVICE

7.1. Metallurgy

In a study of flange and valve seals for use in the Sherwood Project a literature survey indicated that flat washer-shaped gaskets made of oxygen-free high-conductivity (OFHC) copper, aluminum, or gold are suitable for large flanges and that indium O-rings have been used successfully in some systems. Simple copper O-rings are unsatisfactory in bakeable systems. The need for gasket replacement (and, in some cases, surface refinishing) when remaking seals probably precludes the use of metal gaskets in valves.

The wettability of some base materials by an In-Ga-Sn eutectic alloy considered for use in a liquid-metal seal was tested at temperatures up to 450°C. The use of such seals is not recommended at this time.

Demountable joints or valves which would be closed and opened by the solidification and melting, respectively, of a filler metal were considered; and preliminary tests indicated that this type of seal would be useful in ultrahigh-vacuum systems provided that the seal could be opened in the vertical position and further provided that a compatible filler-metal and base-material combination can be found which would also satisfy the special requirements of thermonuclear experiments. The literature indicates that the alloy In-Ag-Cu might be usable, and it is under investigation.

A vacuum furnace with a hot zone 26 in. in diameter and 20 in. in height has been constructed for studies of vacuum degassing, brazing, and processing of experimental equipment.

Failure of the copper tubing used for heating and cooling the DCX liner with steam (400°C) and water (20°C) was shown by examination to be accompanied by intergranular defects. Tests at 500°C for 200 hr with no steam showed no failure of the tubing.

7.2. Seya Spectrometer

Design and construction has been completed on a new type of vacuum spectrometer to be used in the study of carbon arcs and hydrogen and deuterium plasmas. Positions of the slits and concave grating are fixed, and scanning is done by rotating the grating. The highest wavelength attainable with this spectrometer is about 4450 Å, the limit being set by the length of the scanning screw. The lowest wavelength detected has been 312 Å. At lower wavelengths there is insufficient reflectivity of the aluminum grating surface.

7.3. A Nonlinear Photometer Circuit

A circuit for semilogarithmic photometric recording has been developed, with a minimum of circuit changes, from a conventional circuit for RCA multiplier phototubes.

7.4. Design and Construction Group

Engineering on the Sherwood Project has been organized into a formal section for only about two months. In most cases, activities of the Engineering Section will be integrated with the experimental work and will be reported indirectly in the various projects. The three activities which have been handled solely by the Engineering Section are design and construction of 6000-amp magnet coils for the DCX, installation of a 600-kv, 1-amp d-c supply for ion injection, and design of a system of four evacuable tanks which will be provided with independent, essentially homogeneous magnetic fields. The tanks will be used for basic studies.

8. ENGINEERING SCIENCE GROUP

8.1. Engineering Science

In engineering science studies in support of the Sherwood Project the following work is in progress or was done:

1. A literature survey produced tables of magnetic-field values B_Z and B_r for current sheets, useful in the computation of any rotationally symmetric magnetic fields. Similar tables containing finer intervals, values for the vector potential $\overline{A}$ and for rA, and a larger range of Z and r have been computed by the Mathematics Group of the Thermonuclear Experimental Division.

2. General optimization theorems were worked out for the cross-section shape and the current-density distribution of magnet coils.

3. A field-analog network (Field Simulator) was built in which the field line of a rotationally symmetric magnetic field corresponds to an equipotential line. Another analog computer, in which magnetic equipotential corresponds to an electric equipotential, is being worked on. It will use a wedge-shaped electrolytic tank.

4. In an attempt to determine the effect of slow changes on a pulsed magnetic field, such as might be used in this program in the future, an arrangement for a-c measurements on magnetic models has been developed.

5. A method of conveniently computing sufficiently exact values for the mechanical forces produced by the DCX magnetic mirror coils was developed.

6. Experiments and calculations on heat transfer for cooling of large magnet coils are in progress.

7. Graphical and analytical methods for the fast determination of charged-particle trajectories in magnetic fields have been developed.

PART III. DCX-2 PROGRAM

9. CALCULATIONS FOR DCX-2 DESIGN

9.1. Magnetic Mirror Fields for DCX-2

Calculations of the characteristics of magnetic mirror coils that will give satisfactory particle containment with power and copper economy are in progress.

9.2. Oracle Calculation of Magnetic Fields and Vector Potential

A flexible Oracle code to permit rapid calculation of magnetic fields and vector potential for use in coil design problems has been developed. Values for B_Z/B_0, B_r/B_0, and A/B_0 at a general point (r,Z) are calculated by summing the contributions at this point from many circular loops of current-carrying wire. [The quantity $B_0 \equiv B_Z(0,0)$. The quantities B_Z/B_0 and B_r/B_0 are dimensionless; A/B_0 has dimensions of length.] The quantity $B_0/\mu I$ is calculated and given separately, so that absolute field strengths may be found.

CONTENTS

INTRODUCTION iii

SUMMARY ix

PART I. THE DCX EXPERIMENTAL PROGRAM

1. DCX PLASMA STUDIES 3
   - 1.1 Studies of DCX Plasma by Neutral Particle Collection 3
     - 1.1.1 Experimental Procedure 3
     - 1.1.2 Visual Observation of the Plasma 6
     - 1.1.3 Amplitude of Neutral Detector Signal as a Function of Tank Pressure – Particle Balance 6
     - 1.1.4 Decay Time 7
     - 1.1.5 Density of Trapped Particles 8
     - 1.1.6 Preparation of Thin Copper-Backed Nickel Foils 8
     - 1.1.7 Beam Pulser for DCX Plasma Studies 9
   - 1.2. Microwave Diagnostics of DCX Plasma 14
     - 1.2.1 Microwave Theory 14
     - 1.2.2 DCX Plasma Measurements 15
   - 1.3 Plasma Containment 18
     - 1.3.1 A Study of Ion Orbits and Containment Properties of DCX 18
     - 1.3.2 Unstable Plasma Oscillations in a Magnetic Field 22
   - 1.4 Deuteron and Electron Energy Distributions in DCX 25

2. CARBON ARC STUDIES 26
   - 2.1 Some Spectroscopic Studies of the Energetic Carbon Arc – A Magnetically Constrained High-Vacuum Arc 26
     - 2.1.1 Doppler Slant and Line Broadening 26
     - 2.1.2 Intensity of Spectra for Carbon and Oxygen 29
     - 2.1.3 Spectral Intensity Variation in the Carbon Arc in the LSM 32
   - 2.2 A Mass Spectrometric Analysis of the Constituents of the Carbon Arc 36
   - 2.3 Microwave Diagnostics of the Carbon Arc 37
     - 2.3.1 Carbon Arc Measurements 37
   - 2.4 Cross-Section Calculations for Dissociation of D_2^+ by Carbon Arc 40
   - 2.5 Carbon Arc Floating Potential Measurements 41
   - 2.6 Carbon Arc Total Radiation Measurements 45
     - 2.6.1 Radiometer Design and Characteristics 45
     - 2.6.2 Radiation vs Arc Axial Distance 45
     - 2.6.3 Use of Various Filters 45
     - 2.6.4 Radiation vs Arc Current 48
     - 2.6.5 Radiation vs Magnetic Field Intensity 50

3. ION SOURCE AND ACCELERATOR STUDIES 51
   - 3.1 Ion Source Development 51
     - 3.1.1 PIG-Type Sources 51
     - 3.1.2 A Modified Von Ardenne Type of Source 52
     - 3.1.3 New Ion Source Test Equipment 54

3.2 The DCX Accelerator 54
3.2.1 Ion-Injection System for DCX 54
3.2.2 High-Voltage Regulator for DCX 57

4. VACUUM SYSTEMS 59

4.1 The DCX Vacuum Problem 59
4.1.1 Burnout 59

4.2 Design and Construction of the PPF 61
4.2.1 PPF Design 61
4.2.2 PPF Components 64
4.2.3 PPF Vacuum System Performance 68
4.2.4 Titanium Pumps 69

4.3 Tests of Oil Diffusion Pumps for DCX 70
4.3.1 Diffusion Pump Performance 70
4.3.2 Unsteady Pressure 70
4.3.3 Tests of Vac-Ion Pump 72

PART II. SUPPORTING BASIC AND APPLIED RESEARCH

5. EXPLORATORY PHYSICS 77

5.1 Arc Development 77
5.1.1 Long Carbon Arc 77
5.1.2 Dissociation of D_2^+ by Carbon and Molecular Deuterium Arcs 78
5.1.3 Arc Compression 78

5.2 Multistage Grid Ion Sources 78

6. SPUTTERING 79

6.1 Sputtering Effect of Some Energetic Ions on Various Metals 79

7. AUXILIARY EQUIPMENT AND SERVICE 86

7.1 Metallurgy 86
7.1.1 Valve-Flange Development 86
7.1.2 Getter Testing 91
7.1.3 Vacuum Furnace Installation 91
7.1.4 Analysis of Failure of Copper Tubing 93

7.2 Seya Spectrometer 94

7.3 A Nonlinear Photometer Circuit 100

7.4 Design and Construction Group 101
7.4.1 New Magnet Coils for the DCX 101
7.4.2 Installation of 600-kv, 1-amp D-C Supply 101
7.4.3 Design of Evacuable Tanks 101

8. ENGINEERING SCIENCES GROUP 103

8.1 Engineering Science 103
8.1.1 General Supporting Studies 103
8.1.2 Mechanical Forces and Heat Transfer in Magnet Coils 104
8.1.3 Ion Trajectories 105

PART III. THE DCX-2 PROGRAM

9. CALCULATIONS FOR DCX-2 DESIGN 109
9.1 Magnetic Mirror Fields for DCX-2 109
9.2 Oracle Calculation of Magnetic Fields and Vector Potential 111

Part I

THE DCX EXPERIMENTAL PROGRAM

1. DCX PLASMA STUDIES

1.1 STUDIES OF DCX PLASMA BY NEUTRAL PARTICLE COLLECTION[1]

R. J. Kerr R. A. Dandl C. F. Barnett

Measurements of decay times and the spatial extent of plasmas trapped in DCX have been attempted. At the lowest pressures achieved (5×10^{-7} mm Hg), a proton plasma of density $\sim 10^9$–10^{10} cm^{-3} was trapped for 12 to 14 msec. At these pressures, the trapped beam, which is confined to a thin torus at higher background pressures (10^{-5} mm Hg), appears to have spread along the magnetic axis to a width of perhaps 8 in.

1.1.1 EXPERIMENTAL PROCEDURE

Neutral Particle Collection

The study of particle behavior in DCX has so far depended mostly upon the use of neutral particle detectors. Advantage is taken of the fact that as the 300-kev H^+ ions revolve in their orbit they are likely to experience a charge-exchange collision, which results in the formation of an energetic neutral hydrogen particle. These neutral particles, being undeflected by the magnetic field, proceed in a path tangential to the circle of revolution and can be registered in a suitable detector placed outside the region occupied by the circulating charged particles. The detector consists of a thin nickel foil placed in front of an insulated Faraday cup. The neutral particles pass through the foil (5 to 25 μin. thick) and emerge mostly charged, so that they produce a positive current flowing into the Faraday cup. The foil is of sufficient thickness to ensure charge equilibrium of the emerging particles. The charge state of the particles leaving the foil is independent of the initial charge state and dependent only on the particle energy and foil thickness. Figure 1.1.1 shows a schematic diagram

[1]Written in part by A. H. Snell.

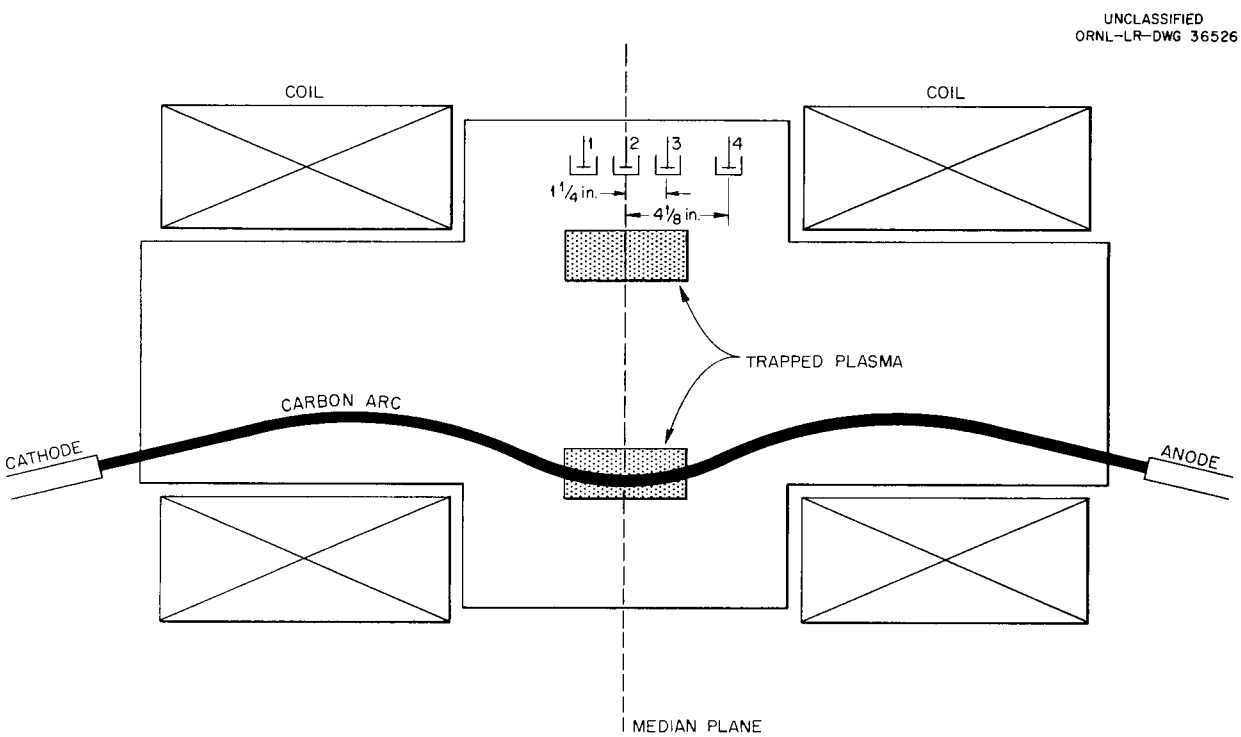

Fig. 1.1.1. Schematic Diagram of Neutral Particle Detector Positions.

of the placement of the detectors. Vacuum locks permit foils to be replaced without disturbing the vacuum. The output from the Faraday cup is fed to a transistor amplifier, whose output voltage is displayed on an oscilloscope. The gain of the amplifier is such that a current of 10^{-9} amp will produce a signal of 1 mv. By pulsing the input beam at the ion source and gating the oscilloscope, one obtains the steady-state amplitude of the neutral signal and also the decay time of the plasma in DCX.

Since the neutral detector is energy sensitive, a calibration was made to determine the transmission of the foil. Plotted in Fig. 1.1.2 is the foil transmission as a function of the input particle energy.

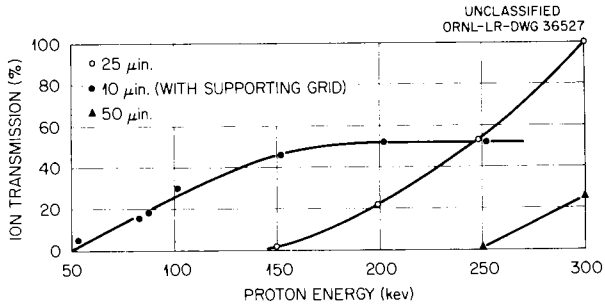

Fig. 1.1.2. Nickel Foil Transmission as a Function of Proton Energy.

Transmission is defined as the percentage ratio of the number of ions arriving per second in the Faraday cup to the number of atoms impinging per second on the front surface of the foil. Results are shown for a 25- and 50-μin. nickel foil and also for a 10-μin. foil. The 10-μin. foil has low transmission because of a supporting copper grid structure used for mechanical and thermal strength. Clearly the 10-μin. foil should be initially less sensitive to energy degradation of the circulating protons than the 25-μin. foil. A comparison of signal amplitudes obtained with the two foils would serve as an indication as to whether or not the ions suffer a damaging amount of energy loss as they pass repeatedly through the carbon arc, and equality of the amplitudes would suggest that signal is not being lost because of energy degradation.

Pressure Measurements

The measurement of pressures in the region of the trapped plasma is very difficult. Measurements at the present time are taken with a Bayard-Alpert ionization gage calibrated for air. If the background gas is composed principally of hydrogen the pressure may be made absolute by calibrating the ionization gage for hydrogen. However, when other noncondensable gases (i.e., N_2, O_2, CO) are present, not only is it necessary to recalibrate the gage, but the composition of the mixture must be known. In addition, in the region of the trapped plasma, ions of thermal velocity are present, created either by ionization from trapped high-energy protons or by ionization from the intense hard ultraviolet radiation from the arc. These ions, if only singly ionized, are still target centers for charge-exchange collisions. Detection of these particles by the ion gage is complicated by the ion density gradient imposed by the magnetic field. Further inaccuracies in pressure measurements result from condensable vapors such as carbon. Since the ion gage is located externally to the magnetic volume with a tube connection to the inner system, any such vapor will condense out before being recorded by the ion gage. These uncertainties in the momentary pressures are probably largely responsible for a considerable scatter in the measurements of neutral detector signal amplitude and decay time of the trapped ion ring.

Recording of Data

Typical data obtained with the foil detectors are shown in Fig. 1.1.3, which presents the oscillograms for the four detectors placed as shown in Fig. 1.1.1. For each of the signals there is a duplicate trace obtained by pulsing the beam again. The ordinate of the trace is the amplitude and the abscissa is the time proceeding from left to right. At zero time, the input beam is cut off and the amplitude is a maximum (downward). As time progresses, the amplitude decreases. The calibration for each detector is given and the cross-hatched lines represent 1 × 1 cm. The amplitude is presumed to be proportional to the density of the high-energy plasma and is determined by measuring the difference between the minimum and maximum signal. The traces also provide the mean decay time, τ, which is defined as the time required for the signal to decay in amplitude by $1/e$; τ is then numerically equal to $(n\sigma v)^{-1}$, where n is the background neutral gas density, σ is the charge-exchange cross section, and v is the proton velocity.

UNCLASSIFIED
ORNL-LR-DWG 36528

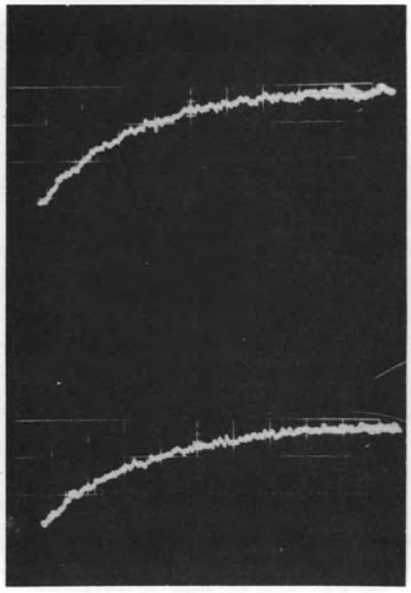

DETECTOR NO. 1:
GAIN 20 mv/cm
SWEEP 2 msec/cm

DECREASING AMPLITUDE

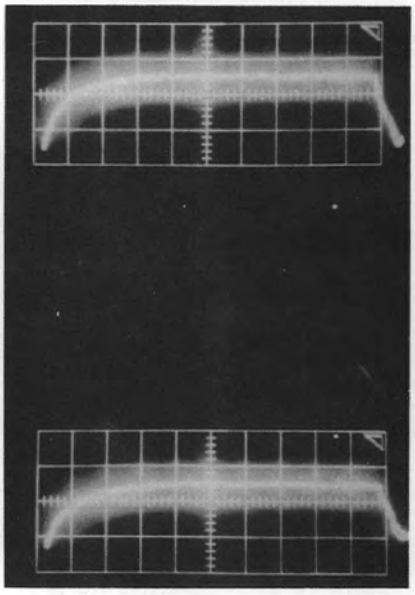

DETECTOR NO. 2:
GAIN 50 mv/cm
SWEEP 5 msec/cm

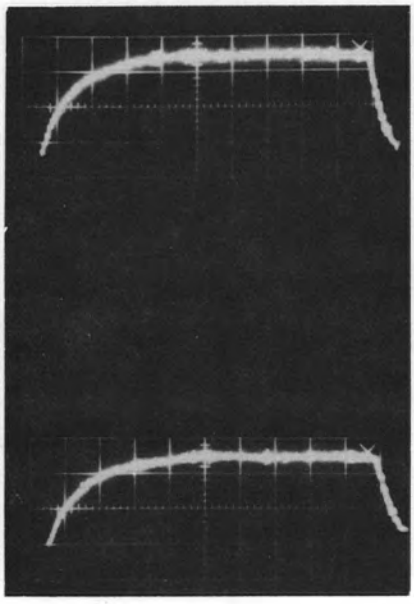

DETECTOR NO. 3:
GAIN 20 mv/cm
SWEEP 5 msec/cm

DECREASING AMPLITUDE

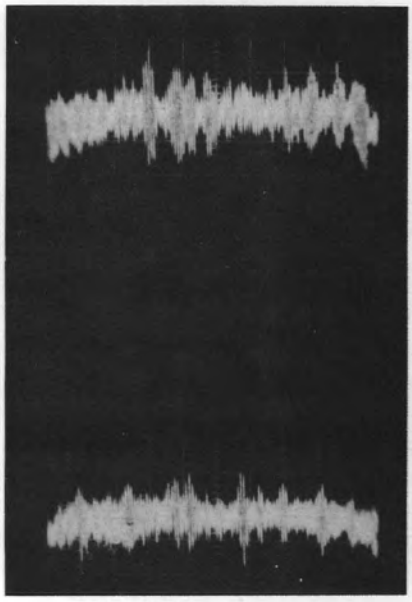

DETECTOR NO. 4:
GAIN 5 mv/cm
SWEEP 5 msec/cm

Fig. 1.1.3. Typical Oscillograms of DCX Neutral Particle Collection Data.

1.1.2 VISUAL OBSERVATION OF THE PLASMA

As a supplement to the instrumental indicators, visual observation gives a satisfying qualitative indication of some of the gross features of the trapped ion ring. Visual observation is made possible by occasional carbon granules that fly about in the vacuum tank and become incandescent as they pass through the ring; visual memory then enables one to build an image of the shape and size of the ion-containing volume. At pressures in the neighborhood of 10^{-5} mm Hg, the ring is a torus about 2 cm in minor diameter standing edgewise upon the arc. The major radius is 5.3 in., as is appropriate for the injection of H_2^+ at 600 kev and the trapping of H_1^+ at 300 kev. (It is convenient at this stage to work with hydrogen rather than deuterium, to avoid the generation of neutrons.) Injection currents are in the range 1–5 ma of H_2^+. At a gage pressure of about 3×10^{-5} mm, the blue glow surrounding the trapped ring can be seen in the gas. If the arc is turned off at this pressure, the trapped ring can still be seen in the darkened tank because there is sufficient breakup of the incoming molecular ions in the residual gas to permit its formation.

As the pressure is decreased to 5×10^{-7} mm Hg (gage) the volume containing the trapped ions spreads parallel to the magnetic axis, becoming about 8 in. wide. As is apparent from Fig. 1.1.1, the neutral detectors are stationed so as to give a quantitative measure of this spread.

At the moment of writing, it has been found that the volume containing the trapped ions also has a tendency to spread radially, but that heretofore the radial spread has been inhibited by the mechanical obstacle presented by the neutral detectors themselves. Although they were placed 2 in. outside the supposed extent of the ring, this was apparently not far enough away. The observations reported here all suffer from the disadvantage that they apply to the trapped beam as partially obstructed in this manner, and it is tantalizing that at the time of preparation of this report observations taken under more ideal conditions are not at hand. We will, however, proceed to present what we have.

1.1.3 AMPLITUDE OF NEUTRAL DETECTOR SIGNAL AS A FUNCTION OF TANK PRESSURE – PARTICLE BALANCE

Figures 1.1.4 and 1.1.5 present observations of the variation of the amplitude of the neutral detector signal as the pressure is varied by the introduction of argon and as a consequence of the reduction in pressure of background gas. The pressures are those measured on the ionization gage, uncorrected for gas composition. In Fig. 1.1.5 one can see the concentration of the circulating ions in a narrow ring at high pressures, for the amplitude of the signal in the central detector (No. 2) rises with increasing pressure, while that in the adjacent side detectors falls. As the pressure is reduced to 1×10^{-5} mm Hg, the volume occupied by the particles spreads, and detectors 1 and 3 receive more signal. Further reduction in pressure produces a further reduction in signal amplitude, partly as a result of the spread beyond the acceptance angles of the detectors, but perhaps also because some loss mechanism other than charge exchange begins to dominate, such as loss to the mechanical obstruction or loss through the mirrors.

When an attempt is made to integrate the outflowing neutrals for comparison with the rate of trapping of charged particles, an approximate balance can be obtained at pressures of about 10^{-5} mm Hg, but at low pressures ($<10^{-6}$ mm Hg) plausible extrapolations of the neutral detector signals over the expanded plasma volume appear to account for only about $1/25$ of the input trapping rate. The presence of the obstacle probably accounts for some of the discrepancy, but the extent of its effect remains to be seen. Detectors are planned for the mirror throat positions, also, for a direct determination of mirror loss; but no results have been obtained from them as yet.

The results of signal amplitude pertain to injection currents of H_2^+ of approximately 2 ma, but for breakup efficiencies in the arc measured at only about 10%. In the past, breakup efficiencies in the range 20–40% have been measured in DCX. Apparently some change in the condition of running the carbon arc has reduced the efficiency for the present set of runs; it will be important to understand this and recover the condition of more efficient breakup.

In Fig. 1.1.5, detector 2 was covered with a 25-μin. foil, while 1 and 3 were covered with 10-μin. foils. Inclusion of the transmission factor from Fig. 1.1.2 would raise the 1 and 3 curves to about the same amplitude as 2. Checks with thick and thin foils respectively on detectors 1 and 3 indicate that the major particle loss is not one of energy degradation to the extent that the particles fail to penetrate the foils with full efficiency

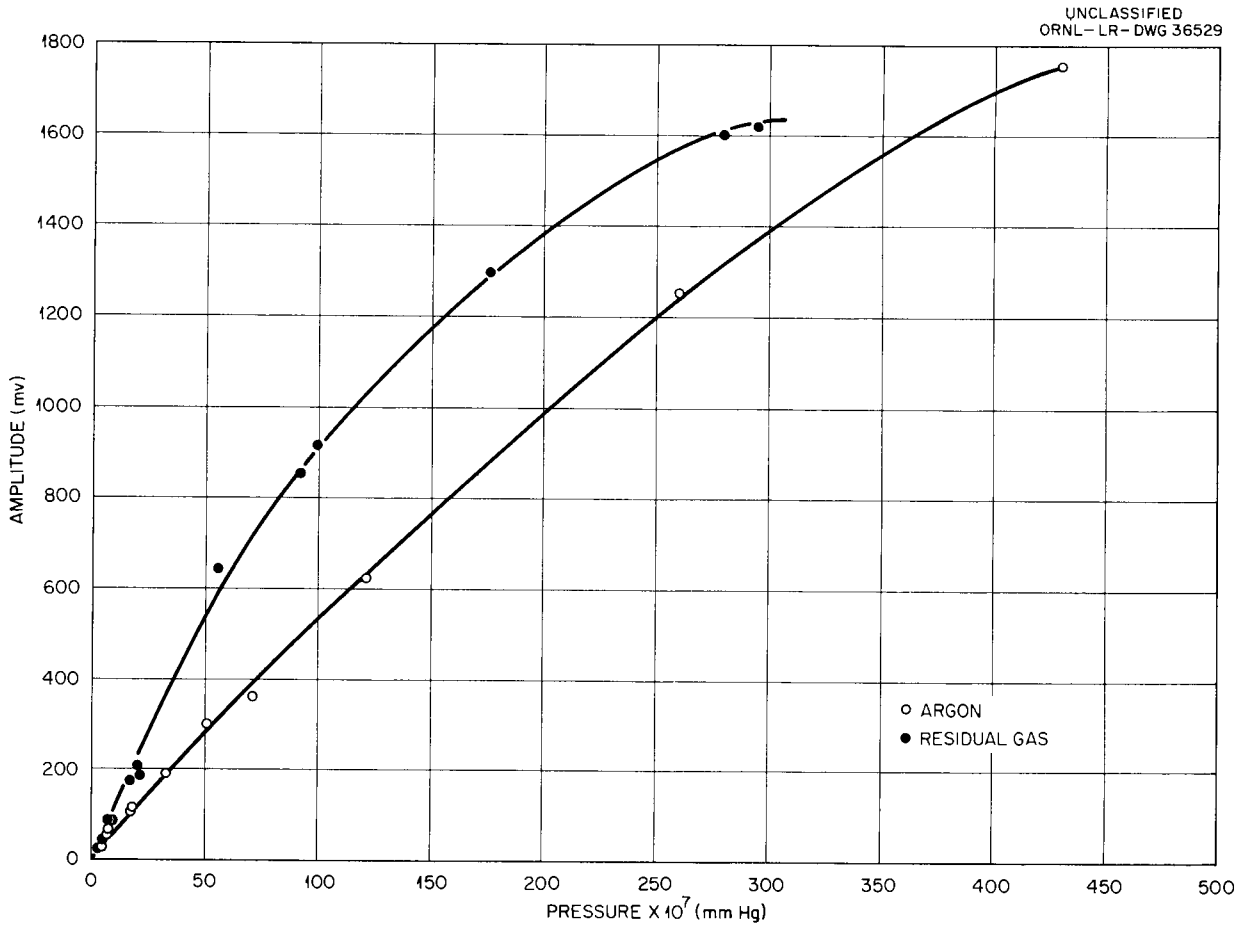

Fig. 1.1.4. Signal Amplitude as a Function of Pressure in DCX Neutral Particle Collection. Center detector.

(Fig. 1.1.2). Simon and Fowler have estimated the energy loss at 1.6 ev per passage of a proton through the carbon arc; it is likely, however, that orbital precession permits the protons to miss the arc on most of their revolutions, and orbital shrinkage would have the same effect.

Detector 4, placed 4 in. from the median plane, does not give a sufficient signal (<1 mv) to give a measurable variation of amplitude with pressure. It will be interesting to see if its signal increases when the obstacle is removed.

1.1.4 DECAY TIME

Figures 1.1.6 and 1.1.7 give results taken from a recent run, showing the variation of decay time of the trapped proton beam with pressure of added argon or residual gas. Actually, $1/\tau$ is plotted as a function of pressure, with τ in msec. These data were also obtained in the presence of the obstacle of the neutral detector mount in the *fringing* part of the trapped beam volume. Evidently the central detector shows at high pressures a shorter decay time than do the side detectors, but when the plasma spreads, at pressures of 10^{-6} mm Hg or less, the decay times become about equal. The longest decay times observed have been 12 to 14 msec, for trapped protons at a pressure of 5×10^{-7} mm Hg. This corresponds to a trapping for about 10^5 turns, or a circulating ion current of about 10 amp.

In Fig. 1.1.7 a straight line is drawn in to indicate the variation that would be expected in $1/\tau$ if the residual gas consisted entirely of argon, the charge-exchange cross section being assumed to be 1.5×10^{-18} cm^2.

The most intriguing feature of the decay time behavior is the apparent lengthening of the ion

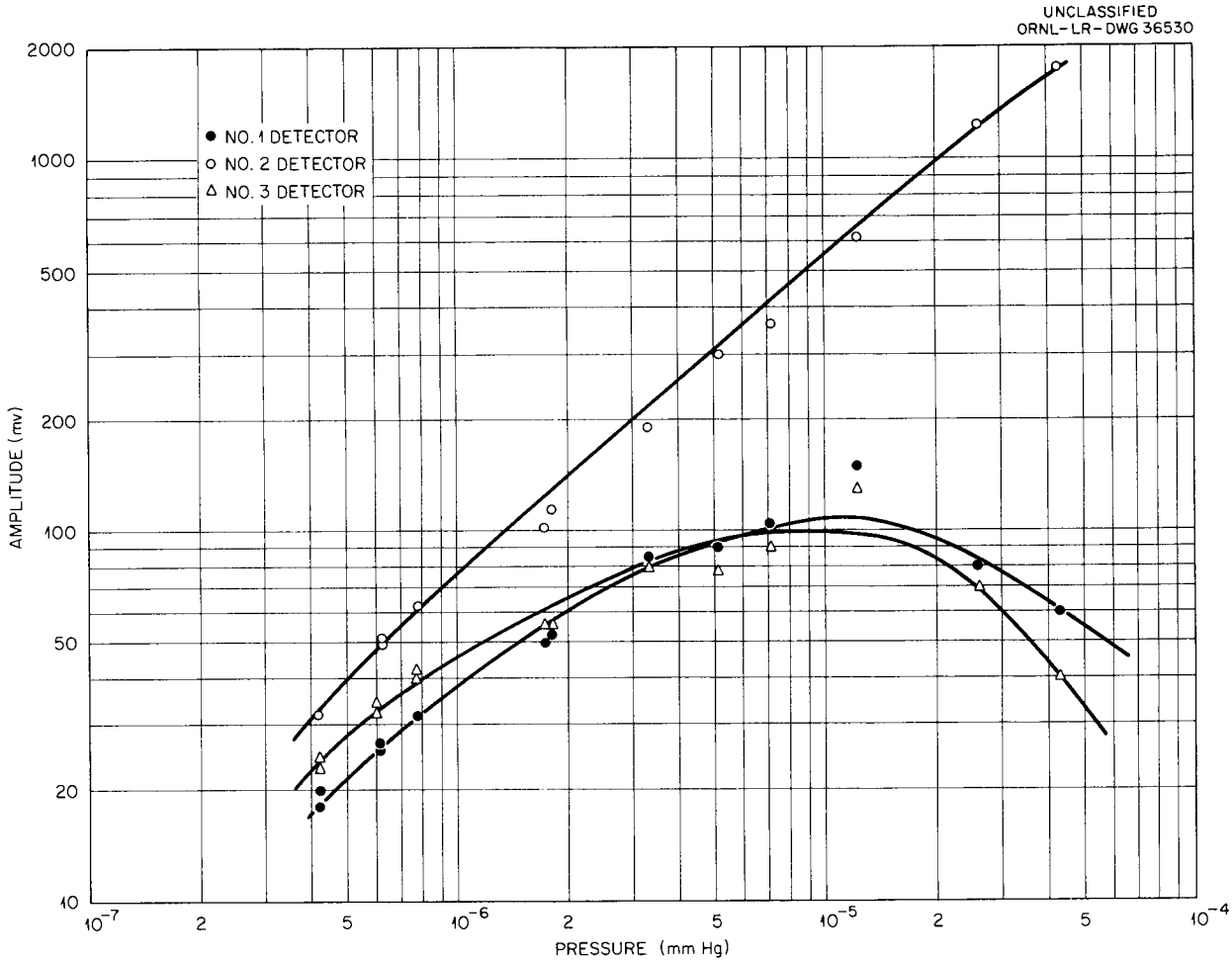

Fig. 1.1.5. Signal Amplitude as a Function of Pressure in DCX Neutral Particle Collection. Three detectors.

lifetime as gas pressure decreases, the lengthening becoming quite marked in the region below 10^{-6} mm Hg. This is naturally being examined very closely, because it is in the direction that would be expected if the residual gas were starting to be burned out within the volume occupied by the trapped ion orbits.

1.1.5 DENSITY OF TRAPPED PARTICLES

If the 2 ma of injected H_2^+ ions are dissociated with an efficiency of 10%, and reside thereafter for a mean time of 10 msec in trapped orbits, the accumulated protons would number about 10^{13}. The volume occupied might be guessed to be several liters, whence one would conclude that the particle density is between 10^9 and 10^{10} per cm^3. Microwave measurements have been attempted across the region occupied by the orbits (see Sec 1.2.2), and a negative result suggests that the density is less than 10^{10}; obstacles were, however, again present in the path of the circulating ions.

1.1.6 PREPARATION OF THIN COPPER-BACKED NICKEL FOILS

M. C. Becker

Nickel foils (5- and 10-μin.) backed with approximately 100-μin. copper are available from the Chromium Corporation of America. For use in the neutral particle detectors, a portion of the copper is etched away, leaving a copper grid for structural support.

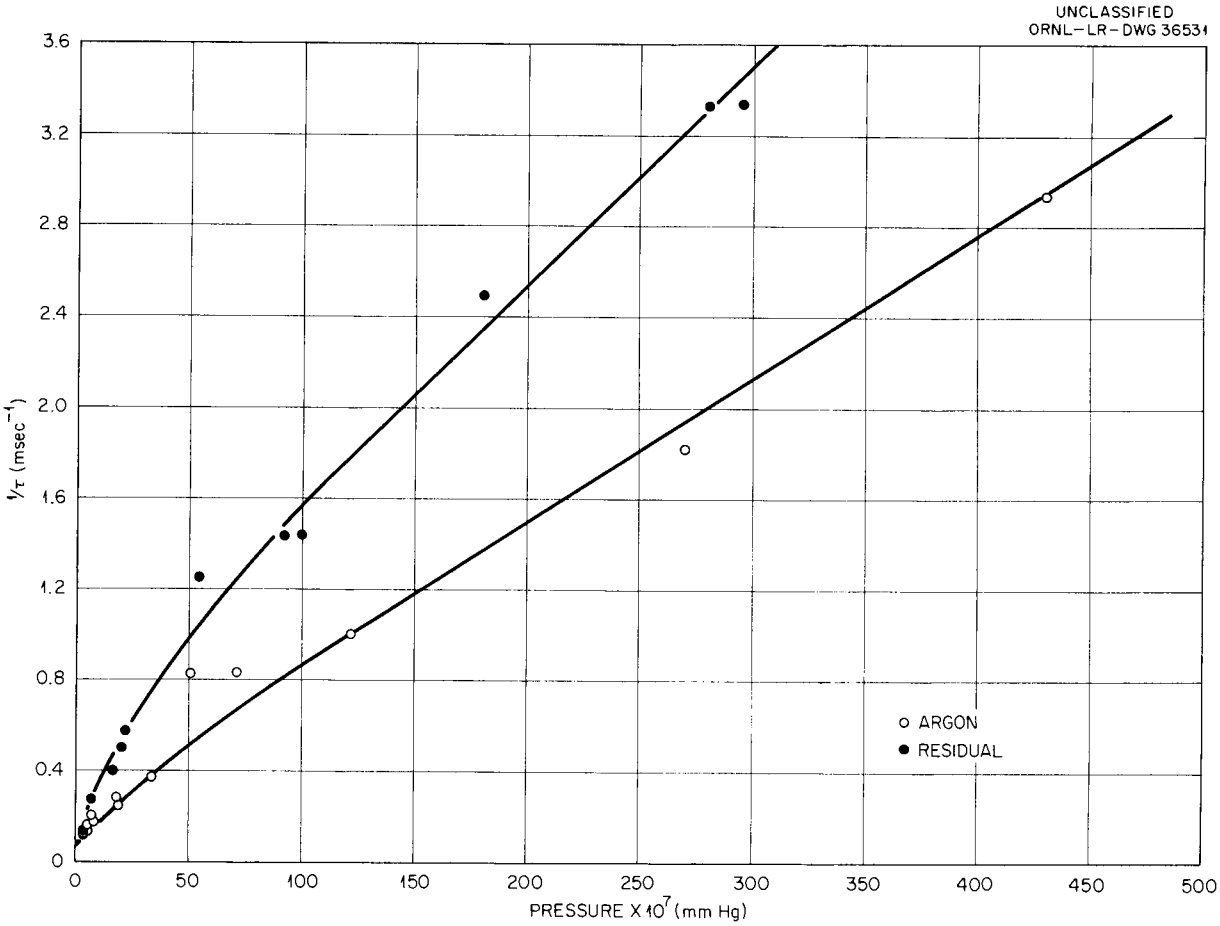

Fig. 1.1.6. $1/\tau$ as a Function of Gas Pressure for One Neutral Particle Detector (Detector No. 2). τ = time required for neutral particle signal to decay in amplitude by $1/e$.

An actual-size photographic negative of an enlarged drawing of the grid is made. Eastman Kodak Photo Resist is applied to the copper backing of the foils and then dried in a dust-free environment at 50°C. The sensitized surface is exposed to ultraviolet light through the negative while held in a contact printing frame. Exposure time with a GE type H100-FL4 UV lamp is 3 min. The image is developed with Kodak Photo Resist developer, fixed with 95% alcohol, and dried once more at a temperature of 50°C.

The copper is then etched off in 10% (by weight) aqueous solution of ferric ammonium sulfate at a temperature of 40°C. Usual etching time is 10 min as the copper backing is not of uniform thickness.

Dry foils are best handled by tweezers at one corner. Wet foils are handled by being floated on the surface of water and then picked from the surface with a narrow glass plate by surface tension. These foils are not pinhole-free, and the size and the number of holes per foil vary from package to package. An average hole size is estimated to be in the range 1 to 2 μin. It is of utmost importance that handling devices be kept free of grease and the environment be dust free. The foils have proved to be sufficiently sturdy in the DCX environment.

1.1.7 BEAM PULSER FOR DCX PLASMA STUDIES

M. C. Becker

The 600-kv beam of DCX is pulsed off for certain diagnostic measurements. Wrap-up decay-time measurements with a multi-window neutral particle

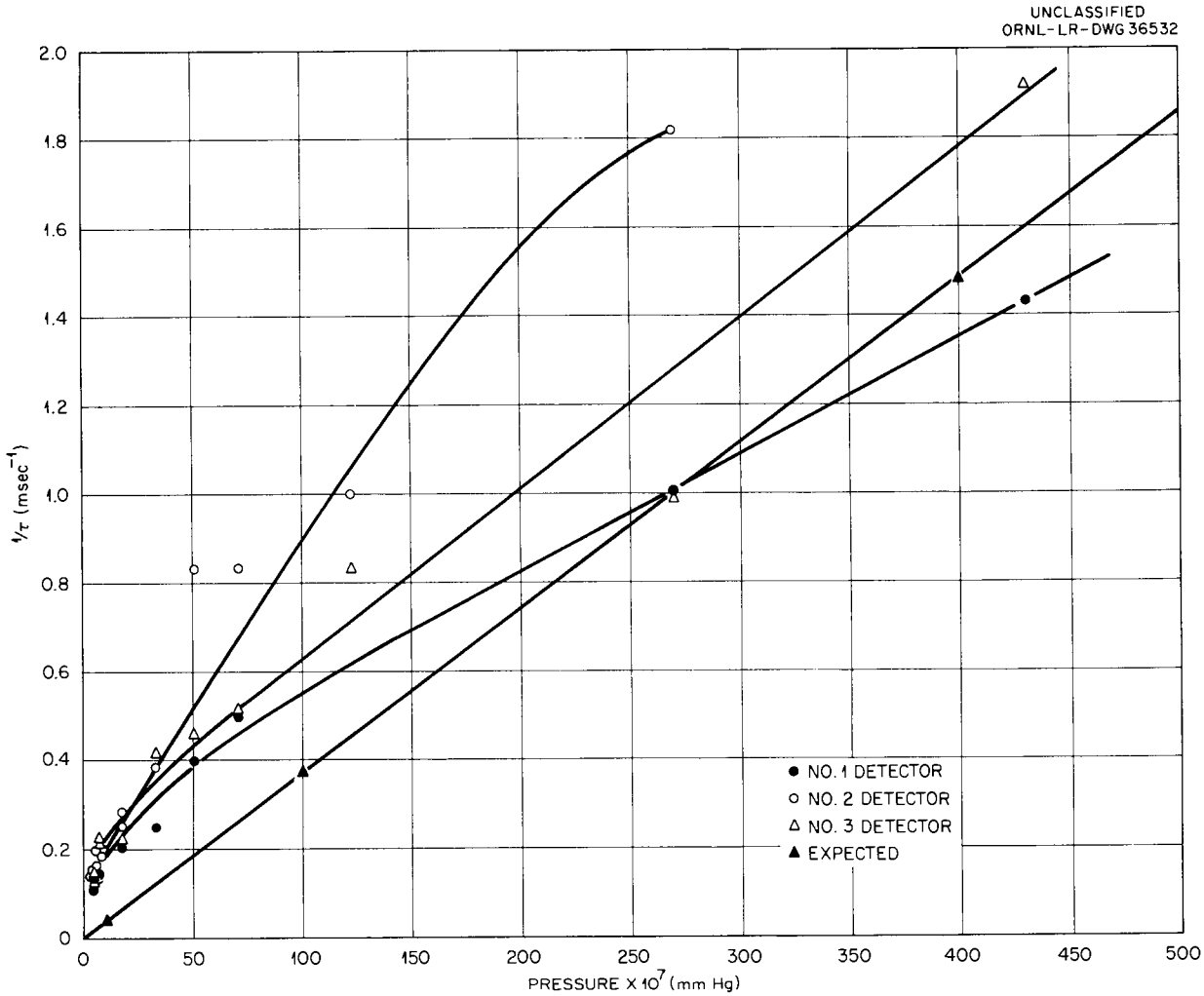

Fig. 1.1.7. $1/\tau$ as a Function of Argon Gas Pressure for Three Neutral Particle Detectors. τ = time required for neutral particle signal to decay in amplitude by $1/e$.

detector are a typical example. These measurements are oscillographed using Tektronix oscilloscopes with modified Aremac cameras attached. The camera shutters are set at "Bulb" and are solenoid operated. The shutter contacts are connected in series and trigger the beam off after all shutters have opened.

Figure 1.1.8 shows a block diagram of the beam pulsing system. Either the shutter contacts or a manually operated switch may be selected to trigger the single-shot multivibrator which generates a positive adjustable-length pulse from a negative base. A cathode follower drives a pulse-shaping circuit which gives the sync-signal for the oscilloscope horizontal sweep. The cathode follower also drives a long cable leading to the transmitter mounted near the base of the accelerator tube. The transmitter uses a 12BY7 and a 6216 in a current feedback circuit to drive a Sylvania R1131C glow modulator tube. A 4-in.-dia reading lens at the transmitter focuses the light of the glow modulator tube on a similar lens at the receiver located in the high-voltage terminal of the accelerator tube. The receiving lens concentrates the light on the photocathode of the 6335 miniature photomultiplier tube. A current feedback amplifier follows the photomultiplier to obtain maximum stable gain from the 6335 as well as to provide a

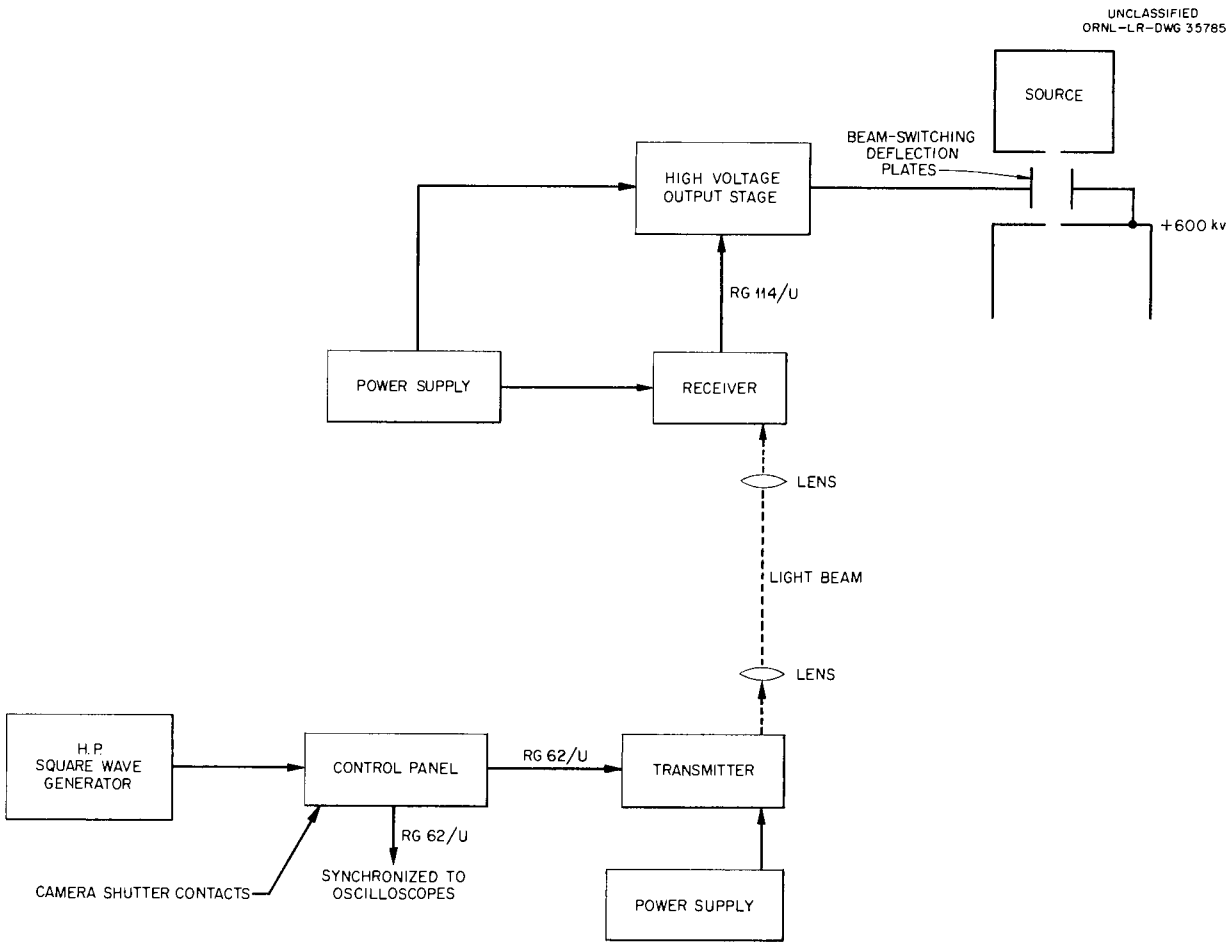

Fig. 1.1.8. Beam-Pulsing System for DCX Plasma Measurements.

low-impedance source for the succeeding direct-coupled stages ending with a cathode follower to drive the high-voltage output stage on a separate chassis. Figure 1.1.9 is a circuit diagram of the system.

The output stage is a compensated bootstrap circuit using two 4-125A tetrode tubes. The 4500-v plate supply uses 2X2A rectifiers, and the 300-v screen supply uses silicon rectifiers. The beam deflection plate configuration varies, but the drive is usually unbalanced with one plate at terminal ground. The driver is capable of handling any plate configuration in use on DCX.

This system gives beam cutoff times (98% value) as small as 0.5 μsec and has been very reliable and free of spurious operation.

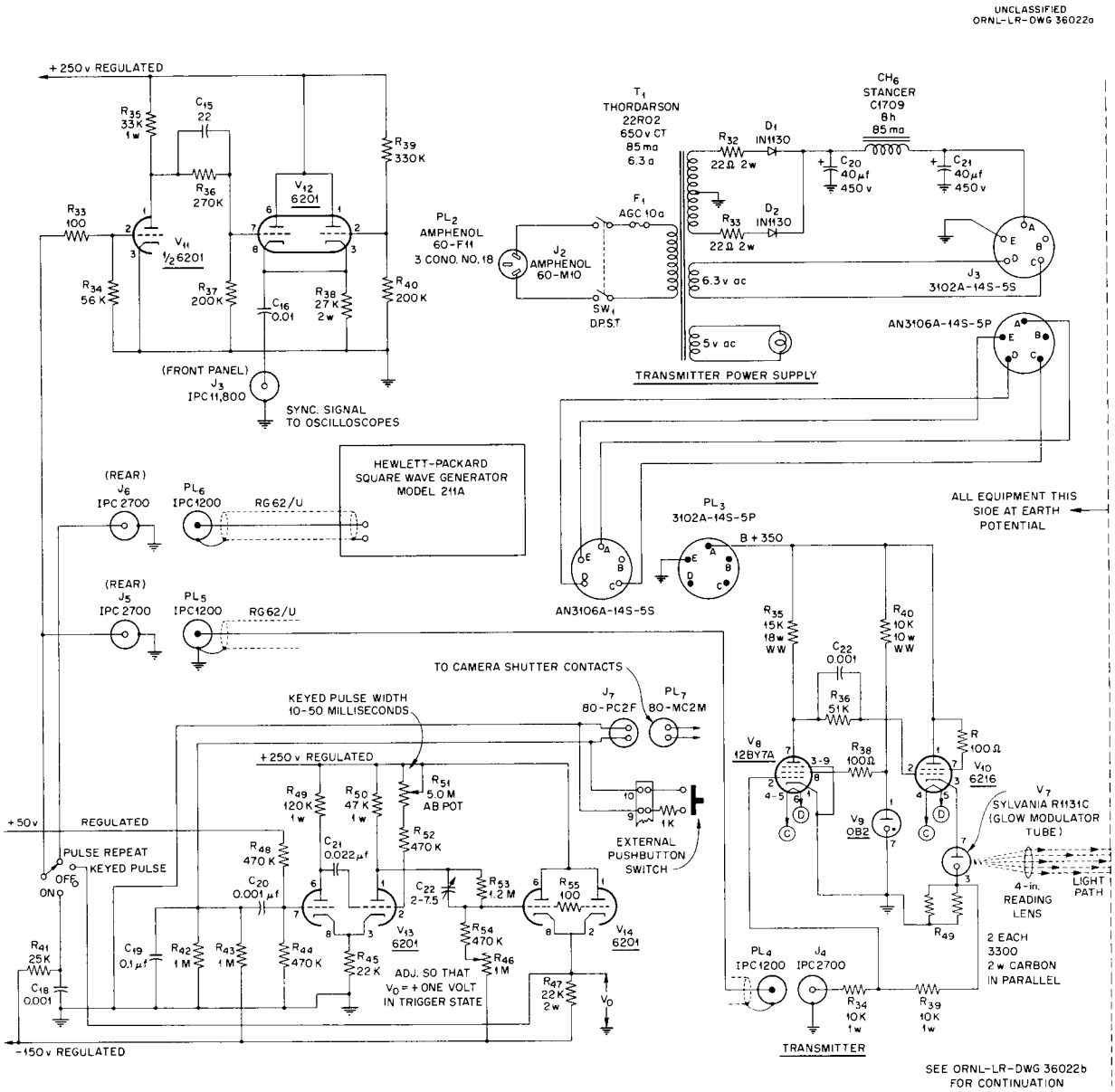

Fig. 1.1.9. Circuit Diagram of Beam Pulser for DCX Plasma Measurements.

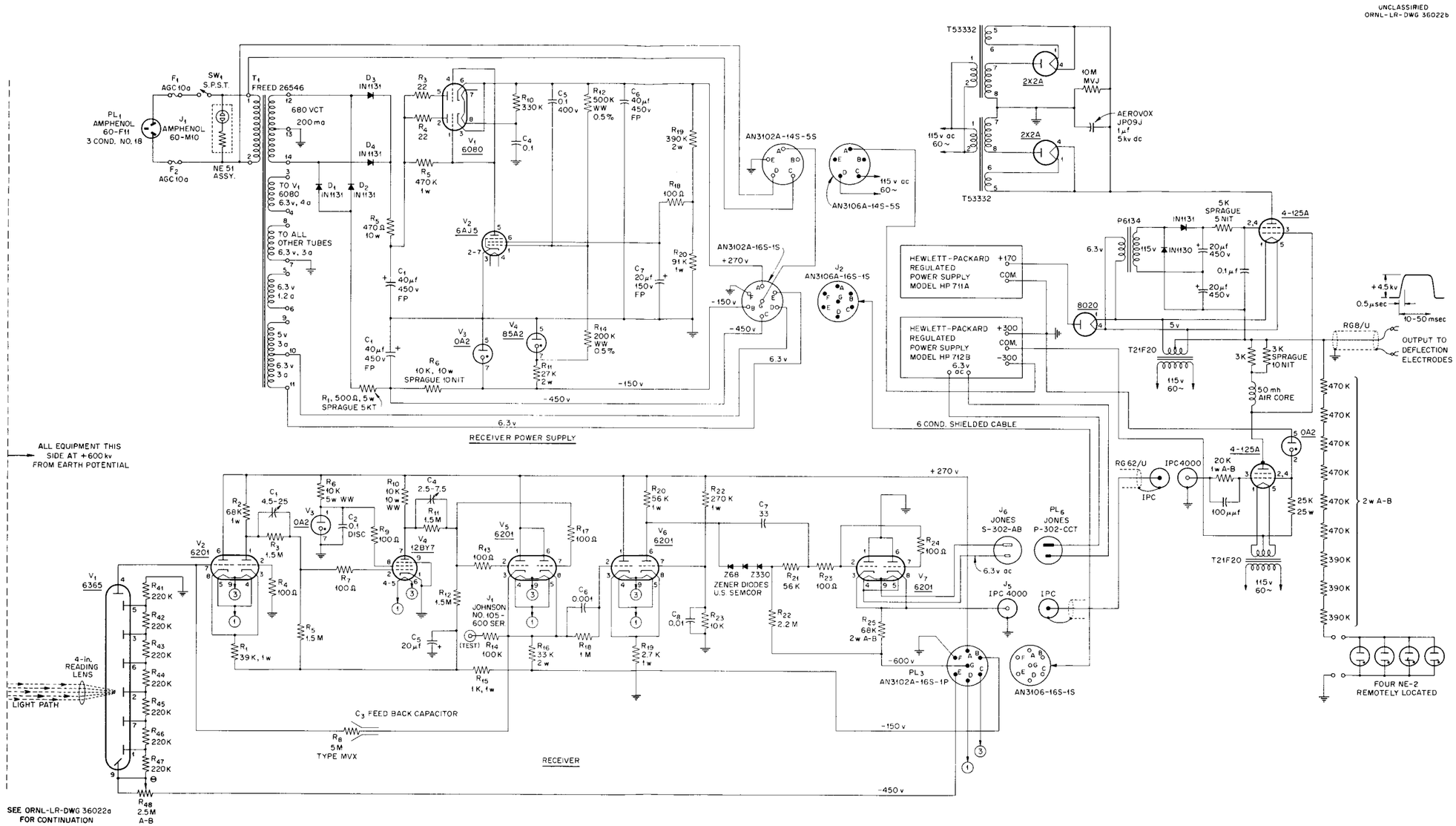

Fig. 1.1.9. (cont'd)

1.2 MICROWAVE DIAGNOSTICS OF DCX PLASMA

H. O. Eason, Jr.

Interferometric microwave measurements of a deuterium plasma during one DCX run gave brief phase-shift indications (with a poor signal-to-noise ratio) of a plasma density of 1×10^{11} electrons/cm^3, with no such indications found on succeeding runs with hydrogen.

Measurements of very low plasma densities by this method depend upon measurements of very small phase shifts at the lowest practical frequency, and bench tests showed that the equipment used could measure a minimum phase shift of 1°, corresponding to a plasma density of 1×10^{10} electrons/cm^3 for a 3-cm path length. A similar interferometer was constructed which it is hoped will, after minor modifications, permit measurements down to 3×10^9 electrons/cm^3, thus making it possible to use this equipment on the lower-density plasmas.

Equipment for synchronous detection of the interferometer output with the DCX input beam switched on and off at a constant rate is being developed in an attempt to increase phase-shift detection sensitivity, increase the signal-to-noise ratio, and eliminate the effect of slow thermal and mechanical drifts.

1.2.1 MICROWAVE THEORY

Microwave diagnostics, a group of measurement methods developed primarily at other laboratories over the past several years,[1-3] as practiced at ORNL makes use of microwave beams in conjunction with the dielectric properties of ionized plasmas in an attempt to measure the electron density of such plasmas. These dielectric properties are well known, having received much attention in connection with the propagation of radio waves through the ionosphere.

The complex dielectric constant, $\bar{K}$, of an ionized medium in simple cases is given by

$$\bar{K} = 1 - \left(\frac{\omega_p}{\omega}\right)^2 \left[\frac{1}{1 + (\nu_c/\omega)^2}\right] - j\left(\frac{\omega_p}{\omega}\right)^2 \left[\frac{\nu_c/\omega}{1 + (\nu_c/\omega)^2}\right] ,$$

where ω is the frequency of the electromagnetic radiation and ν_c is the collision frequency. The radian plasma frequency, ω_p, depends directly upon the electron density, n_e, and is defined by

$$\omega_p = \sqrt{\frac{n_e e^2}{\epsilon_0 m_e}} ,$$

where

$$e = 1.6 \times 10^{-19} \text{ coulomb},$$
$$m_e = 9.1 \times 10^{-31} \text{ kg},$$
$$\epsilon_0 = \frac{1}{36\pi} \times 10^{-9} \text{ farad/meter}.$$

This expression for $\bar{K}$ assumes that any static magnetic field is perpendicular to the direction of propagation and parallel to the microwave electric field, the effect of other orientations being to introduce loss terms due to coupling with particle motions.

In practical cases, for frequencies in the microwave region and plasmas operating at low pressure, $\nu_c \ll \omega$, and the effect of collisions may be neglected. The effective plasma dielectric constant then reduces to

$$\bar{K} = 1 - \left(\frac{\omega_p}{\omega}\right)^2 ,$$

which is less than unity for $\omega > \omega_p$. Since the velocity of propagation through a dielectric medium varies as $\bar{K}^{-1/2}$, the wavelength in this region is longer, and a phase shift is introduced which is a

[1] R. F. Post, T. F. Prosser, and C. B. Wharton, *Microwave Diagnostics in Arc Research*, UCRL-4477 (April 1955).

[2] C. B. Wharton, *Microwave Diagnostics for Controlled Fusion Research*, UCRL-4836 (Revised) (September 1957).

[3] M. A. Heald, *1958 IRE National Convention Record* (Part 9), p 14.

function of electron density. For the case where $\omega < \omega_p$, the dielectric constant is negative and the wave is totally reflected at the boundary of the plasma. These facts constitute the basis for the experimental work described. Work with the DCX plasma is described in this section and work on the DCX carbon arc in Sec 2.3 below.

1.2.2 DCX PLASMA MEASUREMENTS

In marked contrast to the problem of measurement of very high densities, as in the carbon arc (see Sec 2.3, this report), lies the problem of measurement of low densities, that is, when the plasma frequency lies considerably below the microwave frequency. The lower limits on the microwave frequency used are imposed by the relation between the wavelength and the physical dimensions of the device to be studied – especially the plasma itself. This is due to the extreme difficulty involved in focusing or collimating the microwave beam to a least-dimension less than one wavelength, and to undesired resonant effects in the device as a whole. Measurement of very low densities by the microwave method must therefore depend upon measurement of very small phase shifts at the lowest practical frequency.

Phase shifts at microwave frequencies are measured by the interferometer method illustrated in Fig. 1.2.1. Microwave power propagated through the test path is compared with that propagated through the reference path. The phase shifter and attenuator are initially adjusted for an output null at the detector. Introduction of the plasma into the test path results in an unbalanced signal at the detector which is a function of the resistive and dielectric properties of the plasma. Readjustment of the calibrator reference elements for a detector null yields the phase shift and attenuation introduced by the plasma, from which density may be determined when the plasma dimensions are known. The resolution obtainable by this method, and consequently the smallest density which may be detected at a given frequency, depends upon several factors. The most notable of these are the power available at the detector, the resulting signal-to-noise ratio, and the calibration accuracy and resetability of the reference elements.

The above method has been used in attempting to measure the density of the plasma ring in DCX. Due to physical limitations involving point of access and the necessity for making other types of diagnostic measurements during sustained operation of this machine, it was necessary that the test path be constructed in the form of a unit which could be inserted or removed from the machine at will during operation. These factors resulted in the configuration for the test path shown in Fig. 1.2.2, which is a photograph of the unit used at 24,000 Mc. Figure 1.2.3 shows the position of this unit in relation to the plasma ring when set up for operation. The unit is designed to be inserted vertically through the 6-in. gate valve on the top of the DCX tank with a sliding O-ring seal used to provide a vacuum-tight joint. A vacuum lock above this valve allows the unit to

UNCLASSIFIED
ORNL-LR-DWG 35835

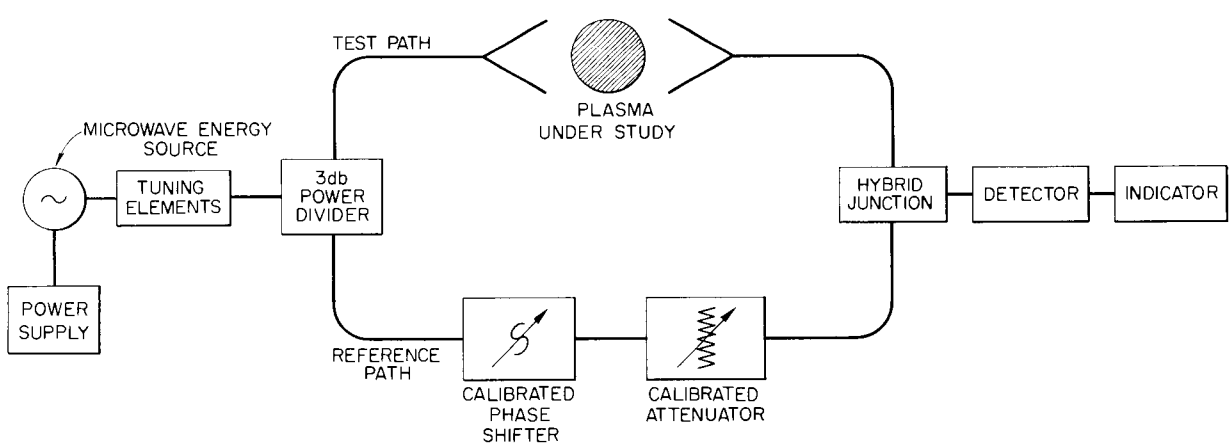

Fig. 1.2.1. Interferometer Used for Measuring Phase Shifts at Microwave Frequencies.

UNCLASSIFIED
PHOTO 33517

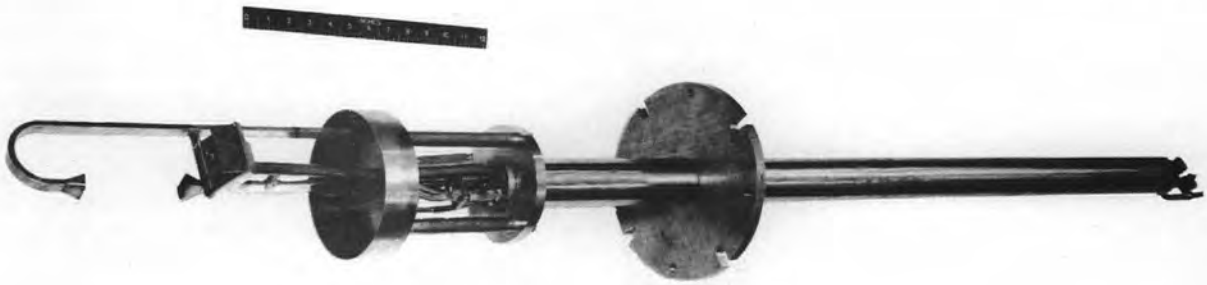

Fig. 1.2.2. DCX Test Path for 24,000-Mc Interferometer.

UNCLASSIFIED
ORNL-LR-DWG 35836

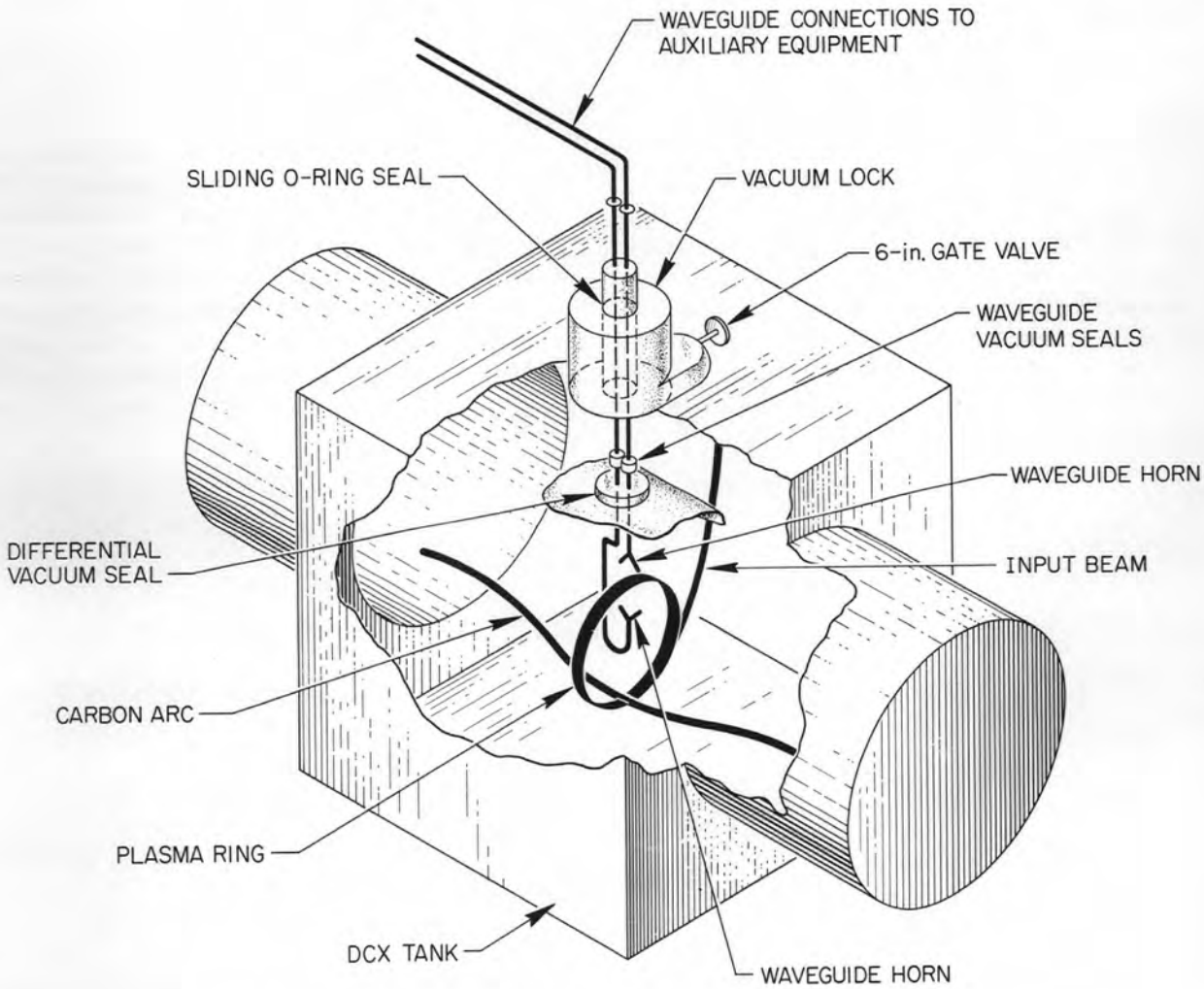

Fig. 1.2.3. Relationship of Interferometer to DCX Plasma Ring.

be inserted during DCX operation. Isolation between the two chambers of the DCX differential vacuum system is achieved by the stainless steel cup, seen in Fig. 1.2.2, which forms a low-conductance joint with a mating section of the liner. Waveguide connections from the outside pass through the tube; these connections use resonant Kovar windows to seal them from the atmosphere. The waveguides, arranged so that the microwave E field is parallel to the static magnetic field, terminate in small horns above and below the top section of the plasma ring as seen in Fig. 1.2.3. Water cooling is used below the Kovar windows to protect them from excessive temperatures. A foil-type neutral particle detector is included in order that information about decay and amplitude may be obtained simultaneously for correlation with the microwave data. Waveguide connections are made from the unit to companion equipment located some 15 ft away. This removes the companion equipment from the DCX fringing field and, when necessary, permits the use of a water shield to protect the operator from radiation.

The unit just described was tested under bench conditions, and it was found that a minimum phase shift of 1° could be measured, corresponding to a minimum detectable plasma density of 1×10^{10} electrons/cm^3 for a 3-cm path length. The unit was used during the September 1, 1958, DCX run with deuterium, and brief phase-shift indications were obtained on the detection apparatus placing the density at approximately 1×10^{11} electrons/cm^3, considering the poorer signal-to-noise ratio under field conditions. The signal-to-noise ratio has been improved on succeeding runs with hydrogen; however, no phase-shift indication has been obtained for hydrogen. (See Sec 1.1.1 for an estimated 10^9 ions/cm^3 hydrogen plasma density, based on interpretation of neutral-particle-collection data.) A similar interferometer operating at 8200 Mc has been constructed which should allow detection of densities as low as 3×10^9 electrons/cm^3, all other factors being equal. However, some difficulties have arisen involving resonances and reflections at this longer wavelength, and it has not been used to date in any actual measurement attempt. It is thought that minor modifications will relieve these difficulties.

An additional step being taken to increase phase-shift detection sensitivity is the development of equipment for synchronous detection of the interferometer output with the DCX input beam switched on and off at a constant rate. This equipment has already slightly improved the signal-to-noise ratio. This method should enable increase in signal-to-noise ratio of at least an order of magnitude as well as elimination of slow thermal and mechanical drifts which plague high-sensitivity measurements of this type.

It should also be mentioned that, since the unit containing the test path must be inserted into DCX through a 6-in.-dia hole, it is inevitable that the return waveguide will interfere with Z spreading of the plasma ring beyond $2\frac{1}{2}$ in. from the central plane. A new test-path unit which incorporates features to help eliminate this difficulty is in the design stage.

1.3 PLASMA CONTAINMENT

The properties of the orbit of a single ion in the azimuthally symmetric DCX magnetic field in the absence of collisions have been studied with the aid of the Oracle. This work parallels earlier orbit calculations by the Livermore group.[1] Our study differs from theirs in our emphasis on orbits which encircle the axis of symmetry of the field, rather than on orbits which do not encircle this axis. Containment properties in the two cases may be quite different. For example, among our orbits, but not theirs, there is a class absolutely contained as a consequence of the conservation of the two known constants of motion of the system. On the other hand, in our studies of orbits not absolutely contained we have so far not seen the seemingly contained, quasi-periodic orbits discovered in the Livermore studies.

1.3.1 A STUDY OF ION ORBITS AND CONTAINMENT PROPERTIES OF DCX

M. Rankin T. K. Fowler

Equations of Motion

The relativistic Hamiltonian for a particle in a magnetic field is

$$H = \sqrt{m_0^2 c^4 + c^2\left(\vec{P} - \frac{e}{c}\vec{A}\right)^2} \ , \qquad (1)$$

where $\vec{P}$ is the canonical momentum vector and $\vec{A}$ is the magnetic potential vector. For an azimuthally symmetric magnetic field – such as the one of the DCX – $\vec{A} = (0, A_\theta, 0)$ so that, in cylindrical coordinates (letting A_θ be A), Eq. (1) may be written

$$\frac{H}{c} = \sqrt{m_0^2 c^2 + p_r^2 + \left(\frac{p_\theta}{r} - \frac{e}{c}A\right)^2 + p_Z^2} \ , \qquad (2)$$

where p_θ is the canonical angular momentum. The equations of motion are then given by

$$\dot{r} = \frac{\partial H}{\partial p_r} = \frac{c^2 p_r}{H} \ , \qquad (3)$$

$$\dot{Z} = \frac{\partial H}{\partial p_Z} = \frac{c^2 p_Z}{H} \ , \qquad (4)$$

$$\dot{p}_r = -\frac{\partial H}{\partial r} = \frac{c^2}{H}\left(\frac{p_\theta}{r} - \frac{e}{c}A\right)\left(\frac{p_\theta}{r^2} + \frac{e}{c}\frac{\partial A}{\partial r}\right) \ , \qquad (5)$$

$$\dot{p}_Z = -\frac{\partial H}{\partial Z} = \frac{c^2}{H}\left(\frac{p_\theta}{r} - \frac{e}{c}A\right)\frac{\partial A}{\partial Z} \ , \qquad (6)$$

$$\dot{\theta} = \frac{\partial H}{\partial p_\theta} = \frac{c^2}{rH}\left(\frac{p_\theta}{r} - \frac{e}{c}A\right) \ , \qquad (7)$$

$$\dot{p}_\theta = -\frac{\partial H}{\partial \theta} = 0 \ . \qquad (8)$$

Since there is no coupling between (7) and (8) and the other equations, they need not be considered in the integration of Eqs. (3) to (6) to find the r,Z motion. However, their information that p_θ = constant and

$$r\dot{\theta} = \frac{c^2}{H}\left(\frac{p_\theta}{r} - \frac{e}{c}A\right)$$

will later be used.

Noting that the total momentum p of the system is vH/c^2 and that $d/dt = v\ d/ds$ we write Eqs. (3) through (6) as

$$r' = P_r \ , \qquad (3')$$

$$Z' = P_Z \ , \qquad (4')$$

$$P_r' = \left(\frac{P_\theta}{r} - \mathcal{A}\right)\left(\frac{P_\theta}{r^2} + \frac{\partial \mathcal{A}}{\partial r}\right) \ , \qquad (5')$$

$$P_Z' = \left(\frac{P_\theta}{r} - \mathcal{A}\right)\left(\frac{\partial \mathcal{A}}{\partial Z}\right) \ , \qquad (6')$$

[1] A. Garren *et al.*, *Non-Adiabatic Effects in Single Particle Orbits*, in *Proceedings of Controlled Thermonuclear Reactions Conference, Berkeley, California, Feb. 1957*, TID-7536 (Part 2), p 170.

where

$$P_r \equiv \frac{p_r}{p} ,$$

$$P_\theta \equiv \frac{p_\theta}{p} ,$$

$$P_Z \equiv \frac{p_Z}{p} ,$$

$$\mathcal{A} \equiv \frac{e}{c}\frac{A}{p} ,$$

and the differentiation is now with respect to arc length. Note that in the above set of equations all variables are now dimensionless except r, Z, and P_θ, which have dimensions of length.

Absolute Containment

In the nonrelativistic limit, (2) becomes

$$p^2 = p_r^2 + p_Z^2 + V(p_\theta, r, Z) , \qquad (9)$$

where

$$V = \left[\frac{p_\theta}{r} - \frac{e}{c}A(r,Z)\right]^2 \qquad (10)$$

is an effective potential for the r,Z motion referred to above.[1] For the DCX, V as a function of r has been plotted for various values of p_θ at the mirror (Fig. 1.3.1) and at the mid-plane (Fig. 1.3.2).

A sufficient criterion for absolute containment[1] is that all energy become "potential" as a particle approaches the machine walls; that is, it is sufficient to require that

$$V \geqq p^2 \qquad (11)$$

at every point on the boundary of the machine. Let $\bar{p}_\theta$ be the largest value of p_θ such that (11) is satisfied. Since within the machine $A > 0$ (with the convention that the Z-axis points in the direction of the magnetic field), $\bar{p}_\theta$ necessarily must be negative, corresponding to orbits which encircle the axis of symmetry. From (9) and (11), a particle is *absolutely contained* if

$$p_r^2 + p_Z^2 < p^2 - V(r, Z, \bar{p}_\theta) . \qquad (12)$$

Analytic Approximation for A

In the absence of an electric current,

$$\nabla \times B = \nabla \times (\nabla \times A) = 0 .$$

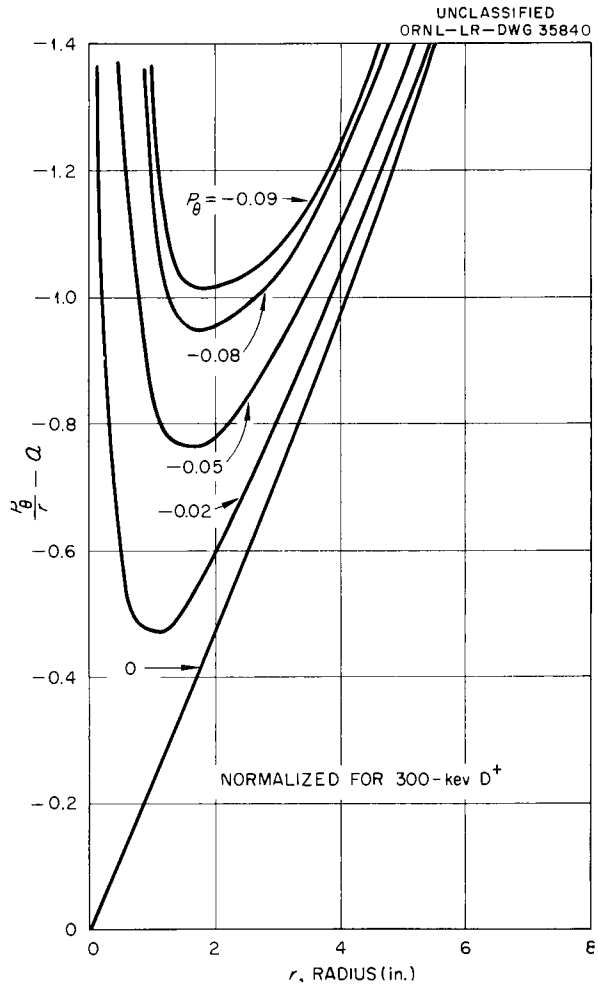

Fig. 1.3.1. $(P_\theta/r) - \mathcal{A}$ vs r at the Mirror of DCX, Normalized for 300-kev D^+.

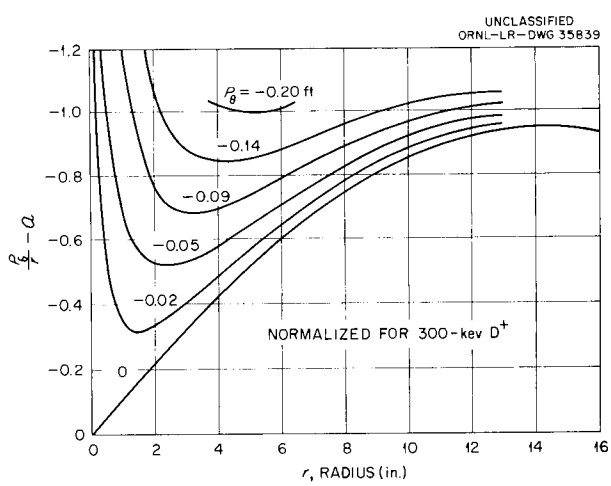

Fig. 1.3.2. $(P_\theta/r) - \mathcal{A}$ vs r at the Mid-Plane of DCX, Normalized for 300-kev D^+.

Since $\nabla \times (\nabla \times A) = \nabla(\nabla \cdot A) - \nabla^2 A$, and since $\nabla \cdot A = 0$ in our case, we must have $\nabla^2 A = 0$. In cylindrical coordinates this becomes

$$\nabla^2 \vec{A} = \hat{a}_\theta \left(\nabla^2 A_\theta - \frac{A_\theta}{r^2} \right) = 0 \ . \qquad (13)$$

Hence A must satisfy the equation

$$\frac{1}{r}\frac{\partial}{\partial r}\left(r \frac{\partial A}{\partial r} \right) + \frac{\partial^2 A}{\partial Z^2} - \frac{A}{r^2} = 0 \ . \qquad (14)$$

We assume $A = A(r,Z) = f(r) \cos Z$, since $\cos Z$ gives an appropriate Z variation for a mirror field. Then we find that $f(r)$ must satisfy the equation

$$r^2 f'' + r f' - (r^2 + 1) f = 0 \ . \qquad (15)$$

The solution of this equation is the Bessel function $I_1(r)$. Hence an analytic representation of A is of the form

$$\sum_n \alpha_n \cos nZ \, I_1(nr) \ .$$

The first form used for A was

$$A = \alpha_0 \rho - \alpha_1 I_1(\rho) \cos \zeta \ , \qquad (16)$$

where $\rho \equiv 2\pi r/L$, $\zeta \equiv 2\pi Z/L$, and L = distance between mirrors (30 in. in the DCX). The two constants α_0 and α_1 were chosen by imposing the conditions $B(r=0, Z=0)$ = 9.6 kilogauss and a mirror ratio of 2:1 as in the DCX. When orbits were followed on the Oracle using (16) for A, many were seen to reach the radial boundary. This was a fictitious radial escape, attributable to the fact that this first-order approximation for A gave (for r values larger than about 6 in.) a much smaller value than in reality exists in the DCX.

To overcome this difficulty the second-order approximation to A was introduced. This is

$$A = \alpha_0 \rho - \alpha_1 I_1(\rho) \cos \zeta + \alpha_2 I_1(2\rho) \cos 2\zeta \ . \qquad (17)$$

The three constants α_0, α_1, α_2 were determined by the two conditions used for the first-order A and the additional condition that $A(r = 14$ in., $Z = 0)$ agree with the actual A (the maximum A) at that point in the DCX. These constants are $\alpha_0 = 2.8242$, $\alpha_1 = 1.9098$, and $\alpha_2 = 0.04095$. This second-order form for A was found to fit the real A to within an error of not more than 5% in the midplane. Comparison of A at the mirror with later Oracle calculations of the DCX A at that plane also showed agreement to within a few per cent.

In the remainder of our calculations, A has the meaning given by (17).

For reference we note that from this form for A it follows that

$$B_Z = \frac{1}{r}\frac{\partial(rA)}{\partial r} = \frac{2\pi}{L}\left[2\alpha_0 + \alpha_1 \cos \zeta \, I_0(\rho) + 2\alpha_2 \cos 2\zeta \, I_0(2\rho) \right] \ , \qquad (18)$$

and

$$B_r = -\frac{\partial A}{\partial Z} = \frac{2\pi}{L}\left[\alpha_1 I_1(\rho) \sin \zeta + 2\alpha_2 I_1(2\rho) \sin 2\zeta \right] \ . \qquad (19)$$

Equations (3′) through (6′) form a system of first-order differential equations. A code to integrate this system using a Runge-Kutta numerical integration scheme was written. Parameters of this code are: h (the interval size), p, P_θ, and the initial values of r, Z, and P_Z. The code then calculates the correct initial value of P_r. The initial sign of P_r is arbitrary and normally has been used as negative.

The code was tested against a case run by the Livermore group. Also, several internal checks on the numerical accuracy of the integration are made. The value of P^2 is calculated after each integration step, and the integration is terminated if there is significant deviation of P^2 from 1. By comparing orbits integrated with two different interval sizes and also by using the test of time reversal of the orbit, it has been found that orbits are reliably determined if $|P^2 - 1| < 0.0001$. The value of h necessary to give this accuracy depends on the value of P_θ and on the length of the integration, since the error is accumulative. As P_θ increases from -0.09 to -0.02, it has been found necessary to decrease h from 0.025 to 0.005.

In analyzing the results of these Oracle data, definite information is obtained only in the cases of those orbits which are seen to escape. Other cases are inconclusive, due to the time scale. An integration path length of 100 ft requires several hours of Oracle computing time but corresponds to an actual time of the order of only 10 μsec. The Oracle calculations are used then as a guide in formulating properties and theories of containment.

Tables 1.3.1 to 1.3.3 show calculated DCX ion orbits under certain conditions for varying P_θ, P_Z, and r_0, respectively. Figures 1.3.3 and 1.3.4 show graphs of the $P_\theta = -0.08$ and the $P_\theta = -0.02$ orbits in Table 1.3.1.

Table 1.3.1. Calculated DCX Ion Orbits for Varying P_θ

Fixed initial conditions: $r = \frac{1}{3}$ ft, $Z = 0$, $P_Z = 0.6$

P_θ	$(mr\dot{\theta})_0$	$(P_r)_0$	Comments on Orbit
−0.09	−0.69	−0.40	Contained for at least $s = 75$ ft
−0.08	−0.66	−0.45	Contained for at least $s = 100$ ft
−0.05	−0.57	−0.56	Escaped* through mirror after two reflections ($s = 10$ ft)
−0.02	−0.48	−0.64	Escaped through mirror after two reflections ($s = 9.6$ ft)

*Escape is defined to mean $|Z| > 1.25$ ft or $|r| \geqq 1.25$ ft.

Table 1.3.2. Calculated DCX Ion Orbits for Varying P_Z

Fixed initial conditions: $r = \frac{1}{3}$ ft, $Z = 0$, $P_\theta = 0.05$

P_Z	$(mr\theta)_0$	$(P_r)_0$	Comments on Orbit
0.6	−0.57	−0.56	Escaped* through mirror after two reflections ($s = 10$ ft)
0.5	−0.57	−0.65	Contained for at least $s = 48$ ft
0.4	−0.57	−0.72	Escaped radially after six reflections ($s = 17$ ft)

*Escape is defined as $|Z| > 1.25$ ft or $|r| \geqq 1.25$ ft.

Table 1.3.3. Calculated DCX Ion Orbits for Varying r_0

Fixed initial conditions: $P_\theta = 0.05$, $P_Z = 0.6$, $Z = 0$

r_0 (in.)	$(mr\dot{\theta})_0$	$(P_r)_0$	Comments on Orbit
2	−0.52	−0.61	Escaped* after one reflection** ($s = 7$ ft)
4	−0.57	−0.56	Escaped after two reflections ($s = 10$ ft)
6	−0.70	−0.39	Escaped after six reflections ($s = 20$ ft)

*Escape is defined as $|Z| > 1.25$ ft or $|r| \geqq 1.25$ ft.

**Because of Oracle memory failure, this was run only to $|Z| = 1.19$ ft.

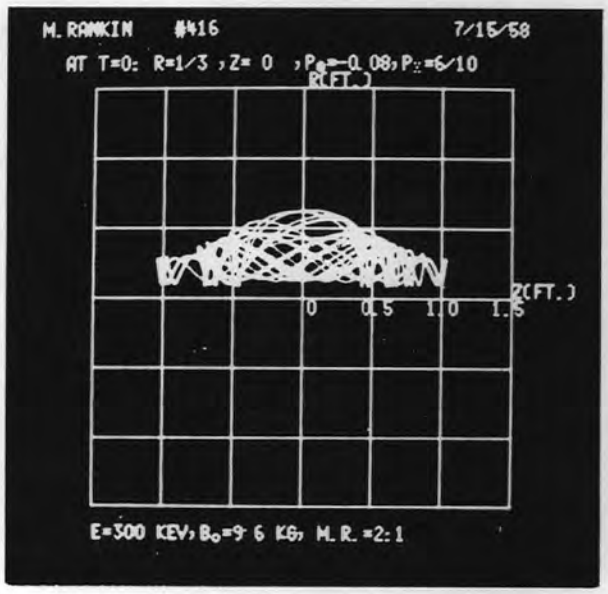

Fig. 1.3.3. Ion Orbits ($P_\theta = -0.08$) for DCX.

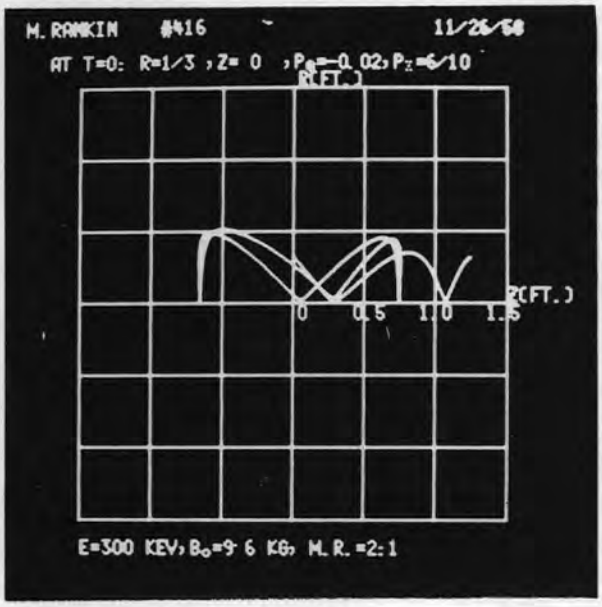

Fig. 1.3.4. Ion Orbits ($P_\theta = -0.02$) for DCX.

$$\nabla \cdot \vec{E} = -\nabla^2 \phi = 4\pi \sum_i e_i \int f_i \, d^3v \ . \qquad (2)$$

In the above, $f_i(\vec{r},\vec{v},t)$ is the distribution function for the ith species of particle (electron or ion), e_i and M_i are its charge and mass, and $\vec{E}$ and $\vec{B}$ are the electric and magnetic field intensities; $\phi(\vec{r},t)$ is a scalar potential. Equations (1) and (2) are linearized and solved by taking the Fourier transform in space and the Laplace transform in time and following the procedure of Bernstein.[3] It is found that the Fourier-Laplace transform of the potential is given by

$$\phi(\vec{k},p) = \frac{-\sum_j (4\pi e_j/k^2\omega_{cj}) \int S_j \, d^3v}{1 - Y(p)} \ , \qquad (3)$$

where $\vec{k}$ is the wave vector which occurs in the Fourier transform, p is the Laplace transform parameter, and $S_j(\vec{v},\vec{k},p)$ is a quantity related to $f_j(\vec{r},\vec{v},o)$, the initial value of the perturbation of the distribution function. The term $Y(p)$ is given by

$$Y(p) = 2\pi i \sum_j \frac{\omega_{pj}^2}{k^2} \sum_{n=-\infty}^{+\infty} \int_{-\infty}^{+\infty} dv_z \int_0^\infty v_\perp dv_\perp \times$$

$$\times \left[\frac{\omega_{cj}}{v_\perp} \frac{\partial f_j^0}{\partial v_\perp} \frac{n\, J_n^2\left(\frac{k_\perp v_\perp}{\omega_{cj}}\right)}{(p + ik_z v_z + in\,\omega_{cj})} + k_z \frac{\partial f_j^0}{\partial v_z} \frac{J_n^2\left(\frac{k_\perp v_\perp}{\omega_{cj}}\right)}{(p + ik_z v_z + in\,\omega_{cj})} \right] \ , \qquad (4)$$

1.3.2 UNSTABLE PLASMA OSCILLATIONS IN A MAGNETIC FIELD

E. G. Harris[2]

Small-amplitude oscillations of a plasma in an externally produced magnetic field were studied by the use of linearized Vlasov equations. Perturbations of the magnetic field were neglected. Instability of a deuterium plasma in a magnetic field of 10^4 gauss was predicted for a density exceeding about 10^7 particles/cm^3. The following set of equations is used:

$$\frac{\partial f_i}{\partial t} + \vec{v} \cdot \frac{\partial f_i}{\partial \vec{r}_i} + \frac{e_i}{M_i}\left(\vec{E} + \frac{1}{c}\vec{v} \times \vec{B}\right) \cdot \frac{\partial f_i}{\partial \vec{v}} = 0 \qquad (1)$$

where $\omega_{pj} = (4\pi N e_j^2/M_j)^{1/2}$ is the plasma frequency of the jth species of particle, $\omega_{cj} = e_j B/M_j c$ is the cyclotron frequency of the jth species of particle, and $f_j^0(v_z, v_\perp)$ is the unperturbed velocity distribution for the jth species normalized to unity. The magnetic field is in the Z direction, and $v_\perp$ and $k_\perp$ are

$$v_\perp = (v_x^2 + v_y^2)^{1/2} \qquad (5)$$

and

$$k_\perp = (k_x^2 + k_y^2)^{1/2} \ . \qquad (6)$$

[2]Consultant from the University of Tennessee.

[3]I. B. Bernstein, *Phys. Rev.* 109, 10 (1958).

We are particularly interested in zeroth order distributions which cause the denominator of (3) to vanish for values of p which have positive real parts; that is,

$$Y(p) = 1 \qquad \text{for } \mathrm{Re}(p) > 0 \ . \tag{7}$$

If (7) is satisfied, there will exist plasma oscillations whose amplitudes increase exponentially.

A previous paper[4] exhibited two distributions which led to unstable oscillations. In that paper the motion of the ions was neglected. In this work the ion motion is taken into account and it is shown that the zeroth order function,

$$f_i^0 = \frac{1}{2\pi}\left(\frac{2}{\alpha_{\perp i}^2}\right)\left(\frac{\alpha_{zi}}{\pi}\right)\frac{e^{-v_\perp^2/\alpha_{\perp i}^2}}{v_z^2 + \alpha_{zi}^2}, \tag{8}$$

can lead to unstable oscillations. Equation (8) is the distribution function for the ions; a similar distribution function is assumed for the electrons. The parameters $\alpha_\perp$ and α_z measure the spread in velocity in the directions perpendicular and parallel to the field. The function given by (8) was chosen because it resembles the Maxwell-Boltzmann function and allows the integrals in (4) to be evaluated in terms of known functions. Substituting (8) into (4) gives

$$Y(p) = -\sum_j \omega_{pj}^2 \sum_{n=-\infty}^{+\infty} e^{-\lambda_j} I_{|n|}(\lambda_j) \times$$

$$\times \left[\frac{i}{\lambda_j}\left(\frac{k_\perp}{k}\right)^2 \frac{n/\omega_{cj}}{\left(p + |k_z|\alpha_{zj} + in\omega_{cj}\right)} + \left(\frac{k_z}{k}\right)^2 \frac{1}{\left(p + |k_z|\alpha_{zj} + in\omega_{cj}\right)^2}\right], \tag{9}$$

where

$$\lambda_j = \frac{\alpha_{\perp j}^2 k_\perp^2}{2\omega_{cj}^2}$$

and $I_n(\lambda)$ is the modified Bessel function of the first kind.

[4]E. G. Harris, *Phys. Rev. Letters* 2, 34 (1959).

We first consider the case $\alpha_{zi} = \alpha_{ze} = 0$. If one imagines the density of the plasma to be built up from zero one finds that the plasma first becomes unstable [that is, a root of $Y(p) = 1$ becomes complex with a positive real part] approximately when

$$\omega_{pe}^2 = \frac{4\pi N e^2}{M_e} > \omega_{ci}^2 = \frac{e^2 B^2}{M_i^2 c^2}, \tag{10}$$

that is,

$$N > \left(\frac{M_e}{M_i}\right)\frac{B^2}{4\pi M_i c^2} \ . \tag{11}$$

If $\alpha_{zi} = \alpha_{ze} = \alpha_z$ and $\alpha_{\perp e} = 0$, then an approximation to the root of $Y(p) = 1$ which first becomes unstable may be shown to be

$$p = -|k_z|\alpha_z \pm i\omega_{ci} + i\,\frac{k_z\omega_{pe}\omega_{ci}\left[\frac{M_e}{M_i}e^{-\lambda_i} I_1(\lambda_i)\right]^{1/2}}{k\left(\omega_{ci}^2 - \frac{k_z^2}{k^2}\omega_{pe}^2\right)^{1/2}} \ . \tag{12}$$

If $\alpha_z = 0$, Eq. (12) predicts instability when

$$\frac{k_z^2}{k^2}\omega_{pe}^2 > \omega_{ci}^2 \ . \tag{13}$$

This is equivalent to (10) if k_z/k is of the order of unity, which is one of the approximations leading to (10). Actually, there is no instability for $k_z = k$, for then $k_\perp = 0$ and hence $\lambda_i = 0$, and

the numerator of (12) vanishes. The approximations made in deriving (12) fail near the onset of instability. For

$$\frac{k_z^2}{k^2}\omega_{pe}^2 \gg \omega_{ci}^2 \ , \tag{14}$$

Eq. (12) becomes

$$p = -|k_z|\alpha_z + i\omega_{ci} + \\ + \omega_{ci}\left[\frac{M_e}{M_i} e^{-\lambda_i} I_1(\lambda_i)\right]^{1/2} \ . \tag{15}$$

Since the maximum value of $e^{-\lambda_i} I_1(\lambda_i)$ is 0.219, Eq. (15) gives the instability criterion,

$$\omega_{ci}\left(0.219\frac{M_e}{M_i}\right)^{1/2} > |k_z|\alpha_z \ . \tag{16}$$

The term $|k_z|\alpha_z$ which appears in (15) is due to the process of Landau damping. Probably no quantitative significance should be attached to it since the v_z dependence of (8) is rather unrealistic.

At still higher densities, instabilities set in which are independent of the motion of the ions. If $\alpha_{ze} = 0$, the criterion for instability is approximately

$$\omega_{pe}^2 = \frac{4\pi Ne^2}{M_e} > \omega_{ce}^2 = \frac{e^2B^2}{M_e^2c^2} \ , \tag{17}$$

or

$$N > \frac{B^2}{4\pi M_e c^2} \ . \tag{18}$$

This is higher by a factor of M_i^2/M_e^2 than the density given by (11). For a deuterium plasma this factor is 1.35×10^7. These instabilities were discussed previously by the author.[4]

If we take $B = 10^4$ gauss (about the field used in DCX), then (11) predicts instability of a deuterium plasma when the particle density exceeds about 10^7 particles/cm^3, a density much below that proposed for any thermonuclear machines. It is difficult to say what the ultimate effect of small-amplitude instabilities will be. The theory presented here is a linear one and yields no information about the factors which must ultimately limit the amplitude of the oscillations. The writer is of the opinion that the amplitude will be limited by the expulsion of particles across the field, or through the mirrors in the case of mirror machines. This is suggested by the trochotron experiments reported by Alfvén *et al.*[5]

There are no experimental data sufficiently clear-cut to allow a careful quantitative comparison between theory and experiment. However, some of the trochotron data[5] agree in order of magnitude with Eq. (18) if reasonable assumptions are made about the cross section of the trochotron beam.

The instabilities discussed here are due to anisotropies in the velocity distributions of the electrons and ions of the plasma. Since any confinement of a plasma by a magnetic field necessarily produces anisotropic velocity distributions, instabilities such as those reported here may be quite commonplace in thermonuclear machines.

---

[5]H. Alfvén *et al.*, *Kgl. Tek. Högskol. Handl.*, No. 22 (1948).

1.4 DEUTERON AND ELECTRON ENERGY DISTRIBUTIONS IN DCX

A. Simon T. K. Fowler M. Rankin

Transport equations are being solved numerically to determine in detail the energy distribution of ions and electrons in the DCX plasma, both in steady state and in a transient condition. In two previous reports[1,2] the steady-state aspect of the problem was studied using a model in which the energy distribution for the majority of the ions and electrons was assumed to be Maxwellian in shape. The present treatment utilizing transport equations is, of course, more exact in that the shape of the distribution is determined, not assumed.

Fokker-Planck Equations. – The dominant mechanism of energy transfer between the components of a plasma is by fairly long range Coulomb interactions. The great majority of the energy transfers per collision are small and the angle of scattering is also small. A situation of this sort is ideally suited for the use of the Fokker-Planck[3] approximation to the Boltzmann transport equation. We have further assumed that the plasma is neutral and is uniformly distributed in space and isotropic in velocity space. All sources and sinks are also assumed to be isotropic, and external fields are considered to be absent. With these assumptions, all spatial and angle dependences drop out of the problem and the resultant equation has only two independent variables: energy, E, and time, t. For a system of two species, ions and electrons, these equations are

$$\frac{\partial P}{\partial t} = -\frac{\partial(A_P P)}{\partial E} + \frac{\partial^2(B_P P)}{\partial E^2} + S_P(E,t) - L_P(E,t) \quad (1)$$

and

$$\frac{\partial N}{\partial t} = -\frac{\partial(A_N N)}{\partial E} + \frac{\partial^2(B_N N)}{\partial E^2} + S_N(E,t) - L_N(E,t) \quad . \quad (2)$$

Here $P(E,t)$ and $N(E,t)$ represent the number of ions and electrons, respectively, in a unit energy interval at a time t. The functions $S_P(E,t)$ and $S_N(E,t)$ are source terms representing injected ions, and $L_P(E,t)$ and $L_N(E,t)$ are loss terms representing leakage out the mirrors. The transport coefficients $A_P(E,t)$ and $A_N(E,t)$ represent the rate of energy loss or gain by a particle in colliding with all other particles, and the coefficients $B_P(E,t)$ and $B_N(E,t)$ are proportional to the energy dispersion produced by collisions with other particles. Equations (1) and (2) are coupled in a complicated fashion by the fact that A_P, A_N, B_P, B_N, L_P, L_N are themselves integral functions of both the P and N distributions.

Numerical Solution. – An IBM-704 code has been devised to solve (1) and (2) simultaneously. First, since under the assumption of isotropy the great difference in ion and electron masses permits hot ions to heat only the coldest electrons, the distributions had to be screened much more closely at low energies than at high energies. Thus, our mesh of 75 energy cells was divided into two regions, the range $0 \leq E \leq 500$ ev being covered with cells of width 20 ev, and the range 0.5 kev $< E \leq 1000.5$ kev with cells of width 20 kev. Secondly, care has been taken to guarantee that the numerical difference scheme satisfies the boundary conditions that particles and energy are conserved in the absence of sources and sinks. A CF memo[4] discussing incorporation of these boundary conditions into the difference equations will appear soon.

Primarily as a test, the code with source and loss terms set equal to zero is presently being used to study relaxation to thermal equilibrium of an isolated plasma of deuterons and electrons initially at different energies. When completed, the results should constitute an interesting sequel to earlier numerical studies of the relaxation of a single species of charged particles.[5]

[1] A. Simon and M. Rankin, *Some Properties of a Steady State High-Energy Injection Device (DCX)*, ORNL-2354 (Aug. 25, 1957).

[2] T. K. Fowler and A. Simon, *Energy Transfer to Cold Electrons in DCX*, ORNL-2552 (July 1958).

[3] M. N. Rosenbluth, W. M. MacDonald, and D. L. Judd, *Phys. Rev.* 107, 1–6 (July 1, 1957).

[4] T. K. Fowler, M. Rankin, and A. Simon, *Boundary Conditions and Conservation Properties of FOPP, a Plasma Fokker-Planck Code*, ORNL CF-59-2-75 (to be published).

[5] W. M. MacDonald, M. N. Rosenbluth, and W. Chuck, *Phys. Rev.* 107, 350–53 (July 15, 1957).

2. CARBON ARC STUDIES

2.1 SOME SPECTROSCOPIC STUDIES OF THE ENERGETIC CARBON ARC – A MAGNETICALLY CONSTRAINED HIGH-VACUUM ARC

J. R. McNally, Jr. M. R. Skidmore G. K. Werner

Spectroscopic studies of the 5-ft-long, 300-amp carbon arc showed Doppler broadening which was equivalent to 50 ev (400,000°K) and slant effects which were believed to be due to the crossed electric and magnetic fields. Slant effects were associated with individual filaments of the carbon arc as well as with the whole arc, indicating localized variations in the electric, and possibly the magnetic, fields within the arc core. High-intensity spectra, with very strong resonance lines of C^+, C^{++}, and especially C^{3+}, have been obtained using an ORNL-constructed Seya spectrometer. Oxygen (O^+ to O^{4+}) resonance lines have been observed in both the LSM (Long Solenoid Machine) and the DCX. Preliminary studies of the intensity variation of selected spectrum lines and integrated visible light as a function of the current of the carbon arc in the LSM have been made, and they indicate increase of average electron flux with current. The upper limits of electron temperature are thought to be $\sim$20 ev at 300 amp and 31 ev at 160 amp, and if the trend toward higher electron energies continues at still lower currents, DCX plasma heat loss in the arc region should be less. Improved water cooling of the anode to decrease the number of carbon particles fed to the arc increased the degree of ionization only very slightly.

Unusual Doppler slant effects and line broadenings in the spectra of magnetically constrained arc systems have been reported.[1,2] These studies have been extended to include three distinct types of arc plasmas: (1) the high-pressure PIG discharge[1,2] which is referred to in the Project Sherwood literature as the Mode I plasma;[3] (2) the low-pressure PIG discharge which is referred to as the Mode II plasma;[4] and (3) the high-current vacuum carbon arc.[5] Some of the spectroscopic results obtained on the carbon arc are reported here.

These arc plasmas are discharges confined by magnetic fields of several kilogauss, either with or without a magnetic-mirror field. The magnetic pressure associated with these arcs is $H^2/8\pi$ or about 1 atm, but because of the vacuum the heat dissipation along the arc is almost entirely by radiation and negligibly by conduction and convection (which would otherwise be important in arcs at gas pressures of 1 atm). Radiation cooling in a 300-amp vacuum carbon arc amounts to approximately 300 w per inch of arc length.

The reduced heat losses apparently result in the entrapment of larger amounts of energy than would occur in conventional atmospheric-pressure arcs and in the attainment of phenomenally high "temperatures." (It is realized that significant ordered motion of the ions both about and along the axis of the arc does not permit a true temperature description in the Maxwellian sense: the random axial motion is comparable in magnitude to the ordered rotational motion but quite larger than the ordered axial motion.) The high ionic "temperature" is verified in part by the high degree of ionization (C^{3+} and O^{4+} impurity lines are prominent) and the fact that the electron excitation energies are quite comparable to the Doppler-determined ion energies.

2.1.1 DOPPLER SLANT AND LINE BROADENING

The Doppler effects are illustrated by Figs. 2.1.1–2.1.5. Figure 2.1.1 shows spectrum lines

[1] J. R. McNally, Jr., and M. R. Skidmore, *J. Opt. Soc. Am.* **47**, 863 (1957).

[2] J. R. McNally, Jr., "The Role of Spectroscopy in Thermonuclear Research," to be published in *J. Opt. Soc. Am.*, April 1959.

[3] A. Simon and R. V. Neidigh, *Diffusion of Ions in a Plasma Across a Magnetic Field*, ORNL-1890 (June 1955); R. V. Neidigh, *Some Experiments Relating Ion Diffusion in a Plasma to the Neutral Gas Density in the Presence of a Magnetic Field*, ORNL-2024 (June 1956).

[4] R. V. Neidigh and C. H. Weaver, *The Effect of a Pressure Gradient on the Magnetically Collimated Arc*, ORNL-2288 (April 1957).

[5] J. S. Luce, *Studies of Intense Gaseous Discharges*, Paper UN/P-1790, Second International Conference on the Peaceful Uses of Atomic Energy, Geneva, Switzerland (1958).

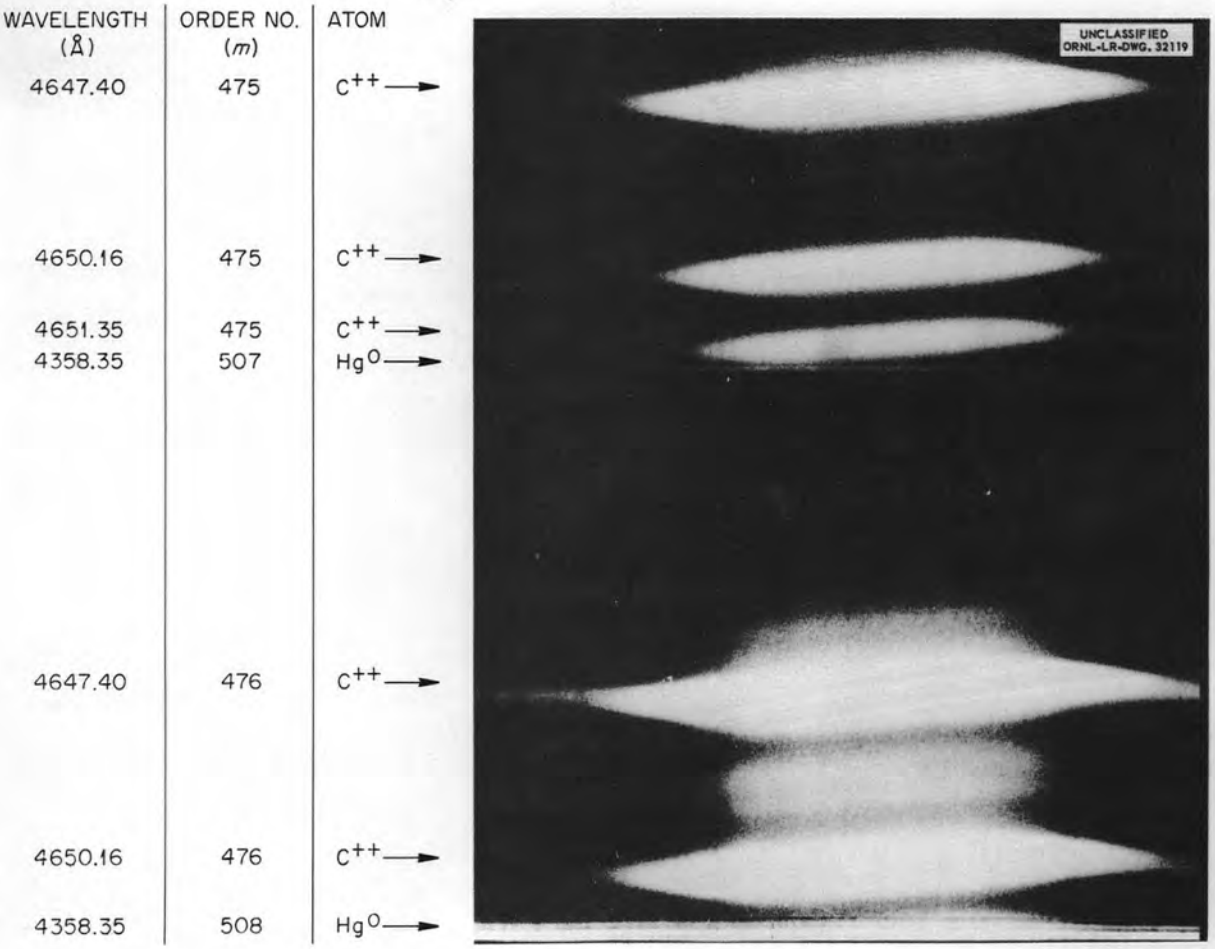

Fig. 2.1.1. Doppler Slant and Broadening in Carbon Arc.

having the typical slant and broadening characteristics. The slant effect is believed to be due to the existence of crossed electric and magnetic fields, the electric field being radially directed to the center of the discharge. This field may be roughly computed from the relation[6]

$$v_d \cong \frac{cEH}{H^2} \cong \frac{cE}{H} ,$$

and since

$$v_d \cong \frac{c\Delta\lambda}{\lambda} ,$$

it follows that

$$E \cong \frac{\Delta\lambda}{\lambda} H ,$$

where v_d is the average drift velocity of the ions (and is independent of the charge state of the ion), $\Delta\lambda$ is the wavelength shift of the spectrum line, E is the electrostatic field in esu, and H is the magnetic field in oersteds. The magnitude of this electric field varies depending on the arc conditions (length, current, pressure, etc.) but does increase with increasing current and arc voltage or arc length. Figure 2.1.2 illustrates the dependence of the direction of slant on the direction of the magnetic field. Figure 2.1.3 shows that the slant is associated with the individual filaments of the carbon arc as well as

[6] H. Alfvén, *Cosmical Electrodynamics*, Clarendon Press, Oxford, England, 1950.

WAVELENGTH (Å)	ORDER NO. (*m*)	ATOM
4647.40	475	C^{++} →
4650.16	475	C^{++} →
4651.35	475	C^{++} →
4358.35	507	Hg^{0} →
4647.40	476	C^{++} →
4650.16	476	C^{++} →
4358.35	508	Hg^{0} →

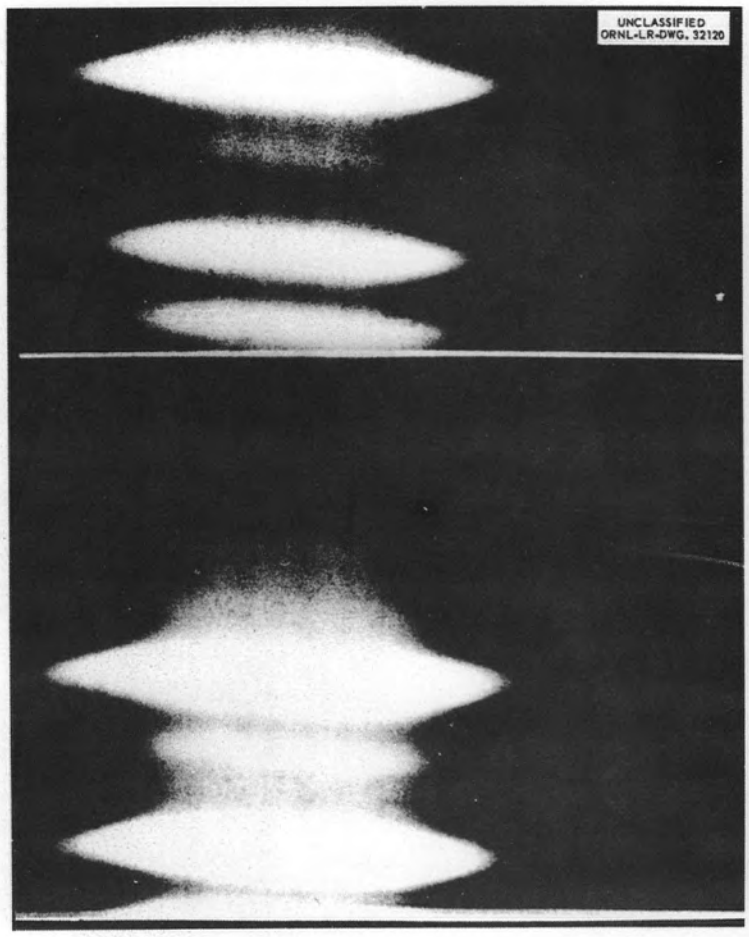

Fig. 2.1.2. Effect of Reversed Magnetic Field on Doppler Slant in Carbon Arc.

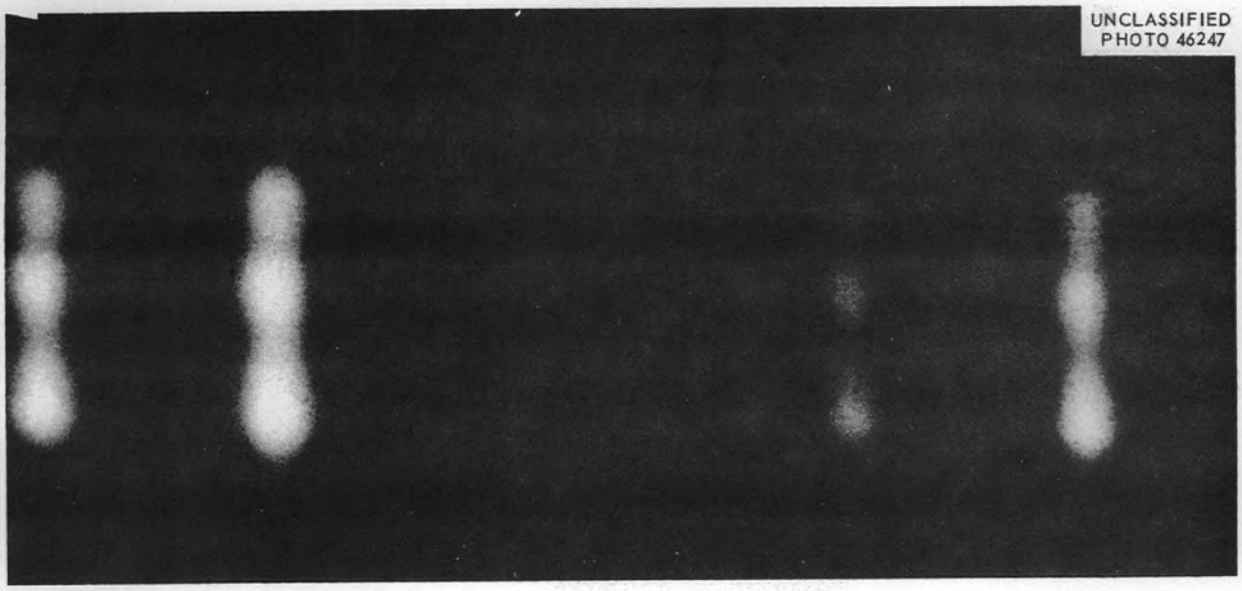

Fig. 2.1.3. Doppler Slant and Broadening in Carbon Arc, Showing Filament Structure.

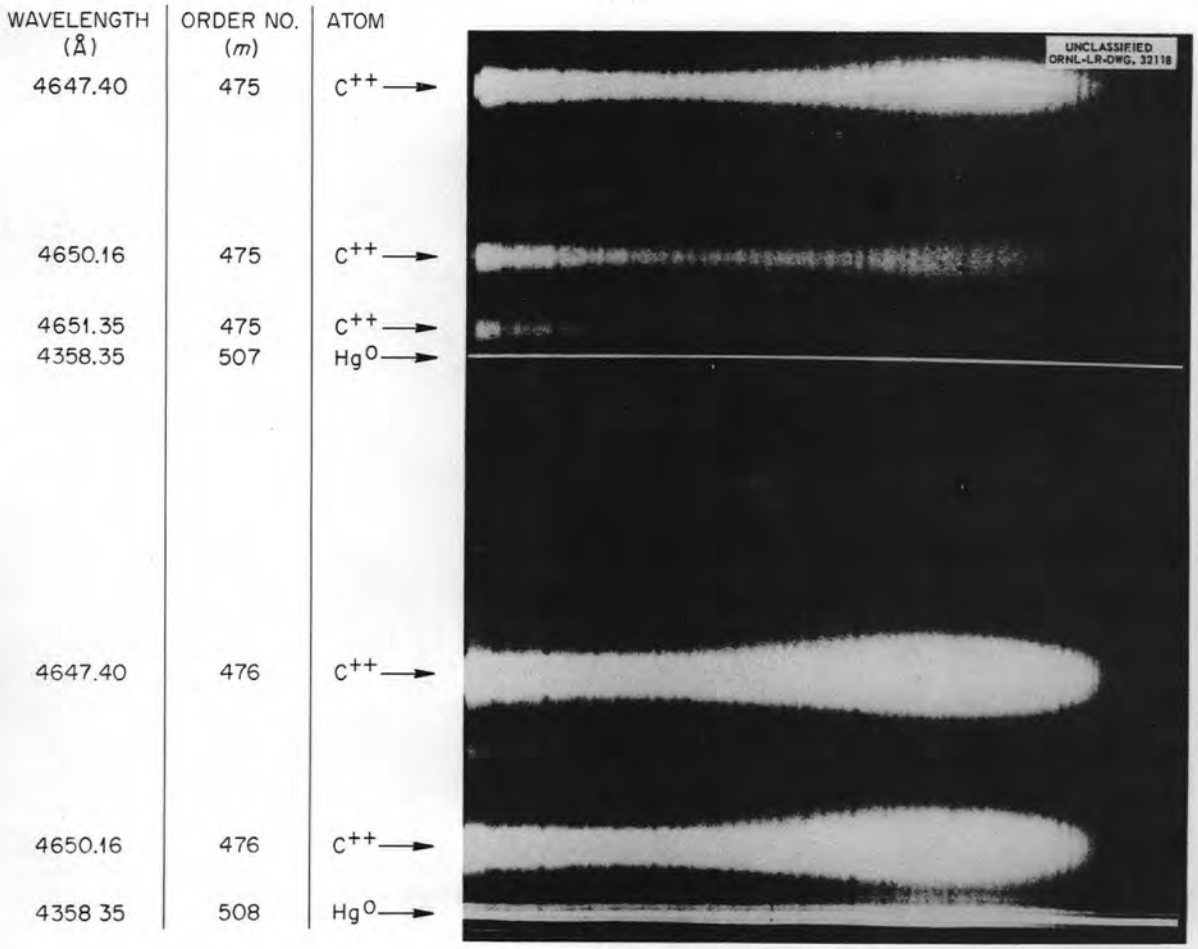

Fig. 2.1.4. Doppler Slant and Shift in λ 4650 Line Group Observed Along 5-ft Carbon Arc. Near the cathode lines are shifted 0.05 Å more to red than at anode. View from anode end.

the whole arc, thus indicating localized variations in the electric, and possibly the magnetic, fields within the general arc core. The radial electric field, E_r, is approximately 100 v/cm but varies with operating conditions.

Observations at high spectroscopic resolution along the arc have also been made. Figure 2.1.4 illustrates the unusually large Doppler broadening, due apparently to ion oscillations, in carbon spectra near the cathode. This increased smearing of the spectrum line is associated with extremely violent ion oscillations along the arc axis. Observations of the arc both transversely and axially have been made simultaneously. This is shown in Fig. 2.1.5.

2.1.2 INTENSITY OF SPECTRA FOR CARBON AND OXYGEN

An ORNL-constructed (see Sec 7.2) Seya-type vacuum spectrometer with a Bausch and Lomb replica grating of 1-m radius and having 30,000 lines/in. was used to obtain high-intensity spectra down to 312 Å (C^{3+}), which requires 40-ev excitation. The resonance lines of C^{+} (1335 Å), C^{++} (977 Å), and especially C^{3+} (1548 Å) are very strong in the vacuum spectra. The resonance lines of oxygen (present as an impurity) have been observed, for example, O^{+} at 834 Å, O^{++} at 835 and 598 Å, O^{3+} at 790 Å, and O^{4+} at 630 Å.

Figure 2.1.6 shows a spatial distribution of spectra obtained of a 10-in.-long magnetically

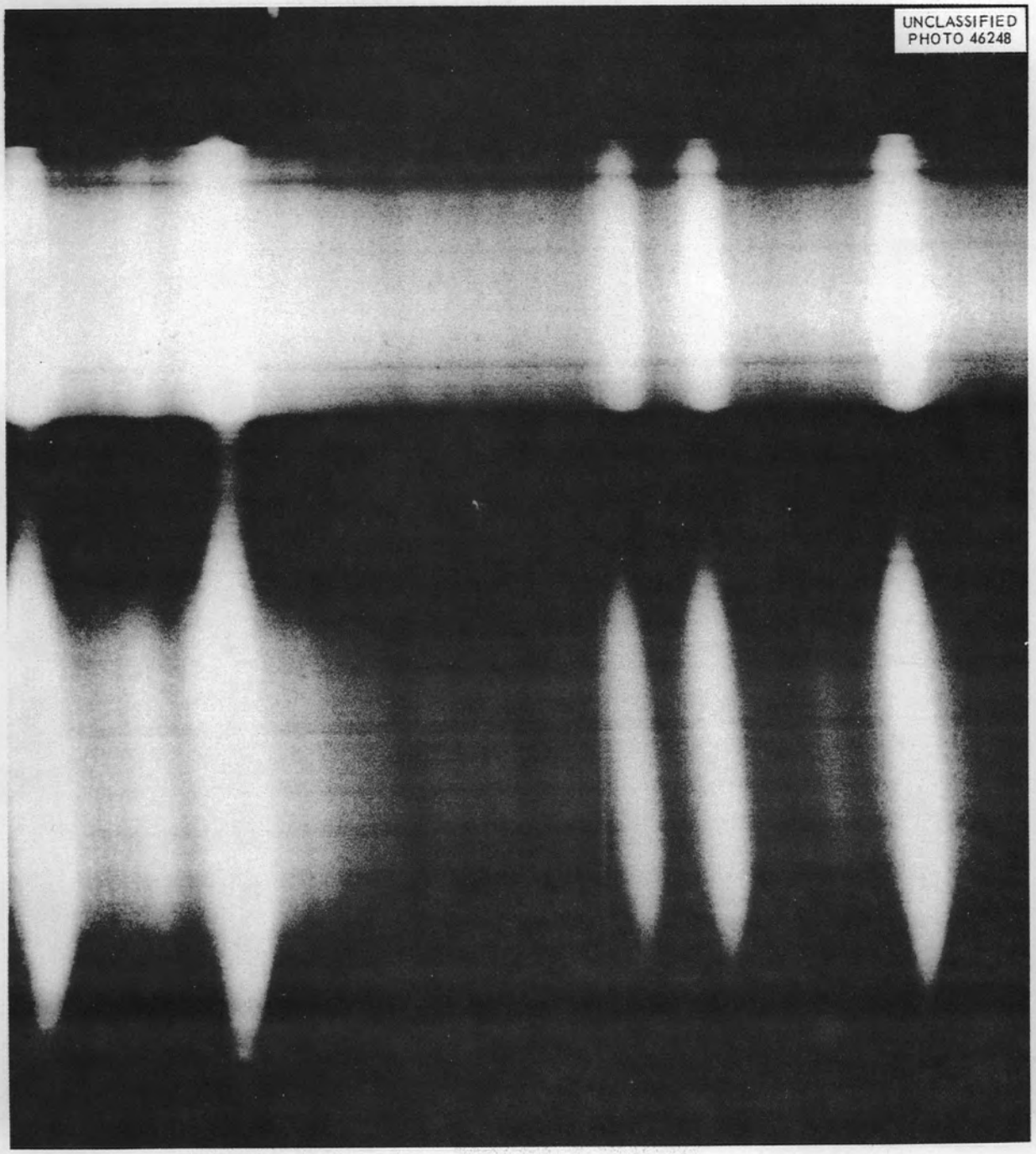

Fig. 2.1.5. Doppler Slant and Broadening Effects in 5-ft Carbon Arc. Top view parallel to arc; bottom view transverse to arc.

UNCLASSIFIED
PHOTO 30010

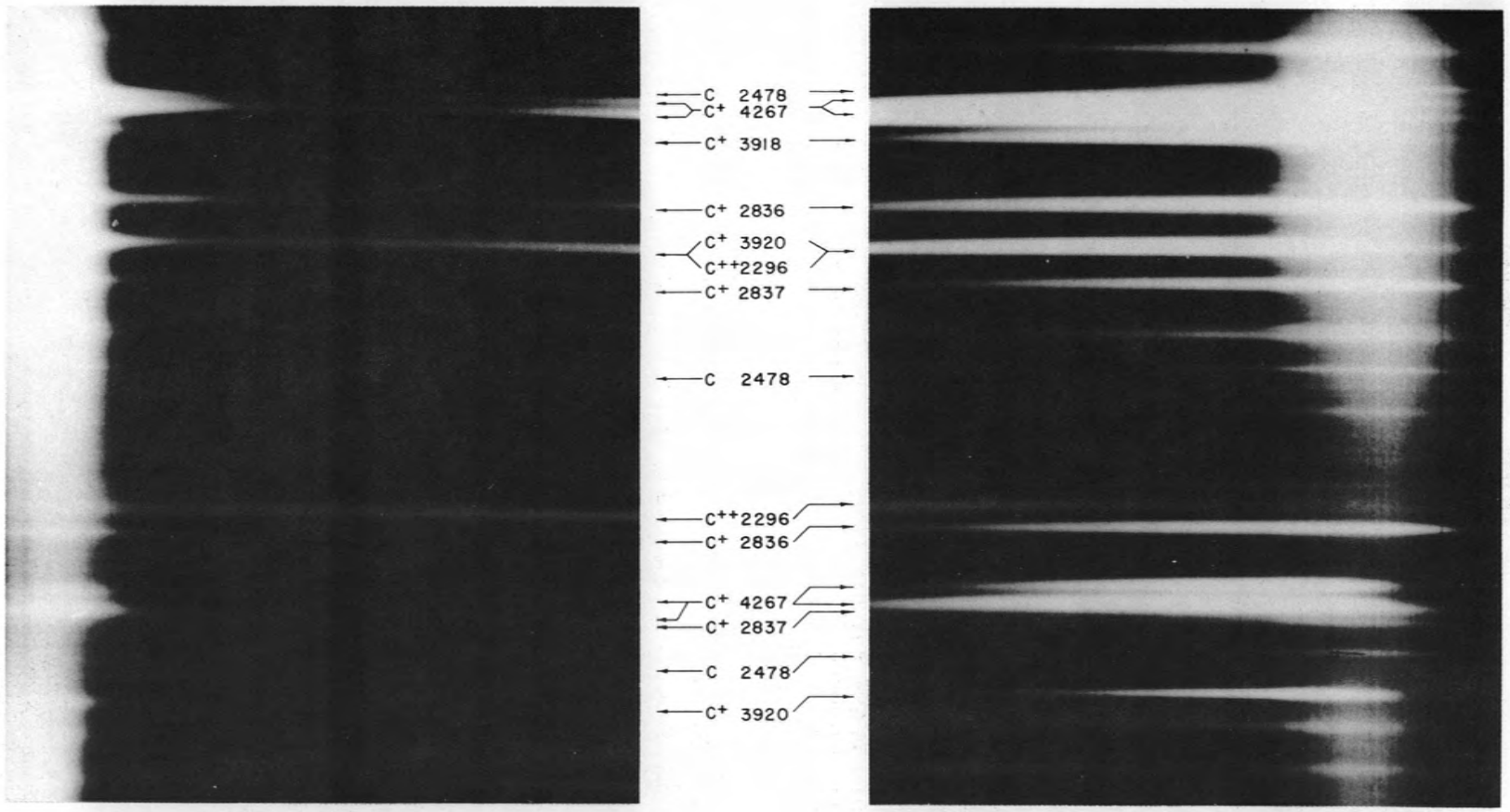

Fig. 2.1.6. Spatial Distribution of Spectra Obtained from a 10-in. Magnetically Collimated Carbon Arc.

collimated vacuum carbon arc. Note the rapid fall-off of intensity of lines of singly ionized carbon with increasing distance from the anode. Simultaneously, as the carbon ions drift from anode to cathode, there is a buildup of C^{++} spectra. Measurements near the center of the 5-ft-long arc in the LSM indicated relatively high abundance of the triply ionized carbon species (1548 Å C^{3+}/977 Å C^{++} $\simeq$ 30, uncorrected for spectrometer efficiency). Measurements along the 5-ft arc (see Fig. 2.1.4) revealed a slight drift energy of ions toward the cathode (about 2 ev) based on the Doppler shift of the center of gravity of the spectrum line but marked energy of random motion based on the Doppler broadening. This random axial motion corresponds to ion energies of about 10 ev near the anode and exceeding 50 ev near the cathode end of the arc. This latter energy of random motion represents a "temperature" of approximately 400,000°K.

2.1.3 SPECTRAL INTENSITY VARIATION IN THE CARBON ARC IN THE LSM

Preliminary studies have been made of the intensity variation of selected spectrum lines and integrated visible light as a function of the current of the carbon arc in the LSM. These results, normalized to intensities of unity for the 300-amp run, are plotted in Figs. 2.1.7 and 2.1.8. Figure 2.1.7 shows the intensity variation of lines of different stages of ionization. The general trend of the curves indicates that the average electron flux, $n_e v_e$, increases with increasing current, as might be expected. The C II line indicates an anomaly at low currents, the intensity rising very markedly at the lowest current. The C III line indicates a leveling off at the lower currents. This suggests that the number of singly ionized atoms (C II) increases relative to the number of doubly ionized atoms (C III) and very much relative to the number of triply ionized atoms (C IV). These numbers must satisfy the relation

$$n_e \simeq n_{C^+} + 2n_{C^{++}} + 3n_{C^{3+}} \ .$$

At about 250 amp the ratios C^{3+}/C^{++} and C^{++}/C^{+} are a maximum if n_e is approximately constant in this range.

Electron Energy and Current. – Figure 2.1.8 shows the intensity variation of two selected C IV lines as a function of arc current. The resonance

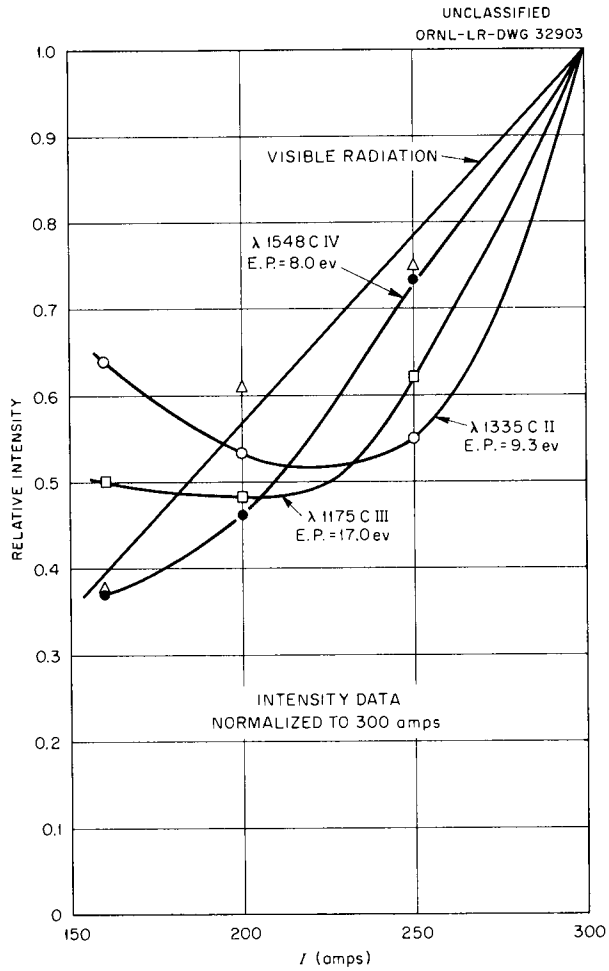

Fig. 2.1.7. Intensity Variation of Carbon Arc Spectra for Different Stages of Ionization.

lines at 1548 Å (excitation energy = 8.0 ev) show an approximately linear increase with current, whereas the line pair at 2526 Å, which have an excitation potential of 55.8 ev, have considerably less slope and show an upward trend at the lowest current. Assuming an electron temperature equilibrium exists, then

$$\frac{(I_1/I_2)\ 300\ \text{amp}}{(I_1/I_2)\ 160\ \text{amp}} = e^{-(E_H/T_H - E_L/T_L)} \simeq 0.47$$

or

$$\frac{T_L - T_H}{T_H T_L} = 0.016 \ .$$

This calculation is independent of the spectrometer efficiency, quantum properties, etc., and

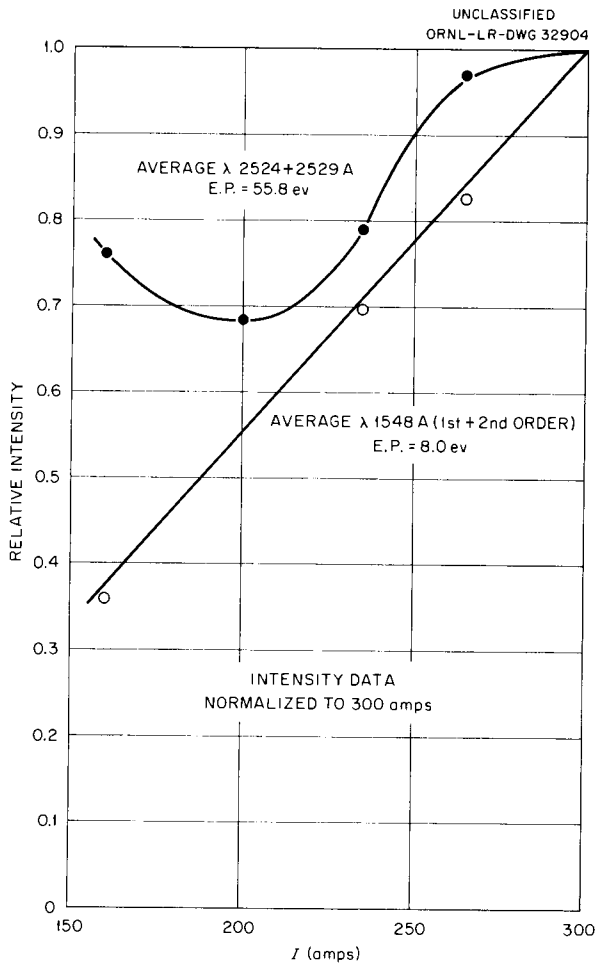

Fig. 2.1.8. Intensity Variation of Two Selected C IV Lines as a Function of Arc Current.

is valid insofar as the assumption of a Boltzmann distribution is valid. Thus, if $T_L = KT_H$, then $K = I/(1 - 0.016\ T_H)$. The possible excitation (electron) temperatures are given below.

Assumed T_{300} (ev)	Computed T_{160} (ev)
10	11.9
20	31.2
30	57.6
40	111.2
50	500
60	Impossible

Inasmuch as no spectral excitation greater than about 60 ev has been observed, it is probable that the *upper* limits of electron temperatures are about 20 ev at 300 amp and 31 ev at 160 amp. Some ions of C V (quadruply ionized carbon) probably exist in the discharge, since it takes only 64.5 ev to ionize C IV; however, the density of electrons of energies $\sim$300 ev is negligible since no spectrum lines of C V have ever been observed in the spectra of the carbon arc. The excitation potential of the first excited state of C V is 298.9 ev. The resonance lines of O^+, O^{++}, O^{3+}, and O^{4+} have been observed in both arcs operated in the LSM and in the DCX. Because of the pile-up of impurity ions in the arc as a result of drift toward the cathode, the intensity of these impurity ions is expected to be enhanced, which is in agreement with observation.

Because high-energy electrons will absorb less heat from the hot ions in the DCX plasma, it will be of considerable interest to see whether the trend toward higher electron energies continues at still lower currents. The losses due to carbon-arc charge-exchange events would appear to be a minimum at about 250 amp since the degree of ionization is near a maximum. Based on spectroscopic evidence the breakup efficiency of the carbon arc would appear to be greater at the higher currents since $n_e v_e$ increases and $\bar{v}_e$ decreases; thus the electron density increases slightly faster than the current increases. This increased breakup efficiency actually occurs, as has been reported by Barnett, Mackin, and Ray.[7]

The effect of running the anode with improved water cooling has been studied in order to determine whether the decreased feed of carbon particles to the arc increases the degree of ionization (an increase in the degree of ionization has been observed in the case of short arcs with anode motion – see Table 2.1.1). This is especially important if charge exchange in the carbon arc is a cause of significant losses in the DCX. In such a case it is imperative that the ratio of the charge exchange loss rate to the breakup trapping rate be minimized. It is concluded that the results of "starving" the arc were in the direction anticipated, but the indications were only of a qualitative nature.

Tables 2.1.2 and 2.1.3 list data on excitation and ionization requirements for different spectrum

[7] C. F. Barnett, R. J. Mackin, and J. A. Ray, *Dissociation of H_2^+ and D_2^+ by a Vacuum Carbon Arc*, ORNL-2420 (Dec. 6, 1957).

Table 2.1.1. Excitation of Carbon by Open Electrodes and Water-Cooled Anode

Atomic Species	Total Ionization Energy (ev)	Wavelength (Å)	Excitation Energy (ev)	Ratio of Lines Measured			
				In Solenoid*	In Tank Track Facility		
					Open Electrodes*	Water-Cooled Anode	
						Midway Between Arc*	Near Anode**
C^0	0	2478	7.7	Not detected	0.0006	Not detected	Not detected
C^+	11.3	2512	18.7	0.004	0.007	0.022	0.036
		4267	20.9	0.022	0.12	0.43	Not scanned
C^{2+}	35.6	4647	32.2	1.0	1.0	1.0	Not scanned
		4650	32.2	0.52	0.48	0.53	Not scanned
		2296	18.1	~2	~2	~2	~2
C^{3+}	83.5	2530	55.8	0.028	Not detected	Not detected	0.0006

* $\frac{\text{Intensity of line}}{\text{Intensity of line 4647}}$. ** $\frac{\text{Intensity of line}}{\text{Intensity of line 2296 } C^{2+}} \times 2$.

Table 2.1.2. Electron Energies Required To Excite Various States of Carbon

Atomic Species	Ionization Energy (ev)	Total Ionization Energy (ev)	Wavelength Excited (Å)	Excitation Energy (ev)	Total Energy (ev)	Combination
C I	0.0	0.0	2478.5	7.7	7.7	$2p\ ^1S - 3s\ ^1P$
			2967.2*	4.3	4.3	$2p\ ^3P_2 - 2p'\ ^5S_2$
C II	11.3	11.3	1037.0	13.7	25.0	$2p\ ^2P_2 - 2p'\ ^2S$
			1335.7*	21.8	33.1	$2p\ ^2P_2 - 2p'\ ^2D_3$
			2512.0	31.0	42.3	$2p'\ ^2P_2 - 2p''\ ^2D_3$
			4267.3	20.9	32.2	$3d\ ^2D_3 - 4f\ ^2F_4$
C III	24.4	35.7	977.0*	12.7	48.4	$2s\ ^1S - 2p\ ^1P$
			2296.9	18.1	53.8	$2p\ ^1P - 2p'\ ^1D$
			4647.4	32.2	67.9	$3s\ ^3S - 3p\ ^3P_2$
C IV	47.9	83.5	1548.2*	8.0	91.5	$2s\ ^2S - 2p\ ^2P$
			2530.0	55.8	139.3	$4f\ ^2F - 5g\ ^2G$
C V	64.5	148.0	40.3	306.4	454.4	$1s^2\ ^1S - 1s\ 2p\ ^1P$
C VI	392.0	540.0	33.7	365.7	905.7	$1s\ ^2S - 2p\ ^2P$

*Resonance lines.

lines and energy states of carbon and oxygen. The excitation of highly ionized atoms of high z can be best studied in the vacuum ultraviolet region since, in general, the resonance lines occur there. Impurities, such as oxygen, must be evaluated since there is always present the serious question as to how much of such impurities may be tolerated because of poisoning effects. We are indebted to B. Edlén for making available a reprint of his publication on line lists.[8] Additional information has been obtained from the familiar NBS tables of C. M. Sitterley.[9]

[8] E. Edlén, *Nova Acta Regiae Soc. Sci. Upsaliensis* s4, 9(6), 104 (1934).

[9] C. M. Sitterley, *Atomic Energy Levels*, Vol. 1, Circular 467, National Bureau of Standards (1949).

Table 2.1.3. Electron Energies Required To Excite Various States of Oxygen

Atomic Species	Ionization Energy (ev)	Total Ionization Energy (ev)	Wavelength Excited (Å)	Excitation Energy (ev)	Total Energy (ev)	Combination
O I	0.0	0.0	1302.2*	9.5	9.5	$2p''\,^3P - 3s\,^3S_0$
O II	13.6	13.6	834.5*	14.9	28.5	$2p\,^4S_2 - 2p'\,^4P_3$
			718.5	20.6	34.2	$2p\,^2D_3 - 2p'\,^2D$
			2411.6	30.8	44.4	$3s\,^2D_2 - 4p\,^2P_1$
O III	35.1	48.7	835.3*	14.9	63.7	$2p\,^3P_2 - 2p'\,^3D_3$
			703.9	17.6	66.4	$2p\,^3P_2 - 2p'\,^3P_{2,1}$
			2455.0	38.9	87.7	$3s\,^1P - 3p\,^1S$
			2695.5	49.6		$3p'\,^3S - 3d'\,^3P_2$
O IV	54.9	103.6	625.9	28.7	132.4	$2p'\,^4P_3 - 2p''\,^4S$
			790.2*	15.7	119.4	$2p\,^2P_2 - 2p'\,^2D_3$
			1343.5	31.6	135.3	$2p'\,^2P_2 - 2p''\,^2D_3$
O V	77.4	181.0	629.7*	19.7	200.8	$2s\,^1S - 2p\,^1P$
			760.5	26.5	207.6	$2p\,^3P_2 - 2p'\,^3P_2$
			1371.3	28.7	209.8	$2p\,^1P - 2p'\,^1D$
			2781.0	72.3	253.4	$3s\,^3S - 3p\,^3P_2$
O VI	113.9	294.9	1031.9*	12.0	306.9	$2s\,^2S - 2p\,^2P_2$

*Resonance lines.

2.2 A MASS SPECTROMETRIC ANALYSIS OF THE CONSTITUENTS OF THE CARBON ARC

R. V. Neidigh

In an attempt to approach an understanding of the mechanism of the dissociation of D_2^+ by the carbon arc[1,2] the constituents of the carbon arc were analyzed. The method involves a straightforward extraction of ions from the edge of the carbon arc plasma by a negative potential. These first results, from measurements on a short arc, verify spectrographic evidence of the presence of triply ionized carbon in a carbon arc, though in a much smaller amount than spectrography indicated for the long arc (see Sec 2.1). The following are the average results, normalized to 100% and with the associated standard deviation:

Atomic Species	Amount (%)	Standard Deviation
C^+	27.5	±5.9
C^{++}	70.7	±11.9
C^{3+}	1.25	±0.30
C^{4+}	0.56	±0.22

The analyzer is schematically diagramed in Fig. 2.2.1. The conditions of the analysis were:

Arc cathode diameter	0.375 in.
Arc length	4–5 in.
Arc current	200 amp
Magnetic field	6000 oersteds
Accelerating voltage	9–10.8 kv
Analyzer slit	0.030 × 0.500 in. (at start of 10-min run)*

*The grounded slit gradually closed with carbon deposit and the slit in the collector box which was at the negative high potential eroded slightly.

[1] J. S. Luce, *Ionization and Dissociation of Energetic Ions by a Carbon Discharge*, ORNL-2219 (Jan. 28, 1957).

[2] C. F. Barnett, R. J. Mackin, Jr., and J. A. Ray, *Dissociation of H_2^+ and D_2^+ by a Vacuum Carbon Arc*, ORNL-2420 (Dec. 6, 1957).

UNCLASSIFIED
ORNL-LR-DWG 35768

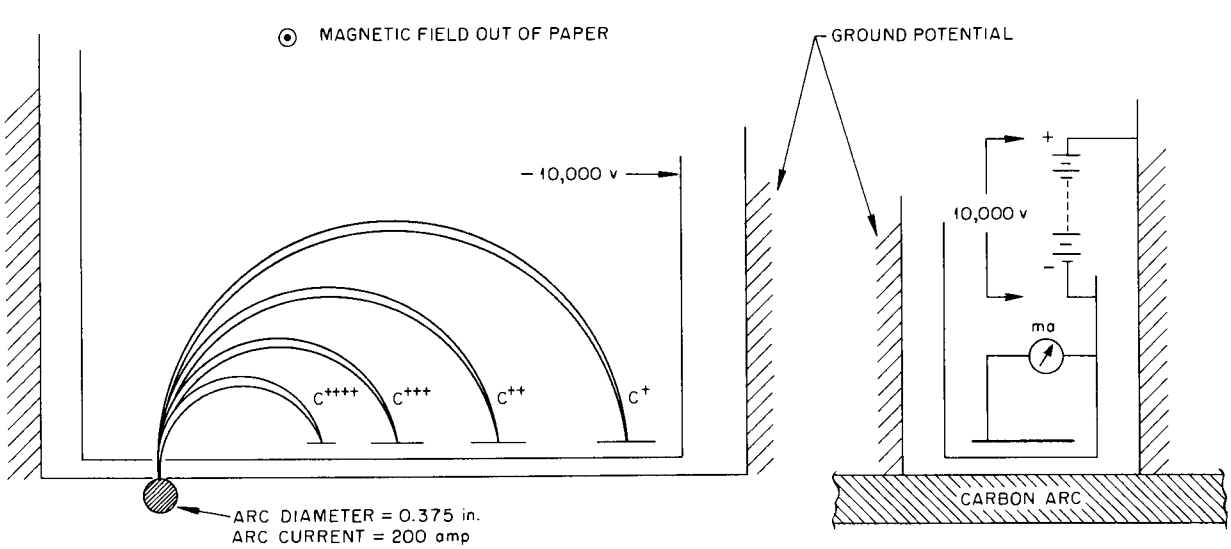

Fig. 2.2.1. Side and End Views of the Analyzer for the DCX Carbon Arc. Power supply and method of measuring currents are shown at the right. The arc was grounded only at the analyzer.

A voltmeter was used to monitor the accelerating potential, and milliammeters were used to monitor the collector currents. All meters were placed together in a shielded cage so that they could be photographed simultaneously.

The inhomogeneous and continually changing structure of the carbon arc made the collector currents vary continually during the 10-min run. Twelve photographs were taken of the collector milliammeters and voltmeter monitor during the run. The ion current data is recorded in Table 2.2.1.

The variable nature of the arc is emphasized by the variation in collector current with time. The resolution was poor, and it may be that other ions with nearly the same e/m were contributing. It is planned to repeat the experiment with a longer arc (5 ft in the LSM) to see whether there is an increase in the C^{3+} and C^{4+} ions. A continuous scan with a high-resolution collector will be used to verify the results. The carbon arc appears to consist of several intense current filaments which rotate about the edge of the cathode. An attempt will be made to run the arc with only one filament, and then repeat the experiment.

Table 2.2.1. Proportions of Four Constituents of the DCX Carbon Arc

Ion Currents (ma)				Accelerating Potential (kv)
C^{+}	C^{++}	C^{3+}	C^{4+}	
3.8	6.6	0.10	0.01	9.5
2.1	5.8	0.19	0.11	9.0
2.8	4.5	0.05	0.00	10.1
0.2	4.2	0.07	0.00	10.2
2.2	8.0	0.10	0.00	10.6
1.4	2.6	0.02	0.01	10.1
1.0	1.8	0.02	0.02	10.2
1.1	2.7	0.08	0.05	10.4
3.4	7.8	0.18	0.13	9.6
1.9	5.3	0.10	0.01	10.8
0.0	0.2	0.00	0.07	9.5
0.2	2.0	0.00	0.00	10.8

2.3 MICROWAVE DIAGNOSTICS OF THE CARBON ARC

H. O. Eason, Jr.

Knowledge of the electron density in the long vacuum carbon arc used for molecular breakup in the DCX is essential to the understanding of the breakup mechanism and its limitations. Microwave measurements, for an arc current of 300 amp and a magnetic field of 2600 gauss, have tentatively established that the plasma frequency of the arc is ~140,000 Mc, corresponding to an electron density of $\sim 2 \times 10^{14}$ electrons/cm^3.

2.3.1 CARBON ARC MEASUREMENTS

Due to physical difficulties involved in making microwave measurements on the arc directly in the DCX machine, these measurements have been made on a similar arc in the LSM. The experimental setup is indicated diagrammatically in Fig. 2.3.1, which is a cross-sectional view perpendicular to the axis of the arc. Microwave power is generated by a suitable source, and waveguide connections are made to a transmitting horn through appropriate matching elements. The electromagnetic waves thus emitted are focused on the arc by a polystyrene lens which also serves as a vacuum window for access to the chamber. The waves passing through the arc are then refocused into a receiving horn by a similar lens on the opposite side and pass through a waveguide connection to a detector. An indicating device, either a tuned amplifier and meter or an oscilloscope, is used to indicate the relative transmission over this path with and without the arc.

An early measurement of this type by W. B. Ard[1] at 25,000 Mc showed transmission losses in excess of 15 db introduced by the presence of the arc, the severe reflections indicating that the plasma

[1]University of Alabama, consultant to Thermonuclear Experimental Division.

UNCLASSIFIED
ORNL–LR–DWG 35834

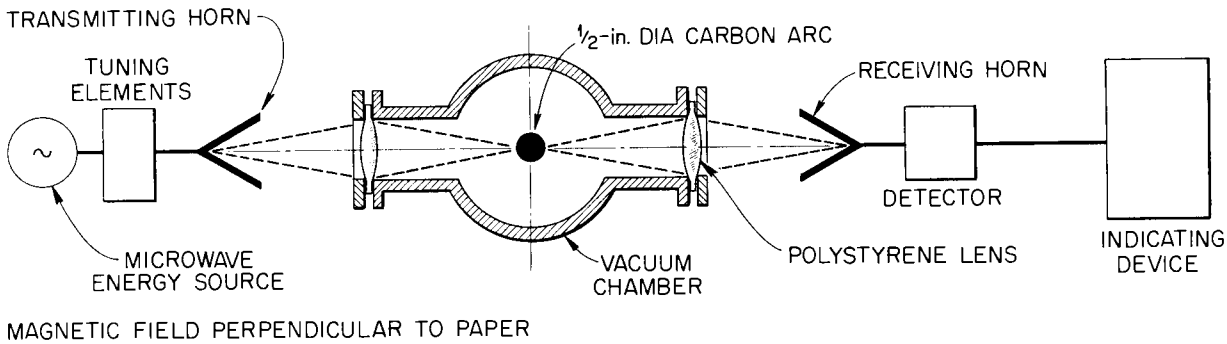

Fig. 2.3.1. Cross Section of Long Solenoid Machine, Illustrating Method Used in Density Measurements.

frequency of the arc was greater than 25,000 Mc, and therefore that the electron density exceeded 8×10^{12} per cubic centimeter. The residual transmission was attributed to scattering and imperfect focusing of the microwave beam.

This measurement was later repeated by this writer at 70,000 Mc. Preparatory experiments, with uncorrected 4-in.-dia polystyrene lenses with equal curvature on both sides and having a focal length of 5 in., showed a residual transmission loss of 7 db at 70,000 Mc for a 24-in. lens spacing. It was also ascertained that practically all the power was focused in a region ½ in. in diameter midway between the lenses, corresponding to the position of the arc. The additional transmission loss introduced by the arc in this case was again approximately 15 db, indicating electron density in excess of 6×10^{13} per cubic centimeter and a need for measurements at still higher frequencies to establish a lower density limit.

Since the reflex klystron used at 70,000 Mc (Amperex DX-151) represents the highest-frequency power source which is commercially available, a crystal multiplier was used in an effort to produce power at the second harmonic of this frequency. The multiplier configuration chosen was the familiar crossed-guide type,[2–4] and a photograph of the device appears in Fig. 2.3.2. The device consists of crossed 4- and 2-mm waveguides separated by a 0.002-in. wall section having a 0.032-in.-dia coupling hole, the center line of which intersects the guide axes. An insulated silicon crystal made from 1N53 material is mounted flush with the inner surface of the 4-mm guide and connected to the insulated center pin of the coaxial connector. A 0.005-in.-dia tungsten catwhisker electropointed to a tip radius of approximately 0.0001 in. is inserted through a 0.013-in.-dia hole in the opposite face of the assembly and through the coupling hole. The whisker is advanced to contact the crystal by a spring-loaded differential screw mechanism having an effective pitch of 400 threads per inch. Tuning plungers are used on both waveguides to match the whisker to the guides. The detector used was a commercial ridged-waveguide-mounted crystal designed for the 4-mm band and connected to the receiving horn by means of a tapered transition. This detector is to be replaced by a 2-mm waveguide-mounted crystal detector, now being fabricated, which is similar in construction to the multiplier.

Results obtained with the harmonic generator just described were only moderately successful, the conversion loss to the second harmonic being of the order of 30 db when driven by 50 mw of power 100% amplitude-modulated at 70,000 Mc. The power output at 140,000 Mc, however, was sufficient to provide a 40-db signal-to-noise ratio with the lens system previously described and with, following the detector, a high-gain narrow-band amplifier tuned to the modulation frequency.

[2] W. C. King and W. Gordy, *Phys. Rev.* 93, 407 (1954).

[3] W. C. King, *Trans. Inst. Radio Engrs.* MTT-2(3), 13–16 (1954); C. M. Johnson, *Trans. Inst. Radio Engrs.* MTT-2(3), 27–32 (1954).

[4] J. M. Richardson and R. B. Riley, *Trans. Inst. Radio Engrs.* MTT-5(2), 131–135 (1957).

UNCLASSIFIED
PHOTO 33516

Fig. 2.3.2. Crystal Multiplier (2- to 4-mm) Used in Microwave Studies of Plasmas.

The residual loss in transmission through the lens system in this case was 8 db, and the power was focused within a ½-in.-dia area at the arc position.

With this equipment, a further attempt was recently made to determine the density of the carbon arc. In this case, the additional transmission loss introduced by the presence of the arc was approximately 4 db at an arc current of 300 amp and a magnetic field of 2600 gauss, as used previously. The relatively low loss introduced by the arc may be explained by proximity of ω to ω_p, reflection from the dielectric interface at the arc, destructive interference caused by nonuniform cross section of the arc presented to the microwave beam, or a combination of any or all of these factors. The marked increase in transparency at this frequency seems to indicate that the plasma frequency of the arc lies in the region of 140,000 Mc and therefore that its electron density is near 2×10^{14} per cubic centimeter. Further experiments are, however, needed to definitely establish this value. It is planned to make further transmission measurements at 210,000 Mc by means of the same equipment with the addition of a beyond-cutoff waveguide filter to remove the 140,000-Mc signal component. In addition, there is prospect of obtaining commercially in the near future the necessary components to make phase-shift measurements at these frequencies.[5]

[5]Progress Reports, AEC-University of Illinois Subcontract No. AT (11–1)–663 with FXR, Inc., Woodside, New York.

2.4 CROSS-SECTION CALCULATIONS FOR DISSOCIATION OF D_2^+ BY CARBON ARC

R. G. Alsmiller, Jr.

Recent spectroscopic information (see Sec 2.1) indicates that there exists a significant amount of triply ionized carbon in the long carbon arc, and the possibility exists that the dissociation of the D_2^+ molecules by the carbon arc may be caused by these highly charged ions. To test this hypothesis the dissociation cross section is being calculated in two different approximations.

A Born approximation calculation of the dissociation cross section is being carried out numerically. The carbon ion is treated as a particle of charge ze; that is, the internal structure of the carbon ion is neglected. The molecular nuclei are treated as fixed force centers, and exact two-center electronic wave functions are used.[1] A classical average is carried out over molecular orientations. The procedure is to calculate the cross section for the excitation of the molecular levels from which dissociation occurs.

The expression for the cross section is quite complicated and will not be reproduced here. For our purposes, the significant thing about the Born approximation expression is that it varies as z^2, and thus triply ionized carbon contributes a factor of 9 to the cross section.

The Born approximation may be expected to give reliable results for energies above 500 kev; for lower energies the results may be quite erroneous. However, the maximum dissociation seems to occur in the vicinity of 20 kev, and it is therefore desirable to obtain some estimate of the cross section in this energy region. From the known density of the arc – approximately 10^{14} particles/cm^3 – and the breakup efficiency of 40–70% it follows that the cross section at 20 kev must be of the order of $(20\text{–}35) \times 10^{-16}$ cm^2. Thus, it would seem that quite distant collisions are contributing appreciably to the cross section.

To obtain an estimate of the contribution from these distant collisions a semiclassical calculation is being carried out. In the calculation the incident particle of charge ze is treated as a classical point charge moving along a straight line trajectory. It is assumed that only the ground state and the first excited state of the molecule need be considered and it is further assumed that, for the distant collisions under consideration, the interaction potential between the carbon ion and the electron may be expanded and only the dipole terms retained. Under these assumptions the following equations are obtained:

$$\dot{b}_0 = i b_1 \frac{C + Dt}{(p^2 + v^2 t^2)^{3/2}} e^{-i(E_1 - E_0)(t/\hbar)} , \quad (1)$$

and

$$\dot{b}_1 = i b_0 \frac{C + Dt}{(p^2 + v^2 t^2)^{3/2}} e^{i(E_1 - E_0)(t/\hbar)} , \quad (2)$$

where

$|b_0|^2$ = probability of finding the molecule in its ground state,

$|b_1|^2$ = probability of finding the molecule in its first excited state,

$E_1 - E_0$ = excitation energy,

v = velocity of incident particle,

$C = (ze^2/\hbar)\, z_{10} (\cos\theta_M) p \sin\phi$,

$D = (ze^2/\hbar)\, z_{10}\, v \sin\theta_M$,

z_{10} = dipole matrix element

$= \int \psi_1^* (\vec{r}) z\, \psi_0 (\vec{r})\, d\vec{r}$,

ψ_1, ψ_0 = electronic wave functions,

θ_M = angle of orientation,

p = impact parameter,

ϕ = azimuthal angle of incident particle;

and the contribution to the cross section for excitation of the first excited state may be written

$$\sigma_D = \frac{1}{2} \int_{p_0}^{\infty} \int_0^{2\pi} p\, dp\, d\phi\, d(\cos\theta_M)\, |b_1|^2 , \quad (3)$$

where σ_D = cross section from distant collisions, p_0 = minimum impact parameter to be considered, and again a classical average has been taken over molecular orientations.

[1] D. R. Bates, K. Ledsham, and A. L. Stewart, *Phil. Trans. Roy. Soc. London* A246, 215 (1953–54).

Equations (1) and (2) are being integrated on the ORNL analogue computer, and the remaining integrations are being carried out numerically.

This calculation will not yield a precise cross section, since only distant collisions are treated and since only the first excited state is considered; however, from the magnitude of (3) it should be possible to determine whether a dissociation cross section of the order of 35×10^{-16} cm^2 can ever be obtained by the mechanism proposed here.

2.5 CARBON ARC FLOATING POTENTIAL MEASUREMENTS

J. F. Potts
R. E. Toucey
P. M. Jenkins
R. L. Simpson

From arc potential data one hopes to eventually learn more about ion and electron drift velocities, current densities, ordered motion, etc. The work reported here is only the beginning.

In an attempt to determine the floating potential distribution in the carbon arc, an axially movable potential probe was inserted in the LSM (Fig. 2.5.1) and flipped radially through the arc at ~100 in./sec by a pneumatic motor. A plot of the LSM magnetic field is shown in Fig. 2.5.2. Both insulated and bare probes were used with generally the same results. Data were recorded from a dual

UNCLASSIFIED
ORNL-LR-DWG 35968

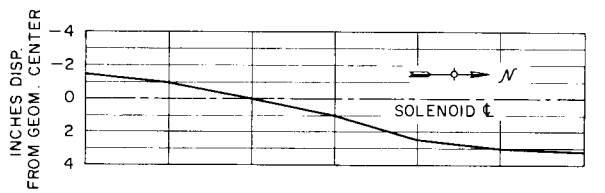

VARIATION OF ARC CENTER WITH RESPECT TO GEOMETRICAL AXIS LOOKING DOWN. DETERMINED FROM BAFFLE BURNING EXPERIMENT.

VARIATION, LOOKING ACROSS, ±0.02 in.

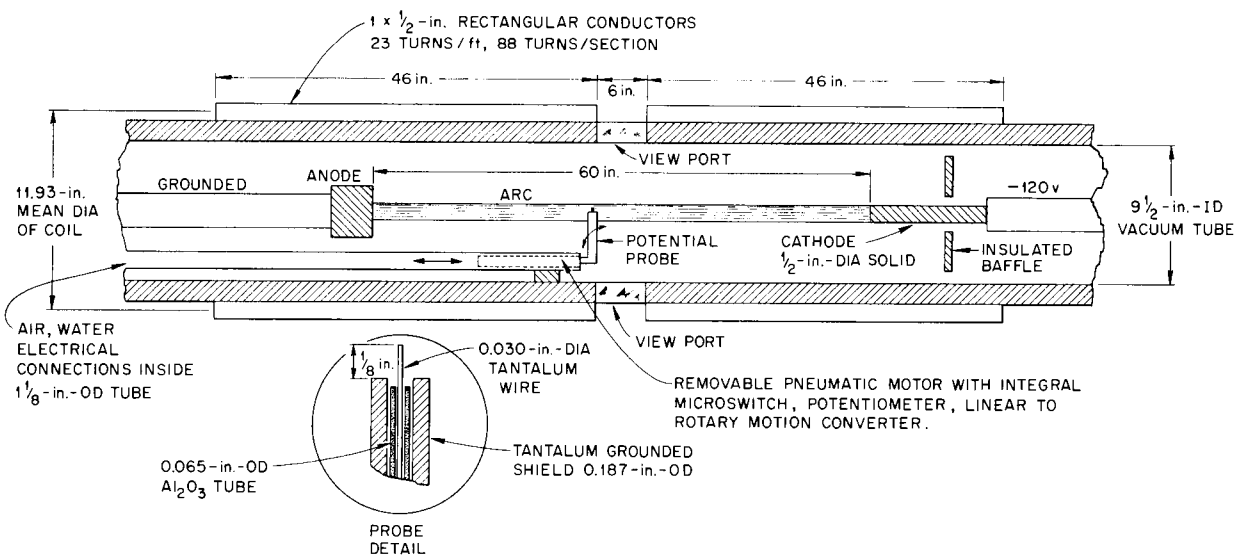

Fig. 2.5.1. Schematic Arrangement of Solenoid, Arc, and Movable Potential Probe in the Long Solenoid Machine.

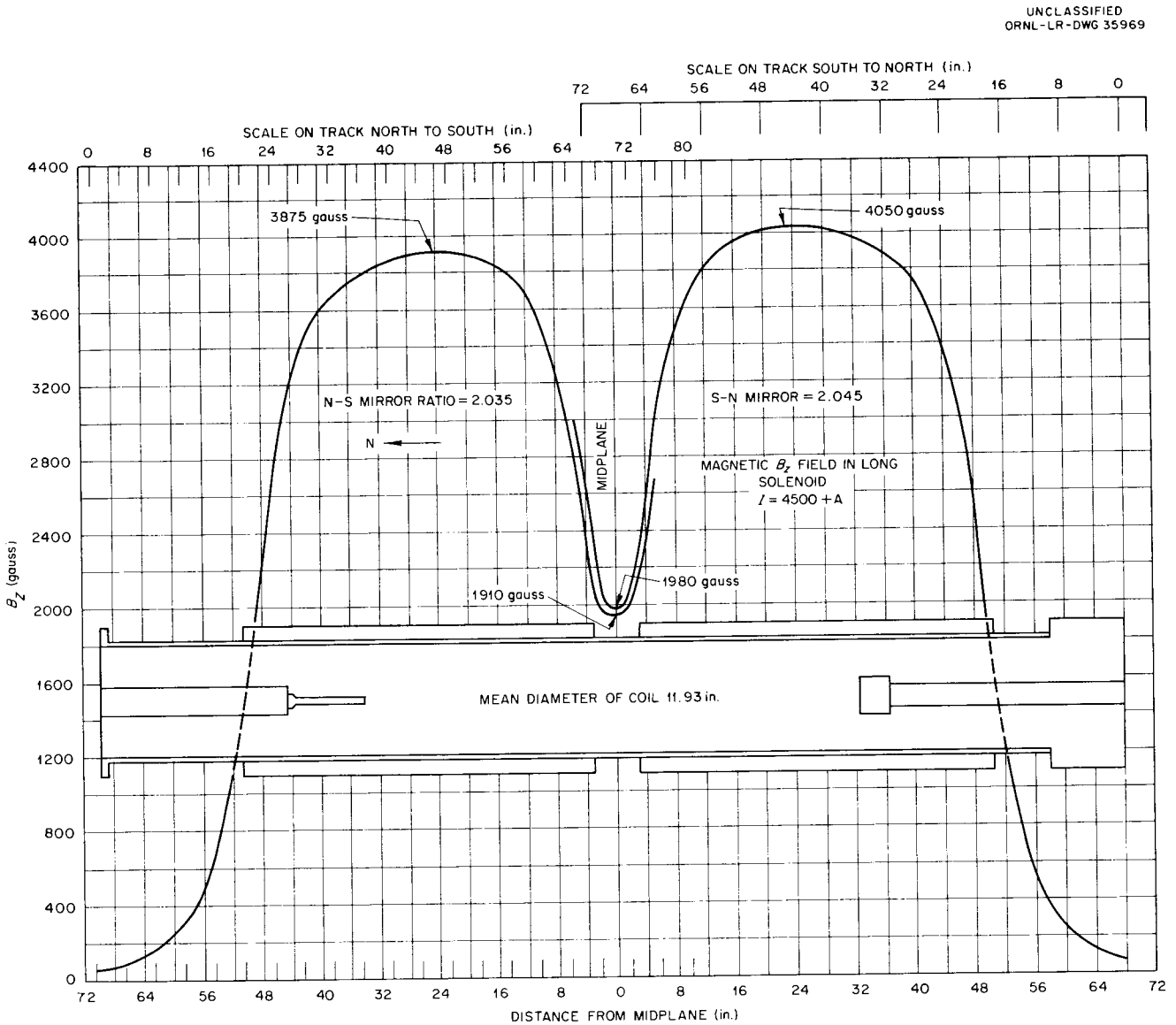

Fig. 2.5.2. Magnetic Field of the Long Solenoid Machine.

beam oscilloscope (one channel measuring floating potential and the other probe position) with an MK-3 Shackman 35-mm camera. Data were taken at axial intervals of $\frac{1}{4}$ to 1 in., several times for each position, at an average rate of one per second – 500 to 1500 pictures being taken per run. The measured axial potential distribution (somewhat affected by probe shorting by carbon, probe temperature variations, and magnetic field skewing) is shown in Fig. 2.5.3.

Typical radial floating potential pictures are shown in Fig. 2.5.4*a–f*. Voltage measurements are referenced to ground (anode potential). Probe position potentiometer sensitivity was the same in every case. The time displacement of the arc position as the probe proceeded from anode to cathode is indicative of the skewing (illustrated in Fig. 2.5.1) of the arc with respect to the axis of the solenoid. Although the peak value of the potential on the return pass through the arc is greater in the oscilloscope pictures shown, this was not always the case. It was, however, characteristic for the positive excursion of the probe potential to be greater in the secondary plasma on the trailing edge of the arc than on the leading edge and greater on the return pass than on the forward pass, suggesting that the floating potential observed was somewhat affected by the probe temperature (Fig. 2.5.4*a* and *b*). These measurements were made with sufficient filtering in the potential circuit to average the high-frequency perturbations in the arc. It can be noted in Fig. 2.5.4 that the rf coupled into the position circuit (see smearing of position signal while probe was passing through arc) is greater near the cathode than in the mid-region of the arc. This is also the case quite close to the anode (not shown here).

Since the data were not exactly reproducible from run to run, it is planned to better protect the probe insulation from the arc (there is some evidence of partial shorting of the probe electrode as indicated by the abrupt attenuation of the potential near the cathode shown in Fig. 2.5.4*e* and *f*), increase the probe flipping speed, and improve the trajectory and mirror ratio of the arc. A probe assembly, to be used principally in studying probing techniques, has been constructed to fit on the assembly used in carbon arc radiation studies (see Sec 2.6, Fig. 2.6.2). Other work will include simultaneous measurements of potential and radiation as a function of arc current and magnetic field.

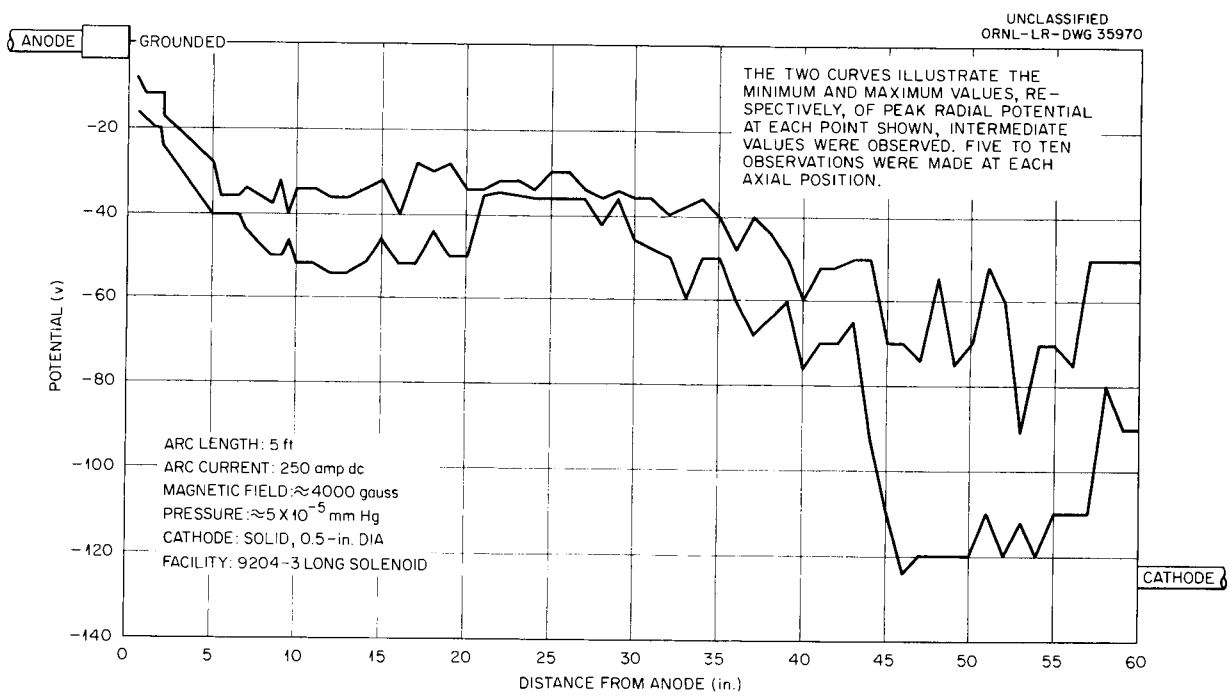

Fig. 2.5.3. Peak Floating Potential vs Axial Distance Along the Carbon Arc in the Long Solenoid Machine.

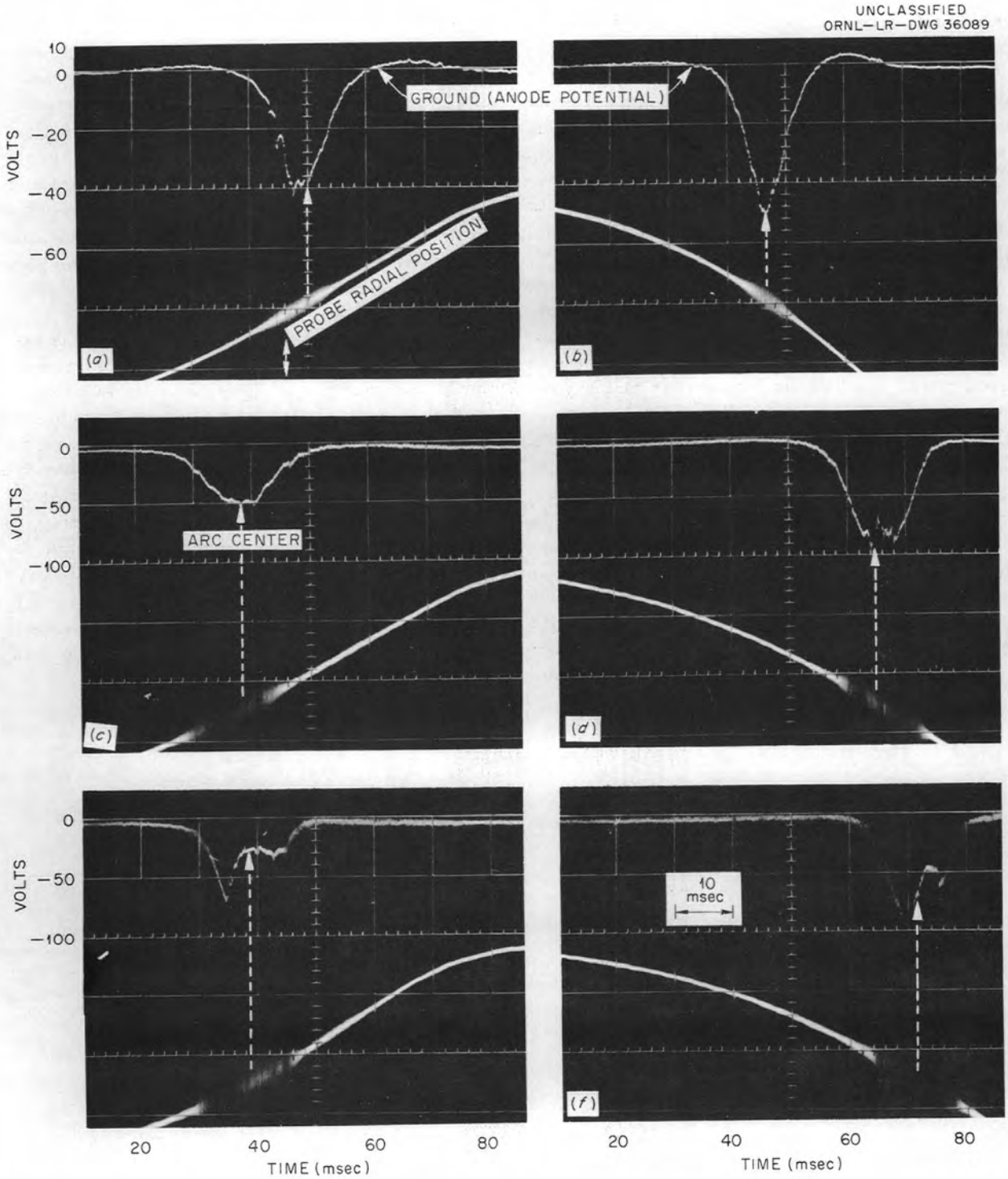

Fig. 2.5.4. Floating Potential of the Carbon Arc in the Long Solenoid Machine. (*a*) 20 in. from anode, East-West radial profile; (*b*) 20 in. from anode, West-East radial profile; (*c*) 51 in. from anode, East-West radial profile; (*d*) 51 in. from anode, West-East radial profile; (*e*) 58 in. from anode, East-West radial profile; (*f*) 58 in. from anode, West-East radial profile.

2.6 CARBON ARC TOTAL RADIATION MEASUREMENTS

J. F. Potts C. H. Weaver

Specially designed circular-foil thermoelectric radiometers[1] were used to study electromagnetic radiation from a 3- to 6-in.-long carbon arc collimated by a magnetic field in a low-pressure environment. Radiant energy was studied as a function of the following:

1. position along arc,
2. various filter media,
3. arc current,
4. magnetic field intensity.

A drawing and a photograph of one of the more successful radiometers are shown in Figs. 2.6.1 and 2.6.2.

The data indicated that the anode radiation peak occurred $\frac{1}{4}$ in. from the anode; that a radiation hump, analogous to a previously discussed potential hump (Sec 2.5), appeared in the middle of the arc; that the total arc radiation was 30% lower near the cathode than near the anode; that a significant proportion of the radiation is from triply ionized carbon; that <2% of the radiation was in the range 3000 Å to 20 μ, 15–30% from 1200 to 3000 Å (probably around 1500 Å); that at ~200 amp a current-dependent change of conduction mode occurs in the arc; that radiation increases almost linearly with magnetic field intensity.

2.6.1 RADIOMETER DESIGN AND CHARACTERISTICS

The circular-foil-radiometer differential thermocouple elements are the water-cooled copper heat sink, the Aquadag-blackened thin nickel foil radiation receiver, and the small copper wire (see Fig. 2.6.1 for details). From the steady-state solution of the equations for relating output voltage to input energy (assuming uniform energy distribution over the $\frac{1}{8}$-in.-dia collimating orifice, unit absorptivity of and no back-radiations from the foil, and no conduction loss from the 0.003-in. central wire) the radiometer's sensitivity is 30.4 mv/(cal/cm^2·sec) or 9 μv output per milliwatt of input radiation. The zero drift of the unit is of the order of ±5 μv/hr or around 1 to 2% in the data reported here. The time constant of the radiometer is about 1.5 sec. It was felt that the geometry chosen was a reasonable compromise between sensitivity, stability, ruggedness, and response time. The variations of radiation with arc current, magnetic field, and some filtering media were determined with the unit shown in Fig. 2.6.1 coupled to the vacuum system through a bellows seal. Radiation vs axial distance was determined with the assembly which, as shown in Fig. 2.6.2, has a provision for moving the detector in three orthogonal directions. Figure 2.6.2 also illustrates the arc position with respect to the radiometer.

2.6.2 RADIATION vs ARC AXIAL DISTANCE

Radiation as a function of axial position was measured with and without a Pyrex filter. The curve (Fig. 2.6.3) shows that the anode radiation peak occurs some distance (here $\frac{1}{4}$ in.) from the anode. The curve also suggests a radiation hump toward the middle of the arc that is analogous to a similarly shaped hump in the potential curves discussed in Sec 2.5. Total arc radiation was 30% lower in the vicinity of the cathode than it was near the anode.

2.6.3 USE OF VARIOUS FILTERS

Various filters interposed between the arc and the radiometer were: (1) crystalline silver chloride which transmitted from λ 4000 Å to at least 20 μ, (2) Pyrex which transmitted from 2800 Å to 3 μ, (3) quartz (very thin cover slide) which transmitted from around 1500 Å through the visible spectrum, (4) lithium fluoride which transmitted from about 1200 Å to 3 μ. No signal was detected from the point midway between the electrodes through the Pyrex or silver chloride, placing the upper limit of transmission at around 2%. The lithium fluoride transmitted from 10 to 35% of the total radiation, the uncertainty being principally due to the effect of carbon deposit from the arc on the filter. Seven per cent transmission through the quartz filter is in agreement with the above since the sharp falloff of the quartz began at 1500 Å. This establishes that a significant portion of the total radiation is from triply ionized carbon. Conclusions here are that less than 2% of the radiant energy from the carbon arc is in the range 3000 Å to 20 μ and that

[1] R. Gardon, *Rev. Sci. Instr.* **24**, 366–70 (May 1953).

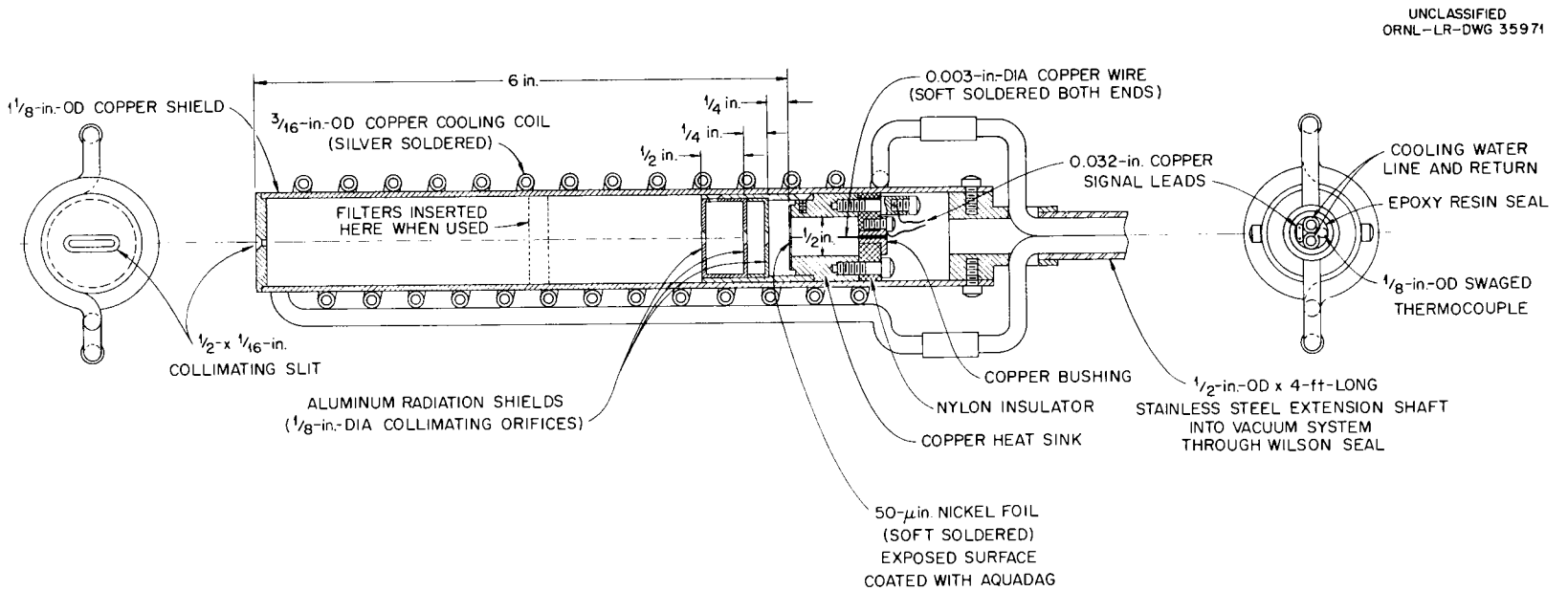

Fig. 2.6.1. Circular Foil Radiometer Assembly for Carbon Arc Radiation Studies.

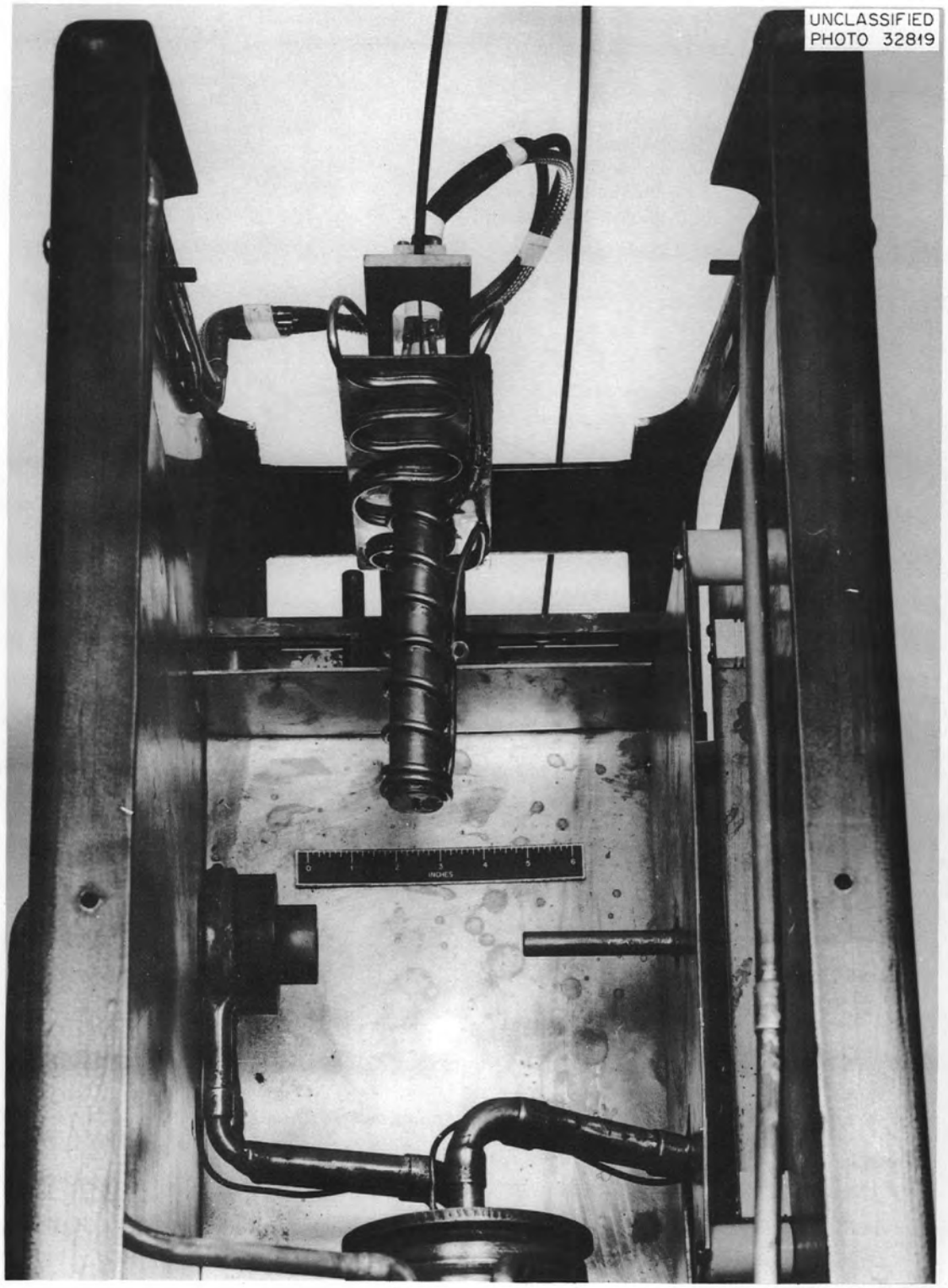

Fig. 2.6.2. Photograph of Circular Foil Radiometer Assembly for Carbon Arc Radiation Studies.

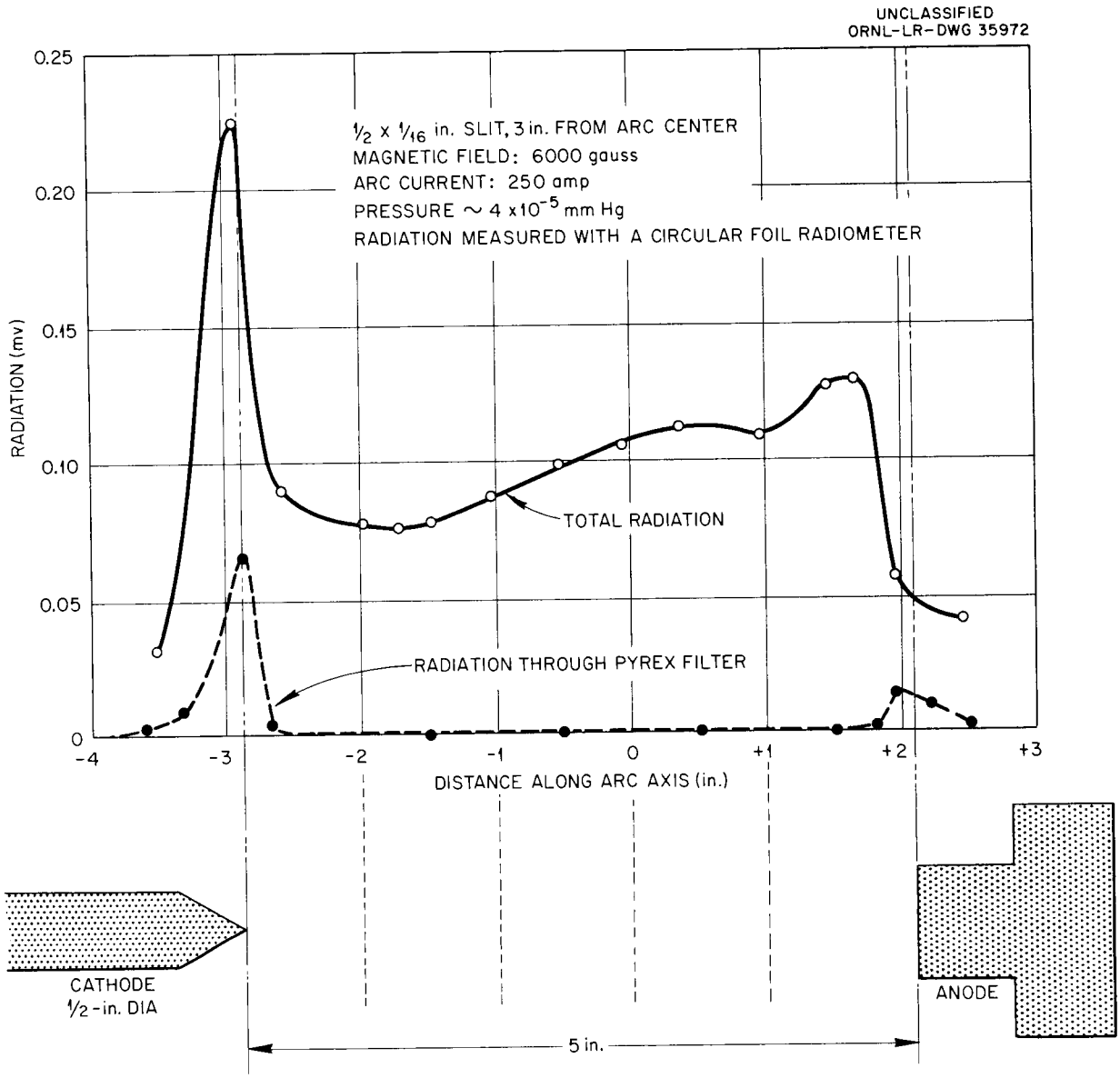

Fig. 2.6.3. Total Radiation of a Carbon Arc as a Function of Axial Position.

at least 15 to 30% is in the range 1200 to 3000 Å, most probably around 1500 Å.

2.6.4 RADIATION vs ARC CURRENT

The variation of total radiation with arc current is illustrated in Fig. 2.6.4. The nonreproducibility of the two determinations was probably due to variations of pressure during the runs. Attempts to determine the effect of background pressure on radiation were not successful because of poor pumping speed in the calutron ion-source research equipment (Building 9735) at the time of these measurements. This also thwarted attempts to use various gases as filtering media. The consistent break in slope of the radiation vs current at around 200 amp arc current strongly suggests a current-dependent change of conduction mode in the arc.

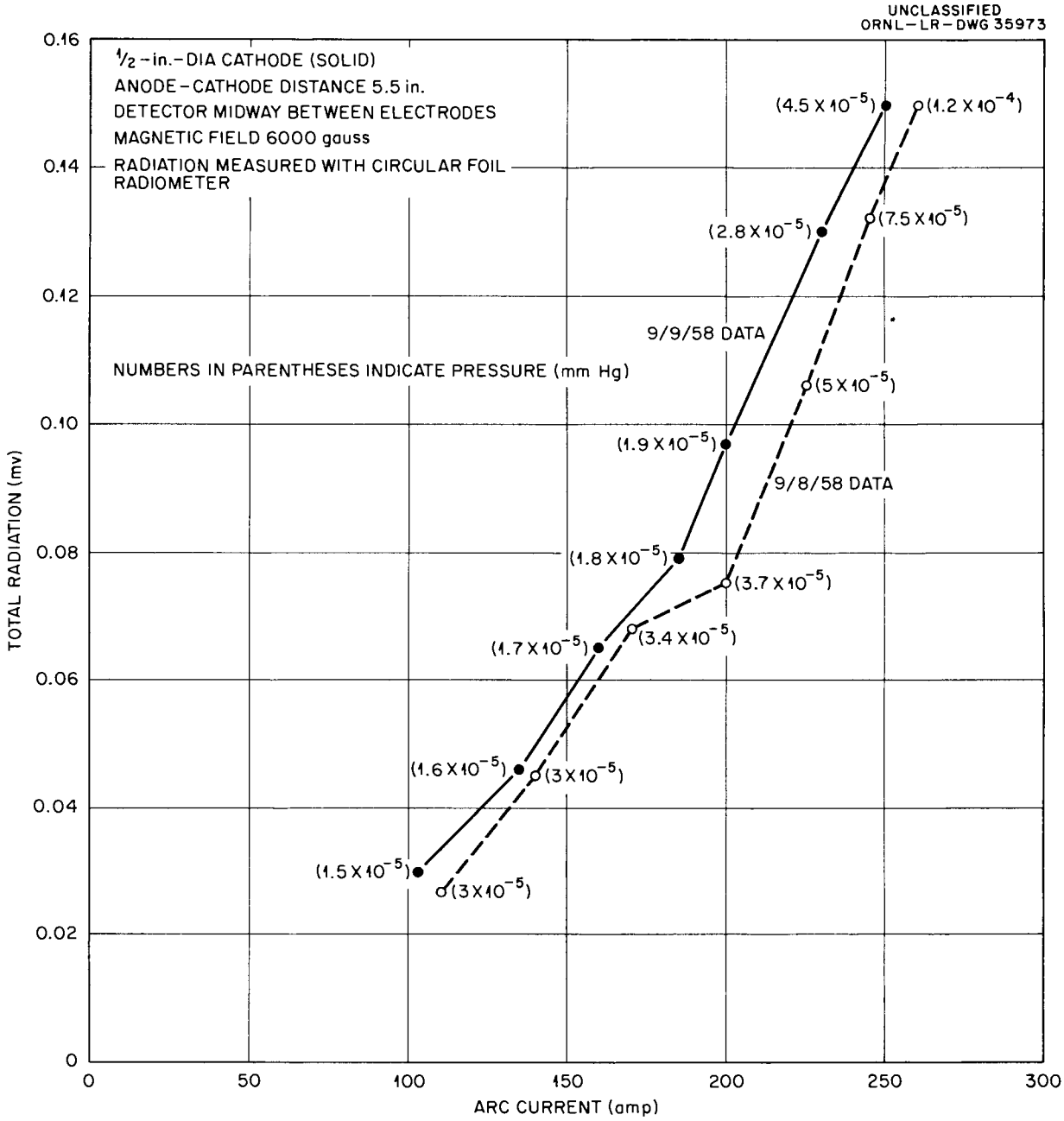

Fig. 2.6.4. Total Radiation of a Carbon Arc as a Function of Arc Current.

2.6.5 RADIATION vs MAGNETIC FIELD INTENSITY

The most startling observation during these radiation studies was that the total radiation increased steeply and almost linearly with an increase of magnetic field intensity. Table 2.6.1 shows the original data and Fig. 2.6.5 the associated curve of radiation vs magnetic field. The arc current was not held constant during this run and so the data of Fig. 2.6.4 were used to normalize the data of Table 2.6.1 to 250 amp arc current. Probably a normalization to constant arc power input should be attempted. The arc source was a "constant-current" supply, and the voltage was fluctuating too wildly for a consistent power normalization. The supply voltage changes from around 50 to 55 v at 850 oersteds to around 70 to 75 v at 8000 oersteds.

Further work in this general area will include measurements of the transparency of the arc to its own radiation, fast variations of radial radiation, effect of ion beams on the radiation at region of intersection of beam and arc, refinements of gross spectral energy measurement, and calorimetric determination of radiant energy. In addition to the above work which will continue on the short arc, the various parameters will be investigated on a long arc in a different facility.

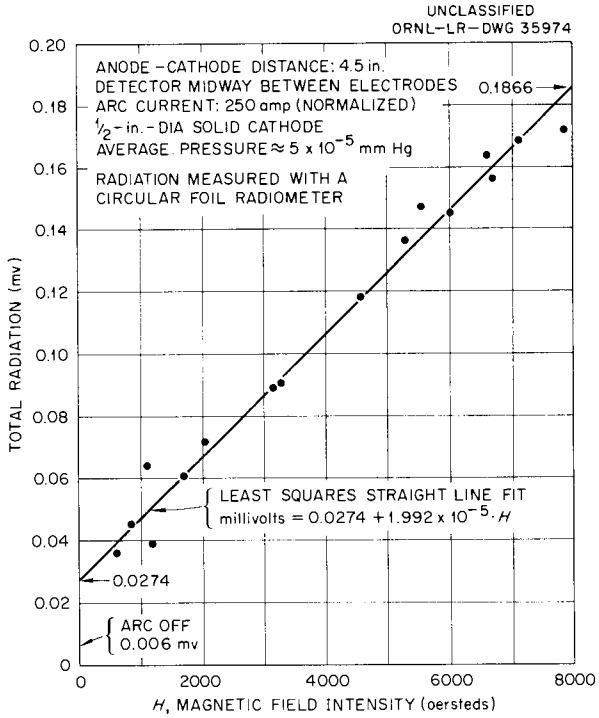

Fig. 2.6.5. Total Radiation of a Carbon Arc as a Function of Magnetic Field Intensity.

Table 2.6.1. Total Radiation vs Magnetic Field Intensity for a 3–6-in.-Long Carbon Arc

Magnetic Field Current (amp)	Magnetic Field Intensity (oersteds)	Arc Current (amp)	Observed Radiometer Voltage (mv)	Normalized* Radiometer Voltage (mv)	Pressure (mm Hg)
					$\times 10^{-5}$
16	600	245	0.031	0.036	4.5
20	850	255	0.050	0.045	5.0
24	1100	225	0.038	0.064	5.2
25	1170	270	0.060	0.039	5.5
34	1700	258	0.069	0.061	5.6
40	2020	255	0.077	0.072	6.3
60	3150	248	0.087	0.089	5.6
62	3250	250	0.090	0.090	6.0
85	4530	240	0.107	0.118	5.8
98	5280	230	0.115	0.136	5.4
103	5520	220	0.115	0.147	5.0
114	6000	225	0.119	0.145	3.6
130	6580	215	0.126	0.163	5.5
132	6650	220	0.124	0.156	5.2
148	7100	215	0.131	0.168	4.6
177	7850	215	0.135	0.172	4.2

*Normalized to 250 amp from curve of Fig. 2.6.4.

3. ION SOURCE AND ACCELERATOR STUDIES

R. C. Davis
G. G. Kelley
E. D. Klema[1]
N. H. Lazar
E. E. Moore
O. B. Morgan
R. F. Stratton

3.1 ION SOURCE DEVELOPMENT

The problems involved in the injection of higher ion currents into the DCX were initially studied along the lines indicated earlier,[2] with the aim of developing a high-current-output PIG-type source. Two modes of operation of PIG-type sources were studied: a low-impedance discharge (mode A) and a high-impedance discharge (mode B). The latter, with 10 kv ion acceleration, a source pressure of 7×10^{-4} mm Hg of hydrogen, and 50 ma anode current, produced a maximum accelerated output of 14 ma, extracted through a $\frac{3}{8}$-in. hole.

The effects of various configurations of the intermediate electrode and the anode plate on the performance of a modified Von Ardenne source were not major and had little effect on maximum output (15 ma in the cup 14 in. from the lens, with 50 kv accelerating voltage), although the alignment of the holes of these parts and of the accelerator electrode is extremely critical.

Changes in the accelerator electrode arrangement permitted output currents of 50 ma, at 60 kv acceleration, with another modified Von Ardenne-type source.

New ion source test equipment was constructed to handle expected higher current sources. Pumping speed out of the testing chamber was 2500 liters/sec for hydrogen and 800 liters/sec for air.

A new high-gradient accelerator tube of high pumping conductance was designed for the DCX and installed.

3.1.1 PIG-TYPE SOURCES

PIG-type ion sources will operate successfully at very low pressures ($\sim 10^{-4}$ to 10^{-5} mm Hg) and under these conditions should favor the production of molecular ions. In addition, high currents of atomic ions (up to several milliamperes) had already been obtained from sources of this type.[3] Published, detailed explanations of the operation of these sources are unconvincing, and therefore their limitations for molecular output at high currents were not clear.

An all-glass demountable vacuum test assembly was built for preliminary studies. Sections of 4-in. Pyrex tubing connected together by O-ring seals were used for the beam tube and were lined with conducting screen to reduce glass-charging effects. An einzel lens assembly of various designs was installed near the source end – the first electrode also serving as the accelerating electrode for ions from the source. With a spacing of $\frac{1}{2}$ to $\frac{1}{4}$ in. from the accelerator to the source, voltages of 30 kv were easily maintained. Several Faraday cups were constructed to study the position and diameter of the extracted beam as a function of source parameters. For the latter experiments, a 2-in.-dia cup was placed 25 in. from the last gap in the einzel lens.

The sources were installed in a section of 3-in. glass tubing. Generally, they consisted of a cylindrical tantalum anode $\sim$2 in. long and $1\frac{3}{4}$ in. in diameter placed along the axis of the cylinder, and of cathode end plates of various shapes perpendicular to the axis. One of the cathodes had a hole on the axis for extraction of ions. A solenoidal magnet 6 in. long, capable of producing fields up to 1200 gauss on the axis, was placed around the glass tubing.

Mode A Operation. – Two modes of operation in these sources were observed. Mode A is apparently the one described in the literature.[4] It is a low-impedance discharge in which visible light fills

[1]Summer participant from the University of Michigan.

[2]*The ORNL Thermonuclear Program*, ORNL-2457, p 16 (Jan. 15, 1958).

[3]C. F. Barnett, P. M. Stier, and G. E. Evans, *Rev. Sci. Instr.* 24, 394 (1953); J. Kistemaker and J. M. Fluit, in *International Congress on the Phenomena of Ionization in Gases*, p 516–29, Venice, 1957.

[4]*The Characteristics of Electric Discharges in Magnetic Fields*, Natl. Nuclear Energy Ser., Div I, vol 5, 345–69 (ed. by A. Guthrie and R. K. Wakerling), McGraw-Hill, New York, 1949.

the entire region bounded by the anode and cathodes. In this mode the energy of the ions emitted through the extraction hole indicated the presence of a plasma at close to anode potential.

Mode B Operation. – Most of the studies were concerned with mode B, characterized by a much higher impedance and by the appearance of a small-diameter rod-like glow on the axis. In this mode, favored by low pressure and conical cathodes, most of the ions diffusing through the cathode hole were of low energy. Under typical conditions a voltage of 10 kv was required to produce an anode current of about 50 ma. These conditions produced a maximum accelerated output of 14 ma, extracted through a $\frac{3}{8}$-in.-dia hole. Source pressure under these operating conditions was about 7×10^{-4} mm Hg of hydrogen.

3.1.2 A MODIFIED VON ARDENNE TYPE OF SOURCE

In January 1958, after discussions with C. D. Moak of the Physics Division, a source based on the principles and drawings of M. von Ardenne[5] was constructed. Figure 3.1.1 shows a cross section of a later version of this source and lens system. A general discussion of the source operation has been given by Moak *et al.*[6] Since their requirements were for moderate current and small beam diameter, a parallel development directed toward specific DCX requirements was undertaken. A glass vacuum system using 4-in. Pyrex pipe was constructed for source testing. Two MCF-300 diffusion pumps with baffles and liquid-nitrogen traps were just sufficient to maintain the pressure at 2×10^{-5} mm Hg in the system with normal source operation. A 2-in.-dia Faraday cup could be placed either 14 or 24 in. below the lens system, and provision was later made for beam mass analysis.

For most of the experiments performed with this original source a tungsten button with 0.020-in.-dia hole was used. The source operated stably at pressures down to 50 μ with hydrogen or deuterium. The maximum output current obtained in the cup at 14 in. from the lens was 15 ma with 50 kv accelerating voltage. This figure implies that half the particles emitted from the source are ions, that is, 50% gas efficiency. Mass analysis showed that at least 78% of the ions could be extracted as mass 2 when the source pressure was 50 μ. Table 3.1.1 shows the percentage of the various masses observed as a function of source pressure with 20 kv acceleration voltage.

Table 3.1.1. Effect of Pressure on Per Cent of Various Masses Emitted from a Modified Von Ardenne Ion Source

Electrode 0.060 in. from hole, 20 kv accelerating voltage

Pressure (μ)	Mass 1	Mass 2	Mass 3
	0.186-in.-dia Hole		
65	9	78	13
110	12	63	26
200	13	48	40
500	10	26	64
1000	11	17	72
	0.098-in.-dia Hole		
90	16	72	13
180	13	63	25
250	10	56	34
1000	9	26	64

The alignment of the holes in the intermediate electrode, in the plate, and in the accelerator electrode is extremely critical. The plate may be moved relative to the intermediate electrode by means of the micrometer screws. The optimum position is determined electrically since the arc may not be coaxial with the hole in the intermediate electrode. There are indications that the filament position may affect this alignment. With a 0.1-in.-dia hole in the intermediate electrode a movement of ±0.005 in. from the optimum position reduces the output appreciably.

Several configurations in the region of the intermediate electrode snout and the anode plate were tried. These included changing, independently, the spacing from the intermediate electrode to the plate and the diameter of the hole in the intermediate electrode. These changes had

[5] M. von Ardenne, *Tabellen der Elektronenphysik, Ionenphysik und Übermikroskopie*, vols I and II, Deutscher Verlag der Wissenschaften, Berlin, 1956.

[6] C. D. Moak *et al.*, *Phys. Semiann. Prog. Rep. March 10, 1958*, ORNL-2501, p 75.

UNCLASSIFIED
ORNL-LR-DWG 35841

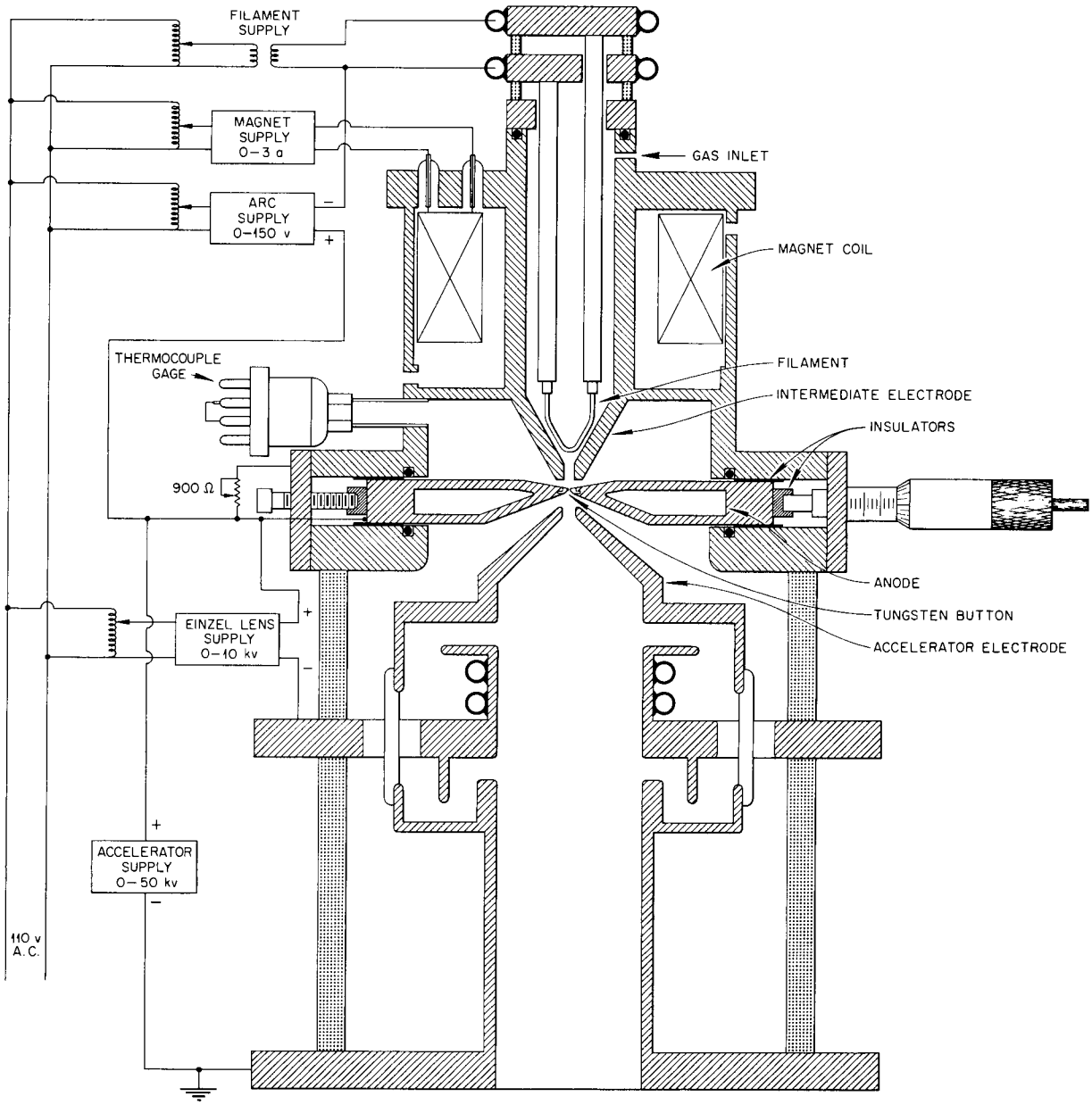

Fig. 3.1.1. Cross Section of a Modified Von Ardenne Ion Source.

no major effect on the source operation. With a small-diameter hole in the snout, however, the flame appeared smaller and somewhat less arc current was required for a given output. The length of the filament supports was changed with no marked change in source operation, but source starting was considerably easier with the longer supports. Some minor changes were made in the shape of the iron affecting the magnetic field in the region of the arc. These modifications had little effect on the maximum output.

Experiments with this particular source were discontinued because of an immediate need for increased ion current in DCX. The source was

installed on the new accelerator tube designed by the High Voltage Group of the Physics Division for injection into DCX. It is the source presently in use on DCX.[7]

Effect of Extraction Method on Beam Output. – A Von Ardenne source following the earlier designs of C. D. Moak *et al.* was made available and was used, together with our acceleration and lens geometry, while other sources were being constructed. It had a 0.032-in. aperture in the tungsten button. Despite a slight misalignment of the button with the intermediate electrode hole, changes in the accelerator electrode arrangement permitted currents of up to 50 ma to be obtained with 60 kv acceleration. Current output was limited to this value by the power supply. The gas efficiency at this current was 50%. The visible spot diameter at the collecting plate (18 in. from the bottom of the lens) was $1\frac{1}{2}$ to 2 in., but from other indications most of the current seemed to be concentrated in a diameter of less than 1 in. This diameter is consistent with the beam spreading expected from the mutual repulsion of the charges in the beam and could not be reduced by changing the focal length of the lens. Hydrogen, nitrogen, and oxygen gas were added to raise the pressure in the system to as high as 10^{-4} mm Hg in an effort to establish a secondary plasma to neutralize the beam. The visible beam diameter was reduced by less than 20%. It is clear that further experiments are necessary to determine how to cope with the problem of space-charge spreading.

[7]During the summer of 1958, while two of the authors were in Geneva, J. H. Neiler of the Physics Division directed the activities of the group, which at that time wos mainly concerned with development and initial testing of the new injection system for DCX.

3.1.3 NEW ION SOURCE TEST EQUIPMENT

A new ion source test facility, with considerably greater pumping speed, has been constructed to handle anticipated higher current sources. The vacuum system is pumped by two MCF-1400 10-in. oil diffusion pumps, modified with cooled caps over the top umbrella to reduce backstreaming of oil. A high-conductance cold trap, in which the direct-through conduction path from the system is just blocked by the presence of a liquid-nitrogen cylinder, is interposed between the 10-in. valve and the pumps. Base pressure in the system is 8×10^{-8} mm Hg. The pumping speed out of the test chamber was measured as 2500 liters/sec for hydrogen and 800 liters/sec for air.

3.2 THE DCX ACCELERATOR

3.2.1 ION-INJECTION SYSTEM FOR DCX

A new ion-injection system for DCX was installed during the summer of 1958. The high-gradient accelerator tube used was designed by the High Voltage Group of the Physics Division. It uses 14-in.-ID ceramic insulator sections with a bore through the accelerating electrode of 7 in., yielding a high pumping conductance up the tube. This tube consists essentially of 5 sections, with each section cemented by vinyl acetate. The electrode assembly is composed of five overlapping cylinders. To provide for better electrical stability the customary potential dividing resistors were eliminated and each of the five electrodes was tied electrically to the output of the five stages of the 625-kv cascade power supply. The tube has performed according to expectations. Maximum total currents accelerated to 625 kev have been 10 ma, with approximately 50% being H_2^+. At larger currents electrical breakdown occurs. Beam focus is still unsatisfactory. The diameter of the total beam at the base of the accelerator is 1 cm; however, in the mid-plane of DCX the radial spread of the beam is about 2 to 3 cm. The Z-focus is a very sharp line due to the magnetic focusing of the mirror field of DCX.

One serious trouble has been encountered in the operation of the accelerator tube. After a month's operation, a deposit covering the surfaces of the ceramic resulted in electrical breakdown between the 125-kv sections. Cleaning the ceramic with detergent and water or trichloroethylene eliminates the trouble until the deposit forms again. No traces of oil can be found coming from the diffusion

pumps since they are baffled with refrigerated baffles operated at −50°C. Cursory examination reveals that the vinyl acetate used in cementing the sections together is being decomposed, the first evidence being a yellow discoloration of the vinyl, which, with age, turns black. A new tube has been constructed in order to expose a minimum amount of vinyl to the vacuum region.

To provide space for ion source power supplies a platform has been installed and insulated for 625 kv above ground. A 5 × 7-ft terminal platform provides adequate space for mounting the power supplies and other equipment necessary for anticipated high-current operation. Figure 3.2.1 is a view of the terminal platform and Fig. 3.2.2 is a closeup of the source assembly. The box on which

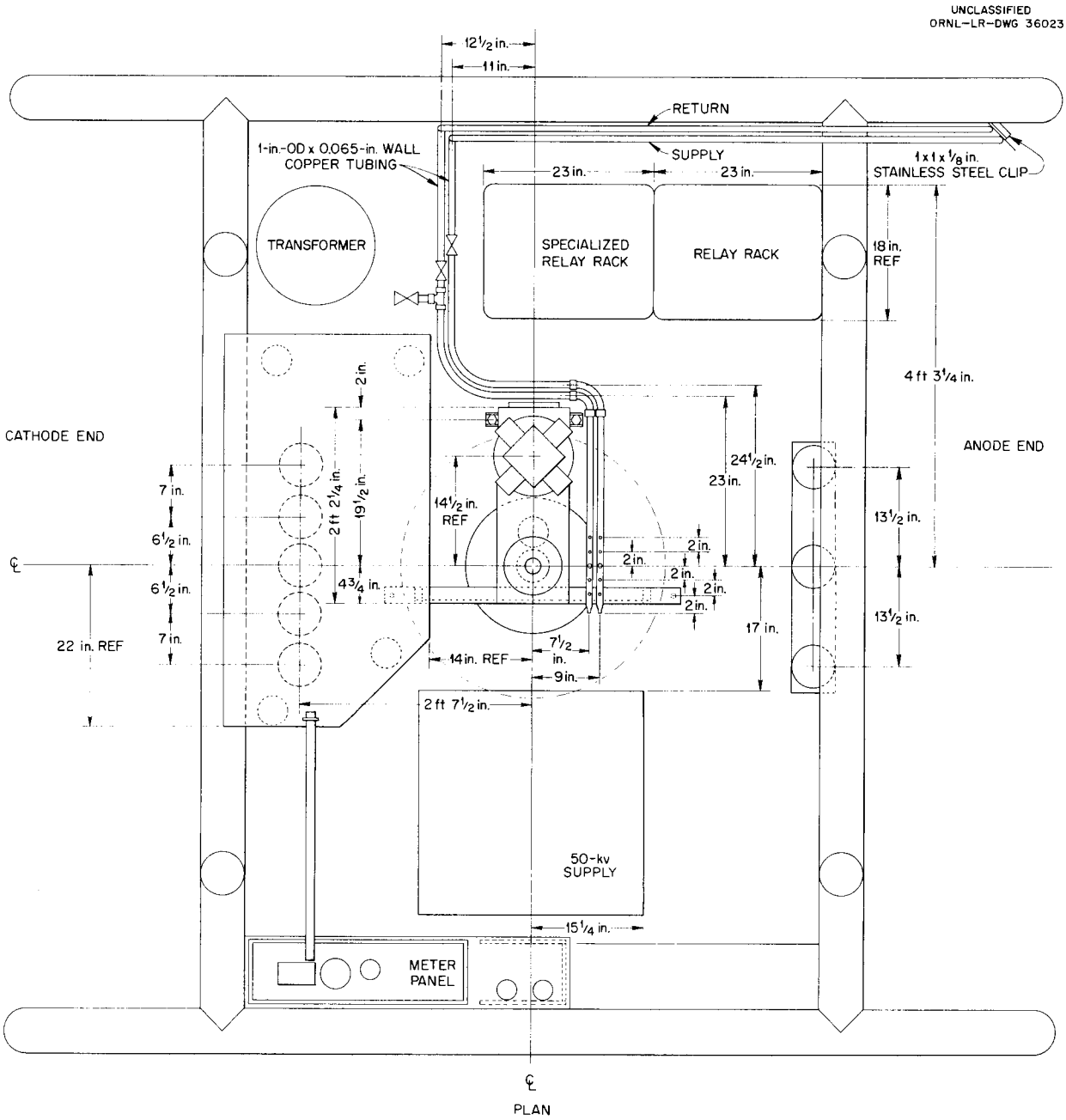

Fig. 3.2.1. DCX Accelerator Tube Assembly, Upper Platform.

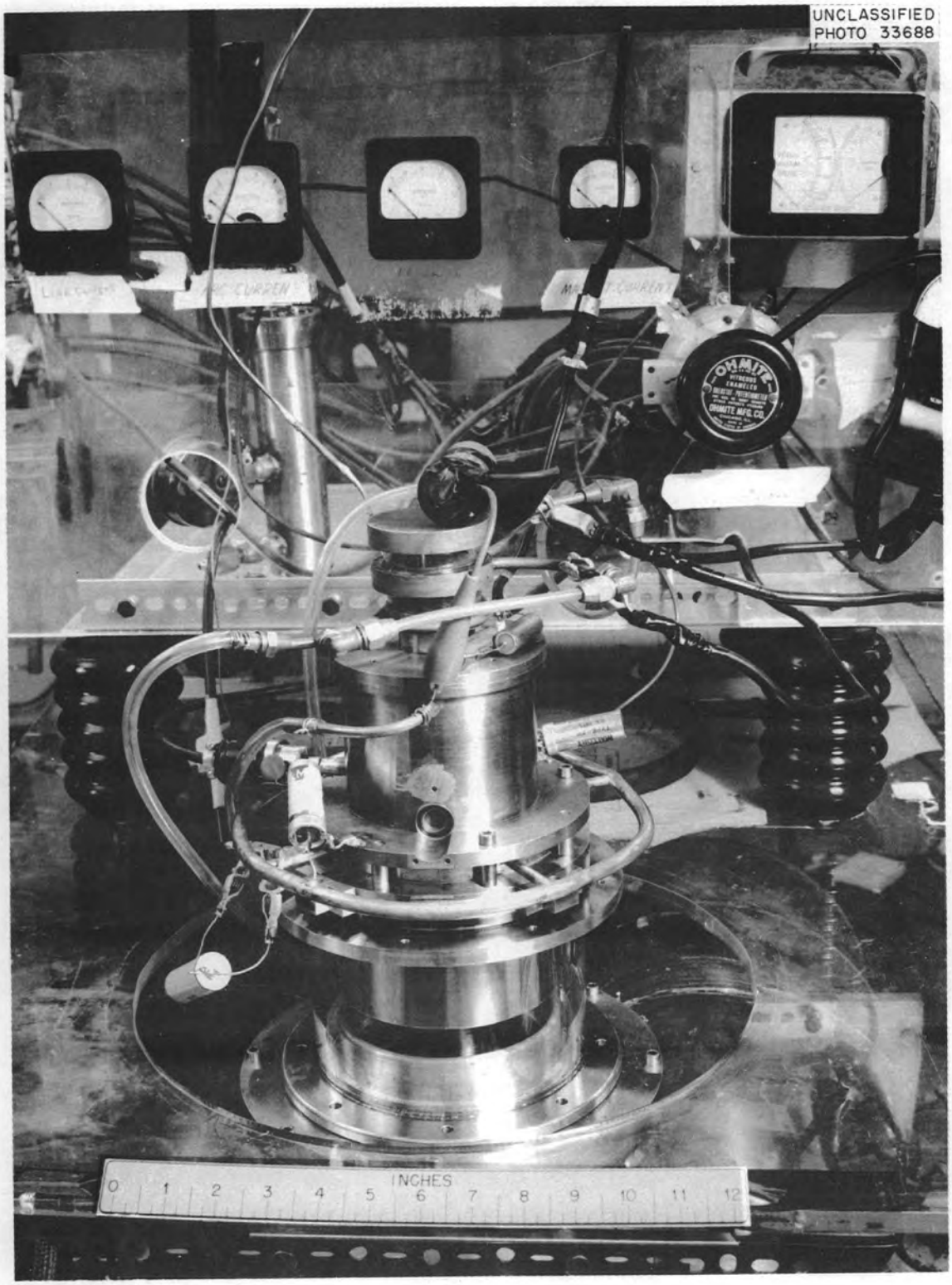

Fig. 3.2.2. DCX Source Assembly.

the source is mounted was found to be necessary to provide sufficient spacing between the source and the accelerator tube for focusing at the arc. The object position of the tube is so close to the entrance aperture that a crossover is required above the tube when the present source and lens system is used. Pumping is provided at the top of the tube by a Varian Vac-Ion pump mounted on the spacer box.

The various adjustments required while operating at high voltage are made by means of Lucite rods driven by commercial antenna rotators.

3.2.2 HIGH-VOLTAGE REGULATOR FOR DCX

F. T. May

A newly designed high-voltage regulator for the DCX accelerator was installed on December 11, 1958, and has functioned, after calibration, without further adjustment or major repairs. The new regulator can bring the voltage from zero to the operating point of 560,000 v in ~3 sec and, at the operating point, hold voltage excursions to within 500 v. Replacement of the old regulator was necessitated by wear and tear in the electromechanical linkage of its regulation loop, as evidenced by slow oscillations of several thousand volts at the operating point and slow response to an "on" signal. These conditions had the obvious disadvantages of uncertainty of accelerating voltage and loss of important time in waiting for the voltage to return to the operating point after being off.

Analysis and Design

Before any work could be started on a new regulator, the characteristics of the unregulated high-voltage set had to be taken and studied. The necessary information was obtained by disconnecting the old regulator and applying an instantaneous voltage superimposed on a constant d-c voltage to the exciter field of the high-voltage motor generator set. The response of the high voltage alone was found by turning the set on with the dc already applied to the field. The data were recorded on a Honeywell Visicorder so that a clear permanent record would be available for comparison during the simulation tests. The data showed that the response was a delayed exponential, which indicated that there were a few exponential components driving the system in series. This is, of course, as expected since the electromechanical components must have finite rise times. The delay time was 0.14 sec and the following rise time was 0.96 sec.

An analog computer (FLEPAC) was used to find the actual time constants from the data; with it a simulated system was set up and the time constants were varied. With the FLEPAC and the Visicorder it was found that the major time constants of the high-voltage set were 0.6, 0.25, and 0.25 sec. The 0.6 sec was the response of the high voltage with only dc on the field. The other two simply satisfied the other electromechanical components as a group. The computer was set up on a ×10 scale and the results converted to "real" time.

The design of the new regulator followed the logic of detecting the error with a reference voltage and feeding it back with its first and second derivatives to apply a correction voltage to the exciter field. A block diagram of the regulator is shown in Fig. 3.2.3. The simulator shown was a vacuum-tube circuit that contained the high-voltage time constants on a "real" time scale. The rest of the circuit was built with transistors since they were very well adapted to this application. A complete circuit diagram is shown in Fig. 3.2.4. With this arrangement, it was possible to watch the simulated response of the high-voltage set on an oscilloscope. The gain and derivative amplifiers in the regulator were set for optimum conditions of fast recovery in reaction to a perturbation at the output, E_0, with a minimum of overshoot.

Testing

After the regulator performed satisfactorily with the simulator, it was tried on the high-voltage set. The only difficulty that arose was pickup of the fundamental ripple frequency of the set. The pickup was enough to saturate the regulator. This was corrected by inserting a filter (Fig. 3.2.5) at the input that attenuated the ripple signal to a much lower level. The regulator held the voltage to within 500-v excursions when the voltage was set at the operating point of 560,000 v. It also

UNCLASSIFIED
ORNL-LR-DWG 35778

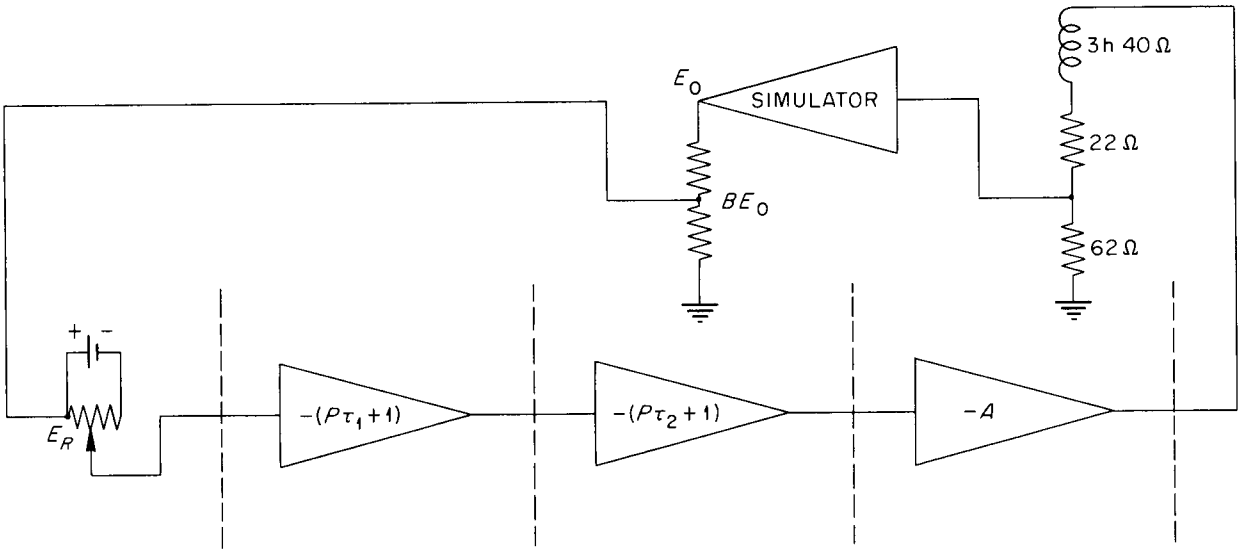

Fig. 3.2.3. Block Diagram of High-Voltage Regulator for DCX.

UNCLASSIFIED
ORNL-LR-DWG 36451

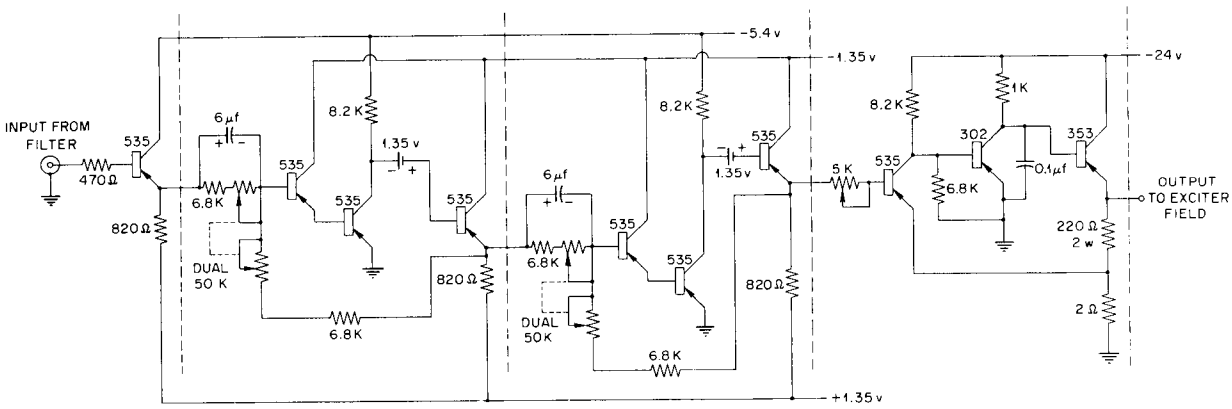

Fig. 3.2.4. Circuit Diagram of High-Voltage Regulator for DCX.

could bring the voltage back to this value from zero in about 3 sec.

Installation

On December 11, 1958, the regulator was installed ready for immediate use. A digital voltmeter (Fig. 3.2.5) was also incorporated in the circuit so that the high voltage could be read more easily. It was carefully calibrated to within the accuracy of the Rubicon potentiometer which had been previously used. Since that date the regulator has been used without the need of any further adjustments or any major repairs.

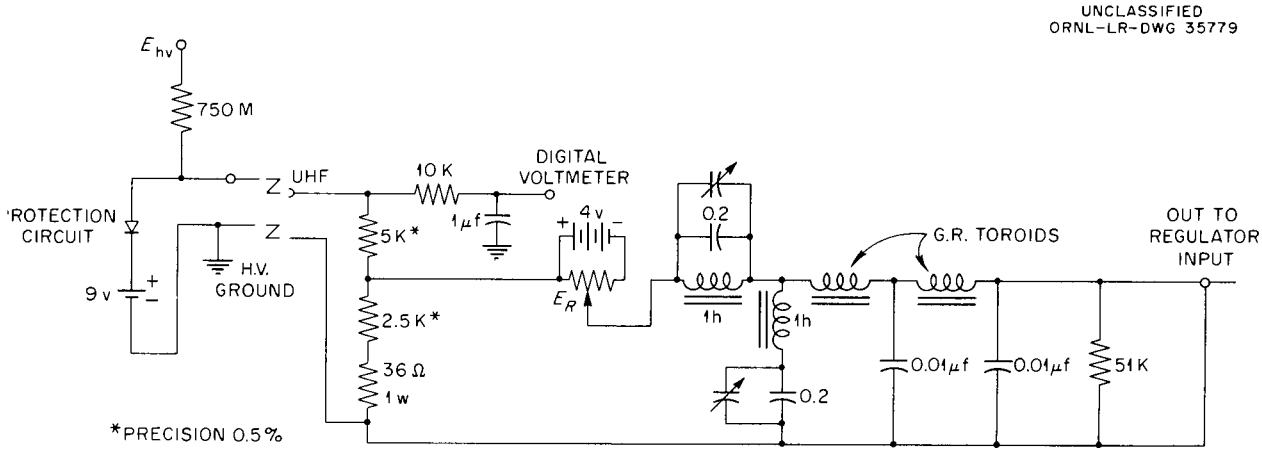

Fig. 3.2.5. Input Filter for High-Voltage Regulator for DCX.

4. VACUUM SYSTEMS

4.1 THE DCX VACUUM PROBLEM

R. J. Mackin, Jr. C. Michelson[1]

The creation of a thermonuclear plasma in the DCX requires that the neutral gas density within the plasma be reduced to about 10^7 atoms/cm^3. It is hoped to achieve this by the process of "burnout," which is expected to lead to a plasma sufficiently dense to shield its interior from gas molecules incident on the surface. The problem is discussed quantitatively in Sec 4.1.1. For a given input current I, expressed in milliamperes, the achievement of burnout is estimated to require a pressure below $2I \times 10^{-8}$ mm Hg for deuterons in deuterium and $2.5I \times 10^{-7}$ mm Hg for protons in hydrogen.

The attainment of the required vacuum is complicated by the carbon arc, which as yet maintains the ambient pressure above 10^{-7} mm, and the influx of gas represented by the ion beam. It is hoped to attack the former problem by an investigation of the gas sources associated with arc operation and to solve the latter problem by high-speed ionic pumping based on the ionizing power of the trapped particles.

[1]On loan from TVA.

A device intended for the study of both problems (the PIG-Pump Facility or PPF) has been constructed and placed in operation. It will be described in Sec 4.2. Novel components of the PPF which have proved satisfactory include a high-conductance liquid-nitrogen trap, demountable seal-ring welded vacuum closures, and a direct-Kovar-sealing bakeable window.

4.1.1 BURNOUT

The chief cause of the escape of trapped deuterons in DCX is believed to be charge exchange. In a charge-exchange collision a deuteron acquires an electron from a gas molecule, becomes a neutral deuterium atom, and goes out of the system. A necessary condition for achieving a thermonuclear plasma in the DCX is that the attenuation of the plasma by charge exchange be reduced to the level of the Coulomb scattering losses. For the present set of DCX parameters, this implies[2] a density of

[2]A. Simon, *Physics of Fluids* 1, 895 (1958); A. Simon and F. M. Rankin, *The ORNL Thermonuclear Program*, ORNL-2457 (Jan. 15, 1958), Appendix A, or *Some Properties of a Steady State High-Energy Injection Device (DCX)*, ORNL-2354 (Aug. 26, 1957).

neutral molecules in the plasma interior of less than about 10^7 per cubic centimeter for deuterons in deuterium or 10^8 for protons in hydrogen.

It is hoped to achieve and maintain this interior neutral density in the presence of a substantially larger external density by the process of "burnout." Burnout is expected to lead to a plasma density so great that gas molecules incident on the surface are ionized before they penetrate appreciably into the volume.

The phenomenon is expected to proceed as follows: If the pressure in the system can be reduced below a certain critical value, gas atoms in the region occupied by the trapped deuterons will be ionized at a greater rate than new ones enter the region. The deuteron density, limited up to this point by charge exchange, will increase, ionizing the gas atoms at a greater rate and permitting further buildup. This regenerative process will continue until the deuteron density reaches a limit, set by mirror losses, at which the plasma interior is effectively shielded. The pressure (in mm Hg) at which burnout is expected to occur for deuterons in deuterium is given by[2]

$$p_0 = \frac{4kT_0}{v_0 S} \frac{\sigma_i + \sigma_{cx}}{\sigma_{cx}} I_+ \qquad (1)$$

$$= 2 \times 10^{-8} I_+ ,$$

where

k = Boltzmann's constant,
T_0 = gas temperature (300°K),
v_0 = molecular velocity,
S = surface area of the region of trapped deuterons (6×10^3 cm^2),
σ_i = the cross section for ionization by a fast deuteron,
σ_{cx} = charge-exchange cross section,
I_+ = input ion current.

For protons in hydrogen, the value is $p_0 = 2.5 \times 10^{-7} I_+$ mm Hg. In nitrogen, the critical pressure is lower by a factor of 6 for deuterons and by a factor of 10 for protons.

A point to be noted is the crudeness of the estimation of the burnout criterion. For instance, if the electrons present in the region of trapped deuterons should acquire mean energies of 50 or 100 ev, the critical pressure for a given current would be raised by a factor of 2 or more. On the other hand, the effects of possible charge exchange with trapped cold atomic and molecular ions, including those in the carbon arc and its aura, are not readily estimated but may lead to significant decreases in the critical pressure.

Finally, the neutral density to be taken into account is that which exists in the presence of the gas influx represented by the input beam. The pressure p is related to the trapped beam current I_+ and to the speed S of the system's pumps (for the gas of which the beam is composed) by

$$p = p_{base} + 1.7 \times 10^{-7} \frac{I_+}{\epsilon S} , \qquad (2)$$

where ϵ is the trapping efficiency (or the net efficiency of trapping plus removal of the undissociated beam), I_+ is given in ma, and S is in kiloliters per second. For a negligible base pressure, achieving the critical pressure for burnout requires

$$1.7 \times 10^{-7} \frac{I_+}{\epsilon S} \leq 2 \times 10^{-8} I_+$$

for deuterons in deuterium, giving

$$\epsilon S > 8500 \text{ liters/sec} .$$

For protons in hydrogen,

$$\epsilon S > 680 \text{ liters/sec} .$$

The largest pump on DCX is the carbon arc, whose speed[3] is estimated to be 4000 liters/sec for nitrogen, 7500 liters/sec for deuterium, and 10,400 liters/sec for hydrogen. Thus additional pumping is expected to be necessary for burnout in deuterium but not for burnout in hydrogen.

The foremost immediate DCX vacuum problem is that of reducing the pressure in the presence of the carbon arc. The base pressure before the arc is ignited is generally about 3×10^{-8} mm Hg. With the arc running, the best pressure is nearly an order of magnitude greater. Thus, associated with the arc is a gas influx of 1.2 micron-liters/sec, greater by a factor of 130 than that without the arc.

A very important correlative problem is the determination of the true pressure in the presence of the arc.

---

[3]R. J. Mackin, Jr., *Controlled Thermonuclear Conference, Held at Washington, D.C., February 3–5, 1958*, TID-7558, p 331, gives relative value; C. F. Barnett, private communication, 1958, has estimated the absolute pumping speed of the DCX arc for nitrogen.

4.2 DESIGN AND CONSTRUCTION OF THE PPF

R. J. Mackin C. Michelson

One component being developed for the DCX vacuum system is an ion pump capable of providing the additional pumping speed essential for burnout with deuterons. The ions to be removed are those produced by the trapped deuterons or protons. Since each trapped deuteron produces, on the average, about 20 ions, each milliampere ionizes the background gas at a rate of 3.5 micron-liters/sec. At 10^{-8} mm Hg, this corresponds to one-third of a million liters per second. The removal of these ions is expected to be accomplished by a more or less elaborate configuration of negatively charged electrodes placed just behind the magnetic mirrors. This configuration is reminiscent of that of a Philips ion gage discharge; hence, the name PIG plates has been given to the electrodes.

PIG plates have been operated in DCX for brief periods of time, and have been shown not to interact seriously with the carbon arc.

The need to conduct detailed development work and study has resulted in the construction of the PIG-Pump Facility (PPF) for the testing of the performance of various electrode configurations in an ultra-high-vacuum system with a mirror magnetic field. The first problem to be studied in the apparatus will be that of the origin and eventual elimination of the gas influx associated with the carbon arc.

Although no arc experiments have yet been completed in the PPF, a certain amount of experience has been gained in its performance as an ultra-high-vacuum system. Closely related experiments are being conducted in a small-scale unit (Pigmy Pump Apparatus) by R. A. Gibbons. They have not yet progressed far enough to warrant reporting.

4.2.1 PPF DESIGN

The approximate size of the PPF was set by the requirement of performing arc-vacuum experiments on roughly the same scale as those in DCX. The dimensions were determined more exactly by the decision to build a system adapted to the use of an available set of magnet coils which were dimensionally and electrically identical to the first layer of the DCX coils. For the same reasons as for DCX, namely, the carbon emission from arc electrodes, the vacuum container is a three-region system, the center region designed to be capable of achieving ultra-high vacua. The DCX is actually a two-region machine.

The requirements imposed on the vacuum system were somewhat unusual. The ultimate pressure was required to be only about 10^{-8} mm Hg, a value halfway between ordinary high vacuum and ultra-high vacuum. The desired pumping speed, however, was nearly an order of magnitude greater than that of even the largest ultra-high-vacuum systems then known to us.

Figures 4.2.1 and 4.2.2 are pictorial plan and end views of the PPF. The inner vacuum chamber is a 12-in. tube, 6½ ft long, pumped by two 10-in. oil diffusion pumps (Consolidated Electrodynamics Corporation, MCF-1400) which are trapped by refrigerated baffles and by high conductance liquid-nitrogen-cooled traps. The designs of certain novel components, namely, the liquid-nitrogen traps, the demountable bakeable joints (seal welds) in the inner vacuum chamber, and the bakeable Pyrex windows, are described below.

The two outer vacuum chambers form 1-ft extensions on the central tube and are pumped by 6-in. oil diffusion pumps which are trapped in the same manner as the 10-in. ones. A bulkhead with an all-metal piston valve separates each low-vacuum chamber from the central chamber. In the low-vacuum chambers, O-ring and seal-weld joints may be used interchangeably. All experimental equipment is removable through the end chambers, and high-vacuum seals are broken only for major modifications.

During arc operation each low-vacuum system will incorporate an arc tube which projects forward from the bulkhead almost to the coil center and which supports the arc baffle-holder. This configuration is necessitated by the 10-in. pumping systems being behind the magnet coils and the electrodes having to be placed near the edges of the coil throats.

The central chamber can be baked down to the quarter-swing valves by superheated steam passed through tubing wrapped on the chamber, trap walls, and arc tube. The same lines are available for

UNCLASSIFIED
ORNL-LR-DWG 35773

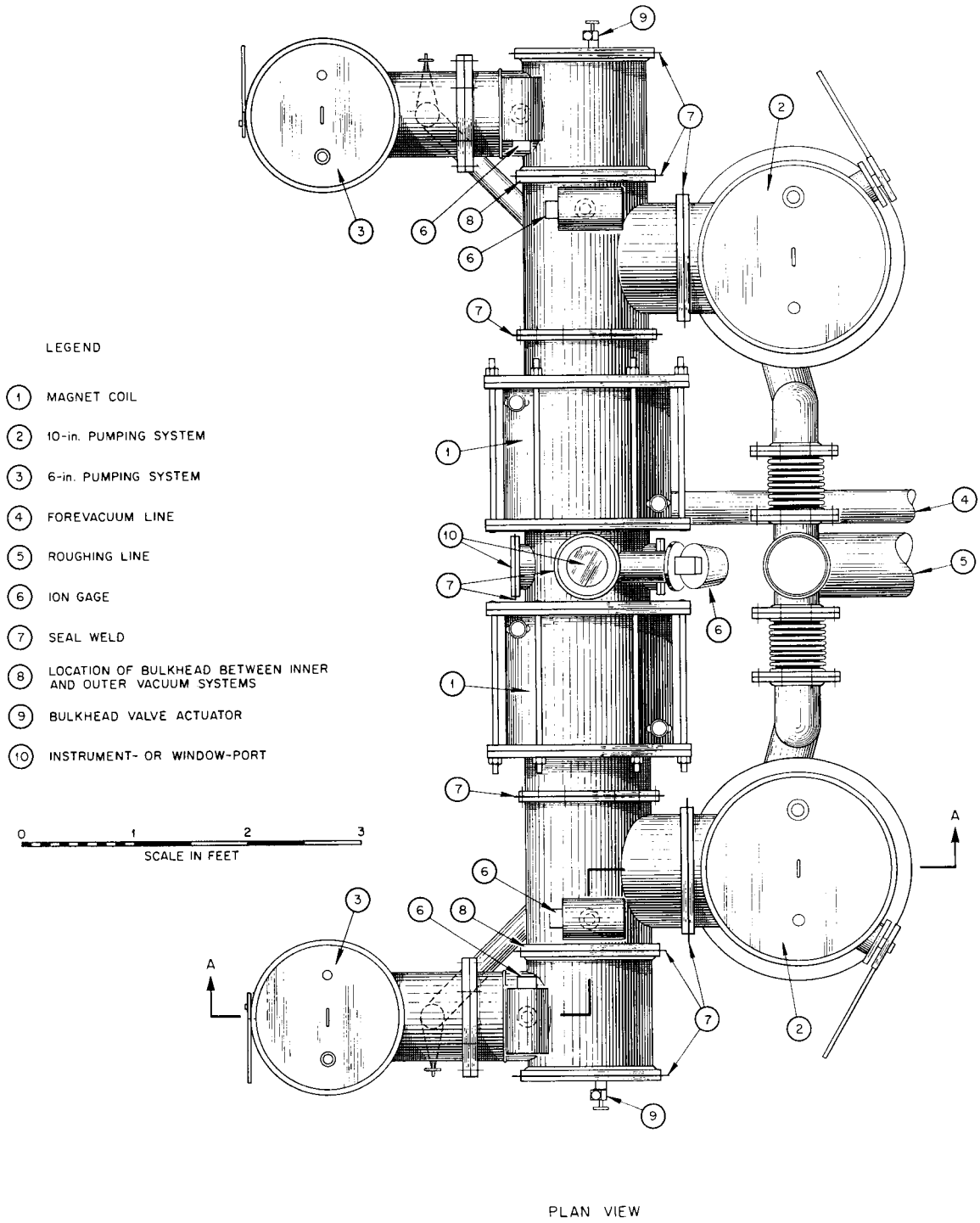

Fig. 4.2.1. PIG-Plate Facility – Plan View.

UNCLASSIFIED
ORNL-LR-DWG 35774

LEGEND

(1) — MAGNET COIL, SHOWING COOLING LINES
(2) — 10-in. PUMPING SYSTEM
a. LIQUID NITROGEN TRAP
b. QUARTER-SWING VALVE (CEC)
c. FREON-COOLED TRAP
d. DIFFUSION PUMP (CEC, MCF-1400)
(3) — 6-in. PUMPING SYSTEM
a. LIQUID NITROGEN TRAP
b. QUARTER-SWING VALVE (CEC)
c. FREON-COOLED TRAP (CEC)
d. DIFFUSION PUMP (CEC, MCF-700)
(4) — FOREVACUUM LINE
(5) — ROUGHING LINE
(6) — ION GAGE
(7) — SEAL WELD
(8) — PUMP SUPPORT FRAME
(9) — TUBE FOR FAST AIR-COOLING OF PUMP

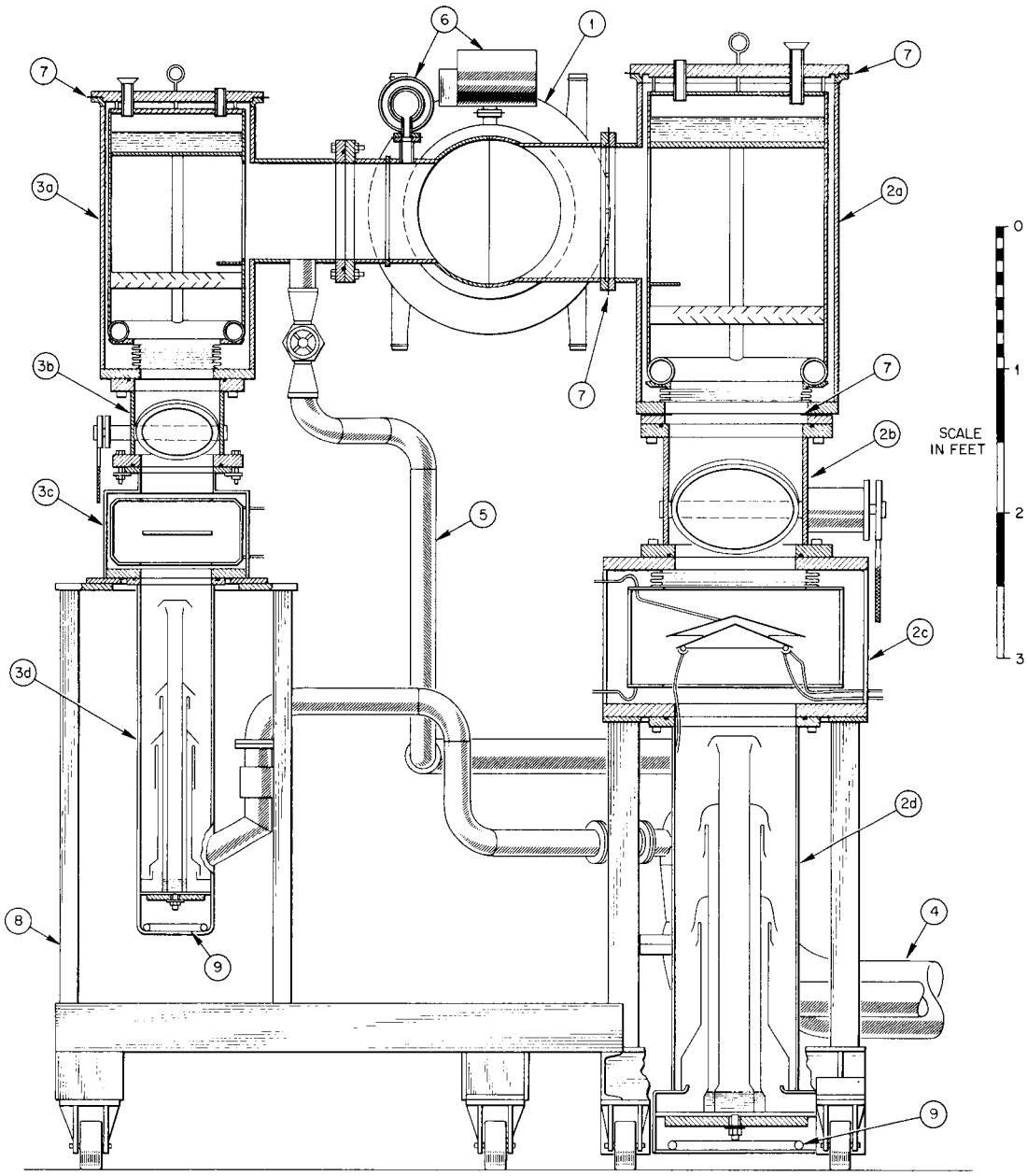

SECTION A — A

Fig. 4.2.2. PIG-Plate Facility – End View.

cooling when an arc is operated in the facility. All bakeable structural parts except the liquid-nitrogen traps are made of Inconel.

The use of refrigerated traps makes possible preliminary experimentation in the mid-10^{-7} mm Hg range without nitrogen trapping and in addition provides a convenient means of holding the system at low pressure during baking. A water-cooled shallow cone is located just under the central (refrigerated) cone of each 10-in. trap in order to permit run-back of much of the trapped oil.

The quarter-swing valves, with their (at present) inevitable O-ring seals, were recognized as being potentially incompatible with the pressure which would be ultimately required. However, they were regarded as virtually essential for system protection and for the practical performance of arc experiments of the type envisioned. As it has turned out, the O-rings below the nitrogen traps have not set the base pressure above 10^{-8} mm Hg. The inclusion of two separately valved pumps in the system has provided a degree of flexibility and a means of system checking even more useful than had originally been envisaged.

Pressures are measured by Bayard-Alpert-type ion gages (Veeco, RG-75) which are magnetically isolated by Fernetic-Conetic shields (Perfection Mica Co.). For protection during bakeout, the gages are encased in vacuum-tight soft-iron casings which are evacuated to a pressure of a few microns.

The magnet coils are single-layer 44-turn solenoids edge-wound from $\frac{1}{4} \times 1$ in. copper bus. They are wound with Fiberglas ribbon between the turns and suspended in their containers by Micarta spacers which permit axial flow of cooling water along the inside and outside of the coil. The containers are lined with Araldite-impregnated Fiberglas. In their present location, with a 5000-amp current, the coils produce magnetic fields of 2.5 kilogauss at the machine's mid-point and 5 kilogauss in the coil throats.

4.2.2 PPF COMPONENTS

Liquid-Nitrogen Traps

The liquid-nitrogen traps were designed around the specifications of incorporation of a cold oil-creep barrier,[1] guarantee of two impacts on a cold surface for any droplet or molecule passing through the trap, and conductivity comparable to the speed of the untrapped pump. There was in addition the boundary condition of a right-angle bend in the trap.

The trap configuration (shown in Fig. 4.2.2) is such that one required "bounce" occurs at a cold wall and the other on the chevron baffle. Only about half the chevrons are shown in the figure, so the opacity is not indicated. It was found possible to remove an inner part of each chevron without sacrificing the surety of a bounce and with some gain in conductance. The replacement of several chevrons at one side by an offset strip came about because the outside wall at each end of the chevrons provided a means by which a few molecules might go through the trap with only one bounce. The significance of the effect of this detail for the trap performance is not at all clear, and it is mentioned mainly as an example of the pitfalls that threaten the unwary trap designer if a three-dimensional model is not made.

The bellows and saddle arrangement at the bottom of the trap provides the oil creep barrier. In assembly the main portion of the trap is lowered through the top so that the torus is seated in the saddle, and a seal-ring closure is made at the top flange. The torus is cooled by nitrogen fed through a downcomer tube from the reservoir at the top. The vapor phase returns through a riser tube at the opposite side. This arrangement constitutes a natural-convection boiler.

The trap assembly is made of stainless steel. The outside walls are $\frac{1}{8}$ in. thick and the chevrons $\frac{1}{32}$ in. thick. During bakeout the trap is heated by radiation from the surrounding tank walls.

Modifications to the design which would be considered desirable in a successor to this trap are location of the oil-creep barrier at the tank side of the trap so as to place the stagnant vacuum region on the pump side, direct heating of the trap itself rather than of the tank walls, a means for removing condensed water from the liquid-nitrogen container, and copper construction to eliminate the torus boiler.

Design and Tests of Seal-Ring Welded Vacuum Closures

The development described in this section will be reported in detail later. An abbreviated account is given here.

[1] Suggested by R. F. Post, UCRL, private communication, 1957.

The basic flange design for the PPF is shown in Fig. 4.2.3. All flange parts are Inconel, although other weldable materials can be used. The C-clamps are required on larger flanges when axial tensile loading exceeds atmospheric compression. (Small flanges of this design are usually sufficiently strong without clamping.) Since the male-lug and seal-ring configuration of this flange design yields a very small cross-sectional area for thermal conduction, excellent thermal isolation is afforded when the flange must join baked and unbaked portions of a vacuum system.

UNCLASSIFIED
ORNL-LR-DWG 35775

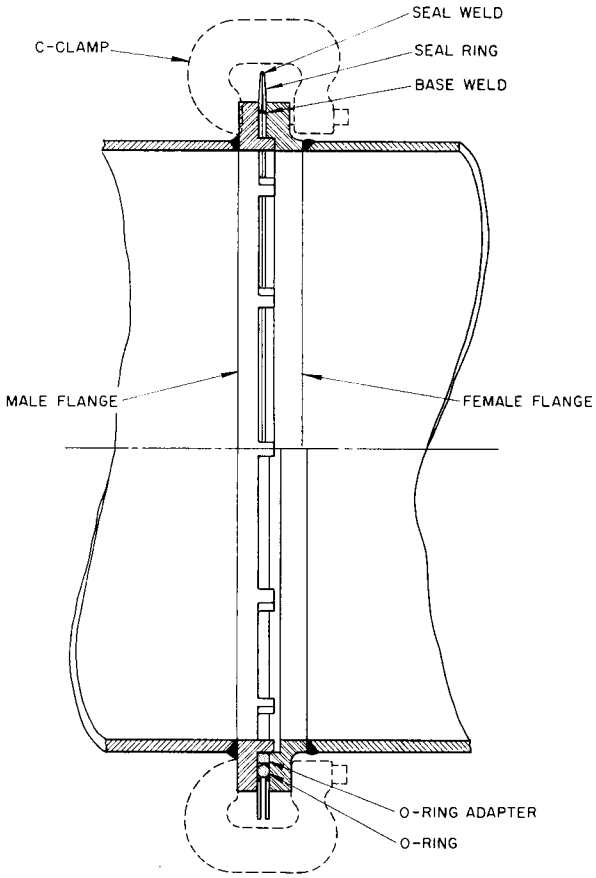

Fig. 4.2.3. Basic Seal-Ring Flange Design.

In order to use this type of flange design, it was necessary to develop methods for welding the thin Inconel seal rings to the heavy Inconel flanges. The jig developed for making the base weld is shown in Fig. 4.2.4. This jig holds the seal ring firmly in place while the base weld is being made.

The seal weld on this type of flange is made by clamping a portion of the total seal ring circumference with the all-copper jig shown in Fig. 4.2.5. This jig pulls the seal rings tightly together and irons out the surface irregularities. The V-shaped configuration helps to retain the inert gas atmosphere around the weld area.

The seal-ring closure principle is not limited to circular configurations. In fact, the flange shape is limited only by the possibility of fabricating the flange, welding jigs, and seal rings. In principle, vacuum-tight bakeable seals can be obtained regardless of the seal configuration. Four

UNCLASSIFIED
ORNL-LR-DWG 35776

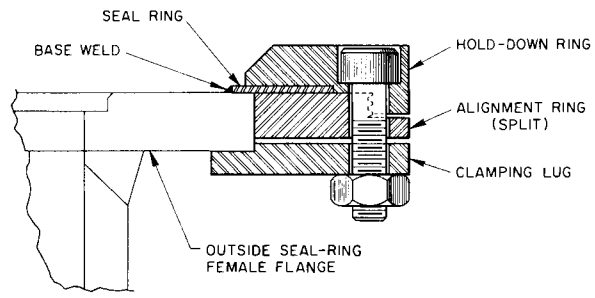

Fig. 4.2.4. Base-Welding Jig for Seal-Ring Flanges.

UNCLASSIFIED
ORNL-LR-DWG 35777

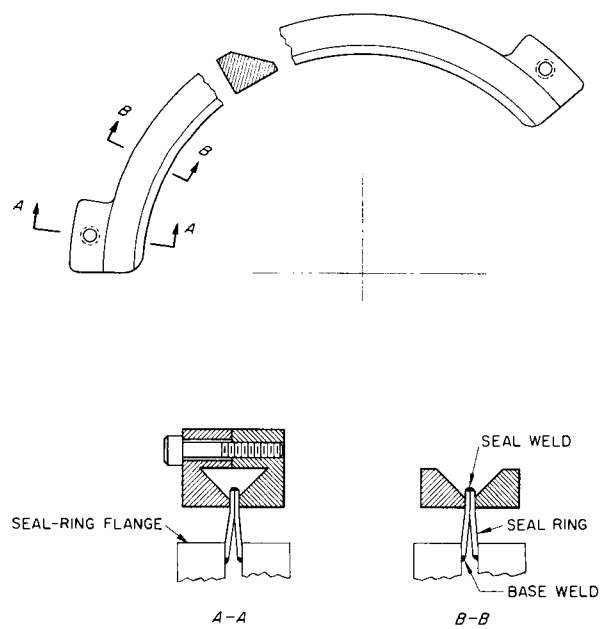

Fig. 4.2.5. Seal-Welding Jig.

of the seals on the PPF are internal, made with the ring mounted on the inner flange edge. The largest seal on the PPF is 18 in. in diameter.

Time was not available for extensive laboratory development and testing of the seal-ring-type flange. Some quick experiments were conducted to test out welding and leak-checking procedures and to measure leak rates during the application of thermal cycles and thermal gradients. A 4-in. nominal ($5\frac{1}{2}$-in.-OD) outside seal-ring flange was fabricated for this purpose. Figure 4.2.6 shows the experimental setup used for the thermal-cycle tests. The test flange was placed on a 2-kw hot plate and evacuated through tubing attached to the top test plate.

The hot plate heated the bottom flange to about 600°C. Natural convection cooling brought the top flange into equilibrium at about 270°C. In order to obtain a more severe thermal gradient, the hot plate was insulated with aluminum paper and the top flange cooled with air and beakers of boiling water. For this condition the bottom flange came up to 700°C and the top flange down to 185°C.

Figure 4.2.6 shows the test flange before heating. Note that the hexagonal bolt head on the hot plate just clears the seal weld. Figure 4.2.7 shows the same flange after heating to about 580°C on the bottom flange. Note the seal-ring curl due to greater expansion of the bottom flange. The hexagonal bolt head now clears the seal weld by $\frac{1}{16}$ in. A maximum thermal gradient condition was established by adding insulation and then cooling.

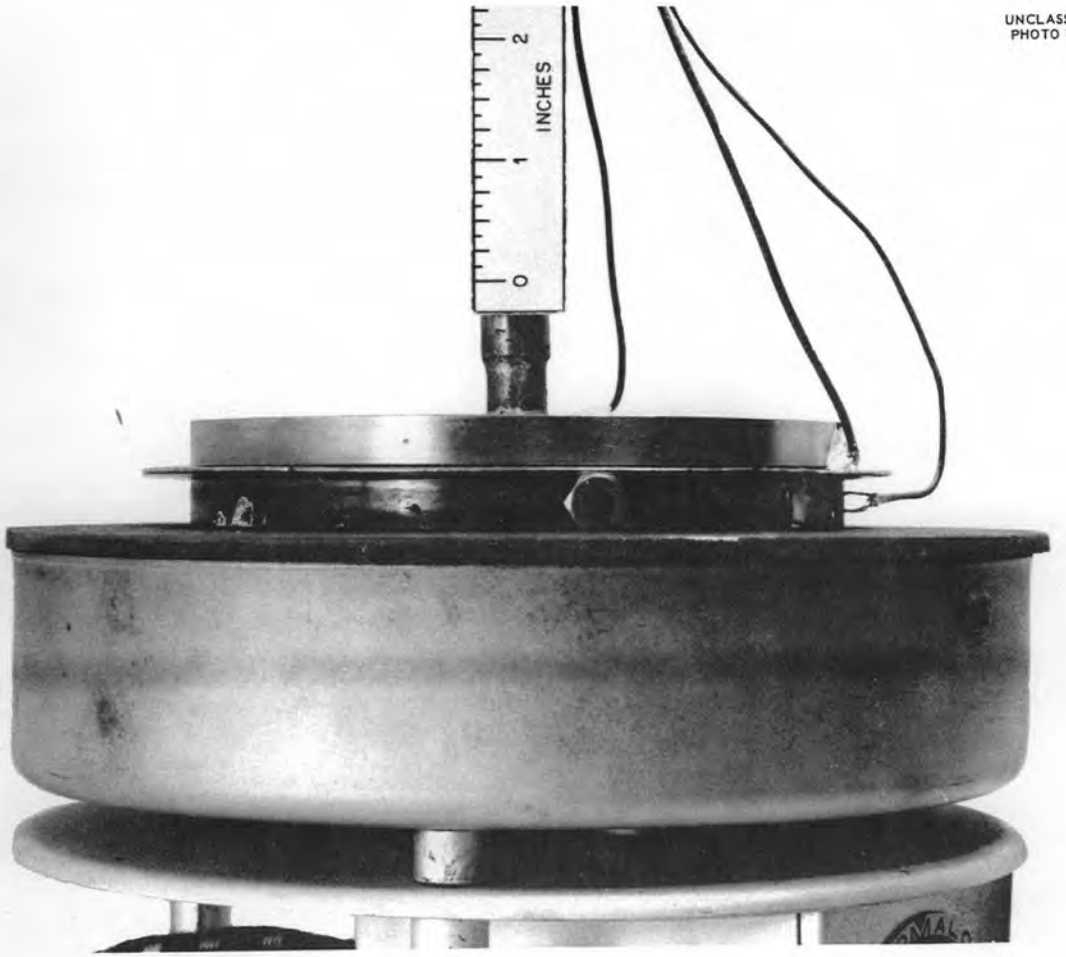

Fig. 4.2.6. Prototype Seal-Ring Flange Before Heating.

UNCLASSIFIED
PHOTO 33275

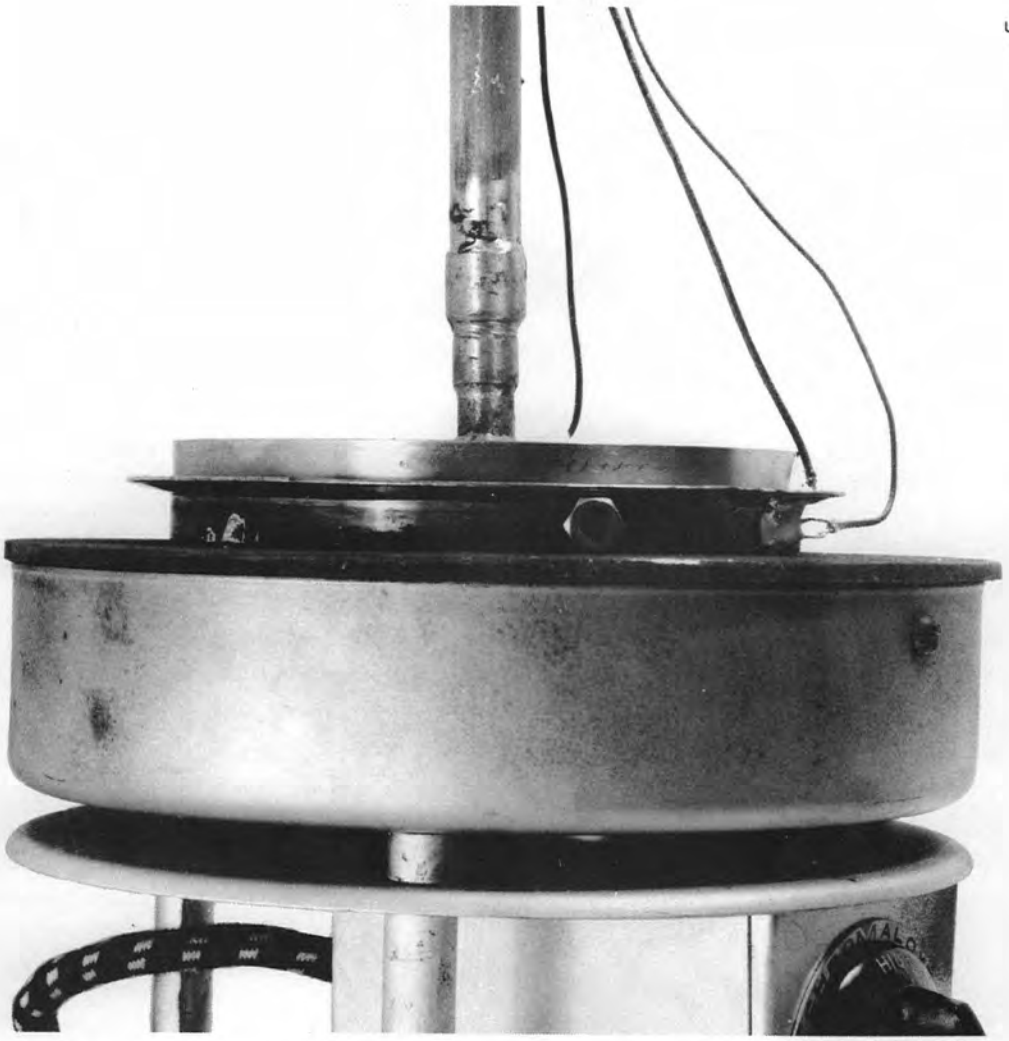

Fig. 4.2.7. Prototype Seal-Ring Flange with 325°C Thermal Gradient.

The recorded temperatures for both cases are given below:

Thermocouple Location	As Photographed (°C)	Maximum Reached (°C)
Inside center of bottom flange	580	700
Outside periphery of bottom flange	585	625
Center of top seal ring	350	285
Outside center of top flange	275	182
Inside center of top flange	260	185
Maximum gradient	325	515

The effect of repeated thermal cycling was tested by heating the bottom flange to 600°C (top flange about 270°C lower) and then rapidly cooling by placing the hot flange assembly on a cold aluminum plate. This cycle was repeated ten times before a silver-soldered joint on the pump-out stem failed. A new set of seal rings was attached to the flange and the cycling repeated ten times without detectable leakage (leak detector maximum sensitivity 1 part in 10^7). Because of the encouraging results of this test, no additional prototype testing or development work was considered necessary before going to full-scale design.

So far, no vacuum leaks have been found in the base welds which were not also detectable by a careful dye check.

Bakeable Windows

Several bakeable window designs were worked out for the PPF. The 3-in. window for the center section of the high-vacuum tank is shown in Fig. 4.2.8. This window, of No. 7056 direct-Kovar-sealing glass (Corning Glass Works), is mounted on an Inconel seal-ring flange. A quartz filter is placed in front of the window to filter out part of the arc radiation and reduce thermal shocking of the 7056 glass when the arc is first struck. The volume behind the 7056 window is pumped by a rough-vacuum system (12 μ) to provide control of vacuum letdown in case of window failure. The outer glass window is replaced with a metal plate when high-temperature bakeout is required. A high-temperature sealing compound is used to maintain the rough vacuum seal. By keeping the 7056 glass under vacuum during bakeout the pressure stresses are made negligible, and the bakeout temperatures can be increased to near the softening point of the glass. Again, there is control of vacuum letdown if failure occurs while the high-vacuum system is hot.

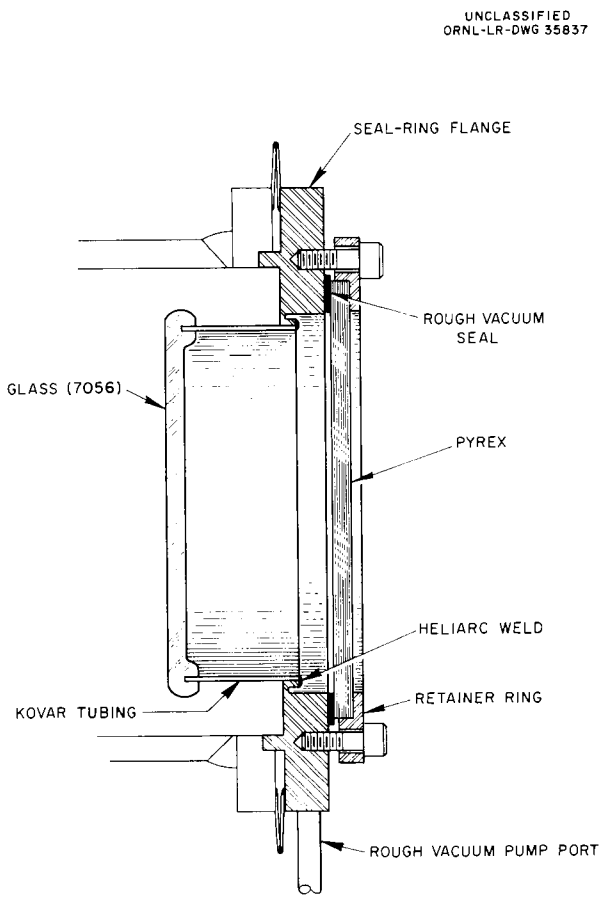

Fig. 4.2.8. Bakeable Window.

This bakeable window is made by first fabricating the Inconel seal-ring flange and then welding the Kovar in place. The Kovar is then machined to finished dimensions and the entire piece hydrogen-annealed in preparation for the glass work. Tubing of 7052 glass is spun around the periphery, and the 7056 glass plate is fused in place over the opening. By this method it is possible to make windows with very short Kovar tubulations, thus giving a large viewing angle for a given window diameter.

This type of window has also been made by fusing the 7056 glass to Kovar and then welding the Kovar to a heavy metal plate, forming a Kovar-to-metal joint similar to that shown in Fig. 4.2.8. Longer Kovar tubulations and water cooling must be provided to keep the glass seal cool during welding.

4.2.3 PPF VACUUM SYSTEM PERFORMANCE

The base pressure in the central vacuum region, after 12 hr under vacuum but without bakeout, was 6×10^{-9} mm Hg. After an 8-hr bakeout at 400°C for the tank body and 250°C for the nitrogen traps, the pressure was 2×10^{-9} mm Hg and was not limited by wall outgassing. The three ion gages on the center section agreed within 30%. This pressure was maintained for several days with no significant increase noted. The base pressure in each of the end regions, which essentially were not baked and which were sealed with neoprene O-rings, was about 2×10^{-8} mm Hg. Octoil was used in all diffusion pumps.

The combined net speed of the pump systems which evacuate the central region was found to be 1000 liters/sec. The conductance of one of the large nitrogen traps was found to be 1500 liters/sec. A 50% increase in the pumping speed could be gained by removing the refrigerated traps.

Initial bakeouts were conducted with the system trapped only by the Freon-cooled baffles. The nitrogen traps were filled while the main chamber was still hot. Because the pressure after this modest bakeout was already below that required, more elaborate baking has not been attempted.

The seal welds were found to stand up well under thermal cycling, even when substantial temperature differences were imposed across them. Such leaks as did appear were sealed[2] with DC-997 silicone varnish (Dow Corning Corp.), which did not char under baking and which could be cleaned off sufficiently well for subsequent weld patching.

In a recent experiment, after some particularly large gasket leaks were sealed with this material, the electron emissions on four Veeco ion gages were less than 10% of their original values. It is suspected that this came about as the result of the action of the varnish or its solvent (xylene) on the gage filaments. Use of the varnish as a leak sealant is now restricted to very small leaks until this adverse effect is disproved.

Arc experiments are now under way in the PPF, but no results are available.

4.2.4 TITANIUM PUMPS

C. F. Barnett

A large source of gas is present in the H_2^+ beam fed into DCX. For example, a 1-ma beam must be pumped at a rate of 2000 liters/sec if the pressure is to be maintained at 10^{-7} mm Hg. One means to provide sufficient pumping would be to allow the unused H_2^+ beam to strike a titanium plate which would vaporize and act as a titanium pump. A difficulty involved in using titanium with deuterium would be the large neutron yield from deuterium buildup in the titanium plate. A 600-kev deuterium beam was allowed to bombard plates of both titanium and tungsten at approximately 800°C. In Fig. 4.2.9 is shown the neutron counting rate as a function of time. As shown, there is a decrease in neutron yield from titanium, while the yield from tungsten increases. Chemical analysis of a plate bombarded with H_2^+ showed negligible buildup of hydrogen in the metal structure. With H_2^+ beam currents of 1 to 4 ma no noticeable pressure rises were observed after sufficient outgassing of the titanium plates; however, analysis of the data revealed that probably large amounts of titanium were getting into the plasma region of DCX. The titanium has been removed until adequate baffling can be provided between the titanium plate and the active region.

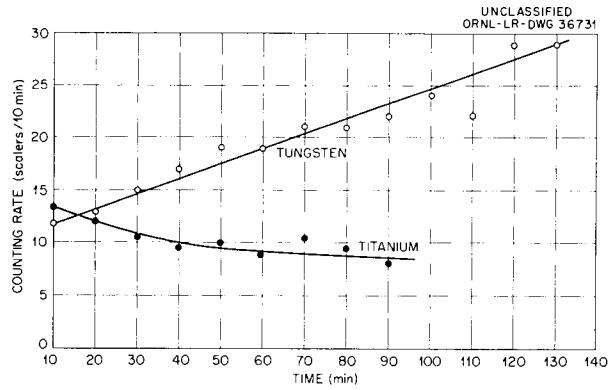

Fig. 4.2.9. Neutron Counting Rate from Tungsten and Titanium Bombarded with 600-kev D_2^+.

Acknowledgments

The authors are considerably indebted to a number of people, including R. M. Warner, who served as Project Engineer during the final construction and operating phase; G. W. Eckerd and A. Gronstrom, who performed much of the detail design and drafting work; and C. W. Wright, the group's technician. Our greatest debt, however, is to the other vacuum groups associated with Project Sherwood, whose ideas and developments have made the present equipment possible.

[2]Suggested by T. H. Batzer, UCRL, private communication, 1958.

4.3 TESTS OF OIL DIFFUSION PUMPS FOR DCX

C. E. Normand

Three models of commercial oil diffusion pumps have been tested for use with the DCX; no significant difference in their performance was noted. Attempts at a general solution of the pressure-fluctuation problem indicated that a radical change in the method of heating the pump fluid is probably needed. A Vac-Ion pump, using the combined effects of the excitation of a cold cathode discharge between titanium electrodes and the gettering action of the sputtered titanium, was found to be unsatisfactory for any but carefully selected applications.

4.3.1 DIFFUSION PUMP PERFORMANCE

Fairly complete performance characteristics have been determined for three models of diffusion pumps that are of interest in the DCX program – Consolidated Electrodynamics Corporation models MCF-1400 and DMC-144D (experimental) and Leybold model DO-4001. The principal characteristics of these pumps are summarized in Table 4.3.1. None of the pumps showed any marked advantage over the others, except perhaps for certain special applications.

Modifications for Eliminating Oil Backstreaming

Gross backstreaming of oil from MCF-1400 oil diffusion pumps was greatly reduced, with little loss in net pumping speed, by any of three simple modifications.

In order that backstreaming rates might be measured, the evacuated chamber (20 in. in diameter by 20 in. high) was so designed that oil condensing in the chamber is drained off into calibrated burets. Once the chamber surfaces are oil-covered, a constant rate of drainage, equal to the rate of backstreaming, is eventually reached, and can be measured. All backstreaming measurements were made with Octoil-S as the pump fluid and at an operating power of 2500 w.

The three modifications were all designed to limit, in one way or another, the passage of vapor into the evacuated chamber from the top cap of the uppermost jet assembly. This approach was based on evidence that much backstreaming originates in this region as a result of oil condensing inside the cap and creeping or flowing to the outside, or lip, where it evaporates rapidly due to the low pressure and high cap temperature.

The following modifications were evaluated:

Water-Cooled Cap.[1] – The top jet cap is completely covered by a single-turn copper water line. Oil evaporation from the jet cap is not prevented – actually, it is probably increased – but the chamber is completely shielded from vapor originating in this region.

Heated Top Jet Cap. – The top jet cap is run at elevated temperature by flowing heated air through a single turn of copper tubing soldered to the cap. Here the aim is to maintain the cap temperature high enough to prevent any oil condensation.

Kerr Modified Jets. – This more extensive modification was proposed and carried out by R. J. Kerr. It consisted of a complete redesign of the top jet assembly, the addition of a bell-shaped skirt around the control chimney between the first and second jets, and the addition to the top jet cap of a heat-conducting copper base resting on the pump bottom. Here again, the top cap ran at higher temperature than in the original assembly. The extent to which other phases of the modification may have affected backstreaming has not been determined.

A comparison of the original pump and the three modifications is made in Table 4.3.2.

4.3.2 UNSTEADY PRESSURE

Most oil diffusion pumps, when operated at the power required for maintaining a reasonably high limiting fore pressure, boil in an unsteady manner. This unsteady boiling gives rise to high-vacuum pressure variations which become highly objectionable as lower pressures are attained. A number of simple modifications have been made on existing pumps in an effort to smooth out their boiling action at higher power input and thereby eliminate these variations in pressure. Among the modifications that were investigated are the following:

1. inclusion of various materials in the pump boiler to facilitate smooth boiling (these

[1] B. D. Powers and D. J. Crosley, *Vacuum* 4, 415–35 (1954).

Table 4.3.1. Characteristics of Three Standard Pumps Tested for Use with the DCX

Pump Type	Barrel Diameter (in.)	Rated					Pump Fluid	Gas Pumped	Baffle	Measured					Pressure Fluctuations (Qualitative Observations)
		Operating Power (w)	Pumping Speed (liters/sec) Air	Pumping Speed (liters/sec) H_2	Limiting Fore Pressure (μ)	Ultimate Vacuum (mm)				Operating Power (w)	Pumping[a] Speed at 10^{-5} mm Hg (liters/sec)	Limiting[b] Fore Pressure (μ)	Observed Base Pressure (mm)	Oil Backstream Rate (cc/hr)	
Consolidated[c] MCF-1400	10	2900	1500	5000	150	6×10^{-7}	Octoil-S	Air	None	1335	1440	60	5.4×10^{-6}		Pressure relatively constant at low power inputs; rapid pressure fluctuations through a narrow range at high power inputs; very large pressure surges at several minutes' intervals at intermediate power
									Water-cooled[d]	1570	750	65	5.2×10^{-6}	*h*	
									Manufacturer's baffle and valve	2520	520	110	3.0×10^{-6}	*h*	
									None	2500		110	1.0×10^{-6}	5.5	
									None	1870		70	1.0×10^{-6}	2.4	
									Water-cooled cap[e]	2500	1350	110	7.0×10^{-7}	0.067	
Leybold DO-4001	$13\frac{3}{4}$	3000	4000		200	1×10^{-7}	Octoil-S	Air	None	2125	2980	55	4.0×10^{-7}		Similar to MCF-1400
									None	3050	3072	105	4.8×10^{-7}	0.054[f]	
									Manufacturer's	2125	1274	55	4.0×10^{-7}		
									Manufacturer's	3125	1360	105	4.5×10^{-7}	*h*	
								H_2	None	2125	2742	55	3.3×10^{-7}		
									None	3125	3128	105	4.0×10^{-7}		
									Manufacturer's	2125	1811	55	4.0×10^{-7}		
									Manufacturer's	3100	2035	105	4.5×10^{-7}		
Consolidated[g] DMC-144D	$7\frac{1}{4}$	1800	1200			4.7×10^{-7}	Convoil-20	Air	None	1810	920	400	5×10^{-7}	0.043	Pressure quite free of fluctuations at all powers; some slight "wandering"

[a] Speeds measured are speeds of pumping from a 20-in.-dia × 20-in.-high chamber. Measurements were by metered leak method; pressures by VG-1A ionization gage.

[b] Limiting fore pressure measured by Veeco thermocouple gage.

[c] Data for MCF-1400 were collected rather unsystematically over a long time.

[d] This is a modified circular chevron type of baffle – not quite optically opaque.

[e] The top jet cap is completely covered by a slightly oversized water-cooled shield.

[f] This is average backstreaming rate after several days' operation at various power inputs.

[g] The DMC-1440 pump tested was an experimental model from which a complete line of pumps of various sizes is to be developed by Consolidated Electrodynamics Corporation.

[h] Method used for measuring oil backstreaming rate is too insensitive for backstreaming through baffle.

Table 4.3.2. Effect of Modifications on Oil Backstreaming in an MCF-1400 Oil Diffusion Pump

Modification	Rate of Oil Backstreaming (cc/hr)	Pumping Speed, Air at 10^{-5} mm Hg (liters/sec)	Top Jet Cap Temperature (°C)
Original pump	5.5	1450	202
Water-cooled cap	0.067	1365	<202
Heated cap	0.267	1450	210
Kerr jets	0.122	1380	207

materials included carpet tacks, wire gauze, coarse steel wool, and glass wool),

2. substitution of an immersion-type heater for the external type,
3. installation of a set of heavy aluminum rings in the boiler to provide heat transfer from the boiler bottom to above the fluid surface,
4. insulation of the boiler against heat loss.

None of these schemes were more than mildly effective in reducing pressure variations. It appears now that solution of the problem will probably require a radical change in the method of heating the pump fluid.

4.3.3 TESTS OF VAC-ION PUMP

Tests have been made of the operating characteristics of a Va-1415 (6-in.) Vac-Ion pump by Varian Associates. This pump makes use of the combined effects of excitation in a cold cathode discharge between titanium electrodes and of the gettering action of titanium freshly sputtered by the discharge.

For testing, the Vac-Ion pump was attached to an unbaked stainless steel system of 180-liter volume. A small (65 liters/sec) oil diffusion pumping system was used for evacuating the system to about 1 μ pressure. At this point the diffusion pump was valved off, and evacuation was continued by the Vac-Ion pump alone.

In many of its operating characteristics the Vac-Ion pump differs so markedly from oil diffusion pumps as to make comparisons difficult. For example, not only does pumping speed vary with the pressure at which gas is being pumped, but following any change in pressure a considerable time (perhaps 1 hr) is required for the pump to attain a speed characteristic of the new pressure. During this time the speed may drop to as low as half its final value.

Maximum throughput – a measure of the pump's gas handling capacity – is not clearly definable for the Vac-Ion pump. Maximum throughput does appear to be quite low, however, probably about 10 micron-liters/sec as compared with 500 micron-liters/sec for the MCF-700. The Vac-Ion pump's usefulness is, therefore, limited to applications requiring little gas handling capacity.

The lowest pressure attained by the Vac-Ion pump in the test system at room temperature was approximately 3×10^{-7} mm; with liquid nitrogen in the trap the pressure was reduced to 2×10^{-7} mm.

The pumping speeds for air and for hydrogen were determined over the 10^{-6} to 10^{-4} mm Hg pressure range. Typical average values are given in Table 4.3.3.

The pumping speed for helium could be determined only for very small leak rates – about 1 micron-liter/sec or less. Over this narrow range

Table 4.3.3. Vac-Ion Pumping Speeds for Air and Hydrogen

Pressure (mm Hg)	Pumping Speed (liters/sec)	
	Air	Hydrogen
2×10^{-6}	222	350
5×10^{-6}	207	300
1×10^{-5}	197	265
5×10^{-5}	173	185
8×10^{-5}	166	163

of pressure the pumping speed was about 31 liters/sec. Helium leak rates greater than about 1 micron-liter/sec appear to exceed the gas handling capacity of the pump.

All attempts to measure pumping speed for argon failed because of very low pumping speed and handling capacity for this gas. The lowest leak rates that could be reasonably measured caused the pressure to rise continuously to above the range of the ionization gage.

In its pumping speed for air and hydrogen and in its ultimate pressure, the Vac-Ion pump is about equivalent to a well-baffled oil diffusion pump of comparable size. In gas handling capacity it appears much inferior. The operating power ranges from about 16 w at 2×10^{-6} mm Hg to 525 w at 6×10^{-5} mm and is thus much less, on the average, than for a 6-in. oil diffusion pump – 600 to 1000 w.

Because of its low gas handling capacity, slow adjustment to changing pressure, and very poor pumping of inert gases, this pump appears satisfactory for limited applications only.

Part II

SUPPORTING BASIC AND APPLIED RESEARCH

5. EXPLORATORY PHYSICS

J. S. Luce

The Exploratory Physics Group was established in November 1958 and was assigned as its primary objectives research on the specific problems of DCX-2, the first large-scale machine to be built at ORNL, and research of a general exploratory nature in the broad domain of carbon arcs, molecular ion beam breakup, and high-voltage ion and neutral sources. At present this research is being carried on in a track formerly used in the electromagnetic separation process and in the DCX-EP, one of the carbon arc units demonstrated at Geneva. Additional equipment to be used in the future includes the other Geneva machine and a 50-ft-long solenoid for studies of a long carbon arc.

5.1 ARC DEVELOPMENT

The observed higher ion energy of longer carbon arcs has prompted the construction of a 50-ft-long assembly (to be built in two 25-ft sections) in which a long carbon arc will be studied under vacuum in the magnetic field of the single-layer conductor wound on the outside of the tubular sections. The assembly will also be used in the examination of high-density plasmas, PIG-type discharges (see Sec 3.1.1), deuterium arcs, and and D_2^+ breakup.

In an attempt to overcome the inherently low voltage limitation on the ORNL-developed grid ion sources, which have produced steady-state D_2^+ currents of 2.5 amp, steady-state D^+ currents of 5 amp, and pulsed D^+ currents up to 20 amp, a multistage grid source is being designed which should produce a 600-kev beam. A multistage source which would operate in the containing field of the DCX-EP (rather than in the present injection system) is under design study.

5.1.1 LONG CARBON ARC

The idea for construction of a 50-ft arc was based on ORNL spectrographic data which indicated that the energy of the ions in the carbon arc increases as the length of the arc is increased (parallel to the applied magnetic field). Ten- to twenty-electron-volt ions were observed in a 10-in. carbon arc, while ions up to 100 ev were observed in a 6-ft arc. The ions in a 50-ft arc may exceed 400 ev if the energy absorbed by the ions does not saturate at some critical length. In view of this possibility, the arc equipment will be built in two 25-ft lengths. The required magnetic field will be provided by a single-layer conductor, wound on the outside of tubular sections connected in tandem (Fig. 5.1.1). High vacuum will be maintained by means of pumpout nozzles built into

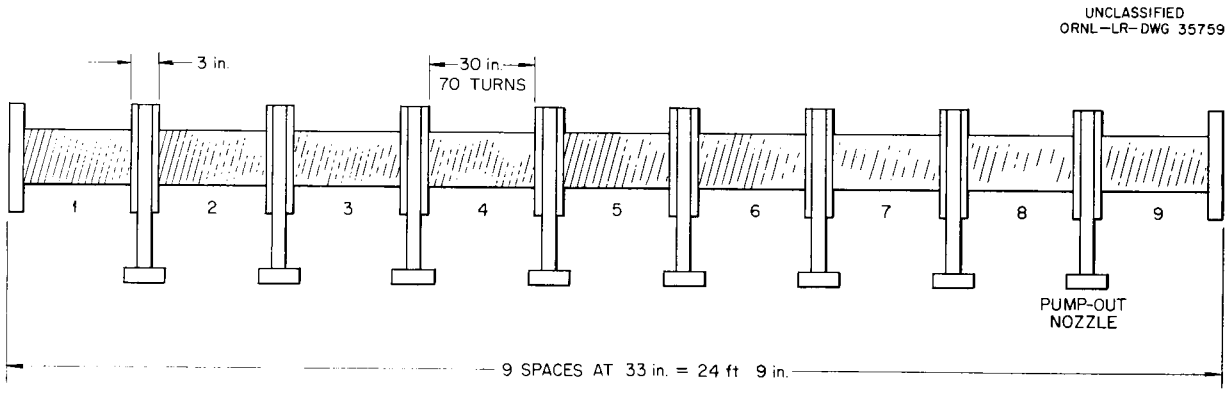

Fig. 5.1.1. Long Arc Assembly for DCX.

the sections at the joints for connections to the vacuum system. The second section will be built only if data from the first section justify the expenditure. Since the carbon arc is a high-density (10^{14} ions/cm^3), high-temperature (up to 100 ev in a 6-ft arc), two-body plasma (complete ionization – no neutrals), its study may be quite important in the study of phenomena in thermonuclear plasmas. In addition, since a long arc may have ions that are of higher energy and also more highly stripped than those in short arcs, use of the long arc in breakup studies offers interesting possibilities.

The assembly will also be used in the study of deuterium arcs and PIG-discharge arcs.

5.1.2 DISSOCIATION OF D_2^+ BY CARBON AND MOLECULAR DEUTERIUM ARCS

In addition to these carbon arc studies, work has begun on experiments aimed at determining the factors that control the ionization and dissociation of molecular deuterium ions that are passed through the arc. Some new results have been obtained that need more study before publication. However, it is interesting to note that quite efficient dissociation occurs in regions of the arc that cannot be seen with the human eye.

Heretofore, the use of D_2 arcs as breakup centers for high-energy D_2^+ beams has been handicapped by impurities and lack of differential pumping. In the DCX-EP it appears possible to overcome these disadvantages, and comprehensive data should be obtained.

5.1.3 ARC COMPRESSION

Arc compression studies will fall into two categories: one involves the compression of an energetic deuterium arc, and the other involves the compression of high-energy trapped ions. A bank of condensers has been assembled, and engineering studies of the coils and associated triggering circuits are in progress.

5.2 MULTISTAGE GRID ION SOURCES

The injection of 600-kev ions into a containing magnetic volume represents a formidable problem when currents in the ampere range are desired. Nevertheless, a number of interesting possibilities exist. At ORNL, two methods are being pursued: one, under development by another group and described elsewhere (Sec 3.1.2), utilizes a modified Von Ardenne ion source and a high-gradient accelerating tube; the other, under design study by this group, is a multistage grid ion source which would utilize the containing field of the DCX-EP for its operation. While plans are also under way to place this source outside the DCX-EP and bring the beam in through a magnetic channel, the simplicity of operating the source in the magnetic field of the DCX-EP makes this method more appealing. However, when a source is placed in the operating volume, serious problems arise from the neutrals which enter the volume from the source. The use of proper baffles and of differential pumping enhances the possibility of using internal sources.

Grid ion sources of the type developed at ORNL (such as the Geneva Exhibit ion source) are capable of producing very large currents of positive ions. Steady-state currents of 2.5 amp of D_2^+ and 5 amp of D^+ and pulsed currents of D^+ up to 20 amp have been produced by these sources. A major difficulty is that the sources are inherently low-voltage devices. The optical system, which is a series of grid structures, produces its optimum focus in the range of 15 to 30 kev. Higher voltage can be used in these units only with a sacrifice in current. To overcome this difficulty, a multistage source which will have a final acceleration of 600 kev is being designed.

6. SPUTTERING

6.1 SPUTTERING EFFECT OF SOME ENERGETIC IONS ON VARIOUS METALS

O. C. Yonts

Among the impurities that cool a hot plasma are the atoms "sputtered" from the container walls by energetic ions. The DCX provides a steady supply of such ions, and since the proposed higher-amperage injected beams will probably increase this supply, a study of the sputtering effect of certain ions upon various metals has been undertaken.

Typical sputtering ratios (numbers of atoms sputtered per incident ion) for unannealed copper bombarded by argon were 6.6 at 6 kev, 7.87 at 10 kev, 9.4 at 20 kev, 8.84 at 30 kev, and 8.90 at 40 kev. Helium-annealed copper gave ratios in the same range: 8.66 at 20 kev and 9.20 at 40 kev.

Some unchecked data for sputtering of copper by helium and deuterium showed ratios of 0.2 and lower for ion energies from 10 to 42 kev. Aluminum showed no weight loss when bombarded for 1100 ma-hr by helium at 30 kev and gave a sputtering ratio of 2.38 when bombarded by 30-kev argon. Ratios for tantalum and molybdenum were slightly higher: 2.7 and 3.1.

A calorimeter for measurement of the energy of the sputtered particles has been built and tested.

This work represents a continuation of that reported earlier,[1] and descriptions of the Beta calutrons and other equipment are repeated here so that they may be related to the figures, which were not shown in the first report.

Experimental Equipment and Procedure

Figure 6.1.1 shows the cutaway drawing of the Stable Isotope Group's two Beta calutrons.[1] The two vacuum tanks are between the poles of the large electromagnet. The ion source is at the bottom of the tank and the receiver at the top. The magnetic field is variable from about 500 to 8000 gauss, and ion accelerating voltages from 10 to 45 kev are available.

For our work with argon, it was only necessary to replace the usual isotope receiver "pocket" with a water-cooled target. This unit is shown in Fig. 6.1.2. The target holder is 6 in. behind the slit of the receiver, which is shown at the top of the photograph, and is placed normal to the ion beam. Angular spread of the beam was about 5° and was limited by a baffle in the 90° position. The seal is an O-ring carefully fitted to the rectangular groove. Water flow is normally several gallons per minute, but can be varied for calorimetric measurement of the energy received by the target.

Figure 6.1.3 shows the 7½-in. ion orbit radius unit used with D^+ at energies above 20 kev and with He^+ at all energies. The source is identical to the argon source except that it has been inverted to allow a closer spacing of target and source. The discoloration on the upper half of the unit is due to energetic neutrals from charge-exchanged ions.

For measurements at energies lower than 20 kev with D^+, it was necessary to construct still a third unit operating on a 2½-in. ion orbit radius. This unit, shown in Fig. 6.1.4, has the ion source facing downward and so arranged that the ion beam focuses at the 90° position. A baffle at this position intersects all but the desired ion beam (D^+). The beam passes through a ¼-in. slit and strikes the target which is placed in the 180° position. The beam is not focused at the target and is about ½ in. wide. The can, shown partially enclosing the target, was part of a current-measuring experiment and was not used while sputtering measurements were being made.

The experimental procedure used in all cases consisted in cleaning, drying, and weighing the copper targets both before and after exposure to the ion beam. Ion current was held at constant value, as read by a ½% d-c milliammeter, and readings were recorded at frequent intervals. Exposure of the target to the ion beam was carefully timed and was accurate to within a few seconds. For copper, sputtering ratios (atoms out/ions in) can then be calculated from

$$R = 0.422 \frac{W}{I\,t} ,$$

[1] O. C. Yonts, *The ORNL Thermonuclear Program*, ORNL-2457, p 138 (Jan. 15, 1958).

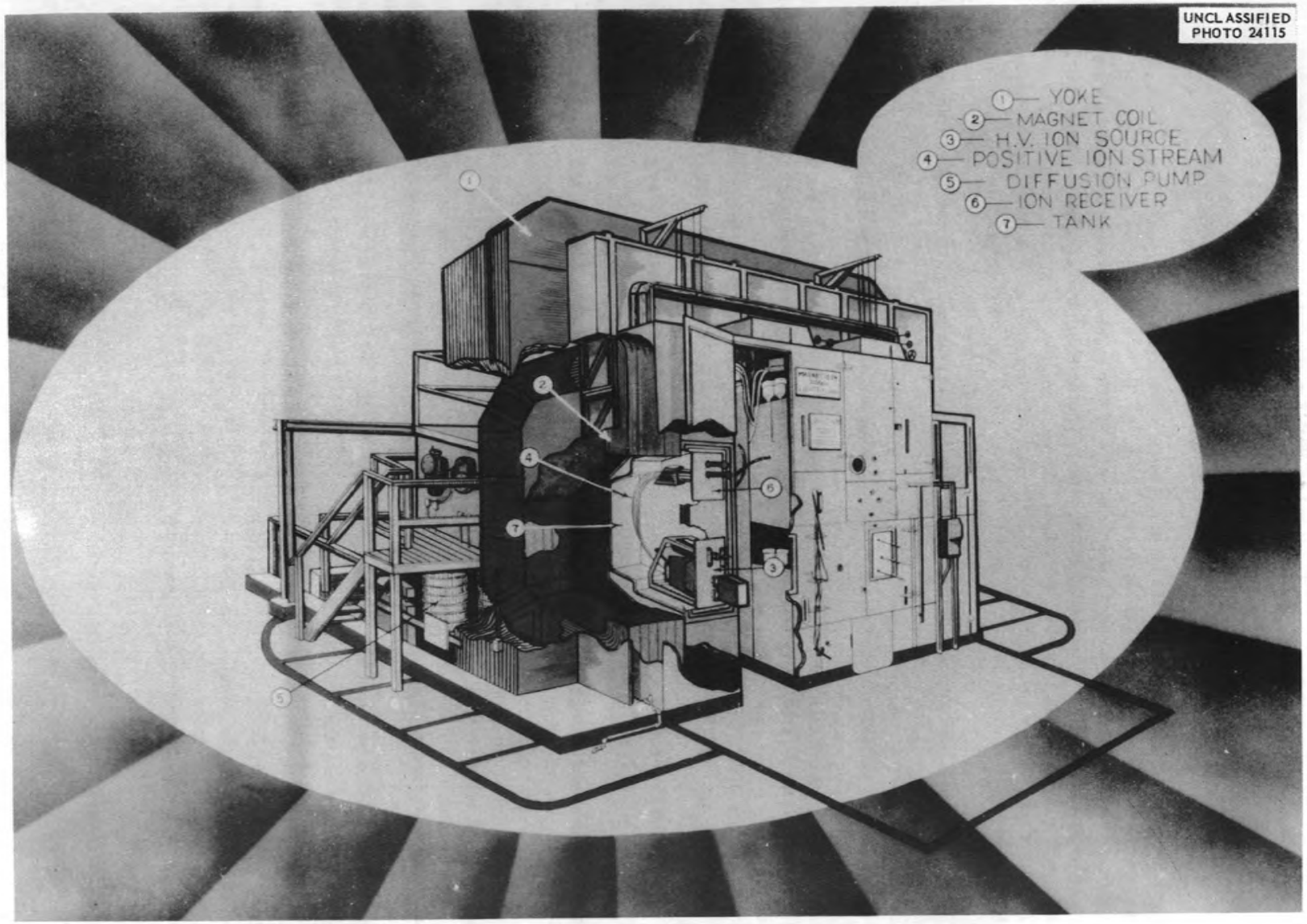

Fig. 6.1.1. Cutaway View of Beta Calutron Used for Studies of Sputtering.

UNCLASSIFIED
PHOTO 27079

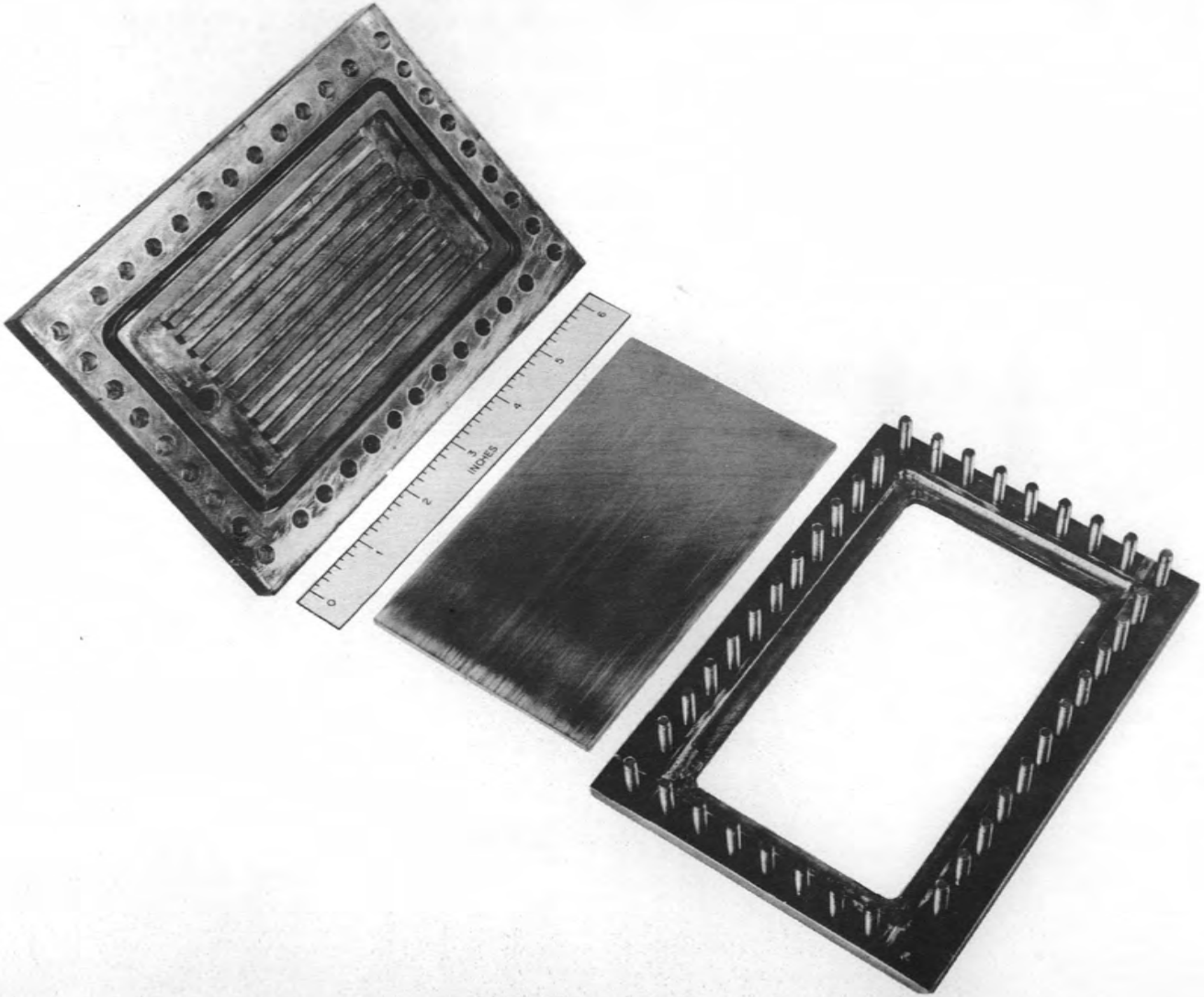

Fig. 6.1.2. Water-Cooled Target for Beta Calutron.

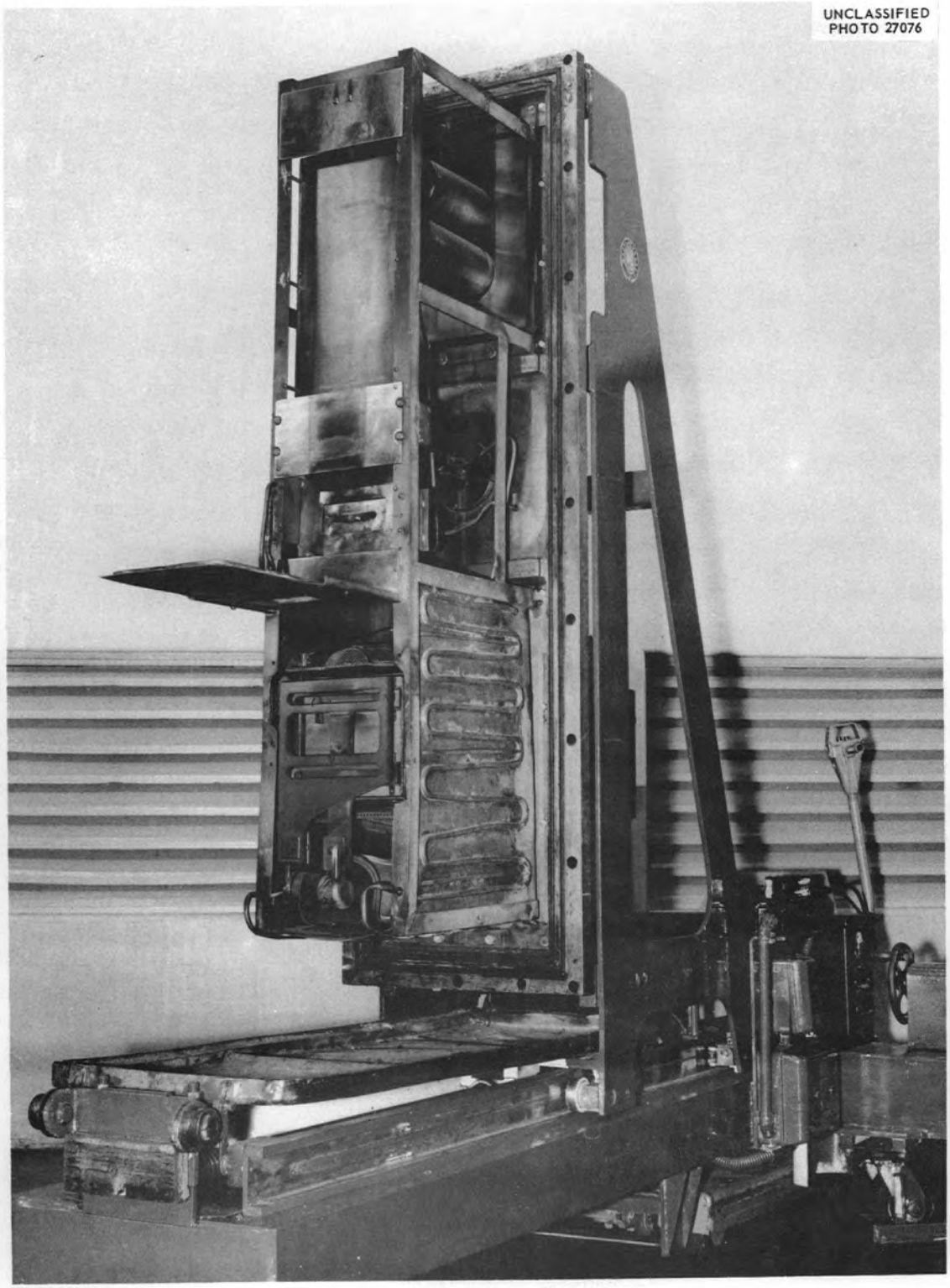

Fig. 6.1.3. Special Calutron for Studies of Sputtering by Light Ions. Ion-orbit radius $7\frac{1}{2}$ in.

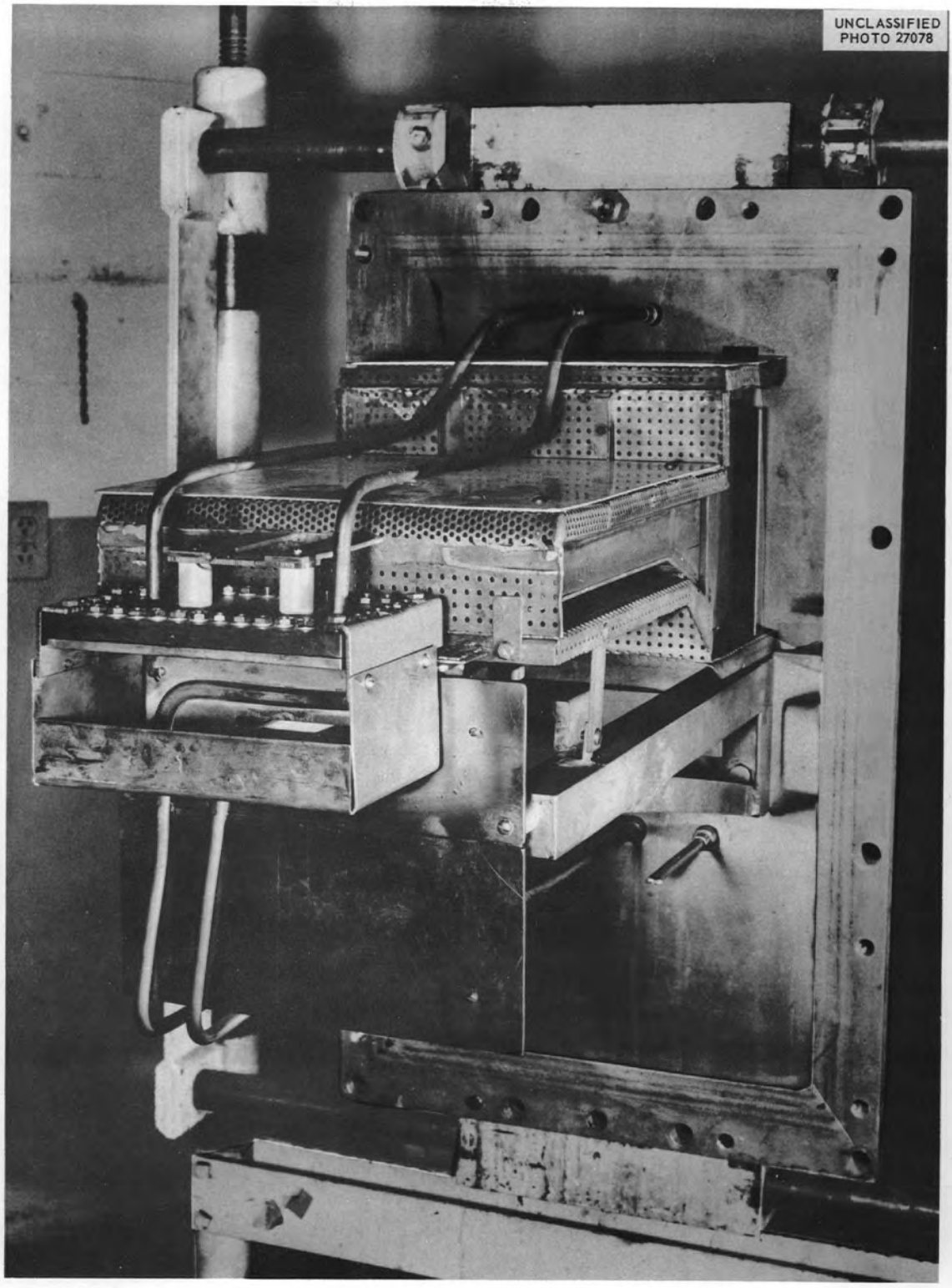

Fig. 6.1.4. Special Sputtering Unit for Deuterium at Energy Lower than 20 kev. Ion-orbit radius $2\frac{1}{2}$ in. The can shown was not used for sputtering measurements.

where

W = weight loss, in mg,
I = ion current, in ma,
t = time, in hr.

Figure 6.1.5 shows our original copper data with a few extra points at 25 kev and around 10 kev which were obtained at a later date. The targets were unannealed. The results show a large scatter of points. As a check on the scatter, a series of determinations were made at 30 kev and the results of this series of measurements are tabulated below:

Sputtering Ratio	Total Argon Current (ma-hr)
8.41	25
8.60	183
8.71	100
8.72	50
8.86	100
9.08	100
9.17	50
9.17	25

The mean value of the eight determinations is 8.84 with a probable error of ±0.06. The probable error of a single determination is ±0.2.

A new series of determinations were made with helium-annealed copper targets. The results are shown in Fig. 6.1.6 and tabulated in Table 6.1.1.

The results of sputtering of copper by helium and deuterium are given below:

Ion Energy (kev)	Sputtering Ratio
He^+	
15.0	0.212
19.5	0.161
23.0	0.210
30.0	0.126
39.0	0.086
D^+	
10.0	0.0501
11.0	0.046
20.0	0.032
30.5	0.035
30.0	0.029
42.0	0.022

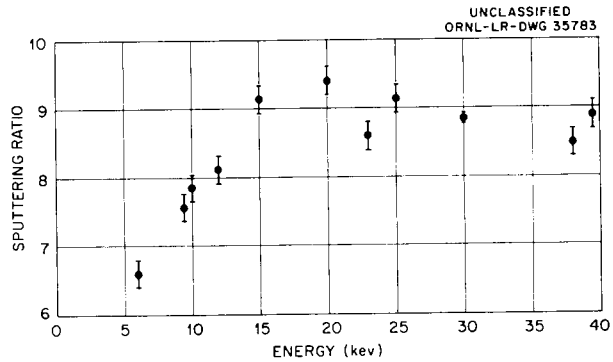

Fig. 6.1.5. Sputtering of Unannealed Copper by Argon Ions.

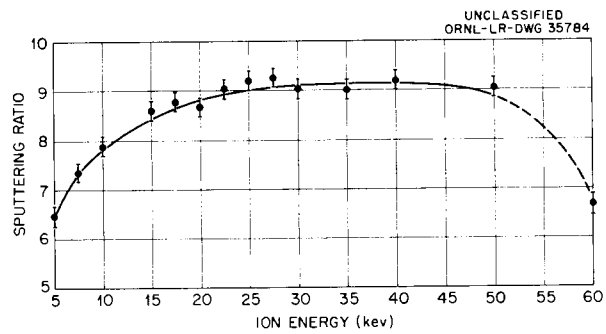

Fig. 6.1.6. Sputtering of Annealed Copper by Argon Ions.

These values were obtained during the early work[1] and have not been checked or duplicated.

More recently, attempts have been made to sputter aluminum with helium. There is no detectable weight loss after a bombardment of 1100 ma-hr at 30 kev. Bombardment of aluminum with argon ions at 30 kev gives a sputtering ratio of 2.38, compared with 8.84 for copper. An upper limit, of sorts, for the amount of sputtering of aluminum by helium can be arrived at by assuming that the weight loss was equal to the amount of helium hitting the target and that all the helium remained in the target, thus making the weight loss zero. The amount of helium hitting the target was about 165 mg, which would give a sputtering ratio of 0.148. The appearance of the target suggests that the sputtering ratio is very much less than this.

Table 6.1.1. Sputtering of Copper by Argon Ions

Energy (kev)	Sputtering Ratio	
	Unannealed Targets	Annealed Targets
5.0		6.48
6.0	6.6	
7.5		7.32
9.5	7.86	
10.0	7.87[a]	7.88[a]
12.0	8.12	
15.0	9.13	8.60
17.5		8.78
20.0	9.4	8.66[b]
22.5		9.07
23.0	8.6	
25.0	9.12[a]	9.20
27.5		9.25
30.0	8.84[c]	9.02[b]
35.0		9.01[a]
38.8	8.50	
40.0	8.90	9.20[a]
50.0		9.05
60.0		6.67[b]

[a]Mean of 2 determinations.
[b]Mean of 3 determinations.
[c]Mean of 8 determinations.

The sputtering ratios of some other materials bombarded with argon at 30 kev are given below:

Target	Sputtering Ratio
Ta	2.7
Mo	3.31
Cu	8.84*
Al	2.38**

*Mean of 8 determinations.
**Mean of 2 determinations.

New Equipment

New equipment has been built and is now being tested for sputtering aluminum with helium and deuterium. This equipment will also be used to sputter titanium.

A calorimeter has been built and tested to measure the energy of the sputtered particles. Some preliminary values have been obtained but will not be published at this time. A neutral beam of approximately $1-5 \times 10^{16}$ particles/sec enters the calorimeter after passing through the collimator.

A moving target receiver has been built and will be used to reduce the total bombardment per square centimeter of target by about an order of magnitude.

Equipment designed to sputter insulators is being built and will be tested soon.

7. AUXILIARY EQUIPMENT AND SERVICE

7.1 METALLURGY

R. E. Clausing J. W. Tackett
J. D. Hudson

In a study of flange and valve seals for use in the Sherwood Project a literature survey indicated that flat washer-shaped gaskets made of oxygen-free high-conductivity (OFHC) copper, aluminum, or gold are suitable for large flanges, and that indium O-rings have been used successfully in some systems. Simple copper O-rings are unsatisfactory in bakeable systems. The need for gasket replacement (and, in some cases, surface refinishing) when remaking seals probably precludes the use of metal gaskets in valves.

The wettability of some base materials by an In-Ga-Sn eutectic alloy considered for use in a liquid-metal seal was tested at temperatures up to 450°C. The use of such seals is not recommended at this time.

Demountable joints or valves which would be closed and opened by the solidification and melting, respectively, of a filler metal were considered, and preliminary tests indicated that this type of seal would be useful in ultrahigh-vacuum systems provided that the seal could be opened in the vertical position and further provided that a compatible filler-metal and base-material combination can be found which would also satisfy the special requirements of thermonuclear experiments. The literature indicates that the alloy In-Ag-Cu might be usable, and it is under investigation.

A vacuum furnace with a hot zone 16 in. in diameter and 20 in. in height has been constructed for studies of vacuum degassing, brazing, and processing of experimental equipment.

Failure of the copper tubing used for heating and cooling the DCX liner with steam (400°C) and water (20°C) was shown by examination to be accompanied by intergranular defects. Tests at 500°C for 200 hr with no steam showed no failure of the tubing.

7.1.1. VALVE-FLANGE DEVELOPMENT

In the development of thermonuclear devices valves and demountable flanges are required which remain leaktight during high-temperature bakeouts. Members of the Welding and Brazing Laboratory of the Metallurgy Division are investigating the following valves and flanges:

1. flanges using metal gasket materials such as OFHC copper, 2S aluminum, gold, indium, etc., as the seal material,
2. joints using a room-temperature liquid metal as the seal material,
3. valves and flanges which are opened by melting of and sealed by solidification of a low-melting, brazing, filler metal,
4. demountable welded flanges, developed independently by several laboratories, suitable for use in many ultrahigh-vacuum applications.

Since the flanges mentioned in 4 above have been suitably developed and since the system that was developed at ORNL is described in Sec 4.2.2, they are mentioned here only to complete the list of devices considered. It should be realized that they are not suitable when valves or flanges must be opened and closed quickly or frequently; however, they have definite advantages for many applications.

Experimental Equipment and Procedures. – The apparatus used in testing valve prototypes consists of a cylindrically shaped container (8 in. ID × 11 in. high) as illustrated in Fig. 7.1.1, which shows a valve test assembly. By interchanging the flange components of the upper and lower vacuum-pumping systems, the valve assembly may be operated in either a vertical or horizontal position. Vacuum pressures in the 10^{-6} mm Hg range are readily obtained and are easily maintained with the two VMF-260 diffusion pumps and water-cooled traps.

In the initial valve test design (illustrated in Figs. 7.1.1 and 7.1.2) a sump or pool of filler metal was utilized to increase its ratio of mass to contact area and to minimize inherent changes in its brazing characteristics by base-metal dilution. This is not a true brazing process because flow is not a prerequisite of making the

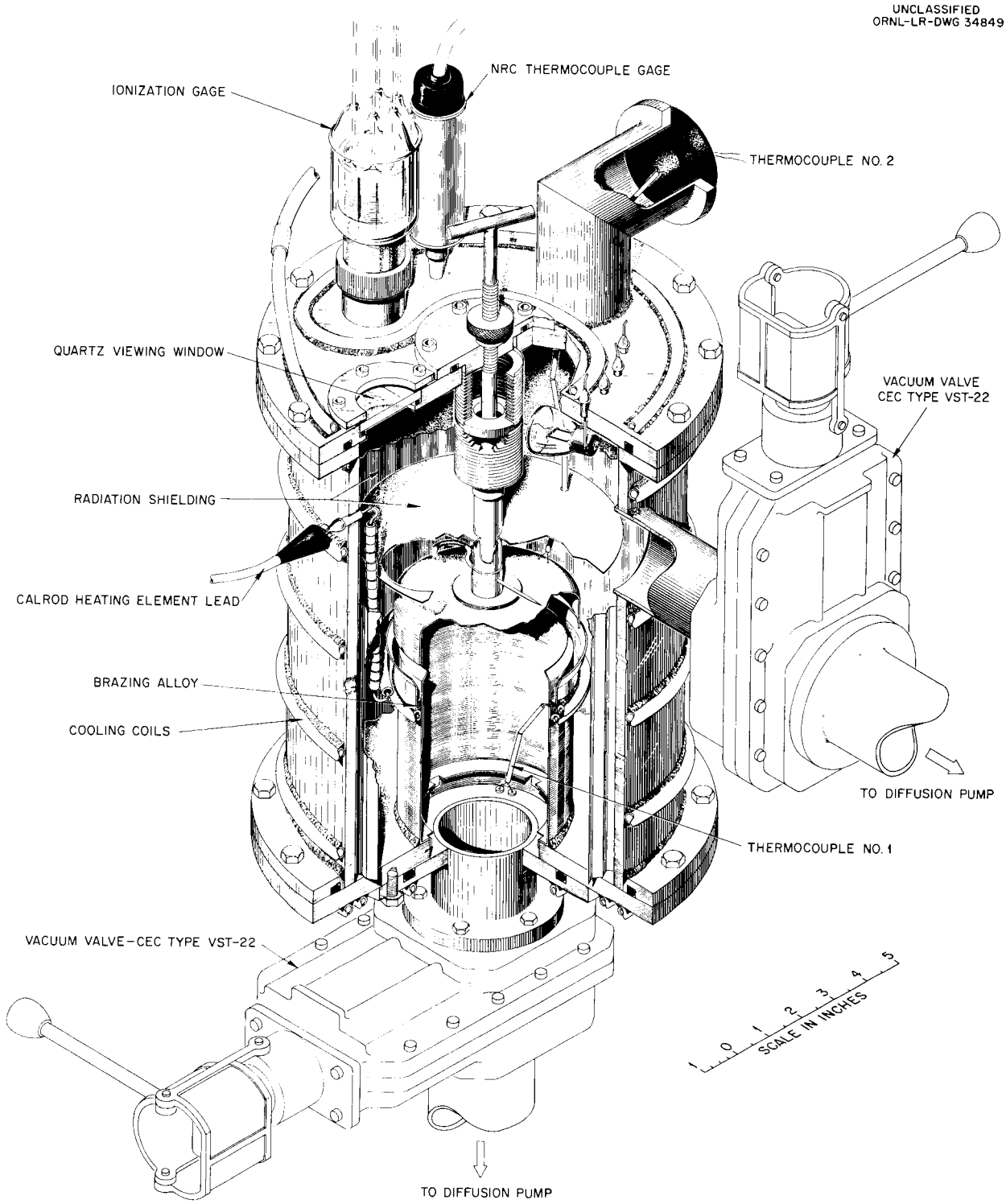

Fig. 7.1.1. Dry Box Showing Valve Test Assembly.

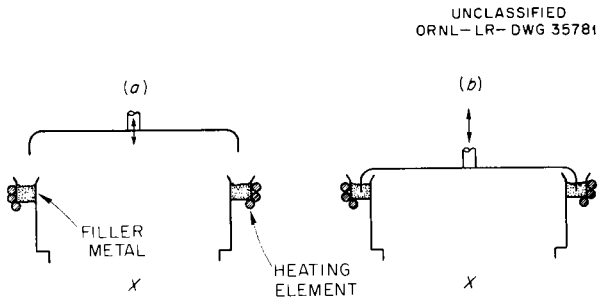

Fig. 7.1.2. Valve Assembly Testing System.

sealed joint. During the initial cycle of the test series the lower portion of the valve assembly (in the open position as illustrated in Fig. 7.1.2*a*) was heated to a temperature just above the melting point of the filler metal (750°C in the case of Ag-Cu-Sn RTSN silver solder). Then the upper portion was lowered into place as shown in Fig. 7.1.2*b*, and the assembly allowed to cool. As the filler metal solidified, the valve was effectively sealed. Helium was bled in through orifice *x*, and the leak rate determined by monitoring the upper portion of the test chamber with a Veeco mass spectrometer leak detector. Subsequent cycles consisted of heating the valve assembly in the closed position to 750°C, opening the valve momentarily (~ 10 sec), closing it again, and then allowing it to cool. For the first ten cycles, the leak rate was checked after each cycle; thereafter it was checked after every five cycles. A bypass valving system was utilized to maintain equal pressures on both sides of the valve while it was being opened and closed. The test was terminated on the completion of 30 consecutive successful closures.

Metal Gaskets

Flanges. – A literature review indicated that numerous flanging methods which involve the use of metal-gasket seals have been developed; many such seals are commercially available. While only a few of the more basic methods are described and discussed in this report, a more complete description is available.[1] The simple copper O-ring seals have not been completely satisfactory because (1) leakage occurs during cooling from the bakeout temperature (a result of differential expansion and additional plastic deformation of the O-ring during the heating cycle), and (2) resealing of the system after it has been opened requires that all flange surfaces be reground and polished to remove a distilled oxide deposit from the previous bakeout. However, many acceptable methods have been developed that utilize a flat washer-shaped metal gasket. Tests[2] indicated that washer-shaped OFHC copper gaskets are suitable for large flange requirements. The largest flanges reported use washers 14 in. in diameter. Special modifications of the flat washer show promise for use in even larger sizes. A diagrammatic sketch of several of the more promising designs is shown in Fig. 7.1.3. Uses similar to those described for copper

[1] J. W. Tackett, *Valve-Flange Development Progress Report*, ORNL CF-59-2-3 (to be published).

[2] N. Milleron, *Some Component Designs Permitting Ultrahigh Vacuum with Large Oil Diffusion Pumps*, UCRL-5259, p 8–10 (Dec. 3, 1958).

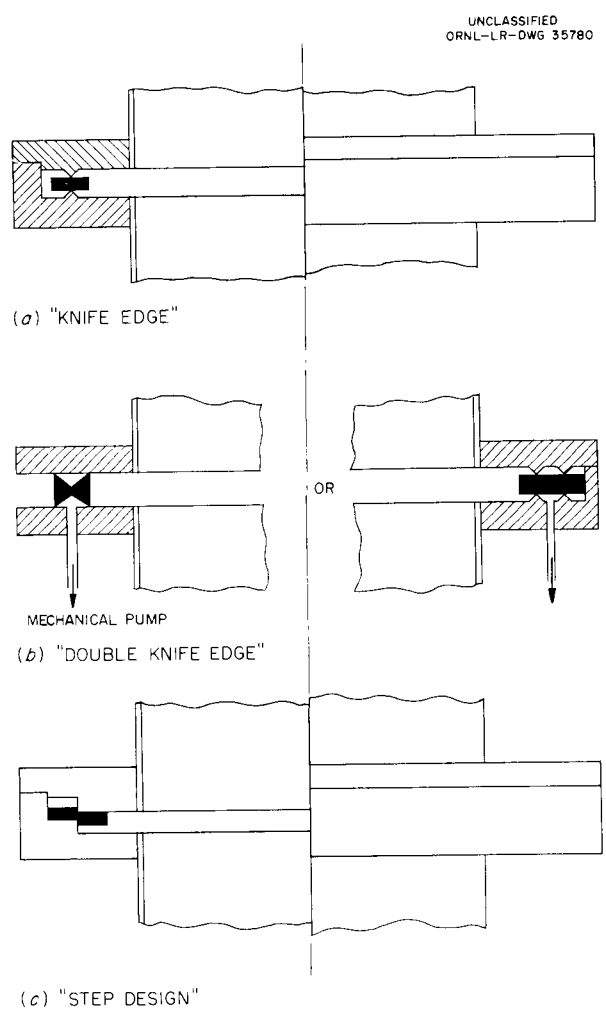

Fig. 7.1.3. Cross-Section View of Oxygen-Free, High-Conductivity (OFHC) Copper Gaskets.

gaskets have also been reported for aluminum and gold. No real comparison was found reported in the literature between copper and the other gasket materials. Since the metal gaskets can be produced easily and cheaply, no attempt is made to re-use them.

Metal O-ring gaskets of indium up to 13 in. ID (up to 9 in. when atmospheric pressure alone is used to deform the metal) have been used successfully in metal-to-metal, glass-to-glass, and metal-to-glass systems. A minimum load requirement of 5.9 kg/cm for $\frac{1}{16}$-in.-dia indium wire has been tentatively set as the load necessary to produce a leak-tight seal. Indium has a very low vapor pressure and has an unusual property of adhering tenaciously to surfaces against which it is pressed.

Valves. – Since the metal-gasket seals cannot be remade without the gasket being changed and since in some instances special preparation of the surfaces is also required, their use in valves cannot be as readily envisioned as their use in flanges. It is further concluded that only experience in particular vacuum systems will give a true indication of the utility of metal-gasket seals.

Joints Using Room-Temperature Liquid-Metal Seals

According to theoretical calculations made by Milleron,[3] the surface tension of room-temperature liquid metal (In-Ga-Sn eutectic alloy) is sufficiently high to make a vacuum seal provided that the mating surfaces of the joint are kept completely wet and the joint clearance does not exceed 0.005 in. While some success with such seals has been reported,[3] liquid-metal alloys have the following undesirable properties:

1. Many common materials are seriously attacked at elevated temperatures (regardless of atmosphere) and some are taken into solution at room temperature.

2. Reaction with air is slow at low temperatures and rapid at elevated temperatures. The formation of a surface oxide slag on air exposure markedly influences the rate of reaction between the liquid metal and base metal and tends to aid in wetting subsurfaces with which there is no apparent reaction.

3. While the liquid metal In-Ga-Sn wets the surface of some materials readily, more often it is desirable, if not necessary, to wet the surface mechanically with an ultrasonic vibrating gun. Fire-polished surfaces are also a common requirement for ceramic base materials.

To help establish the wetting and compatibility characteristics of the liquid metal with various base materials, a series of evaluation tests were initiated by the Metallurgy Group. The first two in a series of three 1000-hr tests are complete and the third is under way. Visual observations are summarized in Table 7.1.1.

During the tests, vacuum pressures were maintained in the 10^{-6} mm Hg range. Because the furnace tube was baked out at 450°C for 72 hr before the initial test run, it was possible to obtain the 10^{-6} mm pressure within 3 hr after the maximum furnace temperature was attained. Visual observations were made at 10- to 25-hr intervals for the first 100 hr of each test run, with subsequent observations being made at 100-hr intervals. After each run the samples were removed from the test chamber, examined more closely, and catalogued for metallographic examination and future reference. The following additional observations were made:

1. The multipinpoint dewetting that was observed on both Al_2O_3 and tungsten during the 200 and 300°C runs did not increase noticeably in number and size of points after it was first noticed.

2. The surface phenomenon observed first appeared to be a dross reaction on the surface of the liquid metal. However, after the specimens on which this reaction occurred were removed from the test chamber and examined more closely, the surface layer was found to have the consistency of soft lead. This would seem to indicate that the thin layer of liquid metal (5 to 10 mils thick) had alloyed with the base metal. In most cases the surface reaction phenomenon was not accompanied by dewetting.

In conclusion, it is believed that a flange or valve which utilizes the liquid-metal seal is not practical for high-temperature use at this time. A more complete account of this investigation is given in another report.[1]

---

[3]N. Milleron, *Utilization of the Surface Tension of Liquid Metals in Making High-Vacuum Seals*, UCRL-4938 (Aug. 30, 1957).

Table 7.1.1. Observed Effects of In-Ga-Sn Eutectic Alloy (Liquid at Room Temperature) on Various Base Materials at Elevated Temperature

Base Material	Effects Observed		
	At 200° C[a]	At 300° C	At 450° C[b]
Fe	Surface reaction in <100 hr	c	Surface reaction in <25 hr
Cu	Surface reaction in <100 hr	c	c
Zr	Surface reaction in <400 hr	c	c
Quartz	Some dewetting in <500 hr	Areas dewet in <100 hr	Completely dewet in <25 hr
Al_2O_3	Pinpoint dewetting in 600 hr	Pinpoint dewetting in <300 hr	Areas dewet and possible surface reaction in <25 hr
Type 304 SS	Apparent surface reaction in 600 hr	Surface reaction in <500 hr	Surface reaction in <25 hr
W	Pinpoint dewetting in 600 hr	Pinpoint dewetting in <400 hr	Completely dewet in <25 hr
Ni	Satisfactory at 600 hr	Surface reaction in <70 hr	c
Ti	Satisfactory at 600 hr	Surface reaction in <500 hr	Surface reaction in <25 hr
Graphite	Satisfactory at 600 hr	Satisfactory at 1000 hr	Completely dewet in <200 hr
Mo	Satisfactory at 600 hr	Satisfactory at 1000 hr	Surface reaction in <25 hr
Ta	Satisfactory at 600 hr	Some dewetting in <800 hr	Areas dewet in <100 hr; apparent surface reaction in >200 hr
Nb	Satisfactory at 600 hr	Satisfactory after 1000 hr	Satisfactory after 200 hr

[a]200° C test was discontinued after 600 hr (power failure).
[b]450° C test run in progress at the time of this report (200 hr complete).
[c]Not run.

Solidified Metal Seals

The basic purpose of this investigation was to determine the feasibility of making a demountable joint or valve which would be opened by melting and be resealed by solidification of a low-melting filler metal. After a preliminary investigation of the mechanisms of brazing processes which tend to limit the utility of this type of joint, it was possible to incorporate in the original valve-flange testing apparatus provisions for a vacuum atmosphere, an inert cover gas, etc.

This series of tests was conducted only to evaluate the valve design, and the base-metal, filler-metal combination (nickel and RTSN, respectively) was used for illustrative purposes and not because its use is applicable in thermonuclear devices. On the contrary, nickel is highly magnetic and the vapor pressure of liquid RTSN is too high at its melting point. However, this type of seal is applicable to ultrahigh-vacuum devices provided that the valve can be opened in the vertical position and further provided that a compatible base-metal, filler-metal combination can be found which also meets the other specified requirements.

A survey of alloys potentially usable as filler metal has been made. At least one alloy system (In-Ag-Cu) which should be compatible with thermonuclear devices was mentioned in the literature and is now under investigation. Candidate alloys will be screened with regard to their dewetting tendencies, resistance to oxidation, compatibility with usable base material, and subsequent effects of dilution.

Tests are now in progress in which modified versions of the valve assembly previously described are being evaluated. In addition, a prototype of a flange assembly is nearing completion, and evaluation tests will soon be started.

7.1.2 GETTER TESTING

Apparatus (Fig. 7.1.4) has been constructed and experiments are planned to test the effectiveness of various substances as getters which will aid in the attainment of the high vacuums needed in thermonuclear machines. It is hoped to obtain information concerning gas adsorption by getters at pressures as low as 10^{-10} mm Hg. Equipment and testing methods are described elsewhere.[4-7] Figure 7.1.5 shows the equipment in operation.

7.1.3 VACUUM FURNACE INSTALLATION

Installation of a large vacuum furnace for vacuum degassing, vacuum brazing, and processing of experimental equipment has been completed. The hot zone has a diameter of 16 in. and a height of 20 in. Measurements made at the retort neck showed that the pumping speed is approximately 600 liters/sec at 10^{-4} mm Hg and that the retort

[4] G. R. Love and R. E. Clausing, *Methods for the Study of Gas-Metal Reactions in Ultra-High Vacuum*, ORNL CF-58-9-93.

[5] D. Alpert, p 609 in *Thermodynamics of Gases* ["Encyclopedia of Physics," vol XII (ed. by S. Flügge)], Springer-Verlag, Berlin, 1958.

[6] S. Wagener, *Brit. J. Appl. Phys.* 1, 225–31 (1950).

[7] J. A. Becker, *Advances in Catalysis* 7, 135–211 (1955).

UNCLASSIFIED
ORNL-LR-DWG 35782

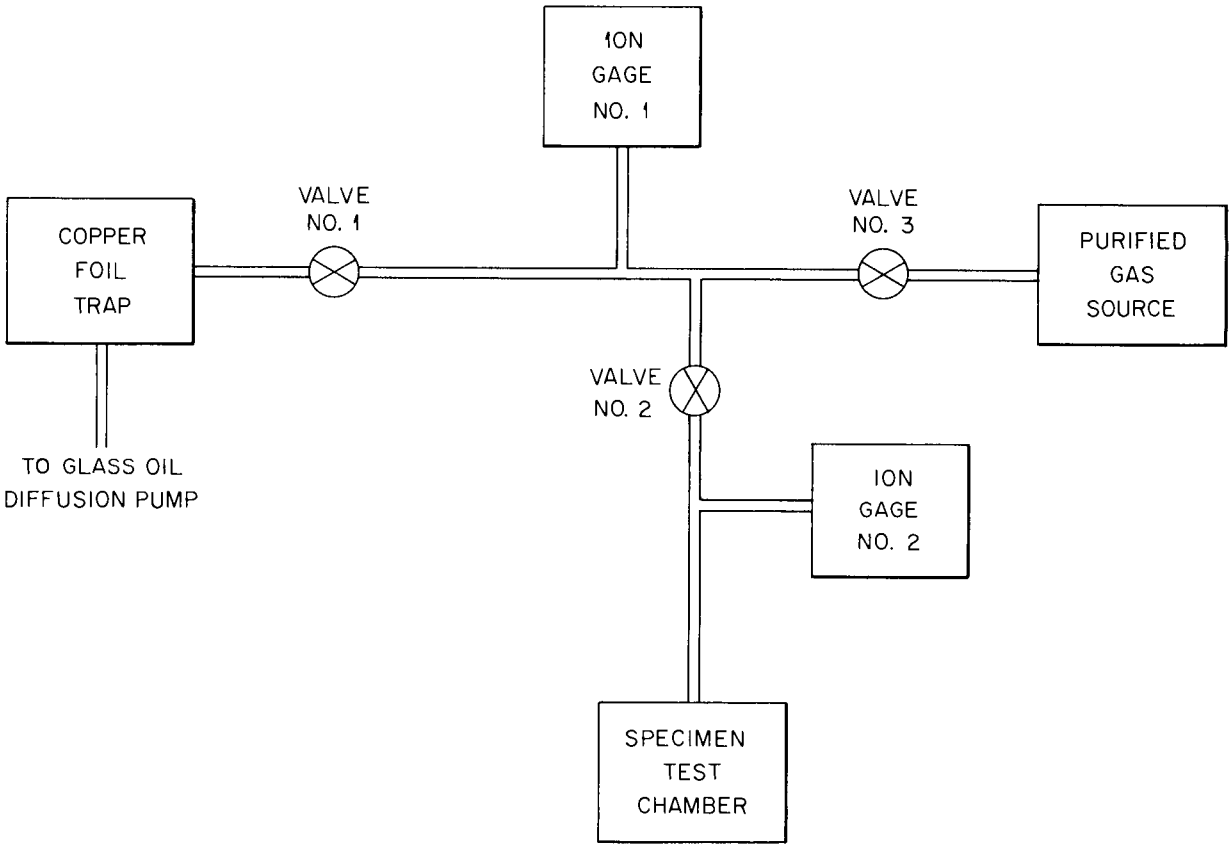

Fig. 7.1.4. Drawing of Apparatus for Testing the Effectiveness of Various Getters.

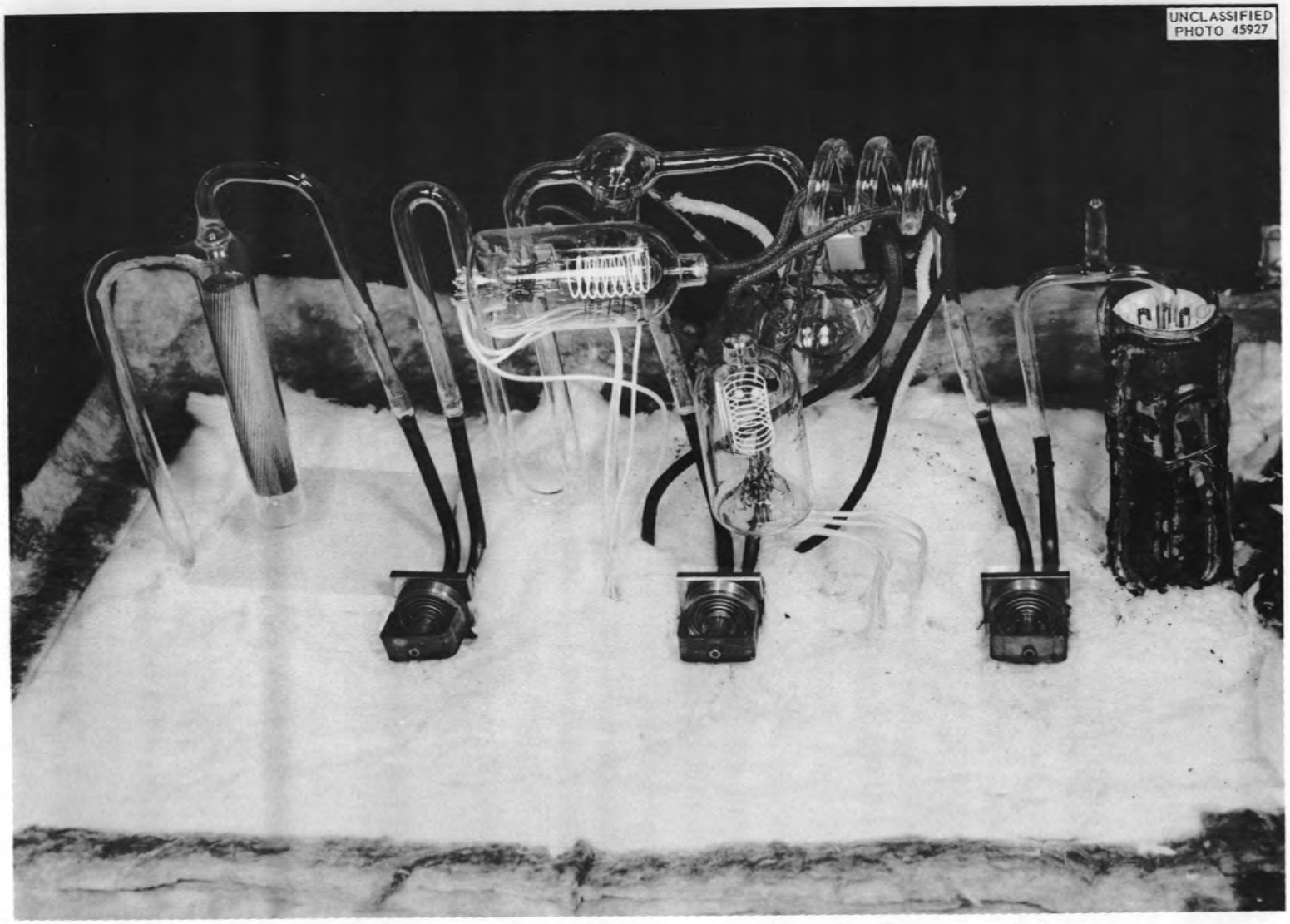

Fig. 7.1.5. Photograph of Apparatus for Testing the Effectiveness of Various Getters. Test cell is above and to the right of the lower ion gage. The gas source is inside the heater on the right.

pressure ranges between 5×10^{-5} and 1×10^{-4} during heating to 2150°F and between 2×10^{-5} and 5×10^{-6} during cooling, under average conditions.

7.1.4 ANALYSIS OF FAILURE OF COPPER TUBING

Leaks in copper tubing used for heating and cooling the DCX liner are a recurrent source of trouble. The cause of these costly failures of copper tubing in alternate steam service at 400°C and water service at 20°C is being studied. A report of the early investigation[8] (to October 15, 1958) has been completed, and a more thorough investigation is in progress. Preliminary results indicate that formation of intergranular defects frequently accompanies failure. Figure 7.1.6 shows a typical cross section of a tube in the vicinity of a failure. The mechanism of defect formation has not been determined; however, the results of incomplete tests seem to indicate that the presence of water during part of the service life of the tubing may accelerate failure. Tubing in service on the DCX liner frequently has failed within the first 100 hr of steam service (this includes at least 100 hr of water service also). In a controlled test in which no water was circulated through the tubes but in which other conditions were similar to DCX operation, no failures had occurred at temperatures below 500°C in 200 hr of operation. There were no signs of intergranular attack at temperatures below 400°C on this same test. A photomicrograph of a sample removed from a section of tubing operated at 500°C for approximately 200 hr is shown in Fig. 7.1.7. Very few intergranular defects are apparent.

A second series of test specimens is being prepared to further investigate the causes of the intergranular defects.

[8] R. E. Clausing, *Progress Report on the Investigation of the Development of Leaks in Copper Tubing Used on the DCX Liner*, ORNL CF-59-1-12 (Jan. 9, 1959).

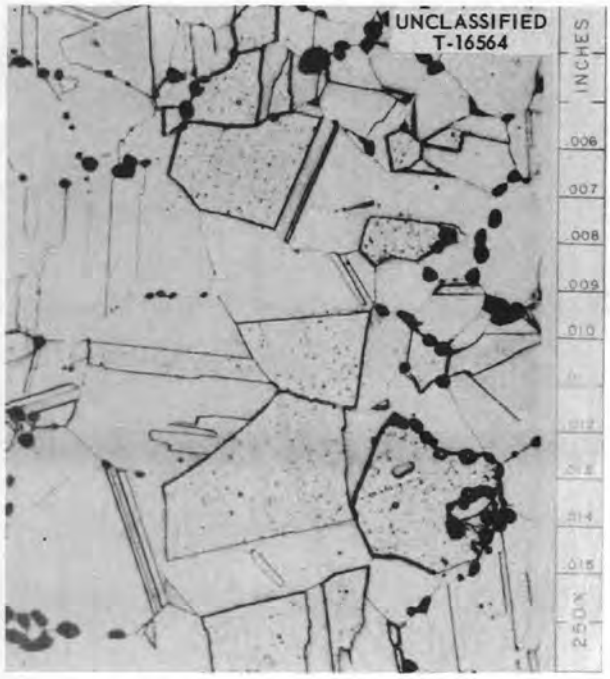

Fig. 7.1.6. Photomicrograph of Cross Section of a Copper Tube in the Vicinity of a Failure. Etched in glycerin. 250X.

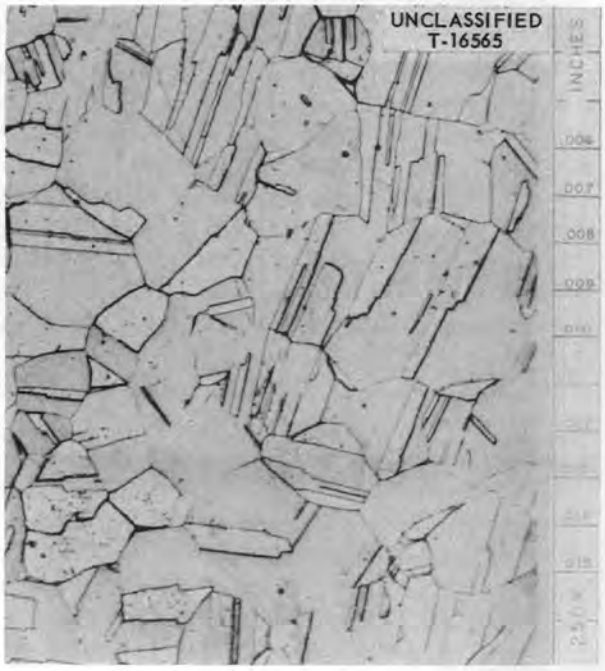

Fig. 7.1.7. Photomicrograph of Cross Section of a Copper Tube Exposed to 500°C Steam for 200 hr. Note the absence of intergranular effects. Etched in glycerin. 250X.

7.2 SEYA SPECTROMETER

G. K. Werner R. L. Knight M. R. Skidmore J. R. McNally, Jr.

Design and construction has been completed on a new type of vacuum spectrometer to be used in the study of carbon arcs and hydrogen and deuterium plasmas. Positions of the slits and concave grating are fixed, and scanning is done by rotating the grating. The highest wavelength attainable with this spectrometer is about 4450 Å, the limit being set by the length of the scanning screw. The lowest wavelength detected was 312 Å. At lower wavelengths there is insufficient reflectivity of the aluminum grating surface.

In discussing feasible designs for a vacuum ultraviolet spectrometer to be built at ORNL, P. G. Wilkinson[1] suggested the mounting devised by M. Seya[2] in 1952. The Seya mounting has the very desirable feature that only one motion, rotation of the concave grating, is used in scanning through successive wavelengths. This is the same scanning mechanism as that used in the Ebert and other plane grating spectrometers. The Seya mounting is optically superior to plane grating instruments for vacuum ultraviolet work because it has one reflection instead of three.

In considering the focal condition imposed by the Rowland circle, it is readily seen that in changing wavelengths the distance from grating to the entrance and/or exit slit must be changed to stay on the circle. In the Seya spectrometer the Rowland circle geometry applies only when the grating is set for zero wavelength (central image), the entrance and exit beams being of equal length and opposite angle. As the grating is rotated from this position (see Fig. 7.2.1), if one considers the Rowland circle as moving with it, one slit lies inside the circle and the other slit lies outside the circle just far enough to maintain focus when the Seya condition is satisfied. The focusing condition is dependent on two factors: the grating rotation must be over a fairly small angle (less than about 20°), and the angle between incident and diffracted beams must be close to 70.25°.

[1]University of Chicago.

[2]M. Seya, *Sci. of Light (Tokyo)* 2, 8 (1952).

This angle can be computed from the formula for focus of a concave grating (neglecting higher order terms):[3]

$$\frac{\cos^2 i}{r} - \frac{\cos i}{R} + \frac{\cos^2 \theta}{r'} - \frac{\cos \theta}{R} = 0 ,$$

where r and r' are distances from entrance and exit slits to grating of radius R, and i and θ are angles of incidence and diffraction.

Let 2α = angle between incident and divergent beams (fixed) and ϕ = angle of grating rotation from the position of symmetry ($i = -\theta$); then $2\alpha = i - \theta$ and $2\phi = i + \theta$. Let $r = r'$ and set them to focus for zero wavelength ($\phi = 0$). Then, for small values of ϕ, it can be shown that

$$\alpha = \tan^{-1}\sqrt{\frac{1}{2}} = 35.265° ,$$

$$2\alpha = 70.53° .$$

[3]H. G. Beutler, *J. Opt. Soc. Am.* 35, 311 (1945).

UNCLASSIFIED
ORNL—LR—DWG 35760

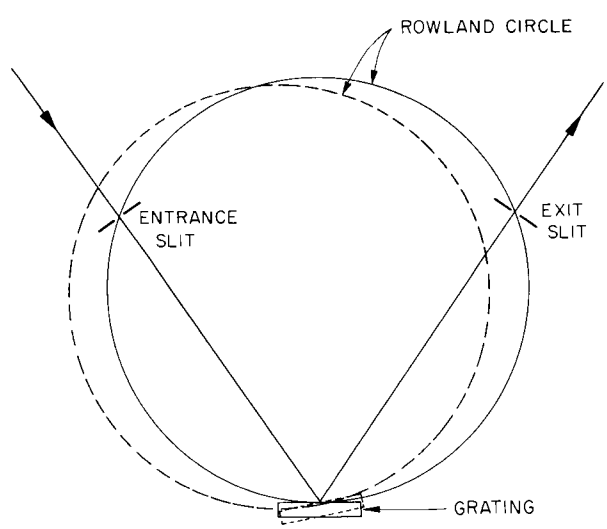

Fig. 7.2.1. Focus Retention with Slight Grating Rotation in Seya Spectrometer.

Seya's figure of 70.25° for 2α is derived by a more detailed computation which takes into account the slight change in focus as the grating is rotated over a practical wavelength range. For a vacuum spectrometer which will not be used in the visible wavelength region, the best value of 2α will lie somewhere between 70.25 and 70.53°.

The change in focus, according to Seya, will be about 0.15 mm for a rotation of 13.6° of a 15,000-line/in., 1-m concave grating. This corresponds to a wavelength range from 0 to 6600 Å. A focal variation of 0.5 mm was reported[4] for a Seya spectrometer built by Namioka,[5] who used a 54-cm, 15,000-line/in. grating.

Using a 6.4-m, 15,000-line/in. grating, we measured focal variations for different values of 2α and ϕ, which are reported in Fig. 7.2.2. This indicates a variation in focal length of about 0.2 mm for a 1-m grating if used between $\phi = 2°$ and $\phi = 10°$ (500 to 2500 Å). Being out of focus 0.1 mm would reduce the theoretical resolution of a 1-m grating of 80-mm width from 96,000 to about 12,000.

At larger angles of ϕ the image becomes poorer because of spherical aberration and because it is simply out of focus. The extent of this is dependent upon the grating width and can be controlled by occulting.

In the case where scanning is accomplished by rotating the grating, whether it be plane or concave, the basic grating equation

$$\frac{m\lambda}{a} = \sin i + \sin \theta$$

can be rewritten

$$\frac{m\lambda}{a} = \sin(\phi + \alpha) + \sin(\phi - \alpha)$$

$$\lambda = \left(\frac{2a}{m} \cos \alpha\right) \sin \phi \ ,$$

where m = order number, a = groove spacing, and α and ϕ are as defined previously.

Thus it is seen that wavelength is exactly proportional to the sine of the angle. To obtain a scanning drive system which is linear with wavelength, we have used the mechanism shown schematically in Fig. 7.2.3*a*. This arrangement has been successfully used in the Jarrell-Ash 8200 plane-grating spectrometer. It should not be confused with the arrangement of Fig. 7.2.3*b*, which is frequently used in grating rotation mechanisms but is limited to angles close to zero, where sine and tangent are almost equal, or to small angular spans away from zero, where sine and tangent are almost proportional. We used the screw and nut mechanism from a Gaertner Scientific Company micrometer slide model 303. The plate in our mechanism is sapphire and the stylus is a steel phonograph needle. This has eliminated the scratching of the plate experienced on the Jarrell-Ash spectrometers which use a glass plate and a steel ball.

The screw is coupled through a worm gear drive to a $^3/_{16}$-in. shaft with an O-ring vacuum seal to the external drive mechanism as shown in Fig. 7.2.4. A Gorrell and Gorrell Company reversible multispeed motor provides scanning speeds of from 500 to 0.5 Å/min. The motor can be disengaged to permit manual operation.

A five-digit counter coupled to the drive shaft shows the transmitted wavelength in angstroms at any given setting. It is accurate to 1 Å and is reproducible to $^1/_5$ Å.

To bring the instrument into exact calibration required three adjustments. Changing slightly the angle of the sapphire plate from 90° to the screw axis or changing the length of the stylus corrected a curvature of the error curve. The slope of the error curve was corrected by changing the length of the radius arm (using shims). The remaining error, a constant displacement, was corrected by resetting the shaft position in one of the coupling gears.

One of the requirements for our vacuum spectrometer is mobility. It must look horizontally into the arc of the LSM, must look downward at an angle of 18° from horizontal through the side port at the arc of DCX, and may be required to look straight down through the top viewing port of any of several facilities. Since it is too heavy (230 lb) to be supported by the flange that connects it to the system being analyzed, an eyebolt is provided at its center of gravity for a supporting chain or rope (see Fig. 7.2.5). This rope is connected to a beam balance with a counterweight adjusted to support only the weight of the spectrometer without imposing any extraneous strains. A bellows coupling at the mounting flange, together with the

[4] P. G. Wilkinson, private communication.

[5] T. Namioka, *Sci. of Light (Tokyo)* 3, 15 (1954).

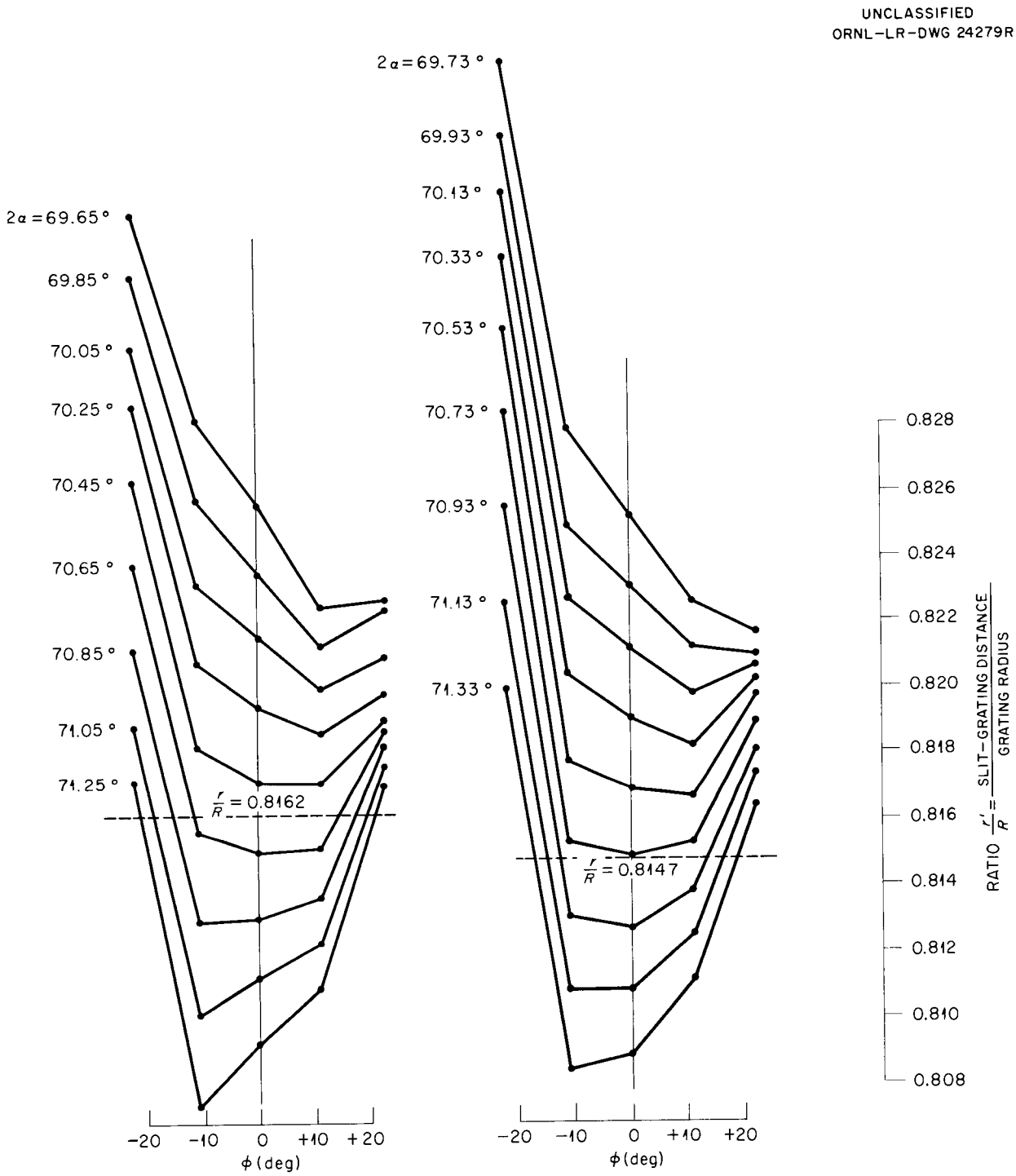

Fig. 7.2.2. Focal Characteristics of a Seya Spectrometer.

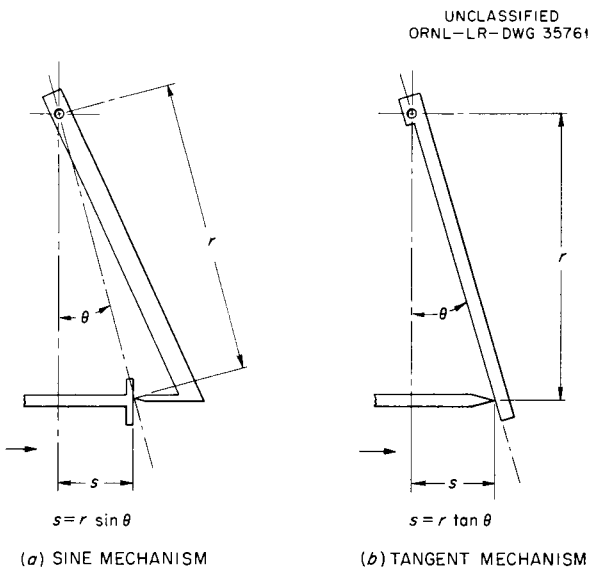

Fig. 7.2.3. Grating Rotation Mechanisms. (*a*) Used as described in Seya spectrometer. (*b*) Used frequently in other spectrometers.

beam balance support, permits easy movement and setting of the instrument to view at slightly different angles into the vacuum system. The astigmatism of the 1-m Seya mounting is such that the conjugate focus of a point on the exit slit is a horizontal line about 62 in. in front of the entrance slit. By placing the arc this far from the entrance slit and setting the exit slit height to 1 mm we can restrict our field of view in the arc to an area about $\frac{1}{8}$ in. high (proportional to exit slit height) and about 7 in. wide (proportional to grating width).

When used at some other angle than horizontal the diffusion pump and nitrogen trap, which mount by a vertical flange to the side of the input leg, are turned and remounted on this flange to new bolt holes to maintain them in a vertical position.

A pair of occulters mounted in a coaxial control and located in front of the grating was intended for any masking that the grating might require. To date, however, we have not found that a grating mask can be made to eliminate any particular ghosts, but the resolution at higher wavelengths (2000–4000 Å) can be improved by using occulting simply to reduce the angular aperture of the grating. Occulting can also be used to check the focus of the spectrometer photoelectrically by a method derived from the knife-edge test.

We have not yet tried to determine the highest resolution of this spectrometer because interest has been in high-speed low-resolution problems. The line widths in the carbon arc, for instance, are too broad to test the resolution of the spectrometer. However, by interpolation between the half-width of the central image (0.15 Å) and the half-width of the lowest wavelength (2537 Å) from a mercury lamp (0.20 Å) the resolution is estimated to be about 2000 at 300 Å, 3300 at 500 Å, and 6300 at 1000 Å.

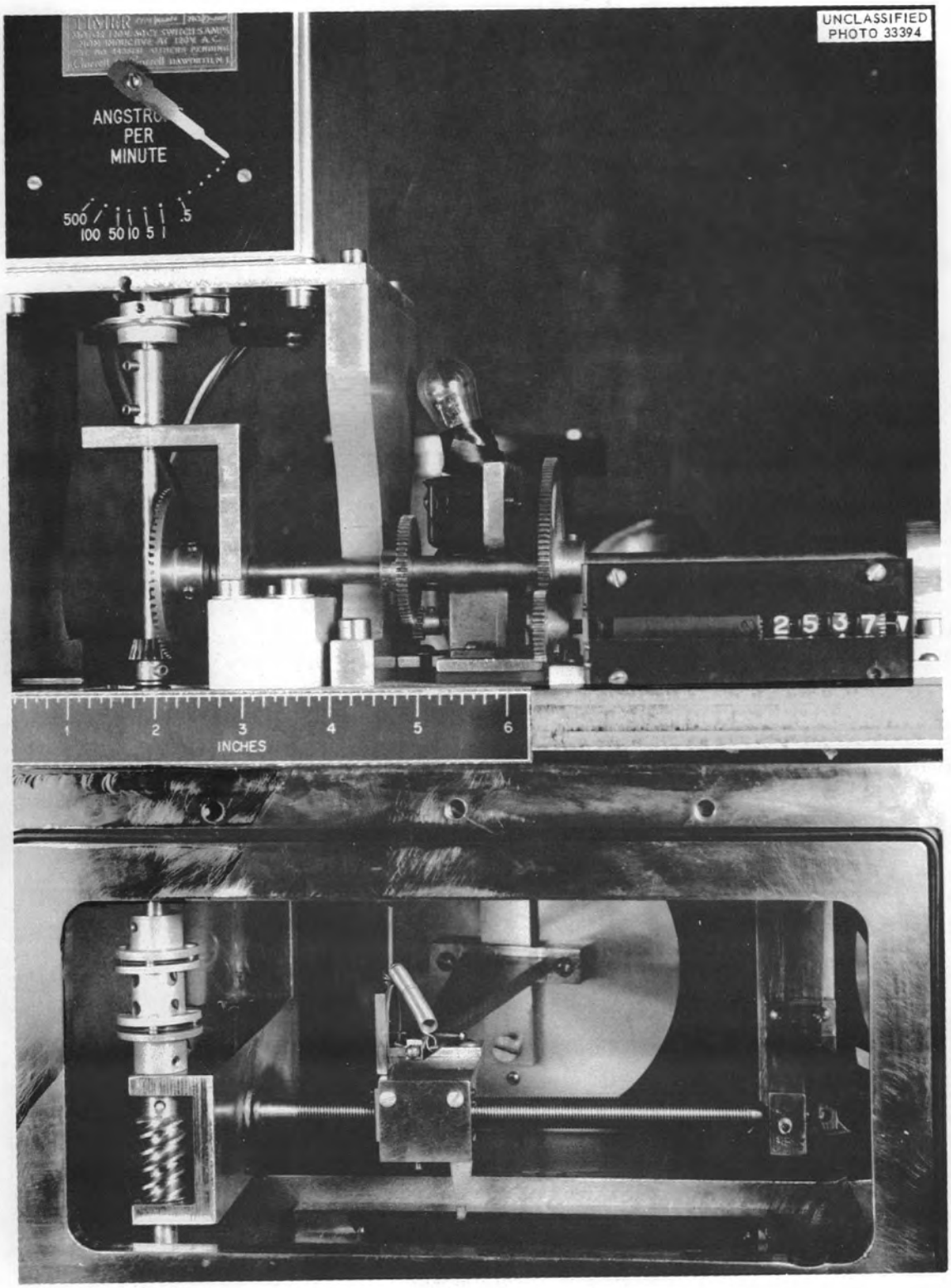

Fig. 7.2.4. Drive Mechanism for Grating Rotation.

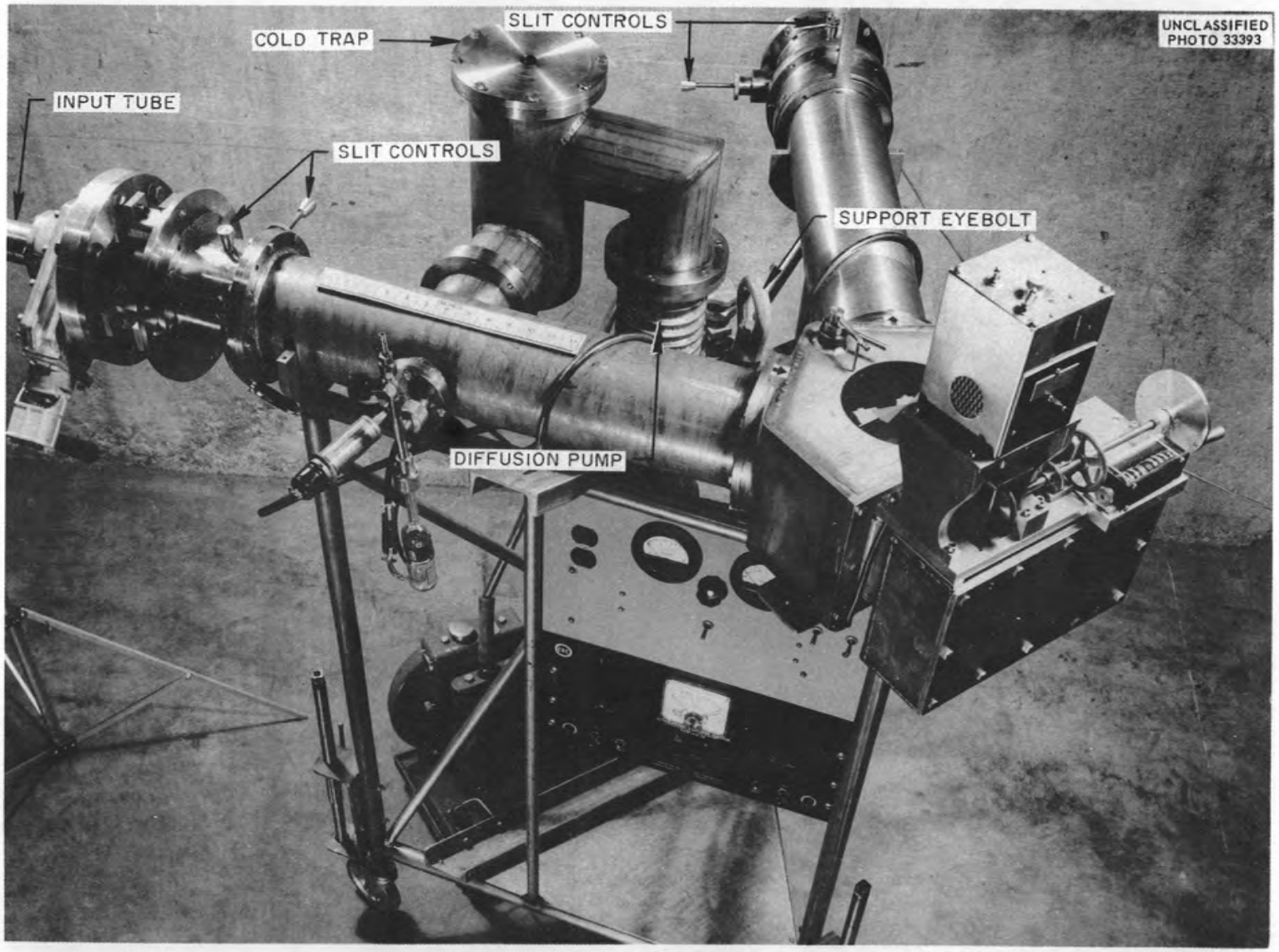

Fig. 7.2.5. Seya Spectrometer To Be Used in DCX Studies.

7.3 A NONLINEAR PHOTOMETER CIRCUIT

G. K. Werner O. B. Rudolph

A circuit for semilogarithmic photometric recording has been developed, with a minimum of circuit changes, from a conventional circuit for RCA multiplier phototubes.

At the suggestion of R. A. Dandl we tried high-impedance voltage dividers and resistances in series with the last few dynodes,[1] but no modification resulted in better performance than simply grounding dynode No. 9 through a resistance of about 100,000 ohms, as shown in Fig. 7.3.1. A performance curve for the circuit is shown in Fig. 7.3.2. Signals that are only slightly greater than the noise level are directly proportional to the input light flux. Above a signal of about 0.05 v, response is roughly logarithmic over four decades, with from 0.1 to 0.25 v output per decade of input, as shown in Fig. 7.3.3.

[1]Investigations along this line have also been reported by R. W. Engstrom and E. Fischer, *Rev. Sci. Instr.* 28, 525 (1957).

With this circuit it is possible to scan rapidly over a spectrum and get a fairly good measure of the intensities and wavelengths of all lines encountered. Scans have been made with the vacuum spectrometer at 500 Å/min, and we were able to measure relative phototube response ("intensity") to better than 10% and wavelengths to about 1 Å.

A separate calibration must be made for each phototube, since they do not have uniform dynode amplification characteristics. This circuit should work equally well for phototubes 931A, 1P21, 1P22, 6328, 6199, 5819, and 6655, which all have the same electrode configuration and dynode material.

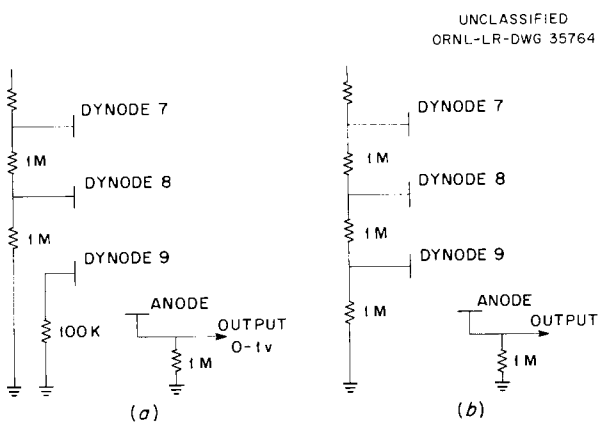

Fig. 7.3.1. Photometer Circuit for Logarithmic Response (*a*); Compared with Conventional Circuit (*b*).

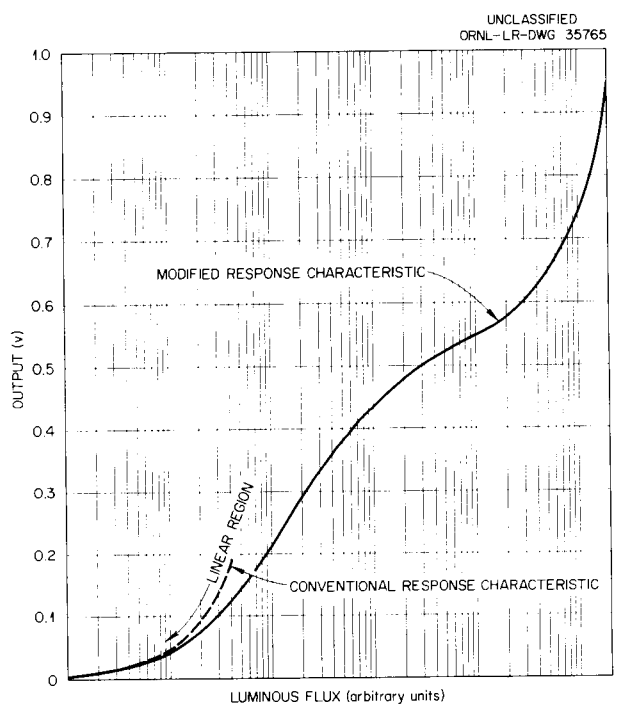

Fig. 7.3.2. Performance of Photometer Circuit for Logarithmic Response.

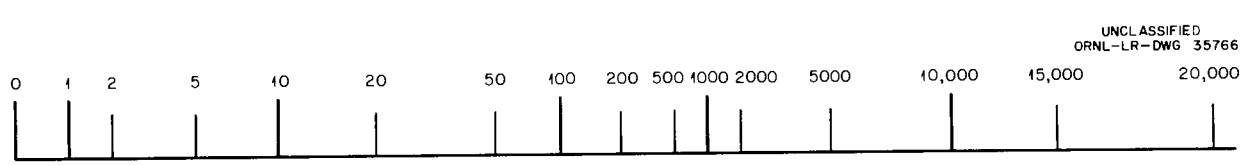

Fig. 7.3.3. Recorder Scale Calibrated for Phototube BQ. 900 v, 100 kilohms from dynode No. 9 to ground, 1 v full scale.

7.4 DESIGN AND CONSTRUCTION GROUP

E. S. Bettis

Engineering on the Sherwood Project has been organized into a formal section for only about two months and therefore this activities report will be very brief. In most cases, activities of the Engineering Section will be integrated with the experimental work and will be reported indirectly in the various projects. The three activities which have been handled solely by the Engineering Section are design and construction of 6000-amp magnet coils for the DCX, installation of a 600-kv, 1-amp d-c supply for ion injection, and design of a system of four evacuable tanks which will be provided with independent, essentially homogeneous magnetic fields. The tanks will be used for basic studies.

7.4.1 NEW MAGNET COILS FOR THE DCX

The original magnet coils for the DCX were designed for a current of 4500 amp. When it became necessary to operate the coils at 6000 amp, the cooling was insufficient to prevent damage to the coils and they were burned out. The original coils were cooled by means of $\frac{3}{16}$-in.-dia holes which were rifle-drilled axially through each layer of the coil and which were on 1-in. spacing around the center line of each layer. (For a theoretical discussion of DCX magnet coils see Sec 8.1.2.)

A new set of coils was designed to be cooled on both edges of each layer, and no rifle-drilled holes were employed. Each layer was wound on an accurately machined mandrel to eliminate the necessity of machining the finished coil. Flags tape was wound between individual turns, and the coil was clamped under a pressure of 20 tons to compress it into a compact form. It was then vacuum-impregnated with bakeable electrical varnish and baked for curing. This operation was repeated once, and then the excess varnish was sanded from each surface of the coil.

Special separators in the form of insulating inserts were used to separate each of the four concentric layers of each coil from each other and from the stainless steel case. The separators were made by clamping a piece of glass cloth in a mold which had, at center spacing of $1\frac{3}{8}$ in., milled parallel channels $\frac{3}{8}$ in. wide by $\frac{1}{8}$ in. deep. When the mold was vacuum-filled with an epoxy compound and cured, it formed a ribbed, insulating mechanical spacer with water passages for axial water flow along the faces of each coil layer.

The individual layers were nested into four concentric coils electrically connected in series and wedged into the container can mechanically restrained by the webbed separators. Micarta rings on each end of each coil layer insulated the coils from the can, and soft rubber gaskets were compressed by the bolted top of the can against the coils. Electrical leads and water inlet and outlet were brought in through the bolted can top.

Edgewise cooling of these coils proved to be satisfactory, and 6000-amp currents were handled satisfactorily with a cooling-water temperature rise of only 16°F.

7.4.2 INSTALLATION OF 600-kv, 1-amp D-C SUPPLY

Another project which has been almost completed consists in the installation of a new 600-kv, 1-amp d-c supply for ion injection. This supply was engineered and built by Allis Chalmers Mfg. Co. It consists of four transformers, each with a silicon rectifier bridge, the d-c output of each transformer being connected in series to produce 600 kv at the output terminal. By means of a tap-changing transformer the voltage of the supply at no load can be brought up from low voltage to rated voltage. An R-C filter reduces output ripple to tolerable values. The supply has been installed and a flowing water load (water running through Tygon tubing) has been provided for testing the supply at rated output. The load test has not yet been run. Figure 7.4.1 is a photograph of this new supply.

7.4.3 DESIGN OF EVACUABLE TANKS

The third project on which work has been done consists only in design thus far. A system of four evacuable tanks in magnetic fields has been designed to be used for basic studies on matters

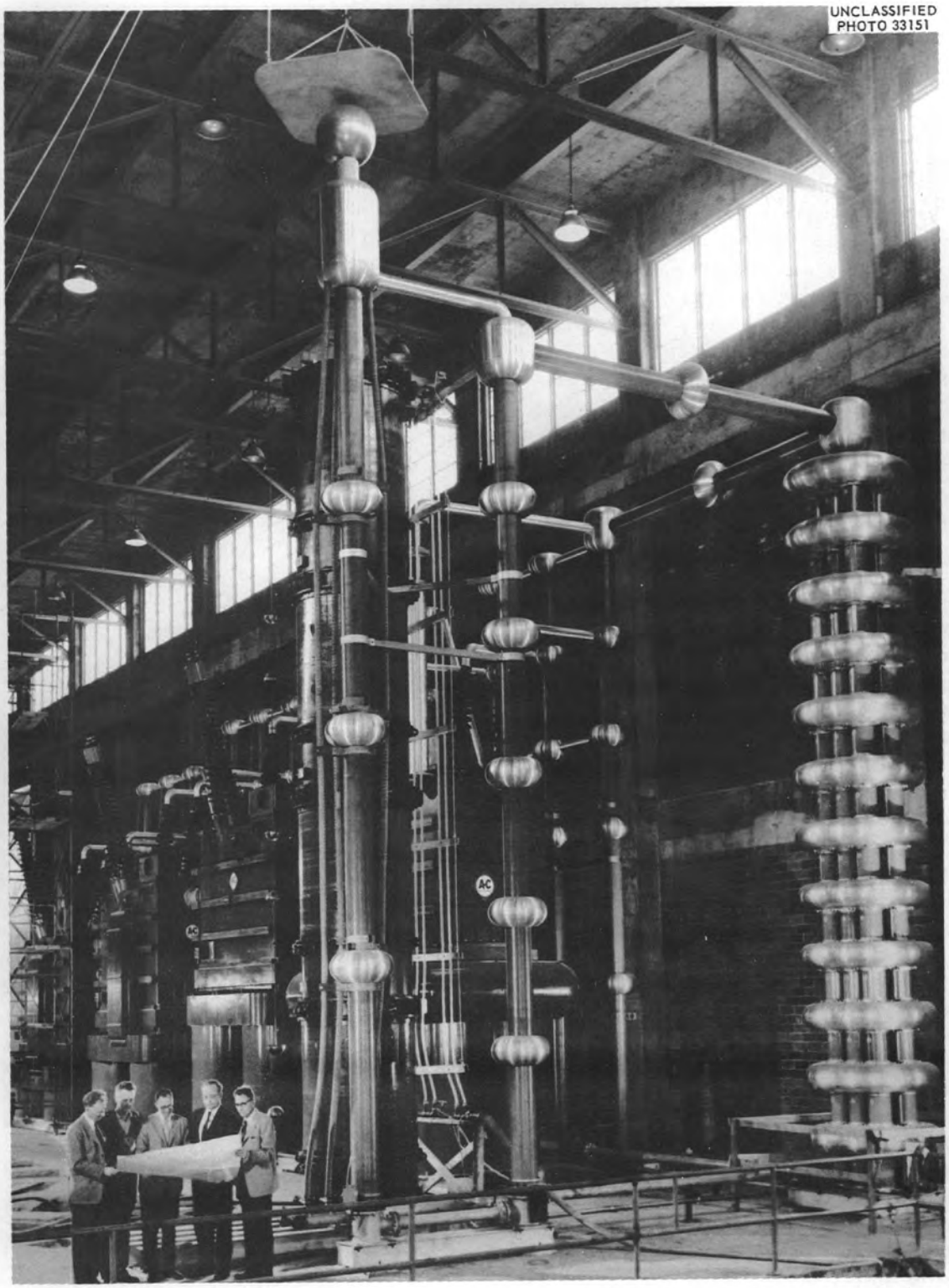

Fig. 7.4.1. Power Supply (600 kv, 1 amp dc) for DCX Ion Injection.

concerning thermonuclear work. The tanks will be of three different sizes, and volumes of approximately 12 to 36 ft^3 will be available for experimental work in an essentially homogeneous magnetic field. The field of each tank will be independent of the other tanks by arrangement of the iron yoke.

Magnet current will be supplied by large rectifier units with a tap-changing switch and series induction regulator on the a-c side to permit control of the magnetic field for each tank. Each unit will be provided with a high-voltage cubicle (one of the old Alpha II cubicles) to supply experimental d-c power.

Design of this experimental system is complete, and its construction, in Building 9201-2, will be completed by the time that the building is occupied by the Sherwood Project.

8. ENGINEERING SCIENCES GROUP

8.1 ENGINEERING SCIENCE

W. F. Gauster

In engineering science studies in support of the Sherwood Project the following work is in progress or was done:

1. A literature survey produced tables of magnetic-field values B_Z and B_r for current sheets, useful in the computation of any rotationally symmetric magnetic fields. Similar tables containing finer intervals, values for the vector potential $\bar{A}$ and for rA, and a larger range of Z and r have been computed by the Mathematics Group of the Thermonuclear Experimental Division.

2. General optimization theorems were worked out for the cross-section shape and the current-density distribution of magnet coils.

3. A field-analog network (Field Simulator) was built in which the field line of a rotationally symmetric magnetic field corresponds to an equipotential line. Another analog computer, in which magnetic equipotential corresponds to an electric equipotential, is being worked on. It will use a wedge-shaped electrolytic tank.

4. In an attempt to determine the effect of slow changes on a pulsed magnetic field, such as might be used in this program in the future, an arrangement for a-c measurements on magnetic models has been developed.

5. A method of conveniently computing sufficiently exact values for the mechanical forces produced by the DCX magnetic mirror coils was developed.

6. Experiments and calculations on heat transfer for cooling of large magnet coils are in progress.

7. Graphical and analytical methods for the fast determination of charged-particle trajectories in magnetic fields have been developed.

8.1.1 GENERAL SUPPORTING STUDIES

Tabulation of Magnetic Fields

The first activity of the Engineering Science Group was to do general studies on magnetic fields. A careful search of the literature showed that several good tables for the magnetic field produced by single circular loops are available.[1] For the computation of the magnetic field produced by actual coils of any given cross section, considerable time is saved by use of field values for current sheets rather than single loops. It was found that tables of this kind had been calculated[2] by K. Foelsch 20 years ago and that it was possible to obtain a microfilm of his work. In

[1] J. P. Blewett, *J. Appl. Phys.* 18, 968–76 (1947); C. L. Bartberger, *J. Appl. Phys.* 21, 1108–14 (1950).

[2] Kuno Foelsch, *Tabellen und Kurven zur Berechnung des Magnetfeldes von kreiszylindrischen Spulen*, Konrad Triltsch, Würzburg, 1936; see also K. F. Müller, *Arch. Elektrotech.* 17, 336 (1926); K. Foelsch, *Arch. Elektrotech.* 30, 139 (1936).

order to simplify the work with these tables, a semigraphical method was developed.[3]

Foelsch's tables are inadequate in several respects: although they contain values of B_Z and B_r, they do not contain values of the vector potential $\bar{A} = \bar{I}_\theta A$ of these rotationally symmetric fields; for computing field lines, values of rA are desirable; and the tables would be more useful if the values covered larger ranges of Z and r and were given for finer intervals. Therefore it was arranged with the Mathematics Panel to compute tables of this kind. For complicated coil arrangements, time is saved by special programing of the magnetic field on the Oracle instead of using tables. For work done along this line, the help of the Mathematics Group of the Thermonuclear Experimental Division is highly appreciated.

Theoretical studies were made, especially on the optimization of d-c magnet coils. General optimization theorems were found for the current-density distribution and for the cross-section shape of magnet coils.[4] These studies are important since the ohmic loss of power for the magnet coils used for DCX experiments is about 10^3 to 10^4 kw.

Field Analogs

Field Simulators (analog networks) can often be used more conveniently than computation for determining the nature of a magnetic field. Field Simulators of a special type developed by Wakefield[5] have been used to good advantage by the Matterhorn Project. A similar device, in which a magnetic field line of a rotationally symmetric magnetic field corresponds to an equipotential line of the Field Simulator, has been built for ORNL; however, it will take some time to put it into full operation.

For some problems it is more convenient to use the analogy: magnetic equipotential (surface of magnetic material with $\mu = \infty$) vs electric equipotential. This can be realized with a wedge-shaped electrolytic tank. Work on such a device has started. The building of an analog network for the magnetic potential and the designing of a device for automatically drawing trajectories of charged particles in magnetic fields[6] are also contemplated.

Magnetic Models

Besides d-c fields, slowly pulsed magnetic fields might be of importance for the DCX program in the near future. To find the influence of even slow changes on the field configuration by calculation only is difficult, and therefore an arrangement for a-c measurements on magnetic models has been developed. Measurements performed with different frequencies can be used for a Fourier analysis of slow impulses.[7]

8.1.2 MECHANICAL FORCES AND HEAT TRANSFER IN MAGNET COILS

Mechanical Forces

The mechanical forces produced by the magnetic mirror coils for DCX experiments are very strong. It is easy to find approximate values for these forces, but an exact calculation is complicated.[8] A computation method was worked out which will give sufficiently exact values with not too lengthy calculations. The calculation of mechanical forces is important for any large mirror device. Another application would be in the installation of large Beta-calutron tanks in the new location for ion source experiments, etc., which raises the problem of evaluating electromagnetic forces. A model was built for this work.

Heat Transfer

In designing large d-c magnet coils, the cooling problem is very serious. The most efficient cooling method is to use cooling canals parallel to the axis. Many short canals in parallel produce

[3] W. F. Gauster, *Controlled Thermonuclear Conference, Held at Washington, D.C., February 3–5, 1958*, TID-7558, p 518–27; C. E. Bettis, in *Proceedings of Symposium on Magnetic Field Design, Gatlinburg, 1958* (in press).

[4] W. F. Gauster, in *Proceedings of Symposium on Magnetic Field Design, Gatlinburg, 1958* (in press).

[5] K. E. Wakefield, *A Resistance Analogue Device for Studying Axially Symmetric Magnetic Fields*, PM-S-23 (Dec. 13, 1956); G. Liebmann, *Phil. Mag.* 41, 1143–51 (1950).

[6] D. L. Hollway, *Proc. I.R.E.* 103 (Part B), 155–60, 161–65 (1956).

[7] W. F. Gauster, *Controlled Thermonuclear Conference, Held at Washington, D.C., February 3–5, 1958*, TID-7558, p 518–27.

[8] J. Hak, *Eisenlose Drosselspulen*, p 92–102, Koehler-Verlag, Leipzig, 1938.

only a small hydraulic resistance, and therefore high water velocities can be used without the need of very high pressure.[9] An application of this principle for the design of the coils for DCX-1 gave very efficient heat transfer. There were, however, serious technological difficulties (see Sec 7.4.1).

In order to overcome these difficulties, experiments were made with stacks of copper plates, separated by insulation layers. This arrangement simulates the actual coils in respect to turn-to-turn insulation, which cannot be measured in the actual winding since the very small resistance of the copper conductor is in parallel with the insulation resistance. Furthermore, it is convenient to have small test pieces which can be made up much more easily than the complete coils.

These experiments showed very clearly the difficulties involved when the axial cooling canals are made by rifle drilling and the great improvement that can be achieved by reaming the holes. Measurements of insulation resistance and of flashover voltage in dry and wet state seemed to indicate that the difficulties in rifle drilling of large magnet coils can be overcome.

For magnet coils which are to produce magnetic fields of only a few thousand gauss, it is convenient to use hollow copper and to let the coolant circulate inside the conductors. The efficiency of this cooling method depends, of course, on the water velocity and therefore on the water pressure. For higher pressures special care has to be taken to make the tube connectors strong enough to avoid leaking.

[9]F. Bitter, *Rev. Sci. Instr.* 7, 479–88 (1936).

In general, the copper temperature of the magnet coils has to be low in order to yield favorable values for the electric resistance (and therefore for the power consumed). In some cases, however, it is not so important to keep the electric power as low as possible as it is to produce the highest field strength with not too large a volume of copper, even if the temperature becomes relatively high. This might be the case, for instance, if there is only a little space in an experimental device for providing an ion-beam deflection magnet close to other parts. In these cases it is possible to apply the principle of "cooling with local boiling,"[10] which is also used by Gambill and Greene for the vortex cooling system for fission reactors.[11] Experiments are being prepared to apply local-boiling cooling to large magnet coils. Care must be taken to stay securely in the right range of water pressure and temperature.

8.1.3 ION TRAJECTORIES

Besides the D_2^+ beam which is used for breakup at the vacuum carbon arc, the ion source of the DCX produces D^+ and D_3^+ beams which are separated from the D_2^+ beam by means of a deflection magnet. Recent observations seem to indicate that weak beams of D^+ and D_3^+ are hitting the vacuum chamber wall. In order to clear up this question, the Engineering Science Group is working out the D^+ and D_3^+ ion trajectories starting from the accelerator tube.

[10]H. H. Kolm, *Rev. Sci. Instr.* 29, 489 (1958).

[11]W. R. Gambill and N. D. Greene, *Chem. Eng. Progr.* 54(10), 68–79 (1958).

Part III

THE DCX-2 PROGRAM

9. CALCULATIONS FOR DCX-2 DESIGN

9.1 MAGNETIC MIRROR FIELDS FOR DCX-2

W. F. Gauster

Calculations of the characteristics of magnetic mirror coils that will give satisfactory particle containment with power and copper economy are in progress.

The magnetic mirror field of the first DCX machine is not supposed to contain thermonuclear reaction products. The DCX-2 will be designed with a stronger magnetic field and a higher mirror ratio. It is hoped that with this device a self-sustained thermonuclear reaction will be demonstrated.

In order to get, first, an approximate idea about the dimensions of the DCX-2, a simple computation scheme starting with a containment calculation was worked out. It was assumed that the thermonuclear reaction products are alpha particles with an energy of 5 Mev. Only the particle movement in the mid-plane of a magnetic mirror was considered. Furthermore, it was assumed that the volume in which thermonuclear reactions will occur is relatively small, so that the alpha particles will start approximately from the mirror center. Under this assumption, the largest distance, r_{max}, which an alpha particle will travel from the center (aphelion of the orbit) can be found by means of the canonical angular momentum constant of the motion:

$$C = rqA + rp_\theta \quad , \tag{1}$$

where

r = distance from the center,

q = particle charge,

A = magnetic potential of the rotationally symmetric field,

p_θ = θ-component of the momentum.

Since the orbit passes through the center, $C = 0$. For $r = r_{max}$ it follows that $p_\theta = p = mv$. Therefore

$$q\,A(r_{max}) + mv = 0 \quad ,$$

or (for a 5-Mev alpha particle)

$$\left|A(r_{max})\right| = \left(\frac{mv}{q}\right) = 127.2 \text{ kilogauss} \times \text{in.} \quad . \tag{2}$$

The distance r_{max} must be equal to the smaller one of the lengths r_A and r_F; r_A is determined by

$$A(r_A) = \text{maximum} \quad , \tag{3}$$

which is the escape condition for the mid-plane; r_F is the radius in which a "critical field line" intersects the mid-plane. A critical field line is a magnetic field line which hits the inner edges of both mirror coil cases (see Fig. 9.1.1). The r_F lines form a rotational surface such that all field lines inside it pass freely through the two coil cases. If we assume an adiabatic particle movement (a very rough approximation), then all particle orbits should stay inside the rotational surface consisting of critical field lines.

Finding the characteristics of mirror coils which will be satisfactory with respect to particle containment and with respect to power and copper economy is a difficult problem which can be solved only by successive approximations. The first assumptions are a reasonable coil shape and current-density distribution in the coil winding; the size (say the inner coil radius a_1) and the absolute value of the flux density B_c at the mirror center are determined later. The mirror ratio must be chosen so that a sufficient part of the thermonuclear reaction products stays long enough inside the mirror. Making a reasonable assumption about the mirror ratio is the most difficult part of planning this type of machine.

As a starting point, symmetrical coils with tapered ends as shown in Fig. 9.1.1 and with current density i = constant were assumed. The mirror ratio determines the ratio Z_0/a_1. Now, the geometrical form of the coil arrangement is known, but the absolute length of one of the dimensions,

UNCLASSIFIED
ORNL-LR-DWG 36754

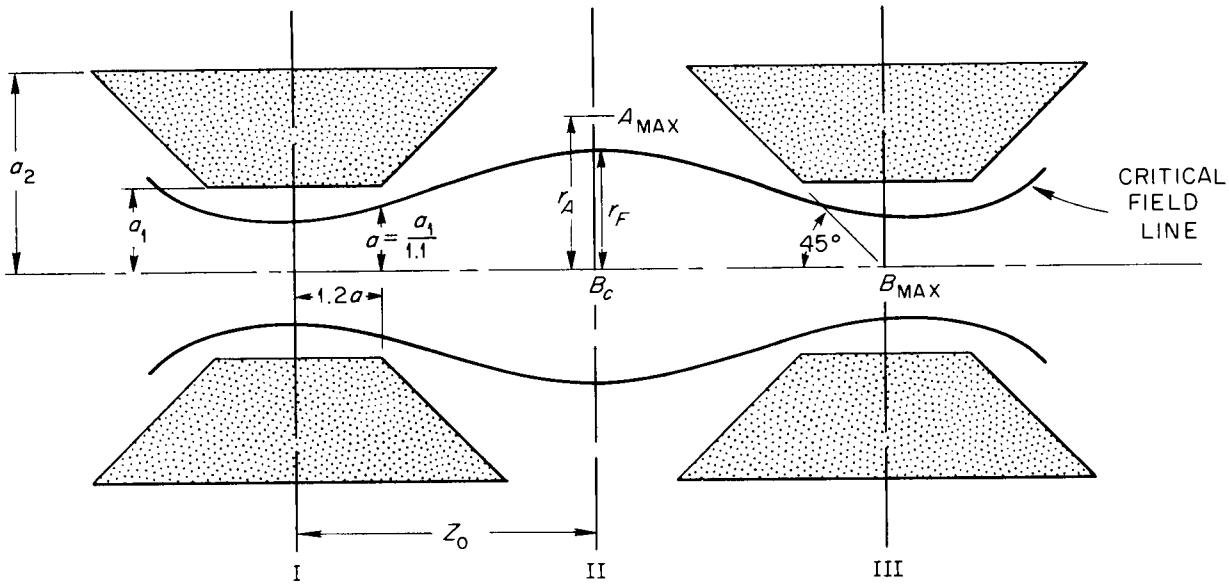

$$\alpha = \frac{a_2}{a_1} = 2.4545$$

NOTE: B_{MAX} ACTUALLY OCCURS A SMALL DISTANCE INSIDE PLANES I AND III. THIS DIFFERENCE CAN BE NEGLECTED.

Fig. 9.1.1. General Coil Configuration and Parameters for Finding the Approximate Dimensions of DCX-2.

for instance, a_1, is still needed. Fabry's equation yields the field strength in the center of one coil:

$$B_0 = G\sqrt{\frac{(P/2)\,\lambda}{\rho a_1}}\,, \qquad (4)$$

where

$P/2$ = power for one coil, here assumed to be 7500 kw = 7.5×10^6,

λ = form factor $\doteq 0.7$,

ρ = specific resistance of copper $\doteq 1.9 \times 10^{-9}$ ohm-cm,

G = 0.170 (for the coil shape and current density distribution assumed).

Combining the magnetic fields produced by both coils, we can find the normalized values

$$B_Z^* = \frac{B_Z}{B_0}\,,$$

$$B_r^* = \frac{B_r}{B_0}\,,$$

$$A^* = \frac{A}{a_1 B_0}$$

for any point of the magnetic field, which is determined by the normalized coordinates $Z^* = Z/a_1$

and $r^* = r/a_1$. By comparing the values r_A^* and r_F^* we can decide on the value r_{max}^*.

With the Oracle we compute the quantity $A^*(r^*)$ which, substituted into Eq. (2), yields as the equation for r_{max}^*

$$\frac{127.2}{a_1 B_0} = A^*(r_{max}^*) \quad . \tag{5}$$

Now it is possible to find the desired unknown a_1 and B_0 from Eqs. (4) and (5).

With a mirror ratio 3.5 the following data are obtained: $a_1 = 12$ in., $a_2 = 28$ in., $Z_0 = 20$ in., $r_{max} = 20$ in. $= r_F < r_A$, $B_{min} = 16$ kilogauss, $B_{max} = 56$ kilogauss. The current density is

$$i = 1.37 \times 10^4 \text{ amp/in.}^2 \quad ,$$

which is a relatively low value (DCX-1 coils have a current density of 2.4×10^4 amp/in.^{2}).

By means of a simple scaling law, data for a DCX-2 machine with other linear dimensions can be found. If we consider an alpha particle with constant energy of 5 Mev, the product of the radius of curvature at any point and the magnetic field strength at this same point has to be a constant. Therefore, by scaling down any length a to a/k, the flux density B has to be increased to kB. From (4) it follows that P also has to be scaled up to kP. Finally, it is easy to show that the current density i is scaled up to $k^2 i$. This point of view is important because with larger mirror ratios a power of 15 Mw would require excessively high copper volume and have an unnecessarily low current density. By scaling down the machine and therefore increasing the power, copper volume and current density can be brought to reasonable values.

The numerical example shown was calculated assuming a simple coil shape with constant current density. By changing the coil shape and the current-density distribution it is hoped to find sensibly better data for a DCX-2 machine; however, much further study is needed. It should be kept in mind that space for instrumentation must be provided.

9.2 ORACLE CALCULATION OF MAGNETIC FIELDS AND VECTOR POTENTIAL

M. Rankin

A flexible Oracle code to permit rapid calculation of magnetic fields and vector potential for use in coil design problems has been developed. Values for B_Z/B_0, B_r/B_0, and A/B_0 at a general point (r,Z) are calculated by summing the contributions at this point from many circular loops of current-carrying wire. [The quantity $B_0 \equiv B_Z(0,0)$. The quantities B_Z/B_0 and B_r/B_0 are dimensionless; A/B_0 has dimensions of length.] The quantity $B_0/\mu I$ is calculated and given separately, so that absolute field strengths may be found.

Tables of values giving B_Z/B_0, B_r/B_0, and A/B_0 have been calculated at intervals of 1 in. along the Z-axis for the present DCX coil configuration. Similar tables have been computed for several other different coil designs.

For a circular loop of wire of radius R located at a distance h from the $Z = 0$ plane and carrying a current I, we have the following formulas:

$$\frac{A(r,Z)}{\mu I} = \frac{\sqrt{(R+r)^2 + (Z-h)^2}}{2\pi r} K(k) \left[\left(1 - \frac{k^2}{Z}\right) - \frac{E(k)}{K(k)}\right] \quad , \tag{1}$$

$$\frac{B_r(r,Z)}{\mu I} = \frac{(Z-h)\, K(k) \left[\left(1 - \frac{k^2}{2}\right)\frac{E(k)}{K(k)} - (1-k^2)\right]}{\sqrt{(R+r)^2 + (Z-k)^2} \cdot 2\pi r(1-k^2)} \quad , \tag{2}$$

$$\frac{B_Z(r,Z)}{\mu I} = \frac{K(k)\left\{\dfrac{2R^2\dfrac{E(k)}{K(k)}}{[(R+r)^2+(Z-h)^2]} - \left[\left(1-\dfrac{k^2}{2}\right)\dfrac{E(k)}{K(k)} - (1-k^2)\right]\right\}}{2\pi(1-k^2)\sqrt{(R+r)^2+(Z-h)^2}} , \tag{3}$$

where

$$k^2 \equiv \frac{4rR}{(r+R)^2+(Z-h)^2}$$

and $K(k)$ and $E(k)$ are the complete elliptic integrals of the first and second kinds.

The following parameters may be varied in the code (see Fig. 9.2.1):

i = number of rows of loops,

n_i = number of loops on row i,

I_i/I_1 = ratio of current on row i to current on row 1,

$(\Delta h)_i$ = distance between loops on row i,

h_{1i} = Z-coordinate of first loop on row i,

R_1 = r-coordinate of first row,

ΔR = distance between rows,

r_0, Δr, r_{max}, Z_0, ΔZ, Z_{max} = range on r and Z and intervals of each at which calculations are desired.

Often it is desired to normalize all the lengths involved in the calculation to some a, usually the distance to the outside of the insulation of the wires in the first row. In this case, the normalization factor used becomes $aB_0/\mu I$. To convert to field strength in gauss the Oracle number should then be multiplied by

$$\frac{I \text{ (in amps)}}{a \text{ (in cm)}} \times \frac{4\pi}{10} .$$

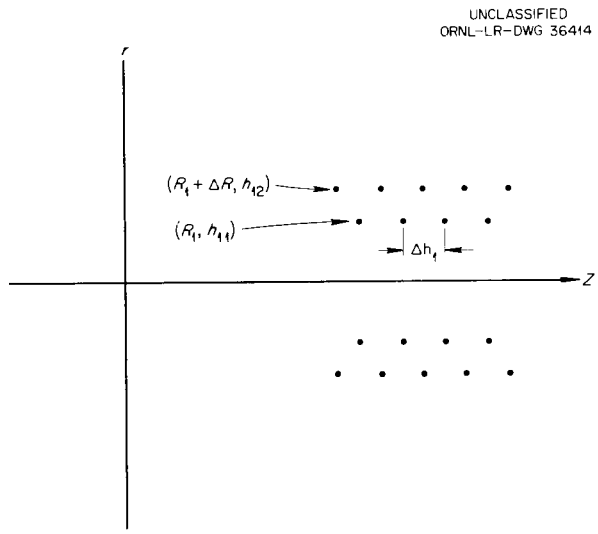

Fig. 9.2.1. Coordinates Z and r Used in Oracle Calculation of Magnetic Fields and Vector Potential.

INTERNAL DISTRIBUTION

1. R. G. Alsmiller
2. C. F. Barnett
3. M. C. Becker
4. P. R. Bell
5. C. E. Bettis
6. E. S. Bettis
7. D. S. Billington
8. E. P. Blizard
9. C. W. Blue
10. R. L. Brown
11. C. E. Center (K-25)
12. R. A. Charpie
13. R. E. Clausing
14. D. L. Coffey
15. F. L. Culler
16. R. A. Dandl
17. R. C. Davis
18. J. L. Dunlap
19. H. O. Eason
20. R. S. Edwards
21. L. B. Emlet (K-25)
22. J. L. Fowler
23. T. K. Fowler
24. J. E. Francis
25. J. H. Frye, Jr.
26. W. F. Gauster
27. J. H. Gibbons
28. R. A. Gibbons
29. W. R. Grimes
30. E. Guth
31. D. P. Hamblen
32. C. C. Harris
33. A. Hollaender
34. A. S. Householder
35. H. C. Hoy
36. W. H. Jordan
37. C. P. Keim
38. G. G. Kelley
39. M. T. Kelley
40. R. J. Kerr
41. R. L. Knight
42. F. A. Knox
43. N. H. Lazar
44. G. F. Leichsenring
45. T. A. Lincoln
46. S. C. Lind
47. R. S. Livingston
48. J. S. Luce
49. J. N. Luton
50. J. R. McNally, Jr.
51. R. J. Mackin
52. W. D. Manly
53. F. T. May
54. C. Michelson
55. K. Z. Morgan
56. O. B. Morgan
57. J. P. Murray (Y-12)
58. R. V. Neidigh
59. J. H. Neiler
60. M. L. Nelson
61. J. Neufeld
62. C. E. Normand
63. J. R. Potts
64. H. Postma
65. M. Rankin
66. R. G. Reinhardt
67. P. M. Reyling
68. M. T. Robinson
69. P. W. Rueff
70. W. K. Russell
71. E. D. Shipley
72. A. Simon
73. M. R. Skidmore
74. M. J. Skinner
75. A. H. Snell
76. R. F. Stratton, Jr.
77. J. A. Swartout
78. E. H. Taylor
79. A. Tell
80. R. E. Toucey
81. R. M. Warner
82. E. R. Wells
83. T. A. Welton
84. G. K. Werner
85. G. C. Williams
86. C. E. Winters
87. H. P. Yockey
88. O. C. Yonts
89. W. R. Chambers (consultant)
90. E. G. Harris (consultant)
91. F. Low (consultant)
92. H. Lewis (consultant)
93. O. G. Harrold (consultant)
94. D. Alpert (consultant)
95. W. B. Ard, Jr. (consultant)
96. J. W. Flowers (consultant)

97. W. Kerr (consultant)
98. E. D. Klema (consultant)
99. H. Mott-Smith (consultant)
100. H. K. Reynolds (consultant)
101. E. Creutz (consultant)
102. H. Snyder (consultant)
103. L. P. Smith (consultant)
104. P. M. Stier (consultant)
105. J. D. Trimmer (consultant)
106. C. H. Weaver (consultant)
107. Sherwood Reading File (P. R. Bell)
108. Sherwood Reading File (V. Glidewell)
109. Biology Library
110. Health Physics Library
111. Reactor Experimental Engineering Library
112–114. Central Research Library
115–134. Laboratory Records Department
135. Laboratory Records, ORNL R.C.
136. ORNL – Y-12 Technical Library, Document Reference Section

EXTERNAL DISTRIBUTION

137. N. E. Bradberry, Los Alamos Scientific Laboratory
138. H. D. Smythe, Princeton University
139. E. Teller, University of California Radiation Laboratory, Livermore
140. W. A. Fowler, California Institute of Technology
141. R. R. Wilson, General Atomics, La Jolla
142. S. Chandraeskhar, Yerkes Observatory, Williams Bay, Wisconsin
143. Oak Ridge Operations Office
144–145. Division of Research and Development, AEC, ORO (1 copy each to H. M. Roth and R. B. Martin
146–147. Controlled Thermonuclear Branch, AEC, Washington (1 copy each to A. E. Ruark and H. S. Morton)
148–733. Given distribution as shown in TID-4500 (14th ed.) under Controlled Thermonuclear Processes category (75 copies – OTS)